1997

Magnesium based hydrogen storage alloy anode materials for Ni-MH secondary batteries

Ning Cui
University of Wollongong

MAGNESIUM BASED HYDROGEN STORAGE ALLOY ANODE MATERIALS FOR Ni-MH SECONDARY BATTERIES

A thesis submitted in fulfilment of the requirements for the award of the degree of

DOCTOR OF PHILOSOPHY

from the

UNIVERSITY OF WOLLONGONG

by

NING CUI, B. Sc., M. E.

Department of Materials Engineering

March 1997

DECLARATION

I hereby declare that this submission was carried out by the candidate at the Department of Materials Engineering, the University of Wollongong, and that to the best of my knowledge, it contains no materials previously published or written by another person nor materials which to a substantial extent has been accepted for the award of a higher degree of any other university or other institution, except where due acknowledgement is made in the text.

Ning Cui

ACKNOWLEDGEMENTS

I would like to express my sincere appreciation and gratitude to my supervisors, Associate Professor H.K. Liu, Professor S.X. Dou, and Professor D.H. Bradhurst, for their invaluable guidance, constant encouragement and support throughout the course of this thesis work.

Sincere thanks are made to the Head of the Department of Materials Engineering, Professor D.P. Dunne, for his kind permission to use the facilities. Special thanks are made to my friend, Mr. X.L. Wang, for his constant encouragement, great help and profound friendship. Thanks are extended to Mr. G. Tillman, Mr. G.K. Hamilton, Mr. N. Mackie, Mr. R. Kinnell and other staff members in the department for their assistance in the use of facilities, equipment, and instruments.

Sincere appreciation is extended to Associate Professor R. Wheway for his very helpful comments and suggestions. Many thanks are also made to my friends, Mr. B. Luan, Mr. S. Zhong, Mr. P. Bain, Mr. X.G. Zheng, Mr. B.H. Xu, Dr. Y.C. Guo, Dr. M. Ionescu for their valued help and friendship through these years. Special thanks should be made to an Australian couple, Mr.& Mrs. Horton for their kind help and care, especially when I was experiencing a difficult time.

Thanks are also due to the Australian DEET for providing the author the OPRS scholarship, the University of Wollongong for providing the Graduate Faculty Scholarship and the Institute of Materials Technology & Manufacturing for providing the Energy Storage Materials Award.

Finally, I would like specially to express my deep gratitude to my wife, F. Zhong, for her unmeasurable love, understanding and constant support during these years, as well as my lovely daughter, J. Cui. My grateful acknowledgement is also made to my parents, sister, parents-in-law, sister-in-law, for their encouragement and support.

ABSTRACT

Nickel-metal hydride batteries using hydrogen storage alloys as the negative electrode materials have received much attention because of their high energy density, superior charge-discharge characteristics and freedom from poisonous materials. Most recent research in this area is focused on the development of superior negative electrode materials, mainly on rare-earth (mischmetal) systems and Ti-Zr-V Laves-phase type multicomponent hydrogen storage alloys.

Magnesium-based alloys have been used as hydrogen storage alloys since the 1970s. These alloys are considered to be the most promising materials for hydrogen-storage because of their high hydrogen-storage capacity, light weight, abundance of the constituents in the earth's crust, and low-cost compared with alternative systems. Of all the magnesium-based alloys, Mg_2Ni is the most remarkable due to its relative high capacity and favourable kinetics. Nevertheless, magnesium-based hydrogen storage alloys have never been used as electrode materials in Ni-MH secondary batteries because of their sluggish hydriding-dehydriding kinetics and poor corrosion resistance in alkaline aqueous solution.

Numerous investigations have been conducted in order to improve the kinetics of hydriding and dehydriding of magnesium-based alloys at ambient temperature.

Department of Materials Engineering, University of Wollongong, NSW 2522, Australia

Nevertheless, all of these investigations have been concentrated only on the hydriding and dehydriding characteristics of magnesium-based alloys in the gas phase. As yet, no work has been directed towards the electrochemical performance of magnesium-based alloys in an alkaline solution.

The aims of this study are to exploit the feasibility of utilizing magnesium-based hydrogen storage alloys as low cost and high performance anode materials for the Ni-MH secondary battery. For this purpose, Mg_2Ni alloy is made by using a vacuum powder-metallurgical method. The electrode behaviour of this alloy in 6M KOH solution are investigated at room temperature. The experimental discharge capacity of Mg_2Ni alloy electrode is only 8 mAh/g, which is almost negligible compared to its theoretical electrochemical capacity (999 mAh/g). The reasons for this are discussed.

Effect of alloy composition on the charge and discharge performance of Mg_2Ni-type alloy electrodes is investigated, using $Mg_{1.95}M_{0.05}Ni$ (M = Al, Ca, La, Ti and V) ternary alloys and $Mg_{1.9}Al_{0.1}Ni_{1-x}Y_x$ ($x = 0 \sim 0.3$) quaternary alloys. The ternary alloys have the same phase structure as the Mg_2Ni binary does, but the unit cell volume of $Mg_{1.95}M_{0.05}Ni$ alloys increases linearly with the increasing radius of substituting elements. The discharge capacity improves with the ternary substituents studied in the order Ca < La < Ti < V < Al. The addition of small amounts of aluminium or vanadium significantly improves the electrode capacity, which makes the specific capacity more than double (from 8 mAh/g for Mg_2Ni to 18 mAh/g for $Mg_{1.95}Al_{0.5}Ni$

and 17.4 mAh/g for $Mg_{1.95}V_{0.5}Ni$, respectively). Titanium substitution seems also to increase effectively the discharge capacity, while Ca and La have almost no positive effects on the electrode capacity. The value of i_0 increases with increasing radius of substituted metals in the same order as the discharge capacity, which suggests that the charge transfer is the rate-determining step for the dehydriding reaction of $Mg_{1.95}M_{0.05}Ni$ alloys at this test condition. The $Mg_{1.9}Al_{0.1}Ni_{1-x}Y_x$ ($x = 0 \sim 0.3$) quaternary alloy electrodes exhibit a higher electrochemical capacity and better discharge rate performance than Mg_2Ni. The discharge capacity and discharge rate characteristics of the electrodes are substantially improved with increasing x value in $Mg_{1.9}Al_{0.1}Ni_{1-x}Y_x$. For the $Mg_{1.9}Al_{0.1}Ni_{0.7}Y_{0.3}$ electrode, a discharge capacity of 170 mAh/g at room temperature has been achieved. However, an increase in the yttrium content leads to a decrease of cycle life of the electrodes.

The discharge process of Mg_2Ni-type hydrogen storage alloy electrodes is characterized by *ac* impedance spectroscopy at various depths of discharge (DOD) in 6M KOH solution at room-temperature. Comparative measurements also are performed on a $LaNi_5$ electrode. An equivalent circuit has been developed by simulating experimental impedance dispersion. The rate-determining step of discharge process for the magnesium-based hydrogen storage alloy electrodes is dependent on both the alloy compositions and depth of discharge. The unmodified Mg_2Ni electrode has a high charge-transfer resistance and mass-transfer resistance compared to $LaNi_5$ electrode. Additions of yttrium and aluminium in Mg_2Ni reduce considerably both

resistances, thereby producing a remarkable improvement in the discharge capacity and rate-dischargeability.

In order to obtain further improvments in the electrochemical performance of Mg_2Ni-type alloy electrodes at ambient temperature, the multicomponent Mg_2Ni-based alloy ($Mg_{1.9}Y_{0.1}Ni_{0.9}Al_{0.1}$) powder is modified by an ultrasound treatment in an alkaline solution and microencapsulation with Ni-P alloy coating by using a low-temperature electroless plating method. The electrode characteristics such as electrochemical capacity, high-rate dischargeability and cycle life are examined and compared with those of the electrode fabricated from the unmodified alloy powder. The surface modification with ultrasound treatment shows a remarkable increase of electrode capacity and high-rate discharge capability but has little influence on the cycle life. The electrode fabricated from the microencapsulated alloy powder has a higher discharge capacity, better high-rate discharge capability and longer cycle life as well. A specific discharge capacity of 220 mAh/g was achieved for Ni-P coated $Mg_{1.9}Y_{0.1}Ni_{0.9}Al_{0.1}$ at room temperature. The electrochemical performances of Mg_2Ni-type alloy electrodes with and without surface modification are characterized using *dc* polarization and *ac* impedance technique, and their phase compositions and microstructures are characterised by X-ray diffraction and scanning electron microscopy. The surface microencapsulation of alloy powder are effective in improving the electrode discharge performance, but seems to be ineffective in preventing disintegration of the Mg_2Ni-based alloy powder.

A new composite alloy Mg_2Ni - *x* *wt.*%Ti_2Ni has been successfully synthesised using a novel "particle inlaying" method. Scanning electron microscopy and energy dispersive spectroscopy reveal that very fine Ti_2Ni particles were inlaid onto the surface of Mg_2Ni particles by mechanical treatment and sintering. X-ray diffraction analysis indicates that the composite alloys are composed of primary alloys Mg_2Ni, Ti_2Ni and new phases TiNi, Ti-Mg formed in the composite procedure. The electrode characteristics of Mg_2Ni - x *wt.*%Ti_2Ni alloys in an alkaline solution are investigated and compared with those of Mg_2Ni. The discharge capacity of the alloy electrode is effectively improved from 8 mAh/g for Mg_2Ni to 165 mAh/g for Mg_2Ni - 40 *wt.*%Ti_2Ni at ambient temperature, which is almost comparable with that for the Ti_2Ni electrode (170 mAh/g). It is believed that the fine Ti_2Ni particles inlaid on the surface of Mg_2Ni particles play a two fold role: firstly, they hydride-dehydride as hydrogen storage materials themselves; secondly, they provide active sites and pathways for Mg_2Ni hydriding-dehydriding. This is supported by analysis of discharge behaviour and electrochemical impedance spectra studies.

It is concluded that the magnesium-based hydrogen storage alloys are promising negative electrode materials for Ni-MH secondary batteries and may provide further improvements in capacity and cycling performance. The development and application of magnesium-based hydrogen storage alloy electrode materials will breathe new life into the Ni-MH battery and electric vehicle industries.

NOTATION

a_i	activity of species *i* in the bulk electrolyte (electrode)
a_i^0	activity of species *i* at the electrode surface
c_i	concentration of species *i* in the bulk electrolyte (electrode)
c_i^0	concentration of species *i* at the electrode surface
e^-	charge on the electron
f	frequency
i	current density
i_o	exchange current density
n	number of the transferred electrons
β	symmetry factor
η	overpotential
σ	Warburg coefficient
ω	angular frequency
C_d	double-layer capacitance
C_n	discharge capacity at discharge current density of *n* mA/g
D	diffusion coefficient
E_a	activation energy
F	faraday constant
M	molarity
	or metal
R	gas constant
R_t	charge transfer resistance
R_p	polarization resistance
R_s	ohmic resistance
T	absolute temperature
Z	impedance

Z_w	Warburg impedance
AES	Auger electron spectrometer
CL	cycle life
DOD	depth of discharge
EDS	energy dispersive spectroscopy
EIS	Electrochemical impedance spectroscopy
HER	hydrogen evolution reaction
MDP	mean discharge potential
MH	metal hydride
RDS	rate determining step
SEM	scanning electron microscopy
XRD	X-ray diffraction
XPS	X-ray photoelectron spectrometer

CONTENTS

CHAPTER 1 INTRODUCTION

Batteries can store energy in a clean, convenient and efficient manner. They are employed nowadays in almost every field of human activity. There is a growing need for high-specific-power, high-specific-energy battery systems suitable for use in spacecraft, communications, power tools and consumer appliances. Electric vehicles (EVs) are a promising means of transport for the future because they are silent and emission-free. However, the major technological barrier to the development of practical EVs is the lack of an economical battery with sufficient energy density and other essential performance criteria, such as high-rate discharge ability, long cycle life, no toxic materials and low self-discharge rate [1-5].

In the past decade, a novel secondary battery, the nickel-metal hydride (Ni-MH) battery using a hydrogen storage alloy as the negative electrode material has been extensively studied because of the following attractive features: (1) high energy density; (2) superior tolerance to overcharge and overdischarge; (3) capability of a high-rate of charge and discharge; (4) no electrolyte consumption during the charge-discharge cycles; (5) no memory effect like the Ni-Cd battery has; (6) no poisonous materials; and (7) compatibility with the Ni-Cd battery [6-13]. Therefore, the Ni-MH

battery is expected to be an attractive commercial secondary battery of the next generation and a promising candidate for the propulsion of EVs.

The Ni-MH secondary battery is the product of a marriage of nickel-cadmium battery technology with advanced hydrogen storage techniques, and uses a hydrogen storage alloy instead of cadmium as an anode material. The performance of this type of battery is greatly dependent on the anode materials — hydrogen storage alloys. The ideal hydrogen storage alloys for anode materials need to satisfy the criteria [14,15] of: (1) high hydrogen storage capacity; (2) fast kinetics of hydriding/dehydriding; (3) superior corrosion resistance in alkaline solution; (4) long cycle life; (5) low weight; and (6) acceptable cost. Therefore, the focus of recent research in this area has been on developing superior anode materials. Rare-earth system (AB_5-type) and zirconium-titanium-vanadium system (AB_2-type) hydrogen storage alloys now have been intensively investigated as anode materials for the Ni-MH batteries [16-24], and they have begun to be used as negative materials for the commercial production of the Ni-MH batteries [5,25-27]. However, for rare-earth system and zirconium-titanium-vanadium system hydrogen storage alloys, since the specific gravity of alloy elements is large, there is a low hydrogen content in these alloy hydrides, which results in a low weight specific capacity of the hydride electrode. Furthermore, the cost of rare-earth, zirconium, vanadium, titanium and other main elements in these alloys are so high that the large-scale application of Ni-MH battery is limited. Thus, the search for light-

weight and economical anode materials for the Ni-MH battery becomes the most important step for the large-scale application of this battery.

It is well known that magnesium is the lightest of the commercial structural metals (specific gravity 1.74) and the sixth-most abundant element. So, magnesium-based alloys have been investigated as hydrogen storage materials since the 70s [28-31]. These types of alloys are superior to other hydrogen storage alloys in respect to their high hydrogen storage capacity, light weight, abundance of constituents in the earth's crust and low cost. Of all the magnesium-based alloys, Mg_2Ni is the most remarkable due to its relatively high capacity and favourable kinetics. It is known that Mg_2Ni can absorb up to 3.8 *wt.*% hydrogen [32]. This quantity is much higher than the capacities of either rare-earth system hydrogen storage alloys (*e.g.*, $LaNi_5$ absorbs 1.5 *wt.*% hydrogen) or zirconium system hydrogen storage alloys (*e.g.*, $ZrMn_2$ absorbs 1.7 *wt.*% hydrogen) [33]. Therefore magnesium-based alloys have been identified as promising candidates for hydrogen storage materials and anode materials for Ni-MH batteries. On the debit side, however, the reaction of Mg_2Ni with hydrogen requires significant higher temperatures (200-300 °C) and pressures (up to 10 atm) due to hydriding and dehydriding difficulties. Moreover, Mg_2Ni alloy is easily oxidised, especially when it comes into contact with the highly corrosive electrolyte. All of these factors seriously affect its practical use as hydride electrodes.

To date, much work has been carried out to improve the hydriding-dehydriding performance of magnesium-based alloys at low temperature [34-40]. Nevertheless, all of these investigations have concentrated only on the hydriding/dehydriding characteristics of magnesium-based alloys in the gas-phase. As yet, no work has been directed towards the electrochemical performance of magnesium-based alloys in alkaline solution except for our present study [41,42,97]. Thus, it is very important to develop new magnesium-based alloys with fast hydriding/dehydriding kinetics at ambient temperatures and with good corrosion resistance in the KOH aqueous solution used for the large-scale applications of Ni-MH secondary batteries.

This study mainly aims to exploit the feasibility of utilizing magnesium-based hydrogen storage alloys as a low cost and high performance anode material for the Ni-MH secondary battery. In this investigation, the magnesium-based alloys were made by a vacuum powder metallurgy technique and/or a vacuum melting method. Starting from Mg_2Ni, modifications were made by (i) alloy element substitutions; (ii) surface modifications of the alloy powders; and (iii) preparing composites of magnesium-based alloys with non-magnesium alloys. The feasibility of using modified Mg_2Ni-type alloys as rechargeable anode materials for Ni-MH secondary batteries was confirmed for the first time [41]. The rechargeable Mg_2Ni-type alloy anodes which can be charged/discharged effectively in a KOH aqueous solution at ambient temperature were successfully fabricated [42]. Their electrode performances (discharge capacity, capacity decay, cycle life, high-rate capability) were evaluated. A

novel "particle inlaying" method was successfully developed to modify Mg_2Ni alloy for the anode materials [97]. The micro-encapsulation and ultrasonic pre-treatment techniques were applied to improve the electrochemical characteristics of the anodes. The effects of various modifications on the phase structure and electrochemical performance of the alloy electrodes were examined. These anode materials were characterised by scanning electron microscopy (SEM), energy dispersive spectroscopy (EDS), X-ray diffraction (XRD), electrochemical impedance spectra (EIS), cyclic voltammogram (CV) and compared with alloys from the rare-earth system, titanium-system. Finally, a modified Mg_2Ni-type alloy anode with a specific discharge capacity of 220 mAh/g was obtained, which almost matches that of rare-earth system anodes used now. The preliminary results indicate that magnesium-based hydrogen storage alloys are promising anode materials for Ni-MH secondary batteries and have considerable potential for further improvement of their electrochemical performance.

CHAPTER 2 LITERATURE REVIEW

2.1 Metal Hydride Theory

Metal hydride research is becoming a rapidly growing branch of materials science, due to the fact that metal hydrides can store hydrogen safely and conveniently. It provides us with the possibility of using hydrogen to replace oil and natural gas used as energy sources today. Especially, the development of the Ni-MH battery using metal hydrides as anode materials, in turn, breathes new life into the scientific study of metal hydrides.

2.1.1 Fundamental Aspects and Classification

The term " hydride" refers to the combination of hydrogen and a metal or a non-metallic chemical element. Gibb [43] has defined a metal hydride as a compound in which there is a metal-to-hydrogen bond. Mueller and co-workers [44] extensively studied the behaviour of hydrides and discovered that metal hydrides can be classified by the nature of the hydrogen bond into three categories: covalent, saline and metallic hydrides. The various categories of binary hydrides formed by metals and metalloids are shown in Figure 2.1 in terms of the periodic table.

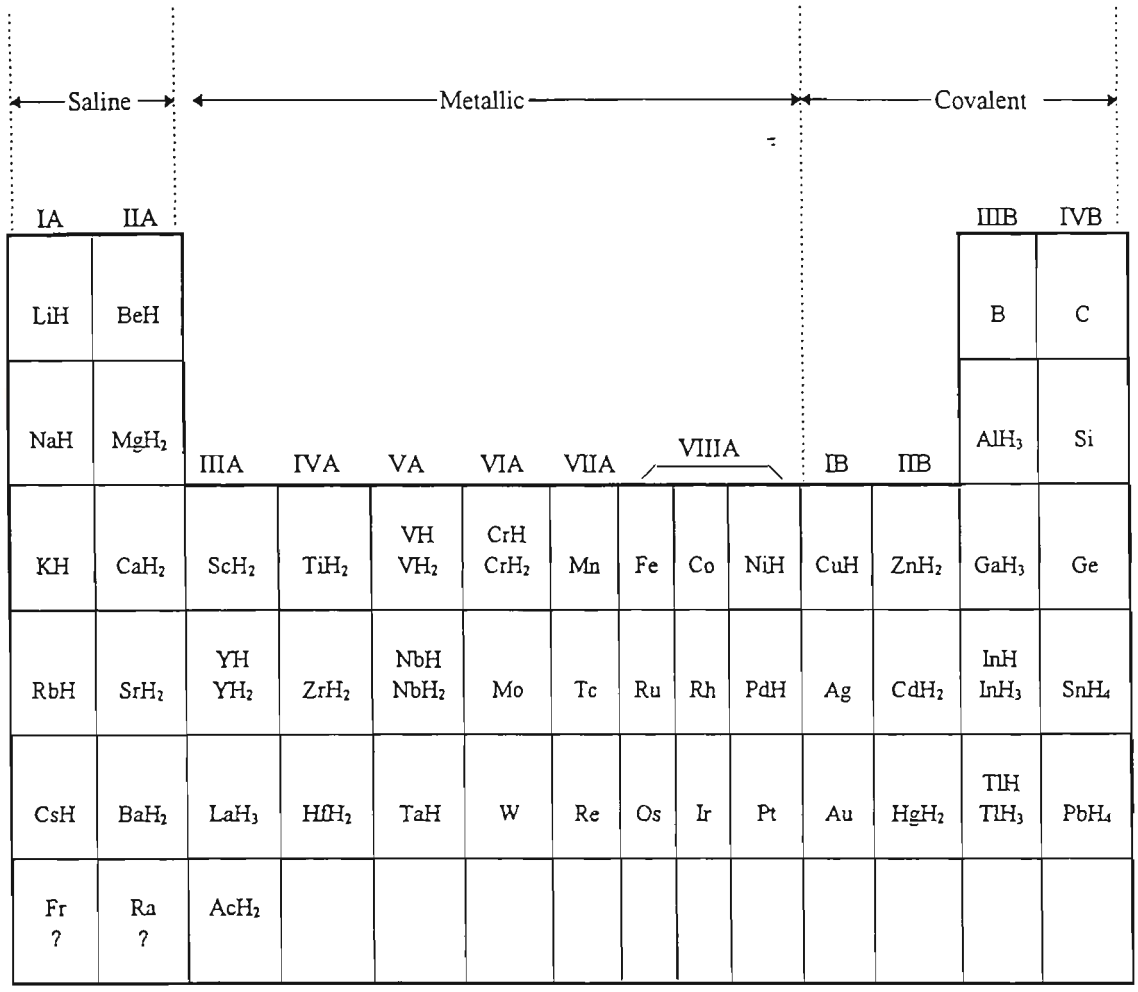

Figure 2.1 Binary hydrides formed by metal in the periodic table [46]

(a) Saline Hydrides

Saline hydrides are formed by the direct reactions of alkali metals and alkaline-earth metals with hydrogen. These hydrides have high enthalpies of formation, high melting points, and are electrically conducting in the molten state. The alkali hydrides have the sodium chloride structure, while the alkaline-earth hydrides (except MgH_2) have an orthorhombic structure which is related to the structure of barium halides [45]. In general, this category of hydrides are too stable for hydrogen storage, with the exception of MgH_2. However, magnesium hydride occupies a special position. The physical properties of this hydride are intermediate between the saline hydrides and covalent hydrides. MgH_2 may thus be regarded as a transition hydride between the saline and covalent hydrides.

(b) Covalent Hydrides

Beryllium hydride and metal (metalloid) hydrides of groups IB through IVB in the periodic table belong to covalent hydrides. The structure of many covalent hydrides is believed to be polymeric [44]. These hydrides have low melting and boiling points. They are generally thermally unstable and their instability increases with increasing atomic weight of the parent element. Since none of these hydrides is formed by reacting elements directly with hydrogen, they have attracted very little interest for the practical application of hydrogen storage.

(c) Metallic Hydrides

Metallic hydrides are formed by the reaction of hydrogen with most of the transition element metals and rare-earth metals. These hydrides have metallic properties such as lustre, hardness, and metallic conductivity, but unlike metals they are quite brittle. Another characteristic of metallic hydrides is their deviation from stoichiometry, *i.e.* these hydrides have a wide non-stoichiometric region, even when they are represented as MH or MH_2.

2.1.2 Bonding and Electronic Structures

2.1.2.1 Chemical Bonding Model

The nature of the chemical bonding in metal hydrides has been the subject of much controversy [47-51]. There are three different models which have been proposed to explain the bonding of hydrogen in metal hydrides:

The first one, the *protonic model* [52], assumes that hydrogen donates its electron to the d-band of the transition metal forming an alloy with the metal. Hydrogen thus may be considered to exist as protons in the hydride lattice. This model is mostly used for transition metal hydrides.

The second one, the *anionic model* [53], is essentially the converse of the first. According to this model the hydrogen accepts an electron from the metal to form a

hydride anion and metal cation, *i.e.* a saline hydride. The bonding of alkali metal and alkaline-earth metal hydrides belongs to this model.

The third one, the *covalent model*, is based on a predominantly covalent bond between the metal and hydrogen. In this model, the bond between hydrogen and the metal is of the nonpolar electron-sharing type where valence electrons are shared on a fairly equal basis between the elements held by the bond [44]. This model is often used for Beryllium and the B group metal hydrides in the Periodic Table.

2.1.2.2 Modern Electronic Band Theory

Several researchers have applied modern electronic band theory to metal hydrides [54, 56-60]. They discussed electronic structure and banding in metal hydrides (monohydrides, dihydrides and trihydrides) and suggested that in monohydrides, the *d*- and *f*-states are only slightly perturbed and the metal *s*- and *p*-states hybridize with the hydrogen 1s-orbital and are strongly perturbed. These states are lowered substantially in energy and become very much hydrogen-like (see Figure 2.2 b). In dihydrides, the Fermi energy falls in a band derived from the metal d-states and a new band appears below the d-band which arises from the anti-bonding combination of the 1*s*-orbital of two hydrogen atoms in the unit cell. The stability of the dihydrides is attributed to this new band which can accommodate electrons at a rather low energy. The position of this band is determined by the hydrogen-hydrogen separation. If the hydrogen-hydrogen separation is small, the new band has high energy and is unlikely

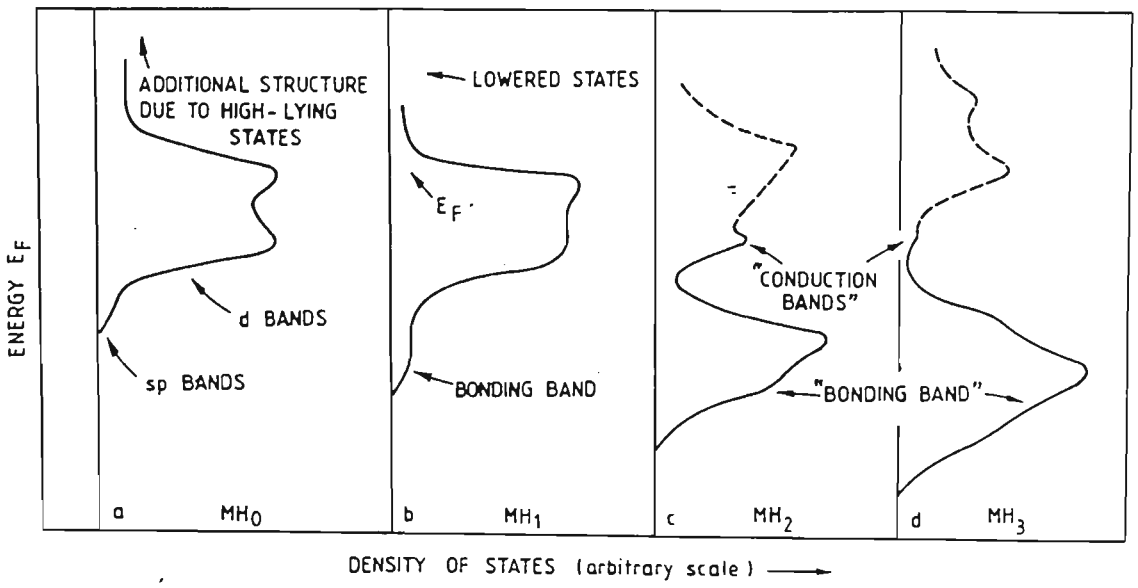

Figure 2.2 Schematic representation of density of states (DOS) on the hydrogenation [60]

to be filled by electrons originally associated with hydrogen. For large H-H separations the band is low-lying and will be filled (see Figure 2.2 c). In trihydrides, another band also appears below the d-band (see Figure 2.2 d) because of the interaction of anti-bonding states between hydrogen in octahedral site and hydrogen in tetrahedral site. The H-H separation or interstitial separation determines the energy of this band. In turn, the interstitial separation is determined by the metal-metal distance.

2.1.3 Intermetallic Hydrides

The binary hydrides in the periodic table (Figure 2.1) fall essentially into two classes: those too stable for a practical application, such as MgH_2 or CaH_2 on the one hand, and the unstable hydrides such as FeH and NiH on the other. The intermetallic hydrides, because they are composed of elements forming stable and unstable hydrides, are expected to bring the enthalpies into a very convenient range for practical purposes [63]. Thus, emphasis in developing new metallic hydrides was placed on the hydrides of intermetallic compounds.

2.2 Hydrogen Storage Alloys

During the early 1970s, intermetallic compounds (or alloys) with rapid hydrogen absorption properties near room temperature were discovered [61]. Since then, the use of hydrogen storage alloys as a novel energy storage material has attracted world wide interest [61-72]. Practical applications for these new materials include hydrogen storage for a multitude of purposes, hydrogen compression and purification, heat pumping, refrigeration, and thermal storage. More recently, utilizing hydrogen storage alloys instead of cadmium as an anode material in alkaline rechargeable batteries has brought about a revolution in power sources, which will improve the prospects for the early use of electric vehicles becoming more widespread. It has been observed that many metals and alloys react reversibly with hydrogen to form hydrides. The kinetics

of absorption of hydrogen by these alloys are very rapid compared with those of the pure elements [63,67,73]. Hence, more recently attention has been given to the investigation and development of various hydrogen storage alloys.

2.2.1 Types of Hydrogen Storage Alloys

Hydrogen storage alloys are usually classified according to the stoichiometric relation of composition into four categories including AB_5-type, AB-type, A_2B-type and, AB_2-type (Laves-phase type). In these alloys, the A component is the one which forms the stable hydride. The B component performs several functions [24]: (i) it could play a catalytic role in enhancing the hydriding/dehydriding characteristics; (ii) it can alter the equilibrium pressures for the hydrogen absorption/desorption and raise it or lower it to a desired level and (iii) it could also add to the stability of the alloys because some the A component could be readily oxidized. Some typical binary hydrogen storage alloys are presented in Table 2.1. The hydriding/dehydriding characteristics of these alloys could be altered by a partial substitution or a small addition of other elements. The roles of these substitutes or additives have been summarized by A. Anani *et al.* [24] as follows: (i) to increase or decrease the crystal lattice constants thereby changing the equilibrium pressure for hydrogen absorption/desorption; (ii) to decrease the hysteresis during hydrogen absorption/desorption; (iii) to catalyze hydriding/dehydriding reactions and (iv) to improve the stability of these alloys thus preventing oxide formation on one or more of the components.

Table 2.1 Some examples of binary hydrogen storage alloys

Type	Hydrogen Storage Alloys
AB_5	$LaNi_5$, $MmNi_5$ (Mm = misch metal) (Ni being partially substituted by Al, Co, Cu, Cr, Mn, Si, and La, Mm by Ca, Nd, Pt, Zr.) $CaCu_5$, $CaNi_5$.
AB	TiNi, TiFe, TiCo, TiCu, TiMn.
A_2B	Ti_2Ni, Mg_2Ni, Mg_2Cu.
AB_2	$TiMn_2$, TiV_2, $TiMn_2$, $ZrNi_2$, $ZrMn_2$, $ZrCr_2$.

According to the affinity for hydrogen of the main element in the alloys, hydrogen storage alloys can be also categorized into: rare-earth system (AB_5-type), titanium system (AB-type or A_2B-type), zirconium system (AB_2- type), or magnesium system (A_2B-type).

2.2.2 Thermodynamic Properties

2.2.2.1 *P-C* Isotherms

The behaviour of a metal-hydride system is generally represented by a pressure-composition-temperature relationship, *i.e.* a *P-C* isotherms. If the system forms a single hydride phase, the characteristic *P-C* isotherm is shown in Fig. 2.3 (a). Initially the isotherm ascends steeply as hydrogen dissolves in the metal to form a solid solution which by convention is designated as the α phase. At low concentrations the behaviour is ideal and the isotherm obeys Sievert's law, *i.e.*

$$H_{solid} = K_s P^{1/2} \qquad (2.2\text{-}1)$$

where H_{solid} is the concentration of hydrogen in the metal. K_s is Sievert's constant and P is the equilibrium hydrogen pressure. As the H content of the solid increases, the system departs from ideal behaviour due to H-H attractive interactions primarily caused by elastic strain in the metal [75]. This is reflected by a decreasing slope in the isotherm. The constant-pressure plateau in Figure 2.3 (a) corresponds to the region where the two phases, hydrogen-saturated metal (designated the α phase) and hydride phase (designated the β phase), coexist. The appearance of the plateau is a consequence of Gibbs' phase rule, $F = C - P + 2$. In this system, the number of components, C, is 2 (hydrogen and metal); the number of phases, P, is 3 (one gaseous, two condensed). Therefore, the degree of freedom $F = 2 - 3 + 2 = 1$. The

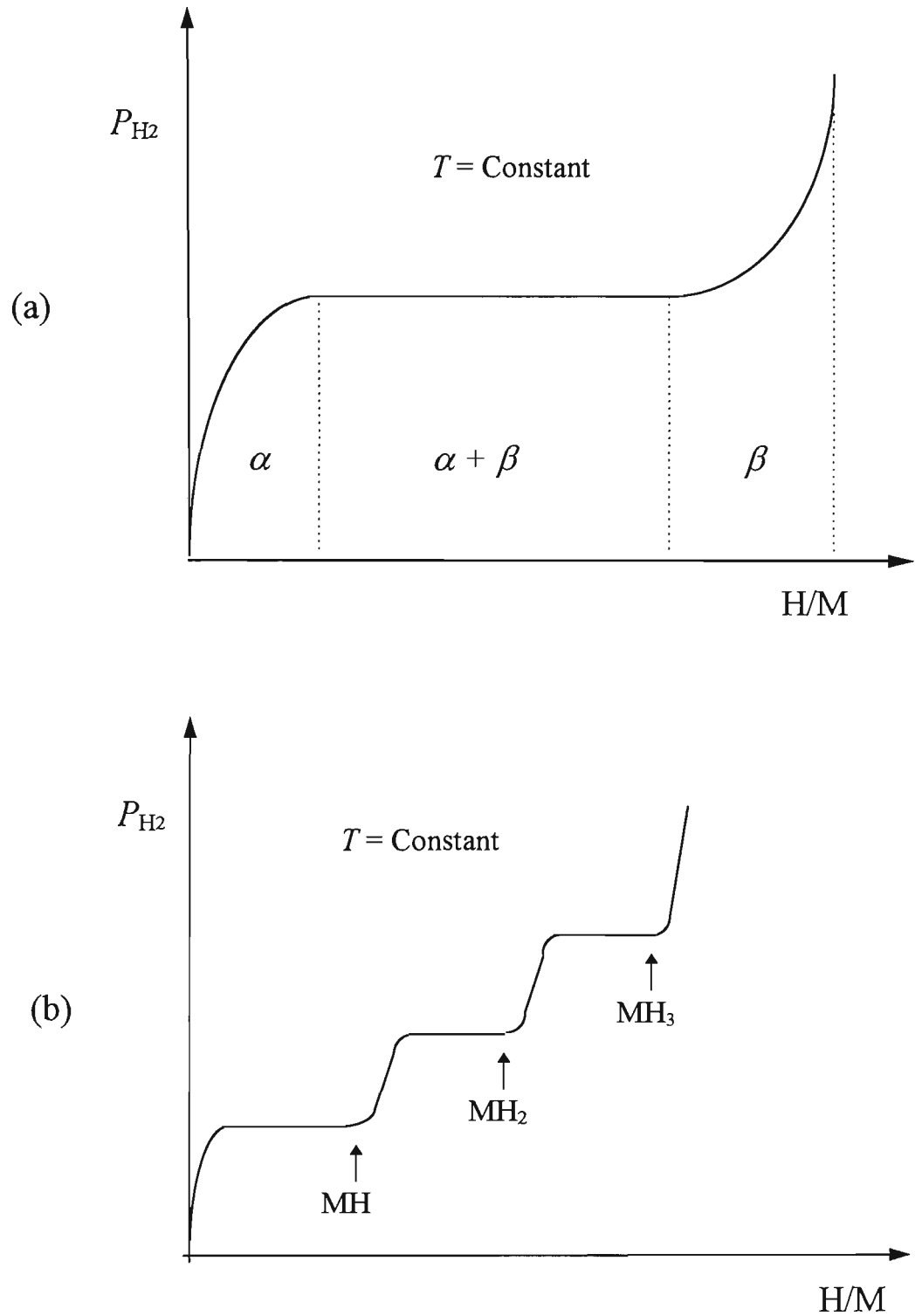

Figure 2.3 Pressure-composition isotherms for metal-hydrogen system in which: (a) a single-hydride-phase forms [74]; (b) multi-hydride-phases form [65]

plateau length in the *P-C* isotherms diagram depends on the temperature. As the temperature is increased there is a decrease in the plateau length resulting in the α-phase approaching the β. At some critical temperature the plateau disappears and the α-phase converts continuously into the β-phase [76]. Sometimes, if a second hydride phase exists, another higher plateau will appear as shown in Figure 2.3(b).

2.2.2.2 Ternary Hydride Stability Models

A number of models dealing with the relative stability of ternary hydrides have been proposed. Most of these models can be characterized as empirical models, the stability of the hydrides being considered to correlate with the interstitial hole size [77, 78], the unit cell volume [79, 80], the compressibility [81] or the shear modulus [82], the heat of formation of the corresponding binary hydrides [83] and the heat of formation of the uncharged intermetallic compounds [84-86] or with features of the band structure [87-89]. Although these models also have their limitations, they are suitable for predicting trends and are useful in the search for new hydrogen-absorbing materials [90]. The concept of a minimal H-H distance imposes a restriction on the maximum hydrogen content of binary and ternary hydrides [84, 91].

2.2.2.3 Hydride Formation Enthalpy and Stability

The chemical reaction equation for the exothermic hydride formation from metals (or alloys) and hydrogen gas is as follows [65]:

$$M + x/2\ H_2 \Leftrightarrow MH_x + \Delta H_f \qquad (2.2\text{-}2)$$

The standard enthalpy of formation, ΔH_f, of a metal hydride MH_x may be determined from the van't Hoff equation:

$$d\ln K/dT = \Delta H_f / (RT^2) \quad (2.2\text{-}3)$$

where T is absolute temperature, R is the gas constant, K is the equilibrium constant for the reaction (2.2-2) and is given by

$$K = a_{MHx} / (a_M f_{H2}^{x/2}) \quad (2.2\text{-}4)$$

Under ideal conditions the activity of solid may be taken as unity and the fugacity as the pressure, (2.2-4) becomes:

$$K = P_{H2}^{-x/2} \quad (2.2\text{-}5)$$

Then (2.2-3) may be rewritten as:

$$d\left(\ln P_{H2}^{-x/2}\right) = \left(\Delta H_f / RT^2\right) dT \quad (2.2\text{-}6)$$

which upon integration yields:

$$\ln P_{H2} = 2/x \left(\Delta H_f / RT\right) + C = A / T + B \quad (2.2\text{-}7)$$

where P_{H2} represents the plateau pressure at a particular temperature T and C is the constant of integration. The enthalpy of formation of hydride can be calculated from the slope of the straight line obtained by plotting $\ln P_{H2}$ versus $1/T$. The van't Hoff curves for various hydrides are given in Figure 2.4, and thermodynamic data for some representative hydrides are listed in Table 2.2.

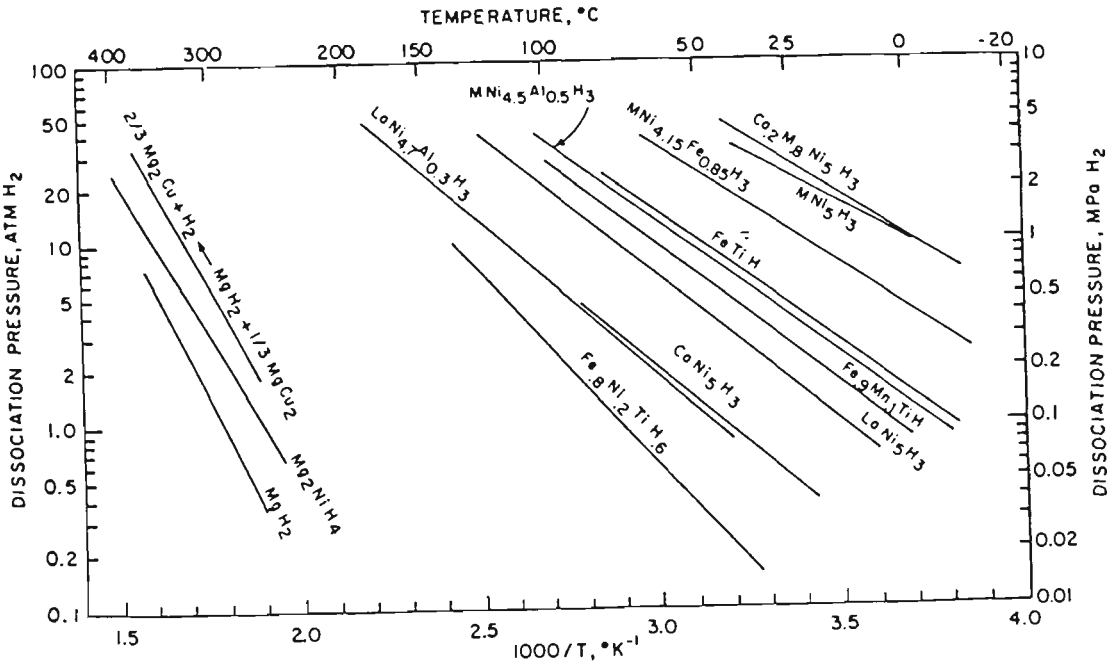

Figure 2.4 van't Hoff plots (desorption) for various hydrides [92]

Miedema and co-workers [93,94] have proposed a semi-empirical theory to estimate the enthalpy of formation of a ternary hydride from an intermetallic compound. It can be expressed as following:

$$\Delta H_f(AB_nH_{2m}) = \Delta H_f(AH_m) + \Delta H_f(B_nH_m) - \alpha\Delta H_f(Ab_n) \qquad (2.2\text{-}8)$$

where AB_n is the original intermetallic compound, ΔH_f is the enthalpy of formation and α is the parameter depended on the structure of the hydrides. According to equation 2.2-8, the more stable are the original intermetallic compounds ($\Delta H_f(AB_n)$ <<0), the less stable will be the hydride AB_nH_{2m}. Equation 2.2-8 is thus called the "rule of reverse stability". It was reported that the rule of reverse stability seems to

agree qualitatively with experimental results for most hydrides of hexagonal AB_5 compounds and hydrides of cubic and hexagonal AB_2 compounds, but it fails in the case of hydrides of AB compounds (CsCl structure) like TiFe, TiCo and TiNi [95].

Table 2.2 Thermodynamic data for some representative hydrides[a] [75]

Hydrides	Conversion	ΔH kJ(mol H_2)$^{-1}$	ΔS J(K mol H_2)$^{-1}$	Ref.
$LaNi_5H_x$	$\beta \rightarrow \alpha$	-30.01	-108	64
$LaNi_5H_x$[b]	$\alpha \rightarrow \beta$	29.4	--	65
$LaNi_{4.6}Al_{0.4}H_x$	$\beta \rightarrow \alpha$	-36.3	-109	66
$FeTiH_x$	$\gamma \rightarrow \beta$	-33.3	-104	67
$FeTiH_x$[b]	$\beta \rightarrow \alpha$	-28.1	-106	67
Mg_2NiH_4	$\beta \rightarrow \alpha$	-64.2	-122	68
MgH_2	$\beta \rightarrow \alpha$	-74.2	-134	69
MgH_2[c]	$\beta \rightarrow \alpha$	-77.1	-137	68
TiH_2	metal $\rightarrow \delta$	-133	-125	69
LaH_2	$\alpha \leftrightarrow \beta$	-206	-147	69

a - Via *P-C-T* measurement; b - Calorimetric measurement

c - Catalyzed

Based on empirical observation and thermodynamic principles, Reilly [75,96] has proposed a relatively simple set of rules for all intermetallic hydrides. These simple rules have been found to be quite useful. They may be summarised as follows:

(1) An intermetallic compound which reacts directly and reversibly with hydrogen to form a distinct hydride phase, has at least one of its metal components reacting directly and reversibly with hydrogen to form a stable binary hydride.

(2) If the hydriding reaction takes place at a temperature where the metal atoms are mobile, the system will assume its most favoured thermodynamic configuration.

(3) In the case where the metal atoms are not mobile at the hydriding temperature, only such hydride phases which are structurally very similar to the starting intermetallic compound are formed because the metal atoms are essentially frozen in place.

2.2.3 Kinetic Properties

The kinetics of hydrogen storage in metal hydrides have been studied by many researchers. However, the results that have been obtained to date are inconsistent due to the difficulties in performing the kinetic experiments [214]. Boser [215] and Miyamoto *et al.* [216] measured the absorption rate of hydrogen in $LaNi_5$ at the initial stage of the two-phase region. They reported that the rate controlling step was the chemical reaction of the hydrogen atom with an α-phase solid solution at the interface of the two phases, while Tanaka *et al.* [217] and Livesay *et al.* [218] reported that the rate controlling step was the diffusion of the hydrogen molecule through the β-phase. Wallace *et al.* [219] and Soga *et al.* [220] revealed that the controlling step was the

chemical adsorption of hydrogen molecules on the nickel surface. Lu *et al.* [221] and Park *et al.* [222] asserted that the controlling step changed with the extent of reaction. A study to determine the effects of aluminium and iron substitution on the reaction kinetics of $MmNi_5$ was made by Huang *et al.* [223]. They found that $MmNi_{4.5}Al_{0.5}$ has thermodynamic and kinetic properties similar to those of $LaNi_5$. It was concluded that aluminium and iron substitutions have deleterious effects on the reaction kinetics of $MmNi_5$ hydride. Recently, Lee and co-workers [224-226] re-investigated the reaction kinetics of hydrogen storage in $LaNi_5$, as well as in $CaNi_5$ and Mg_2Ni. They observed that the reacted fractions for $LaNi_5$ and $CaNi_5$ are linearly proportional to the reaction time at a fixed temperature and pressure. They concluded that the rate controlling steps for $LaNi_5$ and $CaNi_5$ are the dissociative chemisorption of the hydrogen molecule on the alloy surface, whose apparent activation energy was 4700 cal (g-mol H_2)$^{-1}$ for $LaNi_5$ and 2000 cal (g-mol H_2)$^{-1}$ for $CaNi_5$.

A little work has also been carried out on the kinetics of the hydriding reaction of Mg_2Ni [227-233]. However, because of difficulties in performing the kinetic experiments, the results obtained are inconsistent. Akiba *et al.* [227, 228] reported in their experiments that the rate controlling step in the later stage of the reaction was the diffusion of the hydrogen atom through β-phase hydride, while Stucki *et al.* [230] proposed that the reaction rate was heat transfer-limited. On the other hand, Song *et al.* [231] suggested that the rate was controlled by the forced flow of hydrogen molecules though pores, interparticle channels or cracks in the sample and heat

transfer. Han *et al.* asserted that rate controlling step was changed according to the extent of the reaction from the forced flow of hydrogen molecules to chemical reaction at the interface of two phase hydrides. Recently, Jung *et al.* [226] also observed that the rate controlling step was changed as the reaction proceeded. In the initial step in which the reacted fraction was less than 0.05, the rate controlling step was the chemical reaction of the hydrogen atom with α- phase hydride at the interface between α- and β- hydrides, while the rate in the intermediate step was influenced by both the chemical reaction and the diffusion of hydrogen atom through the β-phase hydride. In the latter step in which the reacted fraction exceeds the range from 0.36 to 0.5, the rate controlling step was the diffusion of the hydrogen atom. In view of these results, the discussions and conclusion derived from different researchers are inconsistent since they used different approaches. The kinetic properties of electrochemical hydriding and dehydriding in the electrolyte have so far not been discussed.

2.2.4 Electrochemical Characteristics of Hydrides

In the case of gaseous hydrogen storage as discussed above, the absorption process involves two distinct stages: (i) the dissociation of hydrogen molecules at the surface of the materials into atomic hydrogen, and (ii) the atomic hydrogen then penetrates the surface and dissolves in the lattice. In the desorption process, the atomic hydrogen first comes to the surface from the lattice and then combines at the surface to form

molecular hydrogen. However, hydriding in alkaline solution differs from that in hydrogen gas in stage (i), *i.e.* the hydrogen atoms are directly supplied by electrolysing water rather than by dissociating hydrogen molecules.

2.2.4.1 Hydriding-Dehydriding in Electrolyte

In alkaline solutions the overall reaction during charge and discharge is as follows [97]:

Solid-liquid interface reaction:

$$H_2O + M + e^- \underset{\leftarrow \text{discharge}}{\overset{\text{charge} \rightarrow}{\Leftrightarrow}} MH_{ad} + OH^- \qquad (2.2.4\text{-}1)$$

Solid-State Reaction:

$$MH_{ad} \underset{\leftarrow \text{discharge}}{\overset{\text{charge} \rightarrow}{\Leftrightarrow}} MH_{lattice} \qquad (2.2.4\text{-}2)$$

When charging, hydrogen is generated by electrolysing water according to reaction (2.2.4-1), and presents at the cathode surface in a highly active atomic state. Then it diffuses into the lattice positions of metal phases to form a metal hydride as expressed (2.2.4-2). During discharging, the atomic hydrogen diffuses from the lattice position in the alloy to the metal/electrolyte interface where the electrochemical charge transfer reaction occurs. The metal hydride electrode therefore can be considered as a hydrogen electrode.

Wakao and Yonemura [98] conducted electrochemical measurements on the hydrogen storage alloy electrodes. The equilibrium hydrogen pressure, partial molar enthalpy ΔH and partial molar entropy ΔS of hydride (or deuteride) formation were calculated on the basis of the electrode potentials. They reported that the values determined electrochemically agreed very closely with those obtained from the solid-gas equilibrium. The current is strongly governed by the diffusion process at a large anodic polarization of the hydride (deuteride) electrodes. They concluded that the diffusion species for metal electrodes with a low enthalpy ΔH of hydride (or deuteride) formation are OH^- (OD^-) ions in the electrolyte solution, while the diffusion species at higher values of ΔH are hydrogen (or deuterium) atoms in the metal because of the increasing activation energy of hydrogen diffusion.

2.2.4.2 Electrochemical P-C Isotherms

Sakai *et al.* [99] reported that hydrogen pressure calculated from the equilibrium potential using electrochemical data in a concentrated KOH solution was in good agreement with the equilibrium hydrogen pressure obtained by the conventional Sievert's method based on a gas-solid reaction for the system of alloys $LaNi_{5-x}M_x$ (where M = Ni, Cu, Cr, Mn, and Al). In an equilibrium state, the potential of the anode corresponds to a pressure of hydrogen gas on the surface which is in equilibrium with atomic hydrogen in the hydride ($H_2 \Leftrightarrow 2H$) according to the Nernst equation as follows [100]:

$$E(\mathrm{H}) - E(\mathrm{HgO/Hg}) = [E(\mathrm{H})^0 - E(\mathrm{HgO/Hg})^0] + (\mathrm{RT/2F}) \ln [a(\mathrm{H_2O})/a(\mathrm{H_2})]$$

$$= [E(\mathrm{H})^0 - E(\mathrm{HgO/Hg})^0] + (\mathrm{RT/2F}) \ln [a(\mathrm{H_2O})/\gamma(\mathrm{H_2})P(\mathrm{H_2})] \quad (2.2.4\text{-}3)$$

where $[E(\mathrm{H})^0 - E(\mathrm{HgO/Hg})^0]$ is the standard potential of electrode, $a(\mathrm{H_2O})$ the activity of water, $a(\mathrm{H_2})$ the activity of hydrogen, $\gamma(\mathrm{H_2})$ the fugacity coefficient, $P(\mathrm{H_2})$ the hydrogen partial pressure. On the basis of equation (2.2.4-3), they plotted electrochemical *P-C* isotherms and compared them with gaseous *P-C* isotherms for $LaNi_5$ in Figure 2.5 (a). It was found [101] that electrochemical *P-C* isotherms agreed with gaseous *P-C* isotherms, although the former method provided pressure values a little higher than the latter. The plots of plateau pressure (P_{eq}) *vs.* T^{-1} for both methods are shown in Figure 2.5 (b), the slopes being excellent agreement with each other. Thus, it is more convenient using the electrochemical *P-C* isotherms than gaseous *P-C* isotherms for the study of hydriding-dehydriding behaviour in electrolytes. However, there was no similar work to be found in the literature on other hydrogen storage alloy systems.

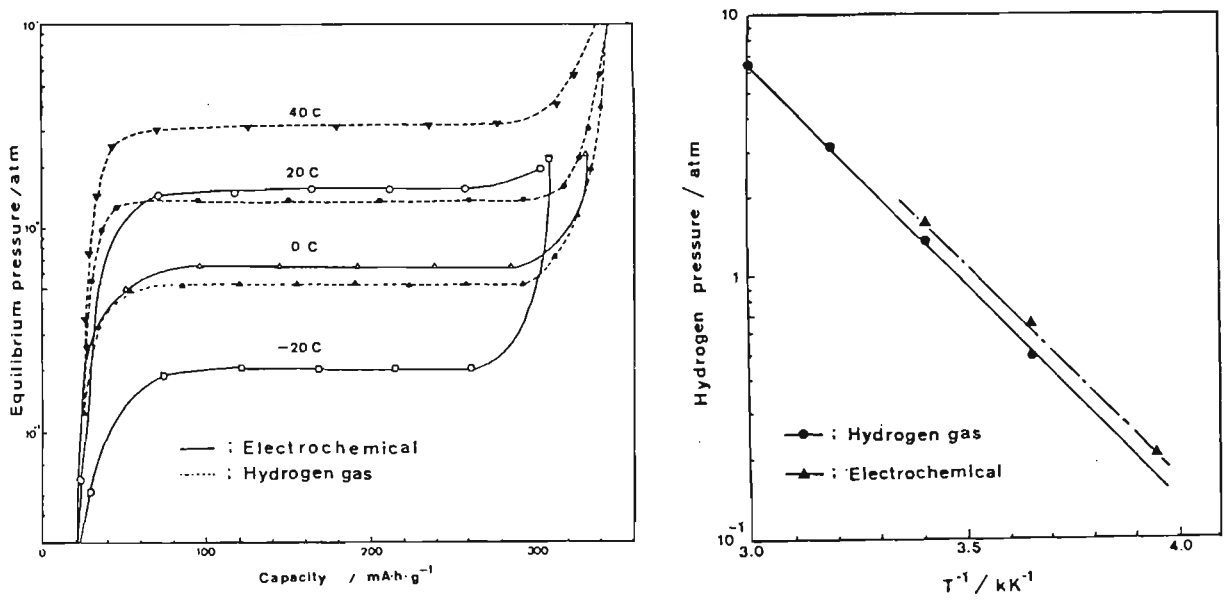

(a) **(b)**

Figure 2.5 Electrochemical *P-C* isotherms for $LaNi_5$ electrode [101].
(a) comparision of *P-C* isotherms by the gas pressure and electrochemical methods; (b) temperature dependence of average hydrogen pressures obtained by the gas pressure and electrochemical methods

2.3 Magnesium and Magnesium-based Alloys

2.3.1 Introduction

Magnesium is light, abundant and cheap compared to the alternative hydrogen storage materials. Magnesium hydride, MgH_2, contains 7.6 *wt.* % hydrogen, which is much more than the hydrogen contents of the other metal hydrides (see Table 2.3). The reversible hydriding of magnesium performs according to the reaction:

$$Mg + H_2 \Leftrightarrow MgH_2 \qquad (2.3\text{-}1)$$

The crystal structure of MgH_2 has been extensively studied by many authors. Ellinger *et al.* [108] used X-ray diffraction to determine that MgH_2 has a body-centred tetragonal lattice of the rutile type, with two Mg atoms at (0, 0, 0) and ($\frac{1}{2}$, $\frac{1}{2}$, $\frac{1}{2}$) and four H atoms at (x, x, 0), (1-x, 1-x, 0), (x+$\frac{1}{2}$, $\frac{1}{2}$−x, $\frac{1}{2}$) and ($\frac{1}{2}$-x, $\frac{1}{2}$+x, $\frac{1}{2}$), where x = 0.306 per unit cell. The crystal structure of MgH_2 is shown in Figure 2.6. The lattice parameters are a = 4.517 Å and c = 3.021 Å. Each Mg atom co-ordinates to six H atoms and each H atom to three Mg atoms with a H-Mg bond distance of 1.95 Å. Zachariasen *et al.* [109] confirmed this structure and the value of 0.306 for x by neutron-diffraction. Studies of Freundlich *et al.* [110] showed that MgH_2 prepared directly from the elements has the same structure as that prepared from an organo-metallic compound.

Table 2.3 Hydrogen contents in some metal hydrides [102-107]

Metal or Alloy	hydride	Hydrogen content *(wt. %)*
$ZrMn_2Fe_{0.8}$	$ZrMn_2Fe_{0.8}H_{3.4}$	1.4
Ti_2Ni	Ti_2NiH_2	1.4
$LaNi_5$	$LaNi_5H_6$	1.5
$ZrMn_2$	$ZrMn_2H_{3.6}$	1.7
FeTi	FeTi $H_{1.95}$	1.9
V	VH_2	2.1
Mg_2Ni	$Mg_2Ni\ H_4$	3.6
Mg	MgH_2	7.6

There has been some controversy as to whether the hydrogen anion (H^-) or the magnesium cation (Mg^{2+}) is the diffusion species and hence the rate-controlling ion, in the Mg-H reaction [112-114]. Luz *et al.* [114] have carried out experimental work to solve this problem. Kirkendall marker wires were placed at the magnesium surface. After hydriding, the position of the markers was noted. Since the markers appeared to move outward during the formation of a MgH_2 layer (Figure 2.7), signifying that the hydride is formed by hydrogen flow past the surface magnesium atoms, hydrogen must be the diffusing species. The model is illustrated schematically in Figure 2.8.

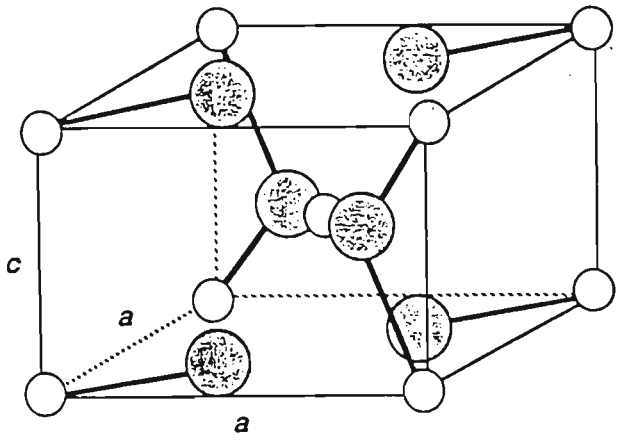

Figure 2.6 Arrangment of H and Mg atoms in the unit cell of MgH_2 of the rutile type [111]. The open circles are Mg atoms, and the shaded circles represent H atoms. The thick line between the atoms are used for visual purposes.

Although pure magnesium is the best selection from the viewpoint of hydrogen absorbing capacity and is relatively inexpensive, it has serious weaknesses. Firstly, the reaction (2.3-1) of magnesium with hydrogen is generally extremely slow, and it requires relatively high temperatures and pressures to get reasonable reaction rates [115-119]. Secondly, Mg has a high affinity for oxygen and its hydride MgH_2 is unstable in water [120]. The latter property limits the electrochemical utilisation of this material. Therefore, numerous investigations have been conducted in order to improve the kinetics of magnesium. The approaches can be summarized as follows: (i) alloying; (ii) composites; (iii) oxide additives; (iv) surface modification.

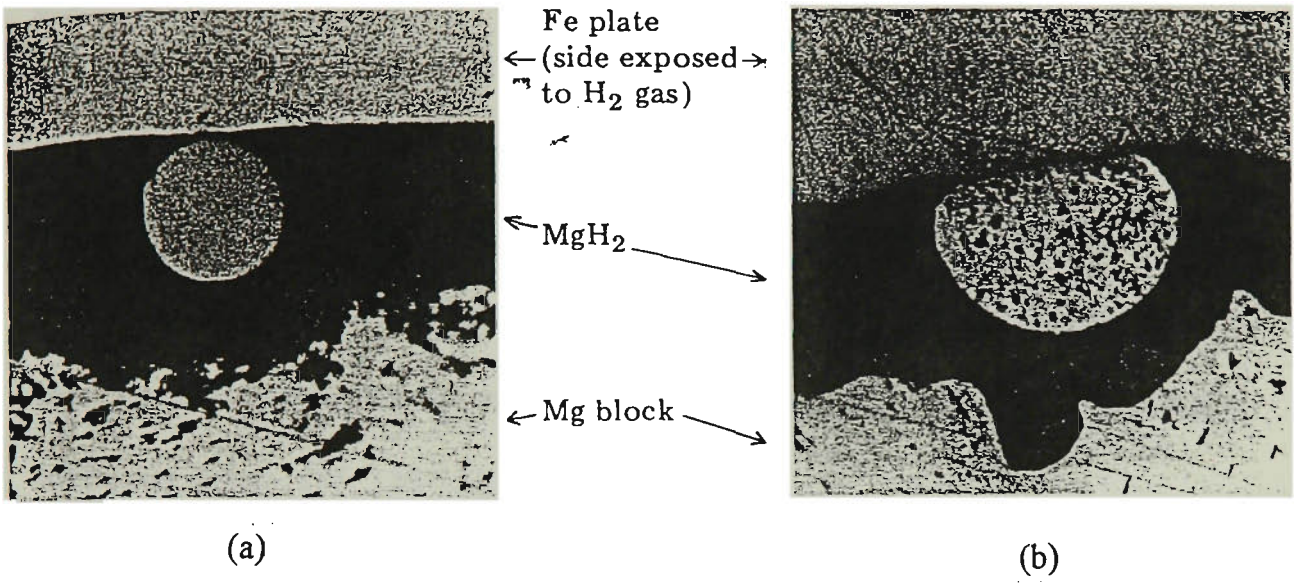

Figure 2.7 A photomicrograph of section perpendicular to Kirkendall marker following hydriding [114]. (a) tungsten wire used as Kirkendall marker; (b) copper wire used as Kirkendall marker.

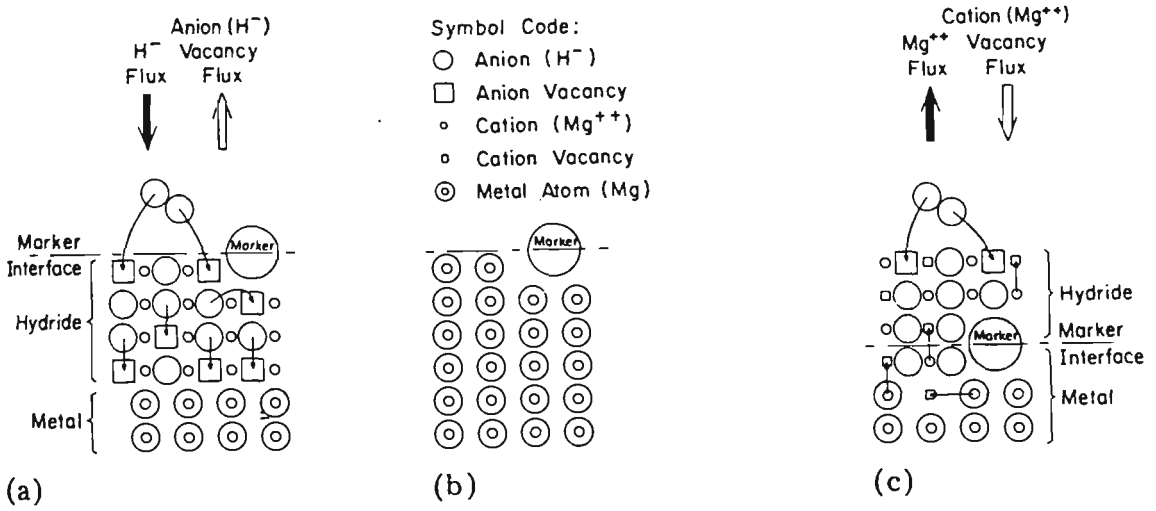

Figure 2.8 A schematic illustration of the dependence of the Kirkendall marker position on the diffusion species upon the hydriding of magnesium [114]. (a) marker position when the H^- anion is diffusing species; (b) marker position prior to hydriding; (c) marker position when the Mg^{2+} cation is the diffusing species.

2.3.2 Alloying

In order to eliminate the limitations of using magnesium alone and to find the optimum alloy for hydrogen storage, extensive studies of numerous metal additions to magnesium (binary, ternary and multi-component) have been carried out. It has been reported that the reactivity of magnesium with hydrogen is modified by alloying it with other metals [135, 120-122, 121-131].

2.3.2.1 Overview of Magnesium-Based Alloys

It was reported that the hydriding reaction of magnesium may be accelerated by the presence of some metals or intermetallics as catalysts [121, 122]. Pezat *et al.* [132] pointed out that additions of rare-earth (La, Ce, Mm) improve the reaction kinetics, while addition of small amounts of transition metals increase markedly the desorption rates. Mintz *et al.* [133] have found that the addition of small amounts (<1 *at.*%) of group IIIA elements enhances the activation process by markedly reducing the activation energy for hydrogenation. Libowitz *et al.* [123] observed originally that the ternary hydride, $ZrNiH_3$, was more unstable than the binary hydride, ZrH_2. The same idea was followed by Reilly and Wiswall [113, 124] for the stable Mg-H_2 system. They reported that magnesium intermetallic compounds, Mg_2Ni and Mg_2Cu, have a fairly rapid reaction with hydrogen at moderate temperatures and a lower decomposition temperature than their parent hydride, MgH_2. They concluded that the

presence of Ni or Cu has a catalytic effect on the hydrogenation of Mg. On the other hand, Mg_2NiH_4 might be expected to be suitable for aqueous service based on a comparision with the $LaNi_5$ alloy system. Although LaH_3 is unstable in water, $LaNi_5H_6$ has good stability and good electrochemical properties [120].

Rudman *et al.* [125, 126] have found that the hydriding kinetics of Mg, which is catalysed by Mg_2Cu, are rate-limited by the diffusion of hydrogen through the growing hydride layer. Also, the dehydriding kinetics of Mg, catalysed by Mg_2Cu, are rate-limited by the diffusion of hydrogen through the growing metal layer. The catalytic role of the Mg_2Cu phase was attributed to the providing of an unoxidized external surface. This model for hydriding and dehydriding kinetics is illustrated schematically in Figure 2.9. The external Mg surface oxidizes and becomes inactive. The Mg surface at the Mg/Mg_2Cu interface is, however, not exposed to oxygen and remains active.

It has been reported that the alloying of Ce with Mg alters the ability to absorb hydrogen at room temperature, but the time required to complete the hydride formation is longer [136]. Pezat *et al.* [135] studied the hydriding/dehydriding characteristics of $LnMg_{12}$, Ln_2Mg_{17} and Ln_5Mg_{41} (Ln ≡ La, Ce, mischmetal). The alloys decompose during hydriding with the formation of MgH_2 and the corresponding rare earth hydride which acts as a catalyst in magnesium hydriding. These alloys react easily with hydrogen. At 325 °C they have the same hydriding rate but at 130 °C Ce_5Mg_{41} shows the fastest hydrogen absorption. Hammioui *et al.* [127]

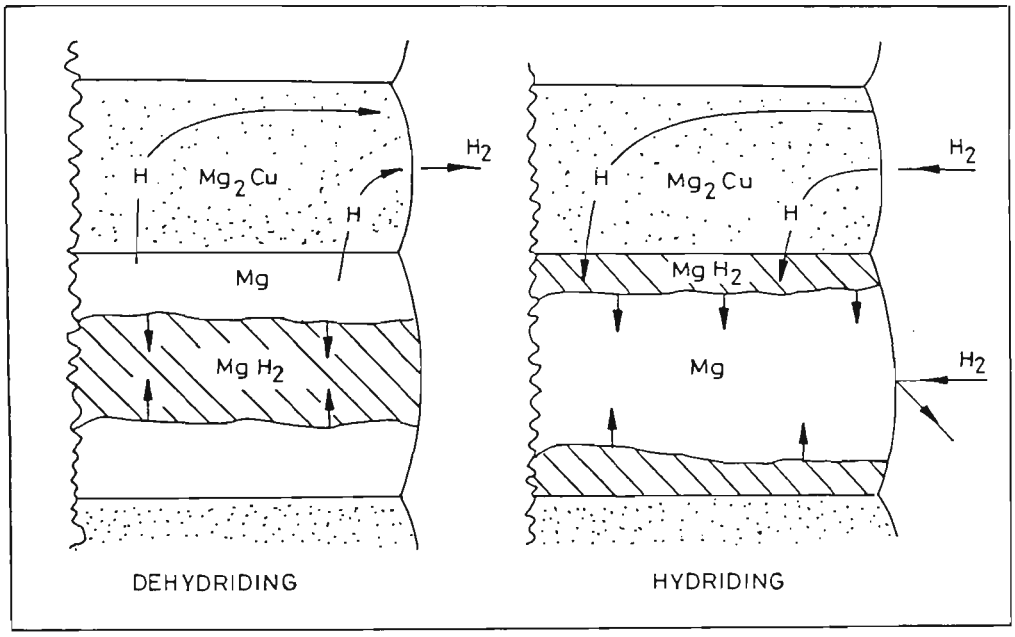

Figure 2.9 Model of Mg_2Cu catalyzed hydriding and dehydriding of Mg [125]

recently re-investigated the influence of cerium and nickel on the hydrogen absorption in magnesium alloys. It was found that magnesium hydride formation is enhanced by the presence of cerium. They attributed this behaviour to three factors: (i) the increase in hydrogen mobility in the magnesium matrix, as a result of diffusion short circuits created by the dispersed stable CeH_3 precipitates; (ii) the nucleation sites developed in the bulk by these precipitates; (iii) the possible increase in surface dissociation steps, in which cerium plays the part of lanthanum in the $LaNi_5$ alloy [127].

Lim and Lee [129] have analysed the hydriding reaction of $CeMg_{12}$ based on the theoretical model developed by Park and Lee [130]. They found that the initial stage of the reaction is controlled by chemisorption of hydrogen on the metal surface. The

rate-controlling step at the latter stage is not clearly understood. It was shown [131] that the reaction rates for both hydriding and dehydriding of $CeMg_{12}$ are 10 times faster than those obtained for pure Mg. The high reactivity with hydrogen was attributed to effects of morphological parameters such as mechanical stresses and strains, and incoherent grain boundaries which increase hydrogen diffusion and hydride nucleation and which are produced by the formation of finely divided precipitates of CeH_3.

The hydrogen absorption and desorption properties of magnesium-scandium alloys were studied by Ogawa *et al.* [136]. They observed that the amount of hydrogen desorbed from Mg-Sc alloys is much smaller than that for pure Mg under ambient pressure and temperature. They suggested that the outer electron of the Sc atom in the solid solution, which has significant "d" character, is responsible for the strong bond between the hydrogen atom and the neighbouring Sc atoms. Thus, the amount of hydrogen desorbed is much smaller than the amount absorbed, predicted from the formula $(Mg\text{-}Sc)H_2$.

Welter and Rudman [137] have investigated a two-phase approach which employs iron particles (5 *atm.*%) as a dissociative adsorption catalyst for Mg. It was found that addition of iron results in significantly faster hydriding kinetics. They attributed this to the catalytic effect of iron particles. The Mg-Fe based ternary hydride, Mg_2FeH_6, has been investigated by Didisheim *et al.* [138, 139]. This ternary hydride shows much higher hydrogen content (5.4 *wt.*%) than Mg_2NiH_4 (3.6 *wt.*%). The hydrogen

concentration per unit volume of Mg_2FeH_6 is exceptionally high (9.1×10^{19} atoms l^{-1}), exceeding, for instance, that of MgH_2 (6.5×10^{19} atoms l^{-1}) by about 40 %. However, with respect to the theoretical stability, Mg_2FeH_6 appears to be less promising for energy storage applications, mainly because of its high enthalpy of dissociation (98 kJ mol H_2^{-1}).

Other elements have been added to Mg in efforts to enhance kinetics and/or reduce stability [140-143]. Douglass [141] has studied the reaction between hydrogen and Mg with some transition elements (Mn, Co, Ag, Y) over a concentration range of 1-5 *atm.*%. It was found that Mg-Co alloys absorbed a considerably smaller amount of hydrogen, whereas the alloys Mg-Mn picked up good amounts of hydrogen. However, dehydriding kinetics were slow. Mg-Ag alloys have rapid hydriding behaviour but a slow dehydriding rate. His studies indicate a smaller catalytic effect of Co on the hydriding reaction than that of Mn and Ag on the dehydriding reaction for well known systems such as Mg-Ni and Mg-Cu. Alloys containing Ag and Y exhibit rapid hydriding kinetics and pick up more hydrogen. Dehydriding is most rapid for Mg-Y alloys, but it is slow for Mg-Ag alloys. The hydrogenation reactions of Mg-Al alloys have been reported by a number of investigators [29, 134, 141-143]. The hydriding reaction rates seem to be very slow. Nachman and Rohy [142] have found that the kinetics of hydriding, dehydriding and the hydrogen absorption capacities of $Mg_{17}Al_{12}$ alloys are greatly improved or altered by the addition of rare-earth, Y, Ni or In.

2.3.2.2 Mg-Ni Based Alloys

It is known [113] that nickel addition is an effective method to improve the kinetic characteristics of magnesium hydriding and dehydriding. Figure 2.10 shows the phase diagram of the Mg-Ni system, which indicates that magnesium reacts with nickel to form two intermetallic compounds, Mg_2Ni and $MgNi_2$. $MgNi_2$ does not react with hydrogen, even at pressure up to 540 *atm* in the temperature range -196 to 300 °C [67]. Darriet *et al.* and Lupu *et al.* [31, 40] claimed that $MgNi_2$ phase has a catalytic role for the first hydriding process although it does not react with hydrogen. However, Mg_2Ni reacts with hydrogen to form the ternary hydride Mg_2NiH_4 [113], even at room temperature; at 200 °C and a pressure of 14 *atm.*, it will react rapidly.

The hydrogen content in Mg_2NiH_4 is about 3.6 *wt.* %, which is still much higher than that in other hydrogen storage alloys (Table 2.3) although it is only about one half of the hydrogen content of MgH_2. The ternary hydride Mg_2NiH_4 is thermodynamically less stable than binary hydride MgH_2. Also, the hydriding kinetics of Mg_2NiH_4 are considerably improved relative to MgH_2. Eisenberg et al. [144] reported that the hydrogen desorption rate for Mg_2Ni is more than 100-times faster than for pure magnesium. Such a high reaction rate is believed to due to the catalytic activity of Ni.

The crystal structure of Mg_2Ni, as illustrated in Figure 2.11, is complex. According to the investigations of Schubert and Anderko [146], the unit cell is hexagonal, with a = 5.18 kX (1kX = 1.002063Å), c = 13.19 kX and c/a = 2.54, having the space group of

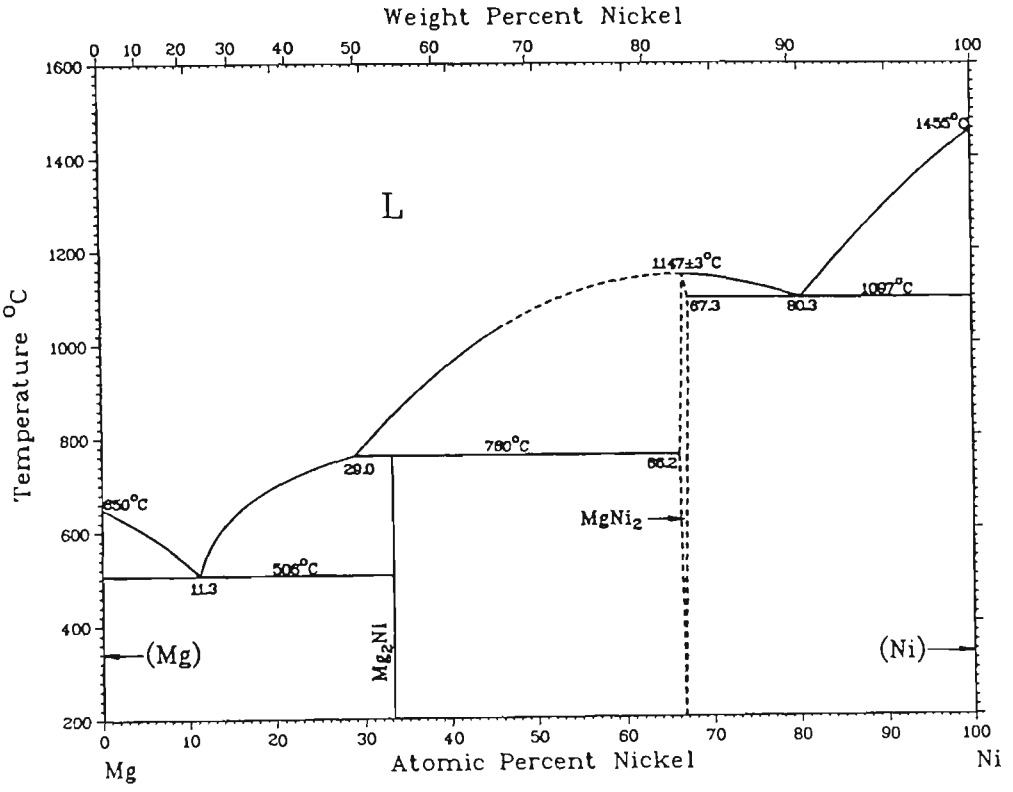

Figure 2.10 Mg-Ni phase diagram [145]

$P6_222$, and the nickel atoms are located on the *3b* (0, 0, $\frac{1}{2}$) and *3d* ($\frac{1}{2}$, 0, $\frac{1}{2}$) while the magnesium atoms Mg_I are on the *6f* ($\frac{1}{2}$, 0, *z*) and Mg_{II} on the *6i* (*x*, 2*x*, 0).

The α solid solution Mg_2NiH_x ($x \approx 0.3$) has the same structure as the Mg_2Ni alloy. Schefer *et al.* [147] determined the crystallographic parameters of $Mg_2NiD_{0.30}$ by using an X-ray diffraction technique. They found that the insertion of hydrogen into Mg_2Ni involves an extension of the hexagonal unit cell parameters. The *c* parameter undergoes a particularly marked increase: Mg_2Ni, a = 5.216 Å and c = 13.20 Å; $Mg_2NiD_{0.30}$, a = 5.23 Å and c = 13.43 Å.

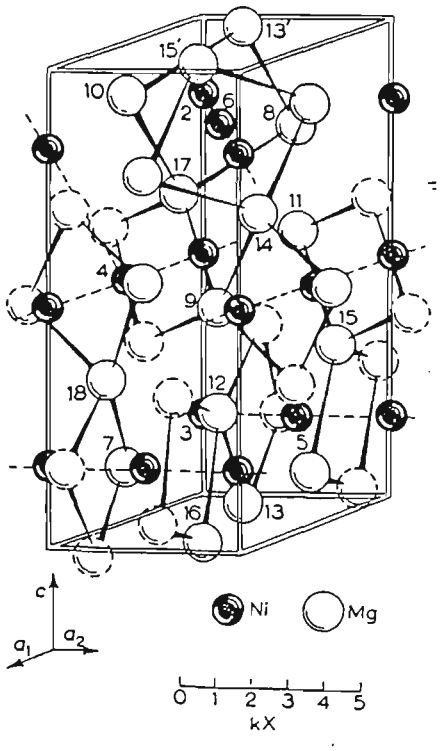

Figure 2.11 The crystal structure of Mg_2Ni [146].

Darriet and co-workers [148] used the neutron diffraction method and the difference Fourier synthesis to determine the position of the deuterium atoms. They found that the deuterium atoms were located in the $z = \frac{1}{6}$, $z = \frac{1}{2}$, $z = \frac{5}{6}$ planes which are equivalent. The repartition of the electron density in these planes leads to three possibilities for the positions of the deuterium atoms as shown in Figure 2.12 (a). They also determined the diffusion paths inside the metallic sublattice. The diffusion paths in the $z = \frac{1}{2}$ plane are shown in Figure 2.12 (b), (c).

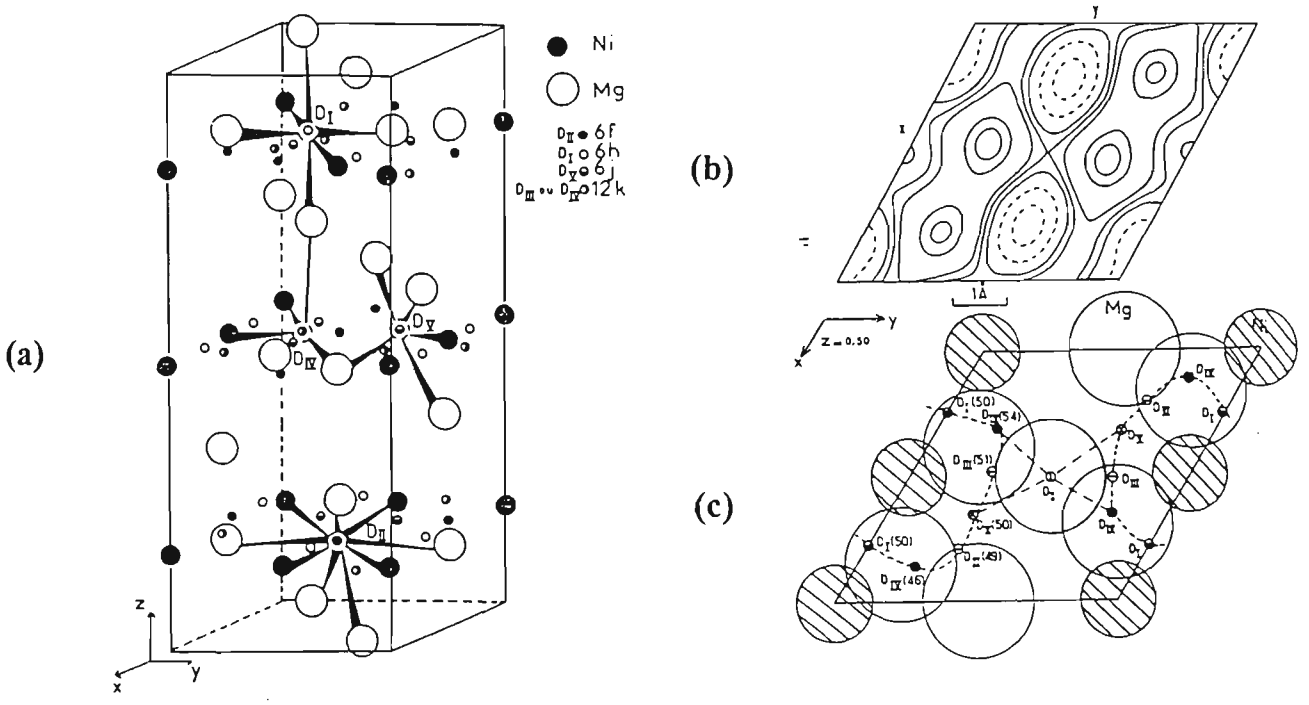

Figure 2.12 The positions and diffusion paths of deuterium atoms in the $Mg_2NiD_{0.30}$ cell [148]. (a) Diagram of the $Mg_2NiD_{0.30}$ unit cell with various co-ordination polyhedra around the deuterium atoms; (b) Difference map of $Mg_2NiD_{0.30}$ (z = 1/2); (c) Schematic projection of the structure along the z axis (---- hydrogen diffusion paths)

(a) Structure and Phase Transformations of Mg_2NiH_4

The crystal structure of the ternary hydride Mg_2NiH_4 has been studied by numerous researchers [113, 149-165]. Various structural models were proposed, differing not only in the symmetry of the structure but also in the kind and number of interstitial sites occupied by the hydrogen atoms. Gavra and co-workers [149] reported that there are two allotropic forms of this hydride and it shows a phase transition from the

low temperature (LT) structure to high temperature (HT) structure at about 230 °C. It has been shown [150-152, 166, 167] that the HT structure consists of a CaF_2 type metal atom arrangement in which the H atoms surround the Ni atoms in disordered configuration. However, conflicting results were reported in the literature[153, 156, 160, 165] for the LT structure.

(i) HT phase

It has been reported [147, 149, 168] that the high temperature (HT) phase of Mg_2NiH_4 has a cubic lattice (a = 6.530 Å) with space groups *Fm3m* or $F\bar{4}3m$. The structure is illustrated in Figure 2.13. Schefer *et al.* [150] and Yvon *et al.* [151] concluded from their neutron diffraction results that hydrogen atoms are distributed in a statistical manner over six equivalent sites located at the corners of an octahedron centred on a nickel atom, although the local configuration of the hydrogen atoms around the nickel atom could not be determined. Noreus and Olsson [152] reported the localized character of the motion of the hydrogen atoms, from their cold neutron scattering experiment, and proposed a model in which a square planar unit of four hydrogen atoms randomly flips around the nickel atom. However, Darriet *et al.* [148] pointed out that preferential sites for the deuterium atoms in the Mg_2ND_4 are D_1 on the *48h* (x, x, 0) and D_2 on *24e* (x, 0, 0). The deuterium located on the D_1 sites are preferentially bound to magnesium ($d_{Mg\text{-}D1}$ = 1.66 Å) rather than bound to the nickel atoms as proposed in previous studies. They suggested that the structure of cubic Mg_2ND_4 can be described as the three-dimensional network of $[MgD_6]$ octahedral

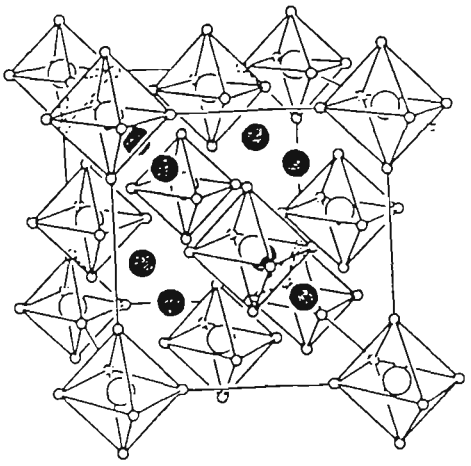

Figure 2.13 Average crystal structure of the disordered HT phase of Mg_2NiH_4 [151]. Large filled circles represent Ni atoms and dotted spheres are Mg atoms. The small open circles represent the average positions of the H atoms. Their average occupancy is 0.69.

with shared vertices (Figure 2.14). The octahedral environment of magnesium in Mg_2NiD_4, like that in MgH_2, results in their thermal stability being very similar.

(ii) LT phase

Unlike the agreement among the various authors on the HT phase of cubic crystallographic structure, controversial conclusions were presented in the literature concerning the structure and phase relations of the low temperature modification [153-160, 165]. It was suggested that, in the low temperature (LT)

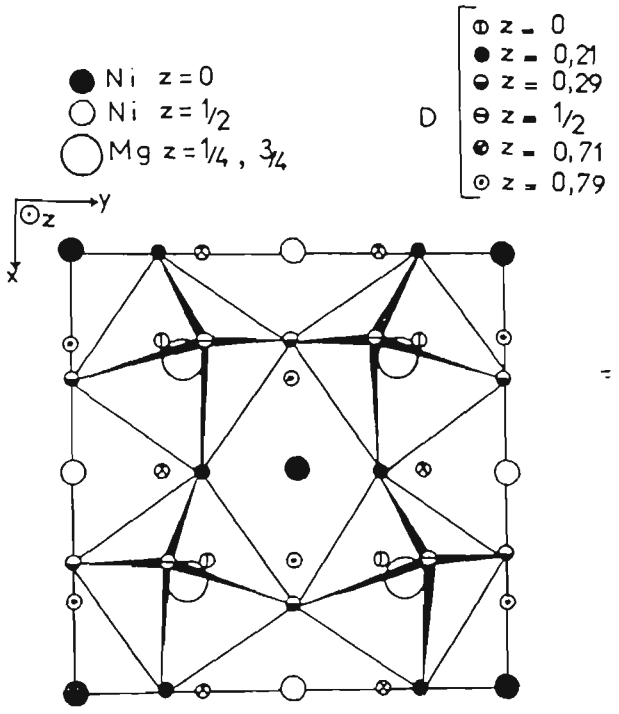

Figure 2.14 The three-dimensional network of $[MgD_6]$ octahedra in the cubic Mg_2NiD_4 structure [148].

phase of Mg_2NiH_4, at least two different LT phases co-exist, one (called LT1 [153]) of monoclinic symmetry with space groups *Cm* [154], *C2/m* [153], or *Cc* [155-157], and another (called LT2 [153] or "intermediate" [156]) of orthorhombic symmetry [156, 158-160] with space group $P2_12_12$ [156] or possibly lower symmetry [154]. Gavra [160] pointed out that under the stress-free hydriding condition of Mg_2Ni powders, a two-phase hydride mixture of LT1 and LT2 is formed in the low temperature (below 210 °C). Each of the hydrided powder particles consists of an inner core composed of the LT1 coated by a film of the LT2. This coating film provides a diffusion barrier for hydrogen preventing the completion of the conversion

of the LT1 phase into the LT2 phase. However, Zolliker and Yvon [165] argued that the structure of LT-Mg_2NiH_4 had mainly monoclinic symmetry and contained various probabilities of microtwinning. The probability of twinning depended on the preparation conditions.

The LT1 phase prevailed in samples which were hydrided at temperatures below 230 °C, *i.e.* below the HT-LT phase transformation temperature, whereas the LT2 phase prevailed in the samples which were cooled from the HT phase into the LT phase [153, 158]. Gavra and co-workers [160] used X-ray diffraction measurements to investigate the effects of compaction pressures on the phase composition of Mg_2NiH_4. They reported that the ratio of LT1 and LT2 depended on the preparation conditions. Under stress-free hydriding conditions performed below 210 °C, a two-phase (LT1 and LT2) hydride mixture is formed. The LT1 phase is stabilized under an applied isostatic pressure. High compaction pressures cause the transformation of the LT2 phase into the LT1 phase, thereby resulting in a pressure-induced insulator-to-conductor transition. Hayakawa *et al.* [156] also proposed that mechanical grinding accelerates the transformation from LT2 phase to LT1 phase.

① *LT1 phase structure*

Ono et *al.* [155] reported that LT1 phase structure of Mg_2NiH_4 has a body-centred monoclinic cell (a = 13.201 Å, b = 6.407 Å, c = 6.491 Å and β = 93.21°) in which the a axis is doubled. This monoclinic cell has been confirmed by the work of Noreus

and Werner [153]. A layer of the monoclinic Mg_2NiH_4 structure is shown in Figure 2.15 as determined by Darriet *et al.* [148]. The framework of this structure consists of a three-dimensional network of distorted [MgD_6] octahedral with shared vertices. The nickel atoms take their places inside the channels formed by these [MgD_6] octahedral. The lattice can be considered as being built up of a sequence of ABX_3 perovskite units and BX_3 ReO_3-type units.

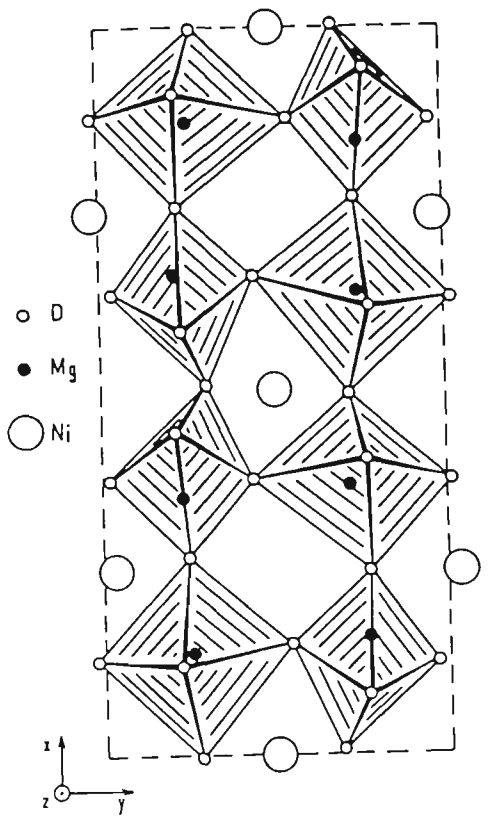

Figure 15 The three-dimensional network of [MgD_6] octahedra in the monoclinic Mg_2NiD_4 structure [148].

The monoclinic hydride structure is hydrogen deficient ($Mg_2NiH_{4-\varepsilon}$ with $\varepsilon < \sim 0.04$) and has a metal-like electrical conductivity [160]. Hayakawa and co-workers [156] proposed that the body-centred monoclinic cell can be transformed to a conventional C-centred monoclinic cell with a = 15.034 Å, b = 6.407 Å, c = 6.491 Å and β = 118.75° as shown in Table 2.4.

Table 2.4 Atomic parameters for the C-face-centred monoclinic cell of low temperature Mg_2NiH_4 [156]

Atom	x	y	z	β
Mg(1)	0.1195(18)	0.4846(20)	0.4251(44)	0.48(41)
Mg(2)	0.1306(21)	0.9842(21)	0.4220(52)	2.07(40)
Mg(3)	0.3620(17)	0.5120(49)	0.7007(68)	1.95(73)
Mg(4)	0.3803(14)	0.9814(46)	0.5828(57)	0.61(54)
Ni(1)	0.2382(5)	0.7280(19)	0.3099(12)	-0.10(31)
Ni(2)	0.0	0.2658(24)	0.0	2.07(48)

Space group, *Cc*.
Unit cell parameters: a = 15.0374(10) Å; b = 6.4114(5) Å; c = 6.4932(5) Å; β = 118.768(4)°
The atomic parameters can be transformed to a body-centred unit cell with a = 13.2024 Å, b = 6.4114 Å, c = 6.4932 Å and β = 93.229° by the matrix

$$\begin{pmatrix} 1 & 0 & 0 \\ 0 & 1 & 0 \\ -1 & 0 & 1 \end{pmatrix} \begin{pmatrix} x \\ y \\ z \end{pmatrix} - \begin{pmatrix} 0 \\ \frac{1}{4} \\ 0 \end{pmatrix} \qquad (2.3\text{-}2)$$

② *LT2 phase structure*

Hayakawa *et al.* [156] suggested that the LT2 phase structure of Mg_2NiH_4 can be described as a distortion of the cubic HT phase cell. The main features of this pattern can be explained on the basis of an orthorhombic cell with a = 6.572 Å, b = 4.520 Å, c = 4.560 Å. Gavra *et al.* [160] also reported that the LT2 phase has an orthorhombic structure, but a cell with a = 11.434 Å, b = 11.257 Å, c = 4.519 Å, which is different from Hayakawa's results. The orthorhombic hydride structure is stoichiometric (Mg_2NiH_4) and is insulating.

The hydrogen distribution in the Mg_2NiH_4 has been investigated by many authors [153, 161-164]. Noreus *et al.* [153] proposed an octahedral model in which four hydrogen atoms form a square plane centred on a nickel atom, as is shown schematically in Figure 2.16 (a). Zolliker *et al.* [161] proposed a tetrahedral model, in which four hydrogen atoms occupy the four corners of a tetrahedral centred on a

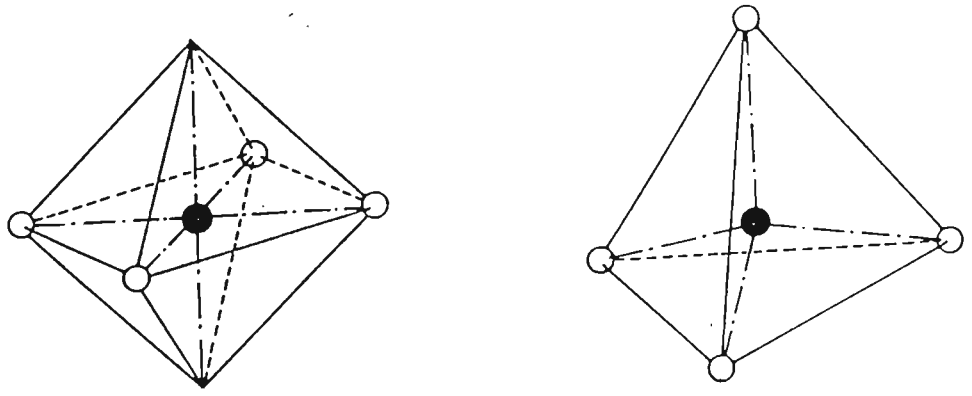

(a) Square (b) Tetrahedron

Figure 2.16 Models of hydrogen distribution [162]. The filled circle is the Ni atom, and the open circles represent H atoms.

nickel atom, as shown in Figure 2.16 (b). However, Hayashi and Hayamizu's nuclear magnetic resonance (NMR) results [162] supported the square planar model rather than the tetrahedral model for the hydrogen distribution in the low-temperature phase of Mg_2NiH_4.

Recently, Orimo and Fujii [169] reported that the Mg_2Ni hydride which was synthesized by reactive mechanical grinding at ambient temperature and under a hydrogen atmosphere reached 1.6 *wt.*% ($Mg_2NiH_{1.8}$) without changing the crystal structure of the matrix Mg_2Ni phase. The dehydriding reaction started at 167 °C. They attributed this result to a hydrogen occupation in the disordered interface phase around the nanocrystalline Mg_2Ni phase formed by the reactive grinding. This disordered interface phase was not detected by X-ray diffraction because the interface thickness seems to be less than a few nanometers.

(b) Thermodynamic and Kinetic Properties of Mg_2NiH_4

A series of pressure-composition isotherms for the Mg_2Ni-H_2 system is shown in Figure 2.17. The hydride is stoichiometric as illustrated by the abrupt termination of the isotherms at a composition corresponding to Mg_2NiH_4. The maximum solubility of hydrogen in the α-phase corresponds to a composition of $Mg_2NiH_{0.3}$. The reaction starting with the hydrogen-saturated alloy may be written as:

$$Mg_2NiH_{0.3} + 1.85H_2 \Leftrightarrow Mg_2NiH_4 \qquad (2.3\text{-}3)$$

Reilly [96] found that the decomposition of Mg_2NiH_4 obeys the first order rate equation,

$$K = \frac{1}{t} \ln \frac{a_0}{a} \qquad (2.3\text{-}4)$$

where t is the time in seconds, a_0 is the initial amount of Mg_2NiH_4, and a is the amount at time t. A semi-logarithmic plot of the concentration of Mg_2NiH_4 *vs.* time is shown in Figure 2.18. The rate constants are listed in Table 2.5.

Table 2.5 The Rate constants for the decomposition of Mg_2NiH_4 [96]

Temperature (°C)	First order rate constant K (sec^{-1})
201	7.0×10^{-4}
227	7.0×10^{-3}
240	1.48×10^{-2}

Nomura and co-workers [170] investigated the kinetics of the reaction between Mg_2Ni and hydrogen. They reported that the rate determining step can be expressed by the equation:

$$\frac{dn}{dt} = k' \frac{(P - P_{eq})}{t} \qquad (2.3\text{-}5)$$

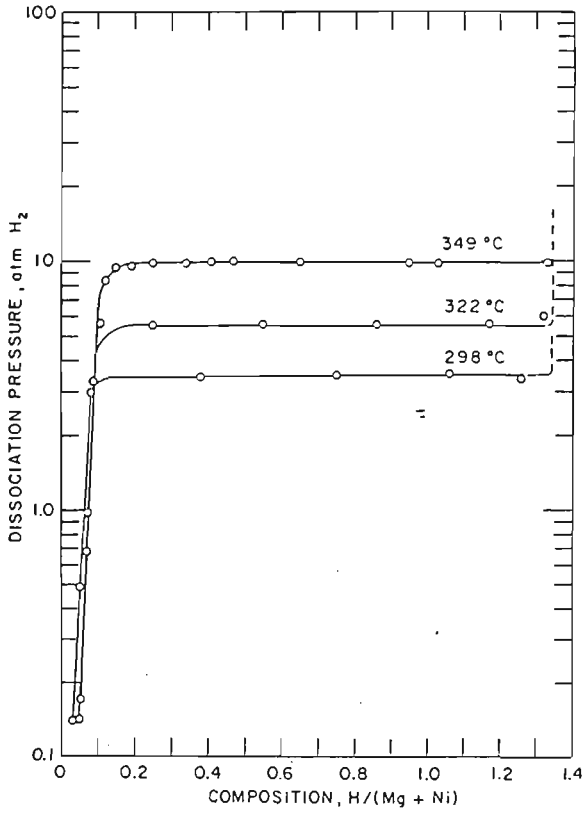

Figure 2.17 P-C-T diagram for the Mg_2Ni-H system [96].

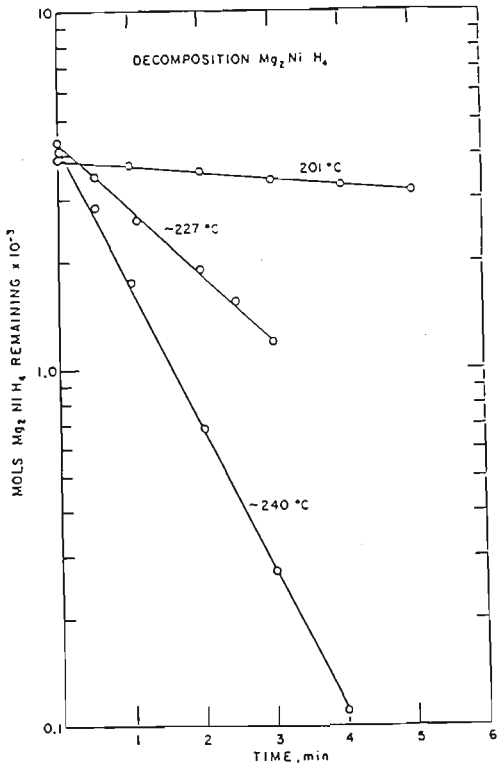

Figure 2.18 Decomposition of Mg_2NiH_4 *vs.* Time [96]

where P is the pressure at time t, P_{eq} the equilibrium pressure, n the hydrogen atoms in per formula unit. They obtained $k' = 3.2 \times 10^{-2}\ (\text{kgf}/\text{cm}^2)^{-1}$.

Lupu *et al.* [171] pointed out that in the Mg_2Ni-H_2 system at pressures considerably lower than the equilibrium, dehydriding is limited by hydrogen diffusion through the α phase, while at pressures close to equilibrium the $\beta \rightarrow \alpha$ conversion becomes rate controlling. The studies of Song [172] on the same system and on a system in which there is, in addition to Mg_2Ni, also less than 5 *wt.*% free nickel [173], indicate that depending on the temperature and pressure of dehydriding, both Knudsen and ordinary diffusion of hydrogen through pores, channels and cracks, as well as nucleation of the α phase can be rate determining.

(c) Modified Mg_2Ni alloys

It has been reported that the hydriding-dehydriding thermodynamics and kinetics of Mg_2Ni can be affected by alloy composition and crystal structure [68]. Oesterricher *et al.* [174] have suggested that partial substitution of magnesium in Mg_2Ni by an element having a larger exothermic heat of hydride formation, such as calcium, scandium or yttrium may result in the rise of the equilibrium pressure. This would bring the modified Mg_2Ni alloys closer to the range of a reversible room temperature hydrogen sorption system. Yvon *et al.* [151] suggested that the maximum hydrogen concentration of Mg_2NiH_4 is mainly limited by electronic factors and that structurally related compounds having more than four H atoms per formula unit could possibly be stabilized if an elements like aluminium were partially substituted for magnesium, or

nickel was partially replaced by a transition metal such as vanadium, chromium, manganese, iron or cobalt. However, the alloys obtained have so far failed to yield hydrides with more than four hydrogen atoms per formula unit [175]. The attempts made [41, 42, 153, 176-179] indicated that the partial substitution of magnesium or nickel in Mg_2NiH_4 results in a change of the hydriding and dehydriding kinetics as well as a change in the dissociation temperature of the hydride.

In order to improve the hydride characteristics of Mg_2Ni further, without substantially decreasing the hydrogen storage capacity, Selvam *et al.* [175] investigated the influence of partial substitution of nickel in Mg_2Ni by other transition metals like Fe, Co, Cu or Zn on the dehydriding behaviour. They found that the alloys, $Mg_2Ni_{0.75}M_{0.25}$ (where M is Fe, Co, Cu, or Zn) upon hydriding lead to the formation of quaternary hydrides. On dehydriding they yield the starting ternary alloys except for copper containing alloys which show multi-phase regions and follow a different path way for the hydriding-dehydriding process. They reported that the thermal stability (defined as the decomposition temperature at 1 atm hydrogen pressure) of the hydrides of iron and zinc substituted samples are comparable to that of Mg_2NiH_4 (around 555 °K) whereas the cobalt containing hydride decomposes around 570° K. The system obtained by partial replacement of nickel by copper in Mg_2Ni gives a hydride which decomposes around 528° K, which shows lower thermal stability and also presents some interesting properties. The thermodynamic quantities obtained for the binary, ternary and quaternary hydrides are summarized in Table 2.6.

Table 2.6 Physico-chemical properties of Mg, Mg_2Ni and $Mg_2Ni_{1-x}M_x$ (M = Fe, Cr, Be, Co, Cu, Zn or V) alloys and the corresponding hydrides [113, 124, 175, 177, 180, 181]

Materials	Cell parameters (hexagonal)		Hydride phases	Hydrogen Content (%) (Expel.)	T_{dec} (°K)	Thermodynamic data	
	a (Å)	*b* (Å)				$-\Delta H$ (kJ mol^{-1} H_2)	$-\Delta S$ (J K^{-1} mol^{-1} H_2)
Pure Mg	3.21	5.21	MgH_2	6.95	590	70.7	119.0
Mg_2Ni	5.20	13.25	Mg_2NiH_4	3.36	555	65.8	118.5
$Mg_2Ni_{0.75}Fe_{0.25}$	5.22	13.27	$Mg_2Ni_{0.75}Fe_{0.25}H_4$	2.94	558	66.3	118.8
$Mg_2Ni_{0.75}Cr_{0.25}$	5.21	13.26	$Mg_2Ni_{0.75}Cr_{0.25}H_4$	3.00	521	60.0	114.9
$Mg_2Ni_{0.75}Be_{0.25}$	5.28	13.41	$Mg_2Ni_{0.75}Be_{0.25}H_4$	--	523	70.7	135.4
$Mg_2Ni_{0.75}Co_{0.25}$	5.21	13.20	$Mg_2Ni_{0.75}Co_{0.25}H_4$	3.08	570	67.7	117.7
$Mg_2Ni_{0.75}Cu_{0.10}$	5.20	13.34	MgH_2, Mg_2NiH_4 $MgCu_2$	3.28	525	61.8	117.6
$Mg_2Ni_{0.75}Cu_{0.25}$	5.21	13.42	MgH_2, Mg_2NiH_4 $MgCu_2$	3.15	528	62.1	117.3
$Mg_2Ni_{0.75}Cu_{0.50}$	5.22	13.50	MgH_2, Mg_2NiH_4 $MgCu_2$	2.95	532	62.4	117.4
$Mg_2Ni_{0.75}Cu_{0.75}$	5.23	13.62	MgH_2, Mg_2NiH_4 $MgCu_2$	2.76	535	62.8	118.5
$Mg_2Ni_{0.75}Zn_{0.25}$	5.24	13.45	$Mg_2Ni_{0.75}Co_{0.25}H_4$	3.12	556	65.9	117.7
$Mg_2Ni_{0.75}V_{0.25}$	5.22	13.29	$Mg_2Ni_{0.75}V_{0.25}H_4$	2.90	523	62.2	119.1

It was pointed out [175], that the ternary alloys containing iron, cobalt and zinc form a quaternary hydride according to the following reaction:

$$Mg_2Ni_{0.75}M_{0.25} + (4-x)/2\ H_2 \Leftrightarrow Mg_2Ni_{0.75}M_{0.25}H_{4-x} \qquad (2.3\text{-}6)$$

The copper containing alloys, however, follow a different route. The hydriding-dehydriding mechanism takes place in two consecutive steps. The first hydriding process creates an irreversible disproportionation of the alloy with the formation of MgH_2, Mg_2NiH_4 and Mg_2Cu:

$$Mg_2Ni_{1-x}Cu_x + (4-x)/2\ H_2 \rightarrow 3x/2\ MgH_2 + x/2\ MgCu_2 + (1-x)\ Mg_2NiH_4 \quad (2.3\text{-}7)$$

Then the absorption-desorption cycles proceed as follows:

$$3x/2\ MgH_2 + x/2\ MgCu_2 + (1-x)\ Mg_2NiH_4 \Leftrightarrow (1-x)\ Mg_2Ni + x\ Mg_2Cu + (4-x)/2\ H_2 \quad (2.3\text{-}8)$$

Explanations for partial substitution of Ni atoms in Mg_2Ni by iron and cobalt were proposed by Mintz *et al.*[153]. They showed no significant substitution occurred in $Mg_2Ni_{1-x}M_x$ (where M is Fe or Co). The highest substitution concentration for Co was about 2 *at.*%. This was supported by Lupu *et al.* [40], who used the extended X-ray absorption fine structure (EXAFS) and Mössbauer spectroscopy to examine the structure of $Mg_2Ni_{1-x}Fe_x$ ($x \leq 0.37$). Their results suggested that only partial substitution of Ni atoms in Mg_2Ni by Fe can be achieved. Most of the Fe is present in a more or less finely dispersed state in these alloys. They are in disagreement with the results of Selvam *et al.* [175] and Darnaudery *et al.* [180].

The effect of the substitution of iron for nickel in Mg_2Ni on the hydrogen desorption from these alloys was also studied by Lupu *et al.* [40]. The hydrogen desorption curves for these alloys are given in Figure 2.19 compared to the pure Mg_2Ni hydride.

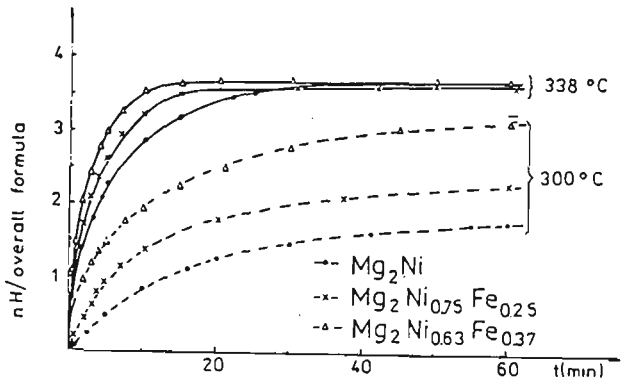

Figure 2. 19 Desorption curves for hydrogen from Mg-Ni-Fe alloys compared to Mg_2Ni [40]

The iron containing alloys show higher dehydriding rates than pure Mg_2Ni. After Nomura *et al.* [170], they obtained the values $k' = 4 \times 10^{-2}$ $(kgf/cm^2)^{-1}$ for pure Mg_2Ni in the equation (2.3-4), 90×10^{-2} and 230×10^{-2} for the alloys $Mg_2Ni_{1-x}Fe_x$ with x = 0.25 and 0.37, respectively. Thus, it was concluded that the presence of Fe considerably increases the desorption rate of hydrogen from these alloys.

Lupu and co-workers [177] reported results on the Be-substituted Mg_2Ni alloys, $Mg_2Ni_{1-x}Be_x$ (x = 0.15 or 0.25). The heat of formation shows an increased stability for the hydrides of the Be-modified alloys compared to that of unmodified Mg_2Ni. Hirata *et al.* [178] have investigated modified intermetallic compounds of composition $Mg_{2-x}M_xNi$ (M = Al , La or Cu, $0.05 \leq x \leq 0.1$). They observed that the stability of the hydride is decreased by partial substitution of Mg by Al. An activation energy of

about 84 $kJmol^{-1}$ was determined for dehydriding, which is lower than those of Mg_2Ni (86.4 $kJmol^{-1}$). The effect of the additives (La or Cu) on the hydriding and dehydriding kinetics of Mg_2Ni has not been fully evaluated yet. It was shown that the average decomposition rate of $Mg_{1.8}Ca_{0.2}Ni$ hydride was 20.33 % per minute, against 14.14 % per minute for Mg_2NiH_4 [181].

In summary, alloy substitution seems to be a good approach for obtaining magnesium-based hydrogen storage alloys with desirable characteristics. This is substantiated by the studies on the addition of Cu, Ni, La, Ce, Fe, Al or Y to magnesium, and the substitution of transition elements to Mg_2Ni alloy. Although the kinetic and thermodynamic behaviour of hydriding/dehydriding of magnesium and magnesium-based alloys could be improved considerably by the addition of alloying elements, these alloys still displayed higher thermal stability and lower dehydriding rates compared to other system of hydrogen storage alloys. Therefore, many other approaches, such as composite alloys, oxide doping and surface modification, have been investigated in order to further improve the hydriding/dehydriding performance of magnesium-based hydrogen storage alloys.

2.3.3 Composites

Recently, there have been some investigations [182-190] that are suggestive of the fact that mixed type composite materials may possess better hydriding characteristics than simple alloys. Nagai *et al.* [184] studied the hydriding behaviour of the

composite material Mg-x%$LaNi_5$. They found that the $LaNi_5$ addition significantly lowered reaction temperature and accelerated the hydriding rate. The composite forms low stability hydrides with better storage capacity and hydriding behaviour than that of the individual components, without increasing weight and cost. Mandal and Srivastava [185] reported that the composite Mg-x% FeTi possesses a much higher storage capacity than FeTi alone and exhibits favourable absorption-desorption kinetics. They claimed that a storage capacity of 3~3.6 *wt.*% for Mg-40% FeTi has been achieved at ambient conditions after suitable activation. The higher storage capacity in this case was attributed to the absorption of hydrogen by FeTi, FeTi-Mg and Mg-TiMg eutectic mixtures. It was suggested [186] that the dissociation of H_2 is expected to take place at the FeTi surface followed by diffusion into the magnesium matrix via FeTi. The improvement in kinetics may be attributed to volume expansion-induced cracking of FeTi domains, the hydrogenation of eutectics of Mg-FeTi and Mg-TiMg or FeTi-Mg complexes.

Composite particles of Mg-YNi_2 have been synthesised and investigated by Orimo *et al.* [187]. In these composite particles, Mg_2NiH_4 is formed, even at 373 °K, under a hydrogen pressure of 5 M*Pa*. They also investigated the hydriding properties and microstructures of the composite material $Ti_{0.6}Zr_{0.4}Mn_{0.8}CrCu_{0.2}$-Mg, and found the MgH_2 phase is formed even at temperatures below 373 K. They concluded that the formation of the Mg_2Cu phase and the diffusion of hydrogen supplied by the hydride phase of the host compound ($Ti_{0.6}Zr_{0.4}Mn_{0.8}CrCu_{0.2}$) are essential for the formation of

the MgH_2 phase [188]. Ye *et al.* [189] studied hydride formation in Mg-$ZrFe_{1.4}Cr_{0.6}$ composite material. The Mg particles were found to be partially covered by the alloy. The alloy island acts a catalyst for the dissociation and recombination of hydrogen atoms, which results in the rapid hydrogen absorption and desorption, even at moderate temperatures (150 °C).

Dutta and Srivastava [190] described the synthesis and hydrogenation-dehydrogenation behaviour of the composite alloy La_2Mg_{17} - *x wt.*% $MmNi_{4.5}Al_{0.5}$. It has been shown that the optimum hydrogen storage characteristics are possessed by the material with x = 10 %, *i.e.* La_2Mg_{17} -10 % $MmNi_{4.5}Al_{0.5}$. The hydrogen storage capacity for this material, where effective dehydrogenation occurs at 400 °C, is 4.85%. The composite has faster kinetics — about 3 times faster than La_2Mg_{17} alone. They suggested that the increased capacity and better kinetics of the composite were due to the multiphase nature of the material (besides the majority phase La_2Mg_{17}, other minority phases exist, *e.g.* $MgNi_2$, Mm_2Ni_7 and Ni are present).

2.3.4 Oxide Doping

Another approach to improve the kinetics of magnesium is oxide doping. Khrussanova and co-workers [191] have shown that the addition of some 3*d* transition metal oxides to pure magnesium followed by mechanical alloying of the mixture leads to very good absorption-desorption properties towards hydrogen. The effects of various 3*d* transition metal oxides (MnO_2, Fe_2O_3, NiO, TiO_2, V_2O_5 and

Cr_2O_3) on the hydriding-dehydriding behaviour of magnesium have been investigated [191-194]. It was found that the character and degree of this effect depended on the nature of the oxides. The most pronounced improvement was found for the mixture of 90 *wt.* % Mg and 10 *wt.* % V_2O_5. They reported [193] that during the initial stage of the process the hydriding rate is limited by the dissociative adsorption of hydrogen on the mixture particles, whereas with the advancing process the rate is successively controlled by surface chemical reactions (during the MgH_2 nuclei are formed and grown) and diffusion. The mixture has a high hydrogen capacity which does not decrease during the prolonged hydriding-dehydriding cycles.

2.3.5 Surface Modification

The limited use of magnesium and magnesium-based alloys in hydrogen storage results mainly from the shortcomings of their slow hydriding kinetics and poor corrosion resistance. Therefore, many efforts have been made with regard to surface modification to improve their poor surface properties [195-199]. Imamura *et al.* [34, 200-203] described hydriding aspects of magnesium-based alloys modified chemically with various organic compounds. They found that the treatment of these alloys with polycondensed-ring compounds such as anthracene, chrysene, perylene or tetrahydrofuran (THF) leads to improved hydriding behaviour [200, 201]. They attributed this improvement to the formation of electron donor-acceptor complexes by charge transfer between the alloys and aromatic molecules.

The effects of nickel plating on the hydriding and dehydriding characteristics of magnesium were studied by Eisenberg *et al.* [204]. They found that the nickel in an electroless plated form (nominal composition, 0 - 10 *wt.*% Ni) had little effect on the initial activation, the maximum achievable capacity and the absorption kinetics. The effect on the desorption kinetics, however, was considerable. It was shown that cycling causes the agglomeration of surface nickel into larger crystallites, thereby reducing the surface nickel dispersion. This can lead to a reduction in the desorption rate. The plot of "effective surface nickel content" against specific desorption rate (SDR) data (Figure 2.20) suggested that the surface nickel is the factor controlling desorption rate rather than bulk nickel. Therefore with better surface nickel dispersion, the rate of dehydriding can be increased. The preferred form of nickel is a thin film which would provide the ideal situation.

More recently, a new surface modification called F-treatment was developed to treat the Mg_2Ni alloy by Suda *et al.* [205-209]. It was found that F-treated Mg_2Ni exhibited an extremely high hydrogen affinity, which resulted in hydriding ability at 40 °C [205] whilst untreated Mg_2Ni did not react with hydrogen under the same conditions. It is thought that with the formation of magnesium fluoride on the particle surface, some microchannels are generated along the interfaces of the Mg-rich Mg + Mg_2Ni eutectic structure. EPMA and ESCA analysis [208, 209] revealed that F-treatment could clean up the MgO and/or $Mg(OH)_2$ surface layers and form a porous, water insoluble magnesium (MgF_2) top-layer overlapping a metallic Ni-enriched

substrate. Such a fluorinated surface structure is believed to be responsible for the improved low-temperature hydriding properties of the Mg_2Ni alloy.

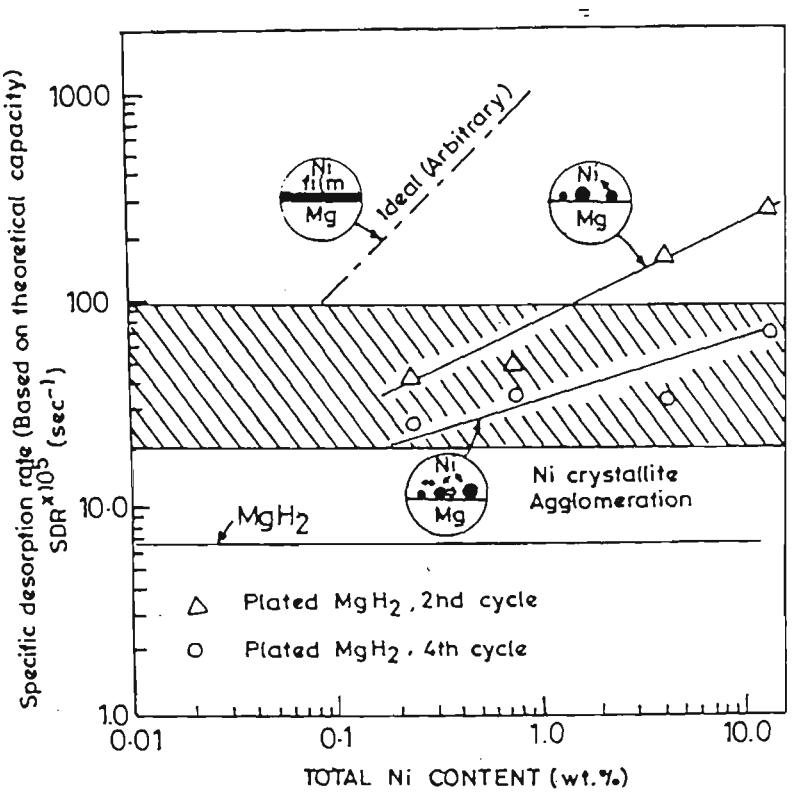

Figure 2.20 The effect of nickel content on the specific desorption rate (SDR) for nickel-plated MgH_2 [209].

2.4 Ni-MH Batteries

The Ni-MH batteries using hydrogen storage alloy as a negative electrode material have several inherent advantages over the conventional lead-acid and Ni-Cd batteries, such as high energy density, improved high-rate capacity, cleanliness and high tolerance to overcharge and discharge. The energy density comparison for various secondary batteries is given in Table 2.7.

Table 2.7 Comparison of energy density of various secondary batteries [210,211]

Battery	Energy Density (Wh/kg)	
	Actual	Theoretical
Pb / PbO	30 - 40	161
Cd / NiOOH	35 - 45	209
H_2 / NiOOH	45 - 70	378
$LaNi_5H_6$ / NiOOH	60 - 80	216
$LaNi_5H_6$ / Air	60 - 90	458

2.4.1 MH Electrode Characteristics and Requirements

The attempt to use hydrogen storage alloys for reversible hydride electrodes in Ni-MH batteries was begun by Justi *et al.* [212] around 1970. The research and

development now are still actively being conducted. The metal hydride (MH) electrode offers an important opportunity for materials engineering and optimization when compared with negative electrodes for other nickel-based battery systems [210]. In these other systems, the negative electrode (*e.g.* Cd, Zn, or Fe) is typically fabricated from the oxidation-reduction reactions associated with battery charge and discharge which convert the electrode back and forth between a metal and a metal oxide that is poor electric conductor. The MH electrode, by contrast, uses a chemical reaction that reversibly incorporates hydrogen into a metal alloy. In this oxidation-reduction reaction both chemical states are metallic, and so electrical conductivity is high in both the charged and discharged states. Furthermore, the small size of the hydrogen atom allows it to enter the metal lattice during formation of the hydride (reduced) state with only about 10% volumetric expansion and without the changes in crystallography associated with oxidation and reduction of the Cd, Zn, or Fe electrode [210]. In addition, the MH electrode not only allows high energy density and high-rate charging and discharging, but also helps to solve the problems which occur in more conventional rechargeable batteries regarding reactions in the three phases, *i.e.*, gas-liquid-solid.

The MH material used for an anode of a Ni-MH battery must satisfy an extensive list of requirements [210, 213], which are:

(i) High hydrogen storage capacity

The amount of hydrogen that the MH material can absorb determines the electrochemical storage capacity of the electrode and, consequently, the energy storage capacity of the battery. It is desirable to have high electrode storage capacity that is electrochemically reversible. Ovshinsky *et al.* [210] point out that to ensure reversibility, an important aspect of the MH design is the range of metal-to-hydrogen bond strengths, which must be about 6 to 12 kcal mol^{-1}. If the bond strength is too low, hydrogen will not react with the alloys and will be evolved as gas. If the bond strength is too high, the MH electrode is extensively oxidized and does not store hydrogen reversibly.

(ii) Good oxidation/corrosion resistance in electrolyte solution

The Ni-MH battery operates in a strongly oxidizing medium composed of a concentrated alkaline electrolyte. The elements which tend to be good hydrogen storage materials tend to be thermodynamically more stable as oxides than hydrides. Surface oxidation causes a higher polarization on discharge and lower charging efficiency. Thus, in this aggressively oxidizing environment, oxidation and corrosion resistance of MH electrode materials is critical.

(iii) Fast hydriding-dehydriding kinetics

The alloy must have good kinetics. For high rate discharge, hydrogen bulk diffusion must be fast and the surface should promote fast reaction of hydroxyl ions and hydrogen. For fast charge, polarization should be low to avoid premature hydrogen evolution. Finally, gas reabsorption must be fast in order to keep the pressure low. It

is also necessary for the surface oxide to have appropriate porosity, conductivity and catalytic properties [213].

(iv) Low cost

Cost considerations are very important. Obviously, it is not practical to use very expensive materials. The raw material availability is also important. In addition to raw material costs, it is important that processing costs be low.

2.4.2 Construction and Principle of Operation of Ni-MH Batteries

The construction of Ni-MH batteries is very similar to that of Ni-Cd types except for the negative electrode materials. Potassium hydroxide (KOH) solution containing lithium hydroxide (LiOH) is the electrolyte. The negative and positive electrodes are separated by an alkali-resistant, non-woven polypropylene or nylon material. The Ni-MH cell may be represented as:

(–) MH (s) | KOH (aq.) | NiOOH (s) (+)

In this battery, the negative electrode is made of a hydrogen storage alloy that can allow electrochemical storage and release of hydrogen during the battery charge and discharge processes. The nickel hydroxide positive electrode is electrochemically reversible between $Ni(OH)_2$ and nickel oxyhydroxide, usually written as NiOOH. During charging, hydrogen is formed at the interface of electrode and electrolyte by an electrochemical reduction of water and is subsequently absorbed by the alloy.

During discharging, the hydrogen in the MH is desorbed and oxidised electrochemically at the interface. The processes of charging and discharging for this battery are shown schematically in Figure 2.21. The half-cell reactions and overall-cell reaction on charge and discharge of the battery can be written as:

at the nickel hydroxide positive electrode

$$Ni(OH)_2 + \underset{\leftarrow \text{discharge}}{\overset{\text{charge} \rightarrow}{OH^-}} \Leftrightarrow NiOOH + H_2O + e^- \qquad (2.4\text{-}1)$$

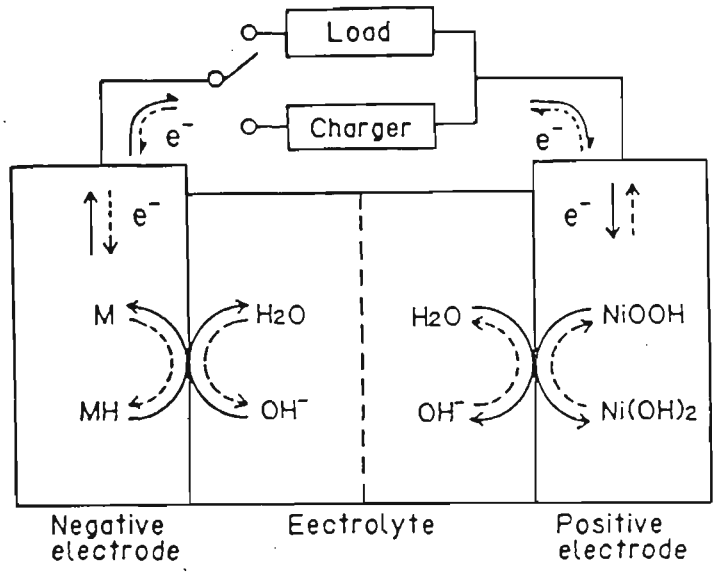

Figure 2.21 Schematic drawing of the charging and discharging reactions of a Ni-MH battery [211]

Broken line: charge $M + Ni(OH)_2 \rightarrow MH + NiOOH$

Solid line: discharge $MH + NiOOH \rightarrow M + Ni(OH)_2$

at the hydrogen storage alloy negative electrode

$$M + H_2O + e^- \underset{\leftarrow \text{discharge}}{\overset{\text{charge} \rightarrow}{\Leftrightarrow}} MH + OH^- \qquad (2.4\text{-}2)$$

the over all cell reaction is:

$$Ni(OH)_2 + M \underset{\leftarrow \text{discharge}}{\overset{\text{charge} \rightarrow}{\Leftrightarrow}} NiOOH + MH \qquad (2.4\text{-}3)$$

In this battery, charging and discharging reactions are not accompanied by the dissolution and precipitation of active materials. This produces an increase in utilisation efficiency of the negative electrode, and allows the actual mass energy density of the battery to be remarkably improved. Another characteristic of the batteries is that the concentration of electrolyte solution remains unchanged during the charging and discharging processes because water is not involved in the overall cell reaction [211]. These results contrast with other alkaline electrolyte systems such as Ni-Cd and Ni-Fe.

The excellent durability of Ni-MH batteries against overcharging or overdischarging is explained by reactions (2.4-4) to (2.4-8) for the case of limited capacity of the positive electrode and shown schematically in Figure 2.22 [210, 211].

During overcharging, the oxygen gas generated from the nickel positive electrode is consumed by the hydrogen storage alloy negative electrode, *i.e.*

$$(+): \qquad 2OH^- \rightarrow H_2O + 1/2O_2 + e^- \qquad (2.4\text{-}4)$$

$$(-): \quad 2MH + 1/2O_2 \rightarrow 2M + H_2O \tag{2.4-5}$$

$$2M + 2H_2O + e^- \rightarrow 2MH + 2OH^- \tag{2.4-6}$$

During overdischarging, the hydrogen generated from the polarity-reversed nickel positive electrode is oxidized into water at the hydrogen storage alloy negative electrode according to the following reactions:

$$(+): \quad 2H_2O + 2e^- \rightarrow H_2 + 2OH^- \tag{2.4-7}$$

$$(-): \quad H_2 + 2OH^- \rightarrow 2H_2O + 2e^- \tag{2.4-8}$$

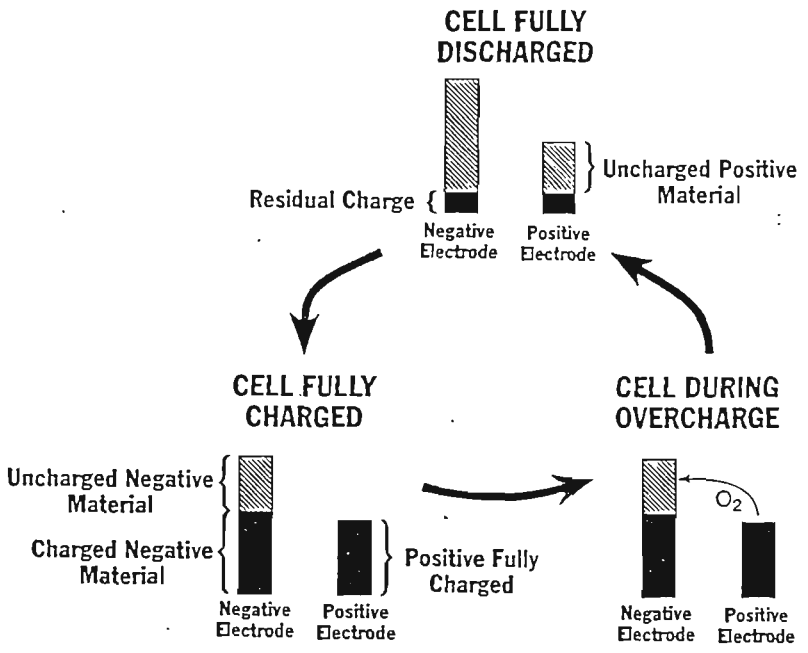

Figure 2.22 Schematic drawing of the charge distribution and oxygen cycle during charge, overcharge, and discharge for a sealed Ni-MH cell [210]

Thus, for both overcharge and overdischarge reactions, no net change occurs. The unique protective function of the Ni-MH battery against overcharging or discharging allows a completely hermetic design of the battery to be achieved.

2.5 Summary

Recent work has shown that the performance of batteries incorporating metal hydride electrodes may constitute an important advance in battery technology. However, although many hydrogen storage alloys will react directly and reversibly with hydrogen to form such hydrides, few, if any, can satisfy all of the criteria required for wide use as anode materials for Ni-HM batteries. The rare-earth system (AB_5-type) and zirconium-titanium-vanadium system (AB_2 Laves phase-type) hydrogen storage alloys have been well studied and have begun to be used as anode materials for the commercial production of Ni-MH battery. However, the major difficulties, at present, lie in the weight and cost of the hydrogen storage alloys.

Magnesium-based alloy, as previously mentioned, has gained much interest as a potential material for technological applications of hydrogen storage, because of its capacity to store large amounts of hydrogen and low cost. However, the major problems for these materials in practical application are: (i) their inability to react rapidly and reversibly at ambient temperature and moderate pressures; and (ii) poor resistance against oxidising.

Although a number of approaches have been investigated to improve hydriding and dehydriding behaviour of magnesium-based alloy in the past, there are still many aspects on which a clear picture has not yet emerged. One needs to discover in more detail the relationship between the thermodynamic, kinetic, structural and compositional properties. Furthermore, this literature review has shown that, as yet no work has been reported where the aim was to study the electrochemical characteristics of magnesium-based hydrogen storage alloy and to investigate the feasibility of these alloys for use as an anode material for Ni-MH secondary batteries. The main purpose of this study is to investigate the hydriding-dehydriding characteristics of magnesium-based alloys in the electrolyte, and to attempt to make this alloy a suitable anode material for the Ni-MH battery.

From the literature review described above, it is known that of all the magnesium-based hydrogen storage alloys, Mg_2Ni is the most remarkable due to its relative high capacity and favourable kinetics. Therefore, Mg_2Ni was selected as parent alloy in this study to exploit the ability of magnesium-based hydrogen storage alloys to be engineered through the use of alloying element additions, composite alloy, oxide doping and alloy surface modifications to produce materials with desirable battery properties.

CHAPTER 3 EXPERIMENTAL DETAILS

3.1 Alloy Preparation

3.1.1 Magnesium-Based Alloys

Materials

Magnesium-based alloys were made by using a vacuum powder-metallurgical method from chemically pure (> 99.5%) metal powders. The characteristics of the metal powders used in the current study are given in Table 3.1. All powders supplied were carefully opened in an argon filled glove box to prevent oxidation. As both the particle size and particle shape of the metal powders are important for the final alloy prepared by powder metallurgy, the starting powders of magnesium and nickel, were examined using a scanning electron microscope. The SEM samples were prepared by dispersing particles on to a conductive double sided tape and then sputtering with a thin gold film. The surface morphology of as-received Mg and Ni powders is shown in Figure 3.1.

The high purity argon gas used for the sintering and processing of the magnesium-based alloys was commercially supplied by BOC GASES Company Limited.

Table 3.1 Characteristics of starting metal powders for magnesium-based alloys

Elements	Purity (%)	Particle size (mesh)	Firm
Magnesium	99.8	50 (μm)	Goodfellow
Nickel	99.7	3 (μm)	Aldrich
Aluminium	99.5	100	Goodfellow
Iron	99.9	10 (μm)	Aldrich
Tin	99.5	100	Aldrich
Yttrium	99.9	40	Aldrich
Vanadium	99.5	325	Aldrich
Cobalt	99.9	100	Aldrich
Titanium	99.9	100	Aldrich
Palladium	99.9	1.0 ~1.5 (μm)	Aldrich
Manganese	99+	325	Aldrich

Apparatus

Since magnesium and magnesium alloys oxidize readily at elevated temperatures, the first requirement, therefore, of magnesium-based alloy making is to prevent excessive oxidation. For this purpose, a high vacuum sintering system was designed and

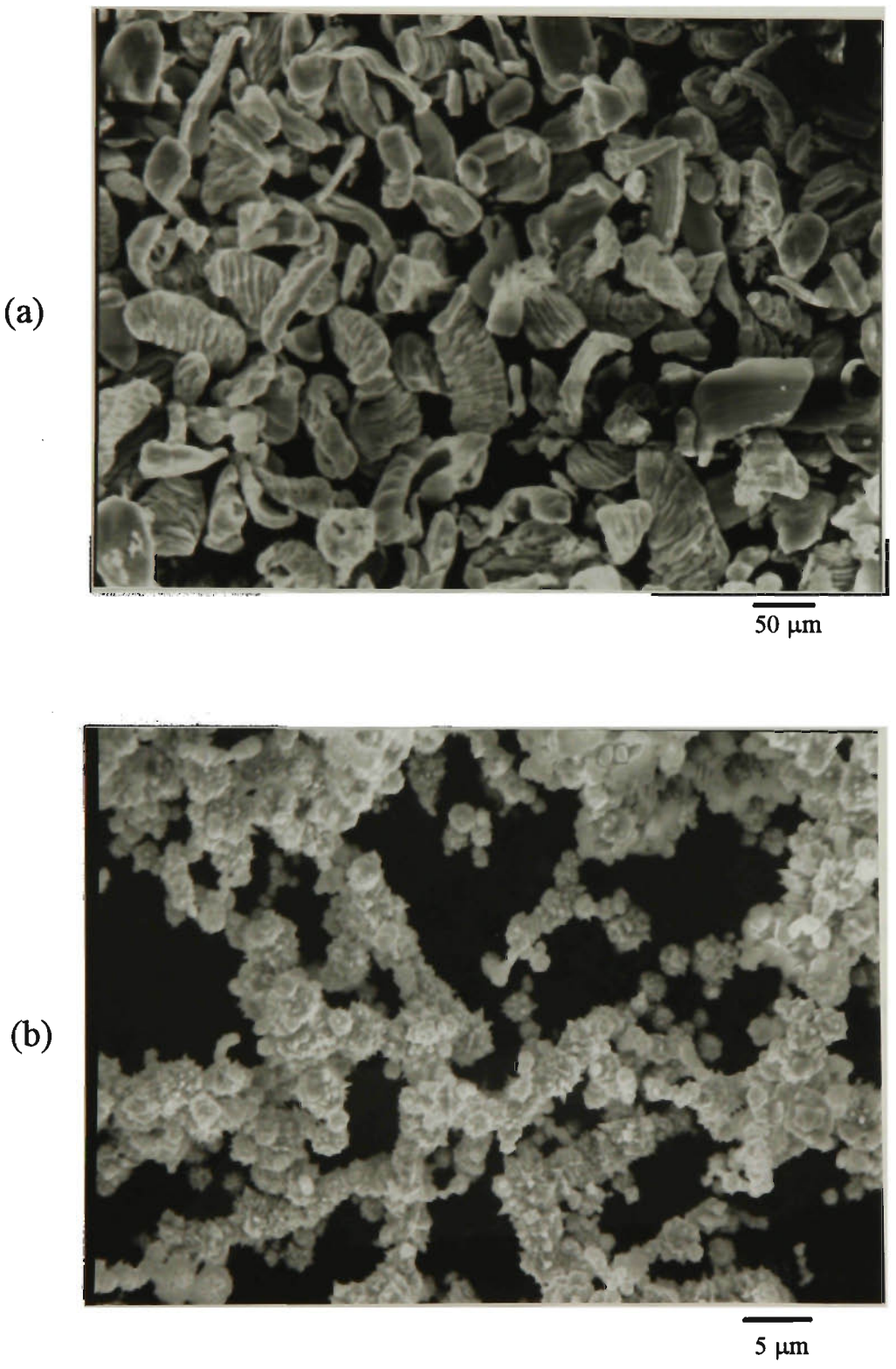

Figure 3.1 Secondary electron images of metal powders as delivered: (a) magnesium powder, and (b) nickel powder.

assembled. It consisted of a tubular electric furnace, a programmable controller, a high vacuum chamber, a mechanical pump, a diffusion pump, and a thermocouple fitted into the vacuum chamber, a thermocouple-meter, an Ar gas cylinder and control valves. The schematic diagram of the high vacuum experimental apparatus is shown in Figure 3.2. A vacuum of 2×10^{-5} Torr can be achieved in this apparatus.

Preparation procedures

The pure metal powders prepared according to the required stoichiometric ratios were thoroughly mixed under an argon gas atmosphere using a laboratory planetary mill (Frisch Pulverisette 5) An excess (5 ~ 25 %) of magnesium from the stoichiometric composition was used to compensate for the small evaporation losses of magnesium as well as to prevent the formation of $MgNi_2$ phase during the preparation of the alloys [175, 234]. The mixed powders were pressed into pellets without binders, transferred into sintered alumina boats, and then put in the vacuum furnace. The vacuum chamber was flushed with argon gas several times prior to sintering to reduce the oxygen partial pressure. In order to minimize the magnesium evaporation, the pellets were sintered under an argon atmosphere first at 560 °C for 50 hours and then at 650 °C for 12 hours, then finally cooled to room temperature in the furnace.

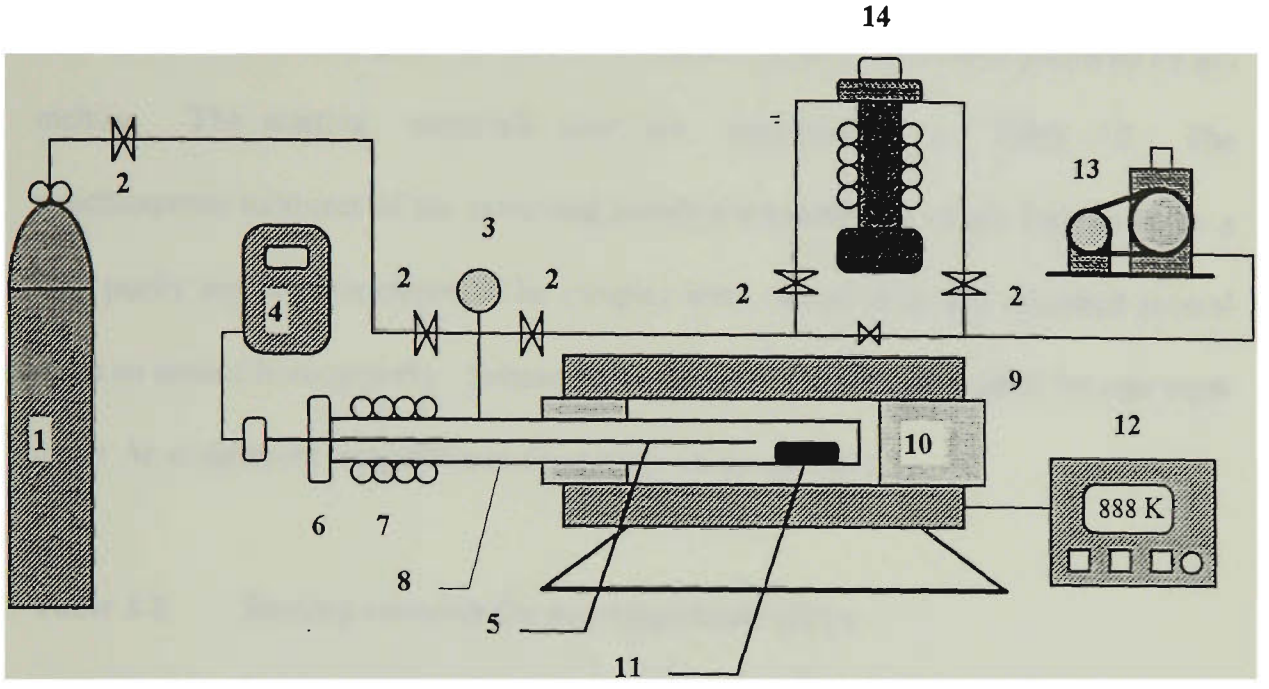

Figure 3.2 Schematic diagram of high vacuum sintering apparatus for magnesium-based alloy sintering.

1. Ar gas cylinder
2. Valves
3. Manometer
4. Thermocouple-meter
5. Thermocouple
6. Screw cap (with o-ring)
7. Cooling coil
8. Vacuum chamber
9. Tubular electric furnace
10. Insulation block
11. Crucible
12. Programmable controller
13. Mechanical pump
14. Diffusion pump

3.1.2 Non-Magnesium Alloys

For a comparative study and synthesis of the composite alloys, $LaNi_5$, Ti_2Ni and $ZrCr_{0.8}Ni_{1.2}$ *etc.* non-magnesium based hydrogen storage alloys were prepared by arc melting. The starting materials used are presented in Table 3.2. The stoichiometric mixtures of the individual metals were melted in an arc furnace under a high purity argon atmosphere. The samples were turned over and remelted several times to ensure homogeneity. Subsequently, the samples were annealed for one week under Ar at different temperatures depending on the samples.

Table 3.2 Starting materials for non-magnesium alloys

Metal	Purity (%)	Shape	Firm
La	99.9	ingot	Aldrich
Ni	99.95	sphere	Aldrich
Ti	99.7	rod	Aldrich
Zr	99.8	foil	Aldrich
Cr	99.95	chips	Aldrich

3.2 Electrode fabrication

The as-produced alloy pellets were mechanically ground into powders. After pulverisation, the fraction that passed though a 75 μm sieve was used for both the XRD structural analysis and the fabrication of test electrodes. Foam nickel sheet was used for the current collector. The foam nickel substrate used was 1.8 mm in thickness, 300~600 μm of pore size, 95% of porosity and 400~600 g m^{-2} area density. Scanning electron micrographs of the as-received foam nickel are shown in Figure 3.3.

The test electrodes made for the charge/discharge cycling test and electrochemical measurements were fabricated according to the following procedure: 0.2 g of sieved alloy powder was mixed with 0.8 g fine nickel powder ($\phi < 3$ μm; see Figure 3.1(b)) and 10% polyvinyl alcohol solution. The main purpose of a fine metal powder additive is to enhance the electronic conductivity of the electrode because during hydriding the electronic conductivity decreases. The mixture was coated on to both sides of a foam nickel sheet (2 × 3.5 cm^2) which was previously spot-welded onto a nickel wire. The mixture coated foam nickel was cold pressed at 200 kgf cm^{-2} after drying. A schematic diagram of the test electrode used in this study is given in Figure 3.4 (a).

(a)

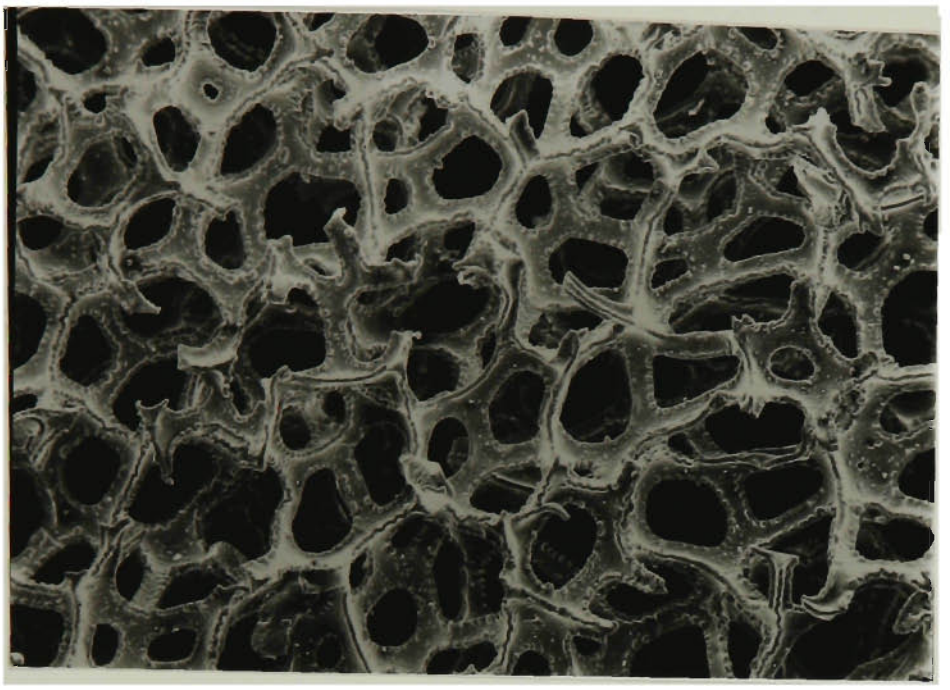

200 μm

(b)

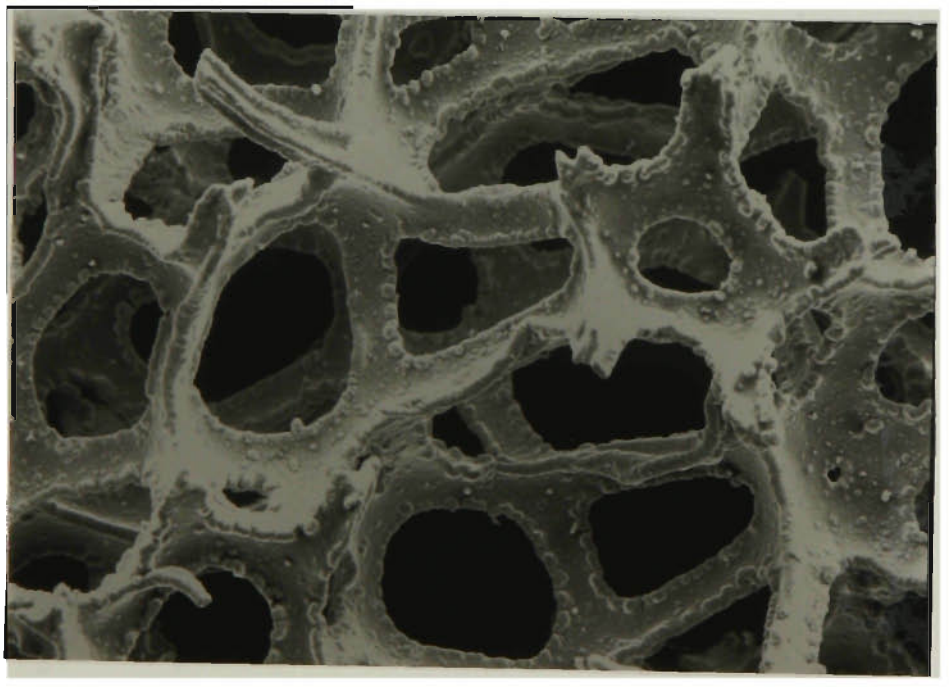

100 μm

Figure 3.3 SEM micrographs of foam nickel sheet as delivered showing a high porosity and homogeneity.

3.4 Charge/discharge cycling

Cycle tests and electrochemical measurements were performed in a double compartment cell, in which the test electrode was separated from the counter electrode by a porous frit. A schematic diagram of the test cell is shown in Figure 3.4 (b). A foam nickel sheet (7×20 cm^2) and a Hg/HgO electrode were used as counter electrode and reference electrode, respectively. The electrolyte used was 6 M KOH aqueous solution. Each electrode was impregnated with the electrolyte for at least 30 minutes prior to the cycle test in order to fully soak the test electrode.

The charge-discharge was controlled with an automatic galvanostatic charge-discharge apparatus (DEC-1) which monitored the potential of the alloy electrode with respect to an Hg/HgO reference electrode. Cycle tests were conducted at ambient temperature. The electrodes were charged to gassing potential, rested for 30 minutes, and then discharged galvanostatically to -500 mV *vs.* Hg/HgO reference electrode. After discharging, a resting period of 20 minutes was allowed before the above cycle regime was repeated. Different charging and discharging currents were used in this study.

(a)

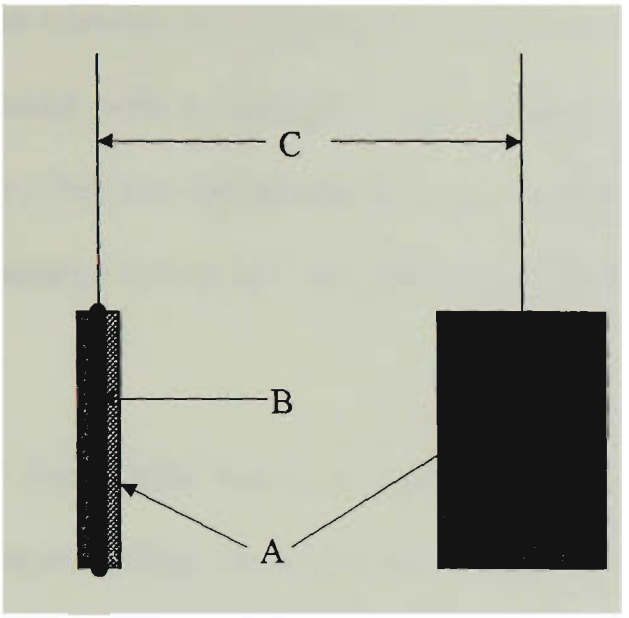

(b)

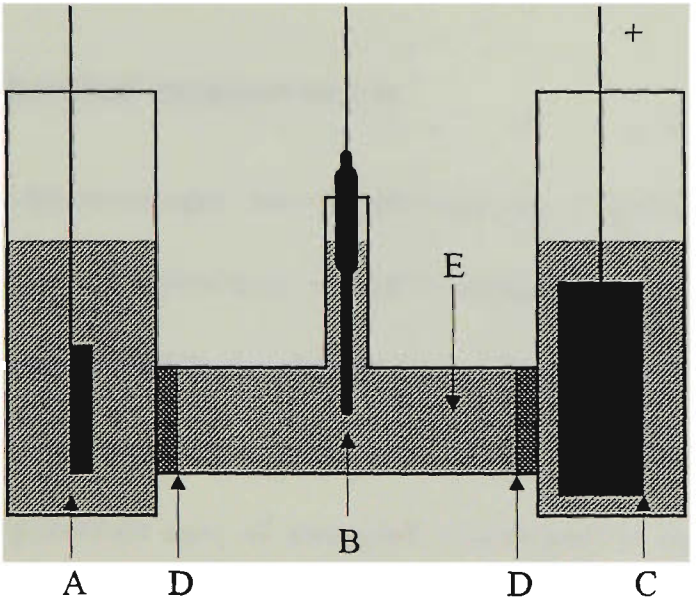

Figure 3.4 (a) Schematic diagram of the test electrode: A, the mixture of hydrogen storage alloy powder, conductive additive and binder; B, current collector (foam nickel); C, nickel wire. (b) Schematic diagram of the test cell: A, the test electrode; B, the reference electrode (Hg/HgO); C, the counter electrode (foam nickel sheet of 7 x 20 cm^2); D, sintered-glass filters; E, the electrolyte (6M KOH).

The test data were recorded by a Macintosh Performa 400 computer (with CHART version 3.3 software) with a MacLab/8 analog-digital interface. The electrode discharge capacity $C(n)$ was determined for every charge/discharge cycle (n) by integrating the discharge current and was expressed in milliamp hours per gram of alloy.

After the cycling experiments had been completed, the electrochemically tested electrodes were removed from the cell, rinsed successively in distilled water and ethanol, and finally dried using a hair dryer. Then the electrodes were used for SEM and XRD examinations.

3.5 Electrochemical measurements

Electrochemical measurements were performed in a two-compartment cell as described in Section 3.4. However, the reference electrode was positioned close to the hydride-forming electrode in the working electrode compartment to reduce solution resistance, while the counter electrode was placed in the second compartment of the cell. The potentials were all measured with respect to the Hg/HgO reference electrode.

3.5.1 ac impedance spectroscopy

Electrochemical impedance spectra (EIS) were measured using an electrochemical impedance analyser (EG&G Princeton Applied Research, model 6310) driven by a

Model 398 Electrochemical Impedance Software (v.1.23) with an IBM-PC 486 DX/66 computer. The ac amplitude was 5 mV, and frequency range studied was between 10 mHz and 100 kHz. The impedance measurements were conducted at different depths of discharge (DOD) or different discharge potentials.

3.5.2 dc polarization method

The electrocatalytic activity for hydrogen electrode reactions was evaluated by a potential sweep method using a scanning potentiostat (EG&G Princeton Applied Research, M362). The potential was swept at 1mV/s after charging a definite amount of hydrogen, and the corresponding voltammograms in the vicinity of the equilibrium potential were recorded by a Macintosh computer (with CHART 3.3 software) with a MacLab/8 analog-digital interface. An apparent exchange current density, which might be taken as a measure of catalytic activity [19, 42], was calculated from a charge transfer resistance by using the following equations,

$$i_o = RT/nFR_t \qquad (3.5\text{-}1)$$

when the charge transfer is the RDS,

$$R_t \approx R_p = (\partial\eta/\partial i)_{i\to 0} \qquad (3.5\text{-}2)$$

where i_o is the apparent exchange current density, R is the gas constant, T is the absolute temperature, n is the number of the transferred electrons, F is the Faraday

constant, R_t is the charge transfer resistance, R_p is the polarization resistance, i and η are the current density and overpotential respectively.

Cyclic voltammetry was performed with an EG&G Princeton Applied Research Cyclic Votammeter (PAR Model CV27) in the potential region between -0.40 and -1.2 V *vs.* Hg/HgO. Various sweep rates from 10 to 200mV/s were employed. E-I traces were recorded by a computer.

3.6 Physical analysis

3.6.1 X-ray diffraction measurements

Crystallographic characterization of the alloy powders and the electrodes were identified by X-ray diffraction (XRD) using a Philips PW 1010 X-ray diffractometer with Cu Kα (λ = 1.540562 Å) radiation and a nickel filter. The tube voltage and loading current were 40 kV and 25 mA, respectively. Lattice constants (a and c) and unit cell volumes (V) of Mg_2Ni-type hydrogen storage alloys were calculated using the following equations:

$$\sin^2\theta = (\lambda^2/4)\{[4(h^2 + hk + k^2)/3a^2] + l^2/c^2\} \quad (3.6\text{-}1)$$

$$V = \sqrt{3}\, a^2 c/2 \quad (3.6\text{-}2)$$

where λ is the wavelength of Cu Kα, θ is the Bragg angle and h, k and l are Miller indices.

3.6.2 Morphology and microstructural examination

Optical metallography

Optical microscopy (Nikon Optiphot Metallurgical Microscope) was used for microstructural examination of the alloys. In this work, only bright-field mode was adopted. The alloy specimens were cut from the as-produced alloy pellets and were cold-mounted in epoxy resin (the ratio of resin to hardener was 5:1). All of the specimens were ground and polished using an automatic polisher (Struers Abramin Grinder, Denmark). The steps of grinding and polishing are listed in Table 3.3. The details of the etchant used for magnesium-based alloy specimens are given in Table 3.4.

Table 3.3 The steps of grinding and polishing using the automatic polisher

Step	Support	Abr. Size	Lubr.	Force	Time	R.P.M
1	SiC Paper	220 SiC	H_2O+Gly.	80 N	2 mins.	300
2	D.P. Plan	15 μm(H)	Blue	300 N	5 mins.	150
3	D.P. Pan	15 μm(S)	Red	300 N	5 mins.	150
4	D.P. Dur	3 μm(H)	Red	120 N	3 mins.	150

Table 3.4 Etchant used for magnesium-based alloys

Etchant name	Composition	Etching time (sec)
Glycol	75 ml diethylene glycol 1 ml HNO_3 25 ml H_2O	5 ~ 7

SEM and EDS examination

The morphologies and microstructures of alloys, powders and electrodes were examined using a Leica-Cambridge Stereoscan 440 scanning electron microscopy (SEM), which was equipped with the link system energy dispersive spectrometer (EDS) with Moran software. The cycled electrodes were cut into two parts. One part was used for surface SEM and XRD analysis, while the other was embedded in an epoxy resin for the cross section examinations. The embedded samples were subsequently polished in various successive steps as described previously. Prior to SEM examination, the specimens were coated with carbon (or gold) film by vacuum physical deposition. The secondary electron image was used for the observation of surface morphologies and the back scatter electron image was used to distinguish the particles and second phase precipitates in the matrix.

CHAPTER 4

EFFECT OF ALLOY COMPOSITION ON THE ELECTRODE PROPERTIES

4.1 Introduction

Nickel-metal hydride (Ni-MH) batteries using a hydrogen storage alloy as the negative electrode material have received much attention because of their high energy density, superior charge-discharge characteristics and freedom from poisonous materials [1-5]. In this type of battery, electrolytic hydrogen is stored in electrodes made of these materials when charging, and the stored hydrogen in the electrode is oxidized when discharging. Rare-earth (mischmetal) system alloys and Laves-phase multicomponent hydrogen storage alloys have now been employed as the negative electrode materials for the mass production of Ni-MH secondary batteries [6-8]. However, a disadvantage is that Ni-MH batteries are presently more expensive than Ni-Cd [235] batteries due to the high cost of negative electrode materials. Thus, intensive research and development are still being conducted.

Magnesium-based alloys are superior to other hydrogen storage alloys with respect to their high hydrogen storage capacity, light weight and low cost. However, their

hydriding and dehydriding kinetics are very slow at room temperature and require high temperatures and pressures to proceed at a satisfactory rate. In addition, magnesium and magnesium-based alloys are more easily oxidized and are incompatible with KOH electrolyte [235]. Both of these factors seriously hinder their practical application. Thus, studies on magnesium-based hydrogen storage materials which can be reversibly charged and discharged in an electrolyte and at ambient conditions are of great importance.

Numerous investigations have been carried out to improve the hydriding properties of magnesium-based alloys at low temperature [174-209]. It has been suggested by Oesterricher *et al.* [174] that partial substitution of magnesium and/or nickel in Mg_2Ni may result in an improvement of hydriding/dehydriding behaviour. This would bring the modified Mg_2Ni alloys into the range of reversible room temperature hydrogen sorption systems. Nevertheless, all these investigations have concentrated only on the hydriding/dehydriding characteristics of magnesium-based alloys in the gas phase. As yet, there has been no work to investigate the electrochemical performance and the hydriding/dehydriding behavior of magnesium-based alloys in an alkaline solution.

In order to explore the feasibility of magnesium-based alloys for use in the Ni-MH battery, and obtain magnesium alloys suitable for the application in rechargeable negative electrodes, the effects of alloy composition on the electrode discharge capacity, rate-discharge and cycle life were investigated in this chapter. This study was based on the investigation of ternary and multicomponent alloys in addition to the basic binary Mg_2Ni composition. Alloying additions consisted of Al, Ca, La, Ti, V,

and Y. Furthermore, alloy microstructure, crystallographic and electrochemical characteristics were also examined to obtain a better fundamental understanding of the role of the additional elements. Finally, an improved Mg_2Ni-type electrode with a discharge capacity of 170 mAh/g at low discharge current and room temperature has been obtained for the first time, and has a future potential for the Ni-MH secondary battery.

4.2 Mg_2Ni Binary Alloy

As shown in Figure 2.3-5, magnesium reacts with nickel to form two Mg-Ni intermetallic compounds, Mg_2Ni and $MgNi_2$. It is known that $MgNi_2$ does not react with hydrogen. Mg_2Ni has been considered as an promising material for hydrogen storage from the viewpoint of capacity, hydride stability and hydriding kinetics. Therefore, it was selected as a parent alloy for investigation here.

As is well-known, liquid phase sintering is a widely used fabrication process in powder metallurgy. The main advantage is the strong increase of the sintering rate, improving the product quality, and allowing shorter sintering times as long as good wetting by the liquid phase take place. The process here started with pure metal powders Mg and Ni (the weight ratio of Mg and Ni is 1.035). A sequence of steps expected for reactive liquid phase sintering is shown in Figure 4.1. This figure corresponds to an increasing degree of reaction in going from the left to the right.

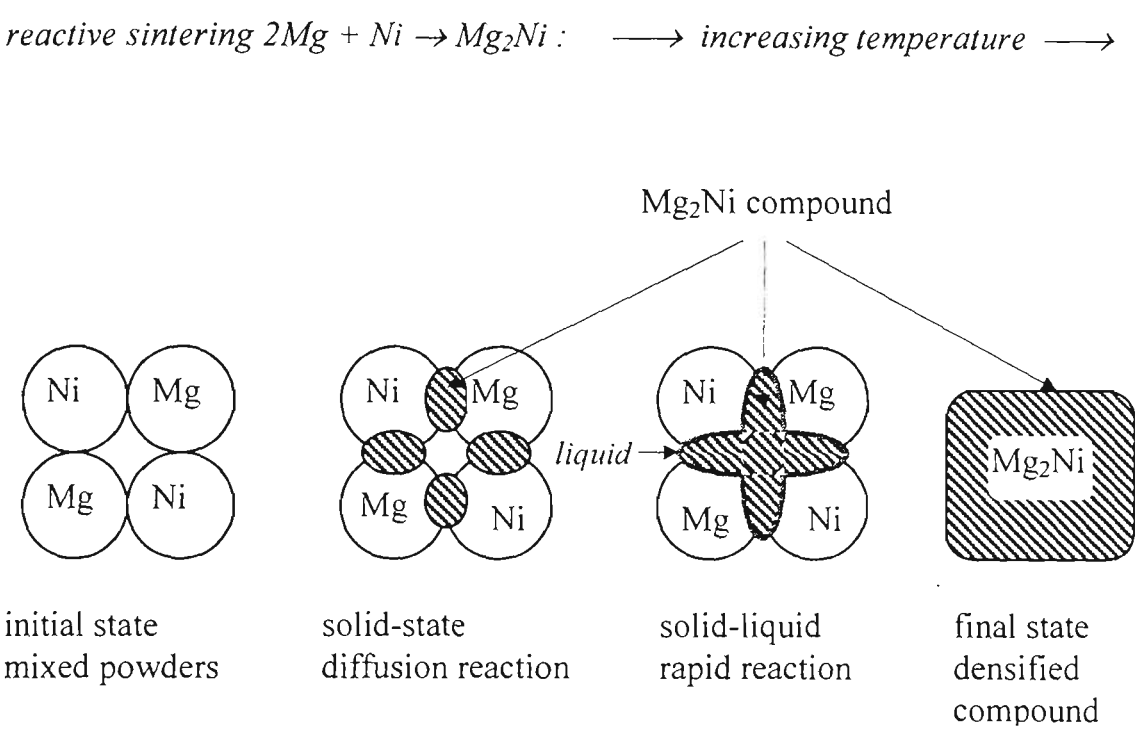

Figure 4.1 A sketch of the reactive sintering process for forming Mg_2Ni from mixed metal powders Mg and Ni. As temperature increases, first a solid reaction occurs, with subsequently a rapid reaction when the eutectic liquid forms. The final product is a densified compound.

The initial compact was composed of mixed powders Mg and Ni which diffusionally interact to form Mg_2Ni during heating. When a liquid forms in the compact, rapid compound formation begins, with liquid flow into the pores. The final compound Mg_2Ni is densified due to simultaneous sintering and reaction at the liquid-solid interface.

4.2.1 Metallographic Examinations

The typical microstructure of as-sintered Mg_2Ni alloy is represented in Figure 4.2. It can be seen that the metallurgical microstructure of a slightly Mg-rich Mg_2Ni alloy made by liquid phase sintering is characterized by a typical lamellar eutectic structure and a primary Mg_2Ni phase. The eutectic structure consists of an alternating Mg and Mg_2Ni network. It was estimated from the metallurgical analysis that the fraction of the eutectic phase is about 25.7%. This value is apparently smaller than the value (27.1 %) calculated from Mg-Ni phase diagram (Figure 2.10), which may be attributed to the small evaporation losses of magnesium during sintering.

The XRD result shown in Figure 4.3 reveals that Mg_2Ni alloy obtained by powder metallurgical method in this experiment has a hexagonal structure with lattice parameters a = 5.198 Å and c = 13.302 Å, which is in agreement with Schubert and Anderko's result obtained by using the flux melting alloy sample [146]. In addition, a few weak diffraction peaks were identified as metallic magnesium in Figure 4.3. There were no $MgNi_2$ phase or magnesium (and/or magnesium alloys) oxides to be detected in the as-sintered Mg_2Ni alloy sample.

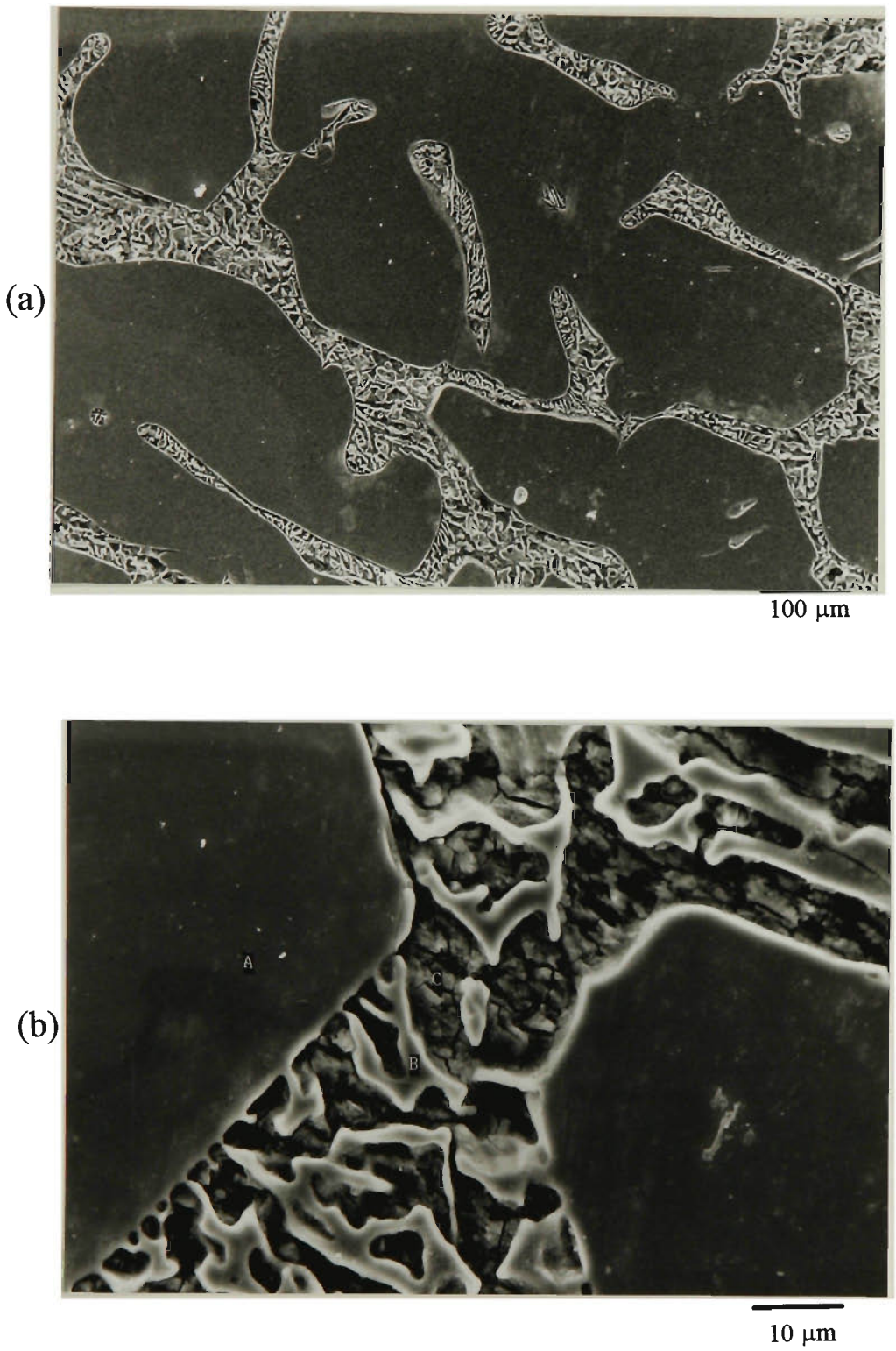

Figure 4.2 SEM micrographs of slightly Mg-rich Mg_2Ni alloy, etched in a diethylene glycolic HNO_3 solution, showing an eutectic [Mg (*e.g.* point C) + Mg_2Ni (*e.g.* point B)] structure in addition to the primary Mg_2Ni phase (*e.g.* point A).

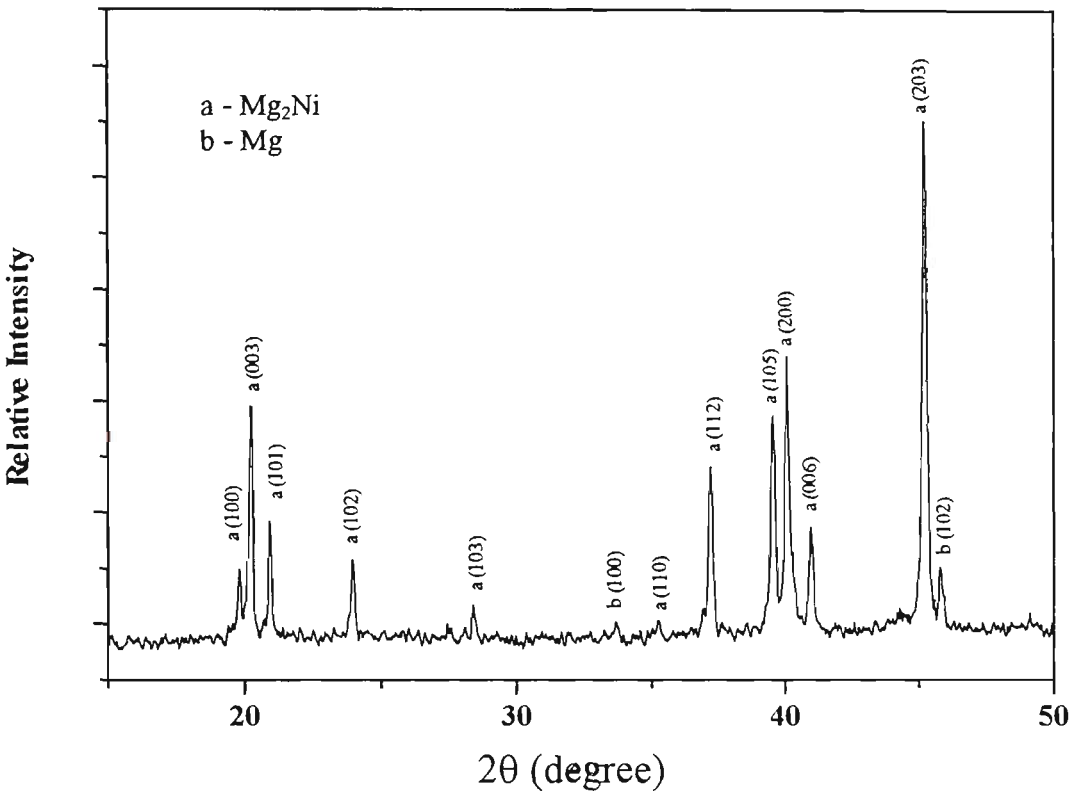

Figure 4.3 X-ray powder diffraction pattern of the as-sintered Mg_2Ni alloy, showing a small amount of pure magnesium phase in addition to the primary Mg_2Ni phase.

4.2.2 Charge/Discharge Behavior

The hydrogen storage alloy electrode acts as a rechargeable electrode in alkaline aqueous solution based on the reversible storage of hydrogen. The reaction which occurs during the charging and discharging of a hydrogen storage alloy electrode (M) in alkaline electrolytes may be represented by as follow:

$$M + x\,H_2O + x\,e^- \Leftrightarrow MH_x + x\,OH^- \qquad (4.2\text{-}1)$$

Equation (4.2-1) shows that on charging the hydrogen storage alloy (M) will react with H_2O at the interface with the electrolyte and the incoming electrons (e^-) to absorb/store hydrogen within its structure metal hydride (MH). The hydroxyl ions (OH^-) produced are released to the electrolyte. On discharging the reaction proceeds from right to left. The hydrogen charged alloy reacts with hydroxyl ions producing water, releasing electrons to the external circuit and becomes depleted of its stored hydrogen. Each absorbed/desorbed hydrogen atom corresponds to the storage of one electron. Thus, the theoretical electrochemical capacity of a metal hydride electrode may be estimated using Faraday's law.

Figure 4.4 shows the typical galvanostatic charge-discharge curves of a Mg_2Ni electrode in 6M KOH aqueous solution at 25 °C. It can be seen that this electrode exhibited a extremely low electrochemical capacity (8mAh/g) even at the very low discharge current density of 5mA/g. This capacity is much less than that obtained by converting the capacity in the gas-phase into electrochemical units. This suggests

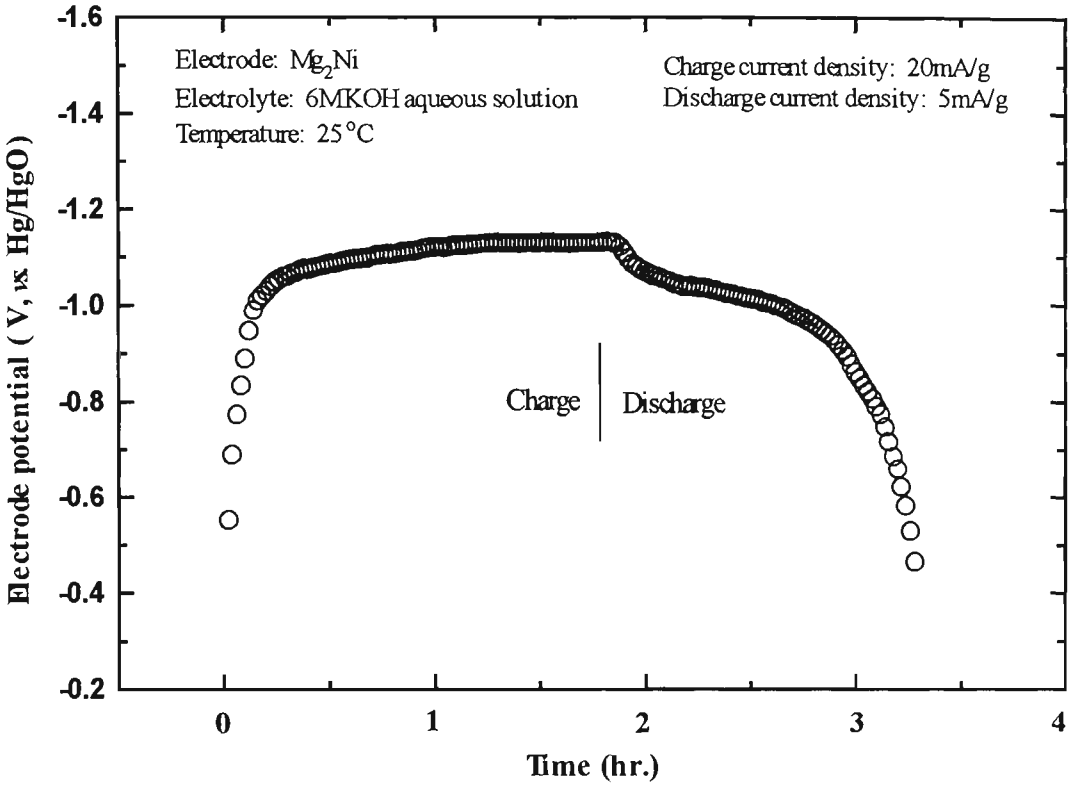

Figure 4.4 Charge-discharge curves of Mg_2Ni electrode in 6M KOH aqueous solution at 25°C.

that the Mg_2Ni alloy has poor electrochemical hydriding/dehydriding behaviour in the electrolyte, so that the amount of the electrochemically absorbed hydrogen is much less than in the gas-phase. Thus, it is considered that the unmodified alloy Mg_2Ni is not suitable for use as a rechargeable anode material in an alkaline solution at room temperature.

In order to improve the electrode performance of Mg_2Ni alloy, the Mg_2Ni powder was micro-encapsulated using a the low-temperature electroless plating technique that will be described in detail in the Chapter 7. Figure 4.5 shows the comparison between the electrode behaviour of the electrodes fabricated from the coated Mg_2Ni powder and those from the uncoated Mg_2Ni powder. The discharge capacity of the Mg_2Ni alloy as well as the rate dischargeability were effectively improved by the surface micro-encapsulation. In the case of the Ni-coated Mg_2Ni electrode, the discharge capacity was remarkably increased up to 54 mAh/g, almost seven times that of unmodified Mg_2Ni. The discharge characteristics of the electrode fabricated from the coated Mg_2Ni powder are represented in Figures 4.6 and 4.7. As can be seen, the discharge capacity of this electrode decreases rapidly over the first three cycles, and then remains almost constant from the fourth cycle onwards.

It has been reported that there existed three types of Mg_2Ni hydrides, namely, Mg_2NiH_4, Mg_2NiH and $Mg_2NiH_{0.3}$ [236]. The molecular weight of Mg_2Ni is approximately 107.3. The theoretical electrochemical capacities of these hydride

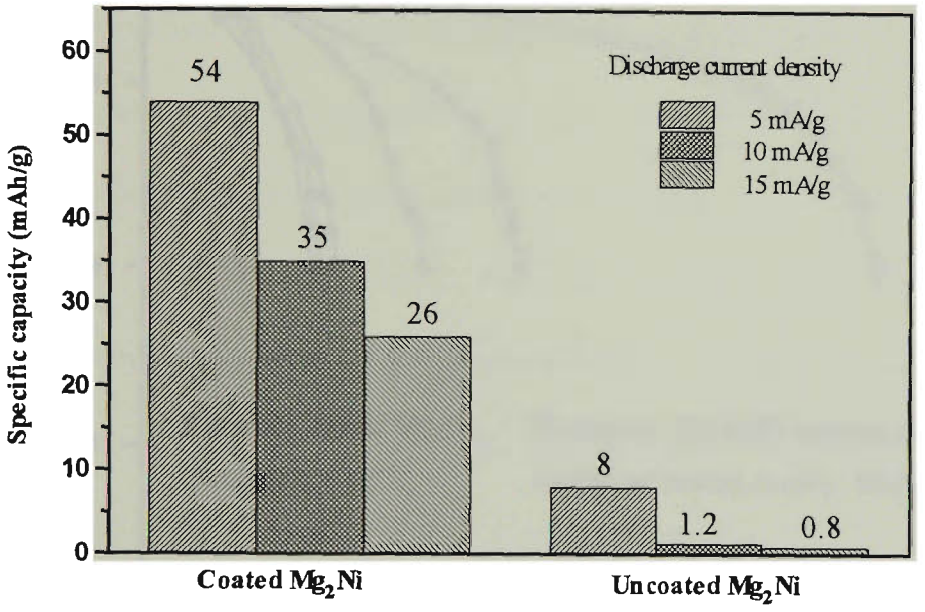

Figure 4.5 The discharge capacity comparison of the electrodes fabricated from the coated Mg_2Ni powder and from the uncoated Mg_2Ni powder at various discharge current densities, showing the discharge capacity of the electrode was remarkably improved by surface micro-encapsulation of the powder.

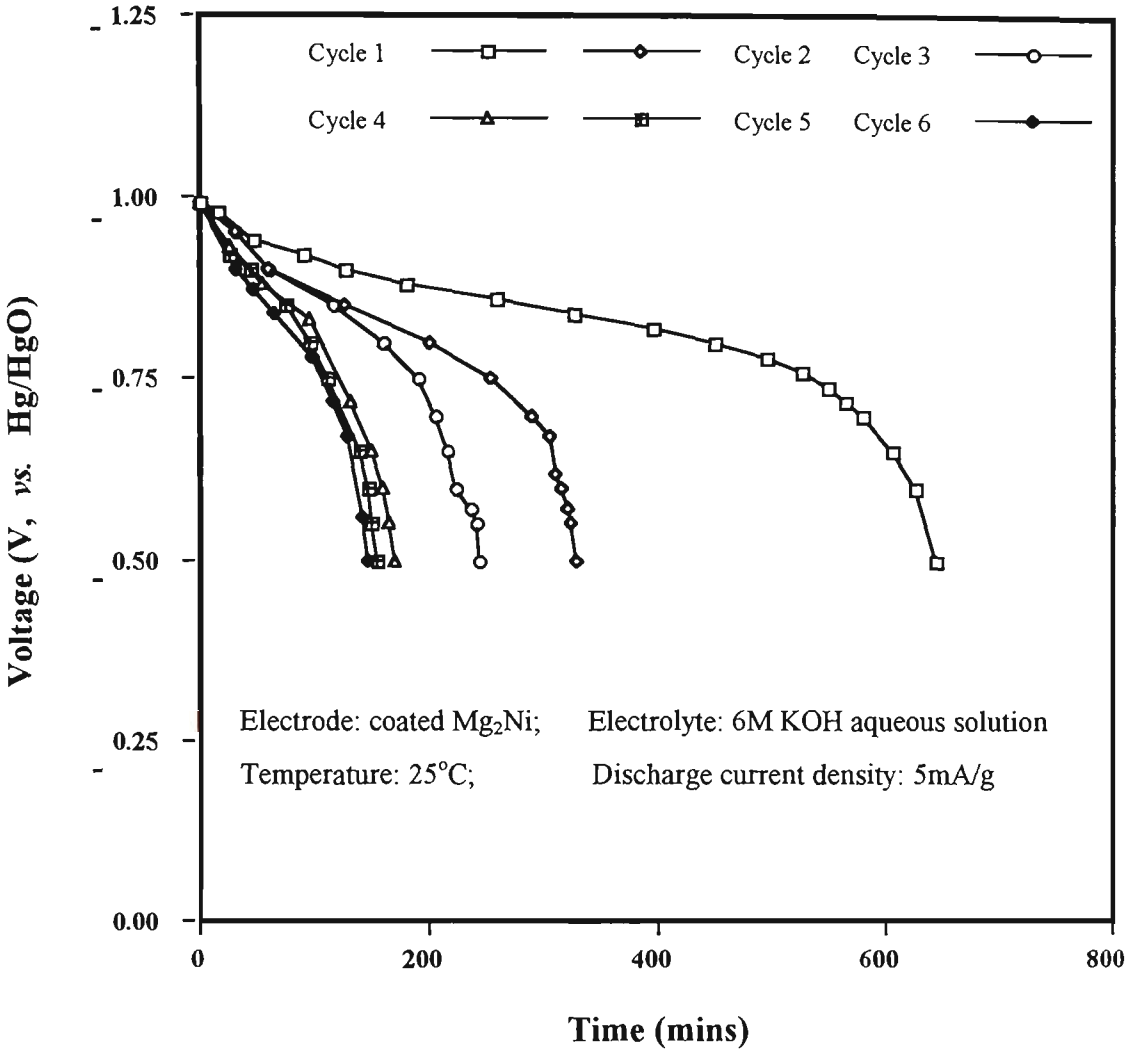

Figure 4.6 Galvanostatic discharge curves of a coated Mg_2Ni electrode in 6M KOH aqueous solution at 25°C.

electrodes can be calculated using H/M data according to the following equation:

$$C_{theory} = \frac{xF}{M} \qquad (4.2\text{-}2)$$

where F and M are the Faraday constant and the molecular weight of the alloy respectively and x is the number of hydrogen atoms per alloy unit.

The calculated values of the theoretical electrochemical capacity are given in Table 4.1. The experimental capacity value of the unmodified Mg_2Ni electrode is only 8mAh/g, which is negligibly small compared to the theoretical values. The reasons for this are probably as follows. First, the surface of Mg_2Ni alloy is usually contaminated by a dense oxide and/or hydroxide layer when exposed in KOH aqueous solution. This surface layer may inhibit the reduction of H^+ ion on the electrode surface. Thus, the oxide and/or hydroxide layer formed on the surface of the electrode may inhibit the nucleation and the growth of the hydride phase during charging, and block the migration of hydrogen to the solution/electrode interface for discharging. Second, the hydride formed at the surface acts as a diffusion barrier for the hydrogen atom [206]. The transport of hydrogen through the hydride layer is expected to be retarded since the diffusion of hydrogen in Mg_2NiH_x (low-temperature phase) is extremely slow, leading to incomplete hydriding when charging. As a result, the thickness of the hydride layer is generally about 0.1 to 1μm [237], which is much smaller than the alloy particle size (about 75 μm). Therefore, the Mg_2Ni electrode is only hydrided partially and only a very low discharge capacity can be obtained.

Table 4.1 Theoretical capacities of Mg_2Ni hydride electrodes

Hydride electrode	Capacity (mAh/g)
Mg_2NiH_4	999
Mg_2NiH	250
$Mg_2NiH_{0.3}$	75

It is well known that a Ni-coating on the Mg_2Ni alloy powder surface can effectively protect the alloy from oxidation in a KOH aqueous solution. The coating on the powder surface acts as an electrocatalyst for hydrogen ion reduction [238], and thus is beneficial to the hydriding/dehydriding reactions. It also causes an improvement in the discharge capacity and rate dischargeability. Even if the electrode is fabricated from the coated Mg_2Ni powder, once the hydride layer reaches a certain thickness, further growth of the hydride layer may become difficult due to the Mg_2NiH_x phase itself acting as a diffusion barrier for the hydrogen atom. Therefore, the discharge capacity of the electrode fabricated from the coated powder is considerably improved, but is still far from satisfactory.

4.2.3 Electrochemical Characterisation

The cathodic polarization curves of the electrodes fabricated from the coated and uncoated Mg_2Ni powders are shown in Figure 4.8. The hydrogen overpotential of the coated electrode is somewhat lower than that of the uncoated electrode. The logarithmic exchange current densities, $\log\{i_o, (A/g)\}$, obtained by extrapolating the Tafel lines to the hydrogen equilibrium potential (-0.926V, *vs.* Hg/HgO) are -0.70 for the Ni-coated Mg_2Ni electrode and -1.40 for the uncoated one. That is, the exchange current density i_o, is a measure of electrochemical activity for hydrogen evolution reaction (HER) [239, 240], increasing to 200 mA/g for the coated electrode from 40 mA/g for the uncoated one. Tafel slopes at low and high current densities and other kinetic parameters are summarized in Table 4.1a. The results in Table 4.1a suggest that the Ni-coated Mg_2Ni electrode has a higher activity for the hydrogen evolution reaction, which is beneficial for the hydriding reaction and electrode capacity. This result is in accordance with the above expectations.

Table 4.1a Kinetic parameters of the coated and uncoated Mg_2Ni electrodes in 6M KOH aqueous solution at 25°C

Electrode	Tafel slope (mV/dec)		i_0	Overvoltage (mV)		β
	LCD*	HCD**	(mA/g)	LCD* ($2x10^{-3}$A/g)	HCD** ($5x10^{-2}$A/g)	
coated	25	260	200	11	102	0.35
uncoated	43	380	40	15	390	0.15

*LCD–low current density; **HCD–high current density

Anodic polarization curves of coated and uncoated Mg_2Ni electrodes measured immediately after charging are shown in Figure 4.9. The anodic peak current for the hydride electrode at around -0.7 V *vs.* Hg/HgO has been attributed to the oxidation of hydrogen being absorbed during the cathodic charging according to the equation (4.1)

[239,240]. Figure 4.9 indicates that the anodic peak current for the coated electrode is much higher than that for the uncoated one. This confirms that the catalytic activity for hydrogen oxidation could be enhanced efficiently by the Ni-coating on Mg_2Ni powder. In addition, the surface modification also improved

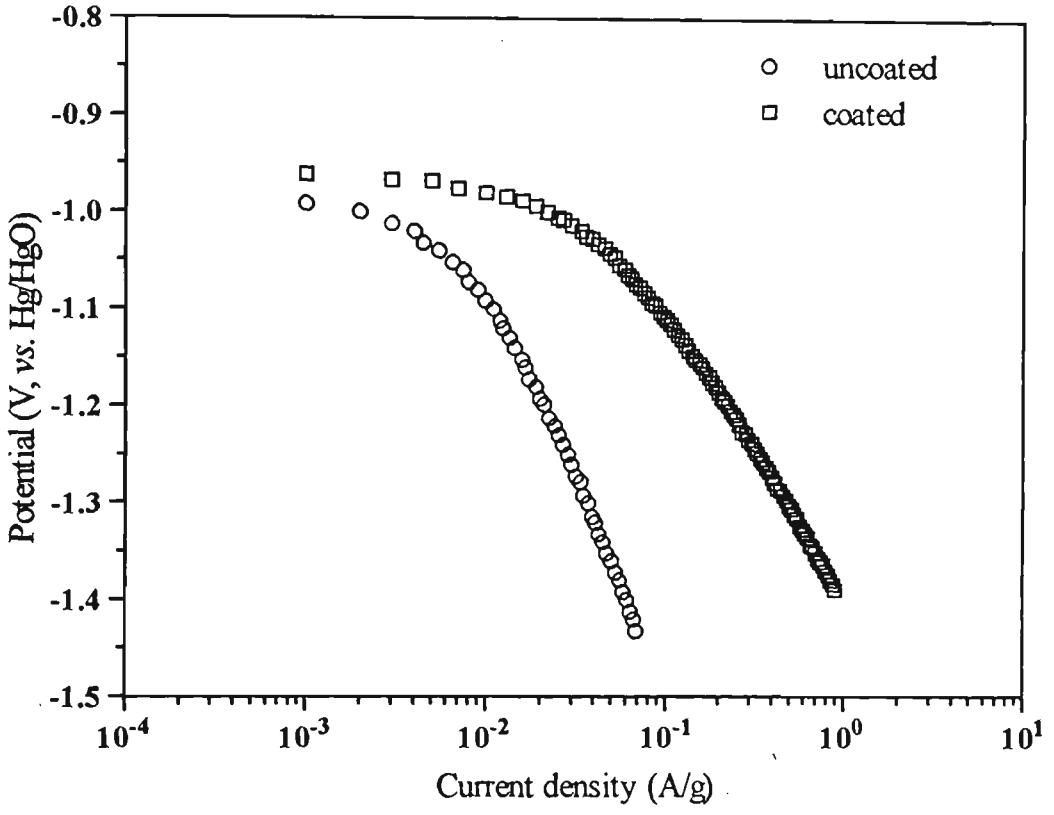

Figure 4.8 Cathodic polarization curves of the coated and uncoated Mg_2Ni electrodes in 6M KOH aqueous solution at 25°C.

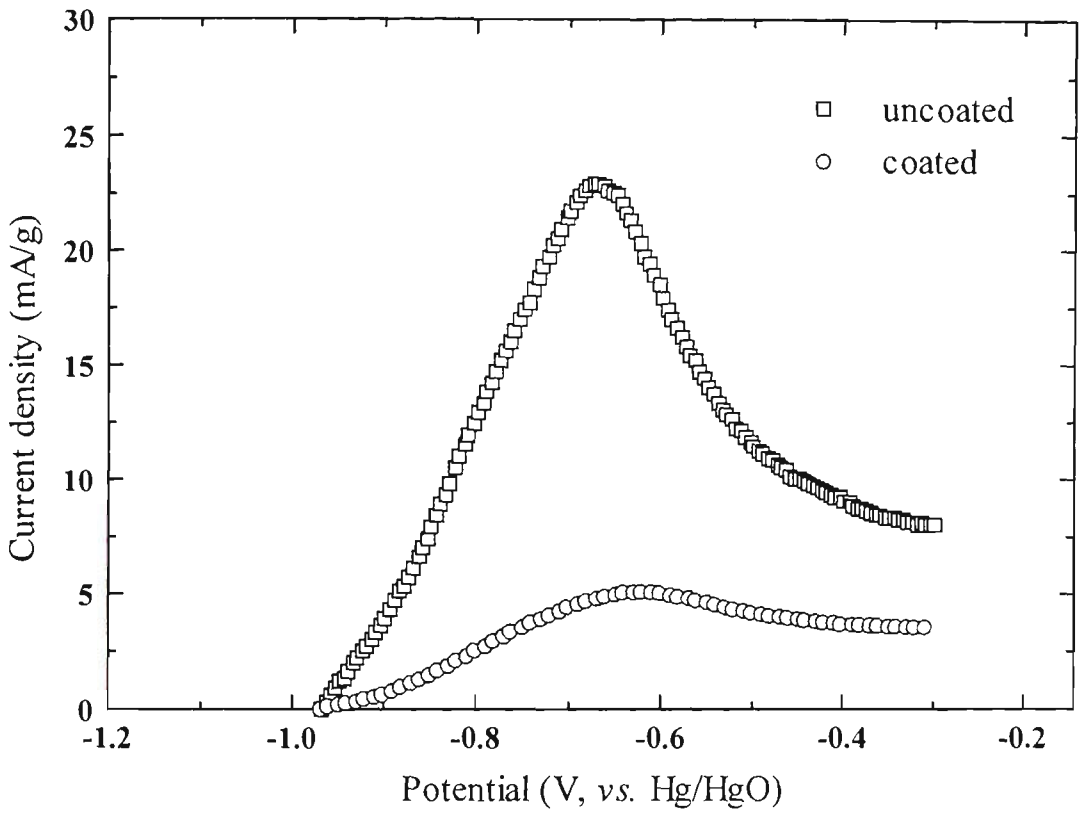

Figure 4.9 Activation profiles of the uncoated Mg_2Ni electrode and the Ni-coated Mg_2Ni electrode.

the efficiency of microcurrent collection as will be discussed in Chapter 7. Both of these effects resulted in a decrease of discharge overpotential and enlargement of discharge capacity.

4.3 $Mg_{1.95}M_{0.05}Ni$ (M = Al, Ca, La, Ti, V) Ternary Alloys

Although the Mg_2Ni alloy has a higher hydrogen storage capacity in the gas-phase hydriding reaction, its electrochemical capacity in alkaline solution, as discussed in section 4.2, is much less than for other types of hydrogen alloys (*e.g.* rare-earth system of AB_5 type, Ti system of A_2B type and Ti-Zr-V system of AB_2 Laves phase type). Substitution has been proved to be one of the most widely used methods to control the physical and electrochemical properties of hydrogen storage alloys. It was reported that the substitution of a small amount of the A site in A_2B alloys could significantly change the hydriding kinetics and stability for hydrides without significantly increasing the cost and hydrogen content of the alloys [177, 178, 181]. Selvam *et al.* [181] found that the dehydriding kinetics were improved by substituting a small amount Ca for the Mg (A) site of Mg_2Ni. Hirata and co-workers [178] studied the effect of partial substitution of Mg (A) with La and Al from Mg_2Ni. They claimed that the stability of Mg_2Ni hydrides were decreased by the substituent element Al. Similar effects of substitution of Ti for Zr (A) in AB_2 alloys were also observed by Pourarian *et al.* and Yoshida *et al.* respectively [245, 246]. In addition, it was also reported that alloying vanadium with some metals would induce these alloys to react

rapidly with hydrogen at room temperature although vanadium metal itself does not readily form hydrides at room temperature [241, 242].

In order to improve electrochemical capacity of the Mg_2Ni alloy without significantly increasing alloy cost, small amounts of Al, Ca, La, Ti and V were adopted here as replacement elements for the Mg (A) site in Mg_2Ni. The effects of substitution on the microstructure, electrode performance, electrochemical characteristics were investigated and discussed.

4.3.1 Microstructure

X-ray diffraction patterns of the $Mg_{1.95}M_{0.05}Ni$ (M = Al, Ca, La, Ti, V) ternary alloys are shown in Figure 4.10. As can be seen from this Figure, all these ternary alloys have the same diffraction pattern as the Mg_2Ni binary alloy sample does, *i.e.* a hexagonal symmetry identical to the $(MgM)_2Ni$ phase together in with a small amount of metallic Mg phase. Minor changes of relative intensity and peak width in Figure 4.10 were observed, which might be ascribed to the different substituted elements and grain size of the alloys. No other new phases were detected in all these ternary alloys, indicating that the replacing elements M (Al, Ca, La, Ti, V) go into the Mg (A) site. SEM micrographs in Figure 4.11 reveal that the metallurgical microstructures of these ternary alloys are also characterized by a lamellar eutectic {Mg + $(MgM)_2Ni$} structure in addition to the primary $(MgM)_2Ni$ phase. However, the unit cell volumes of $Mg_{1.95}M_{0.05}Ni$ alloys were found to change with the different substituted elements. The change of the unit cell volume was attributed to the difference between the

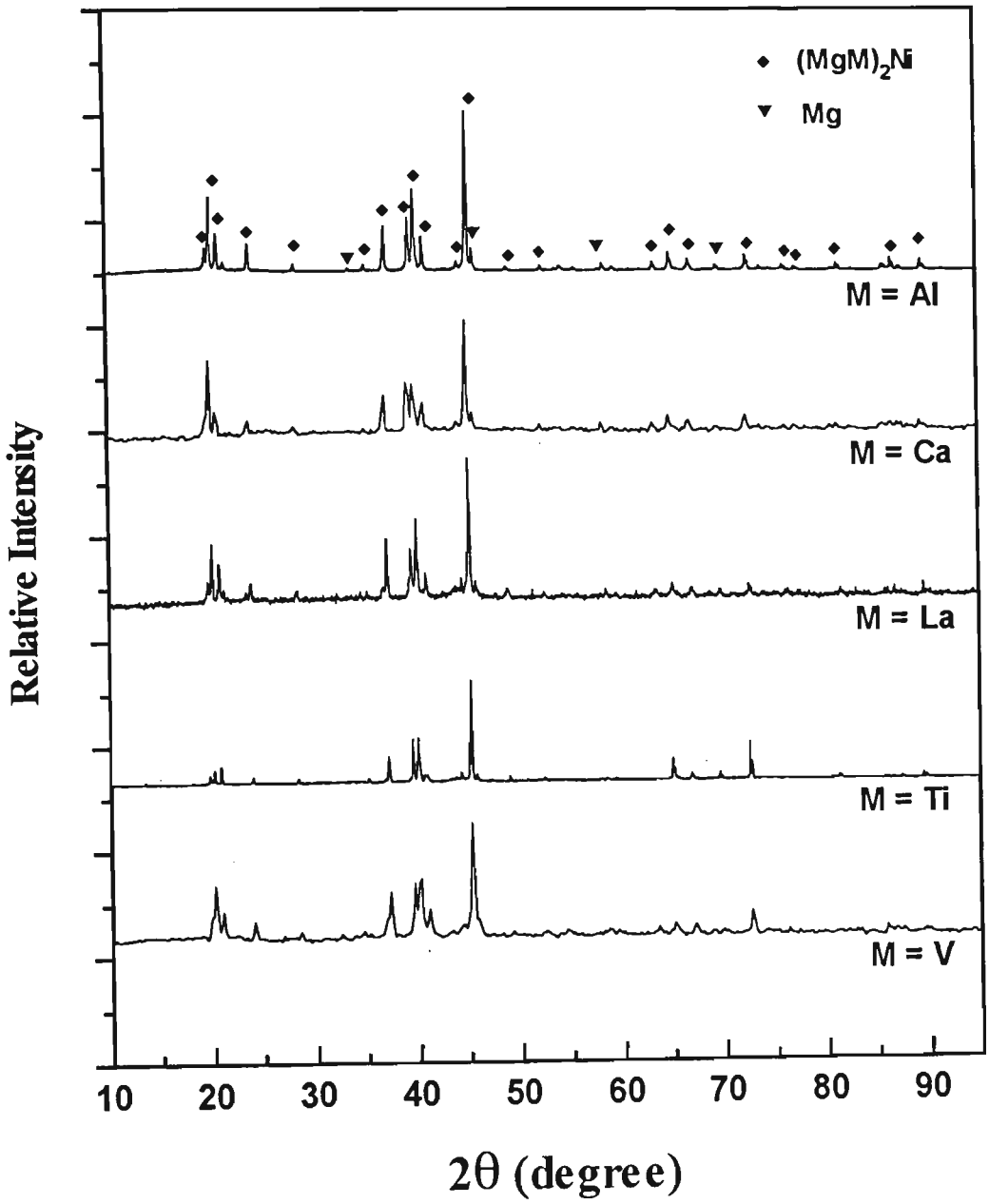

Figure 4.10 X-ray diffraction patterns of $Mg_{1.95}M_{0.05}Ni$ (M = Al, Ca, La, Ti, V).

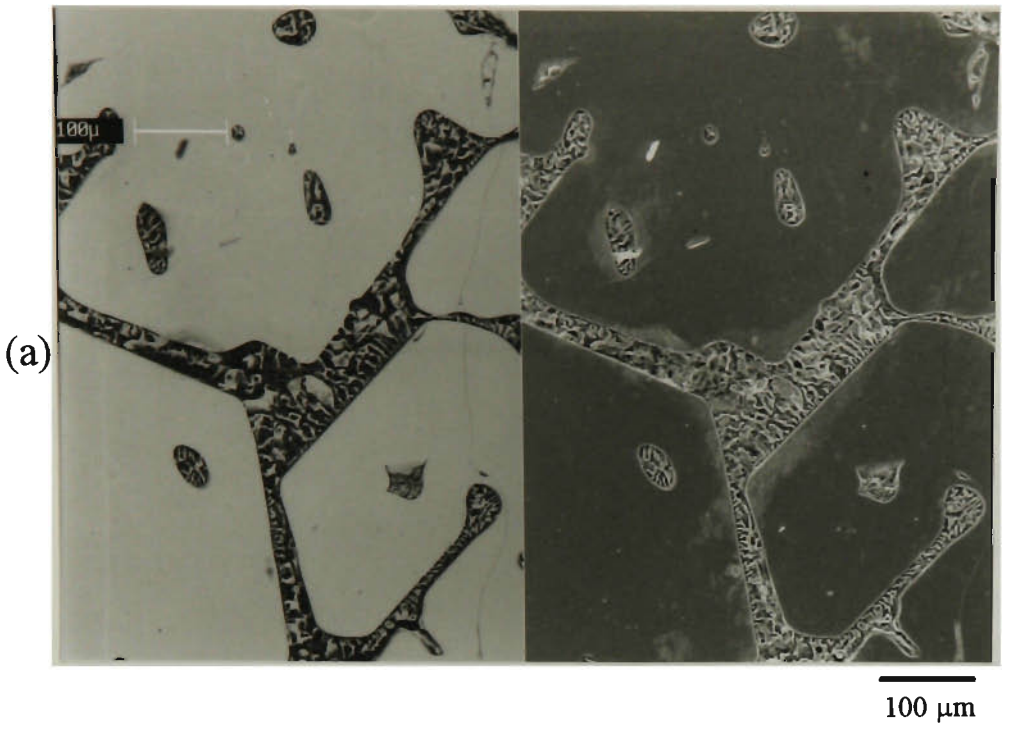

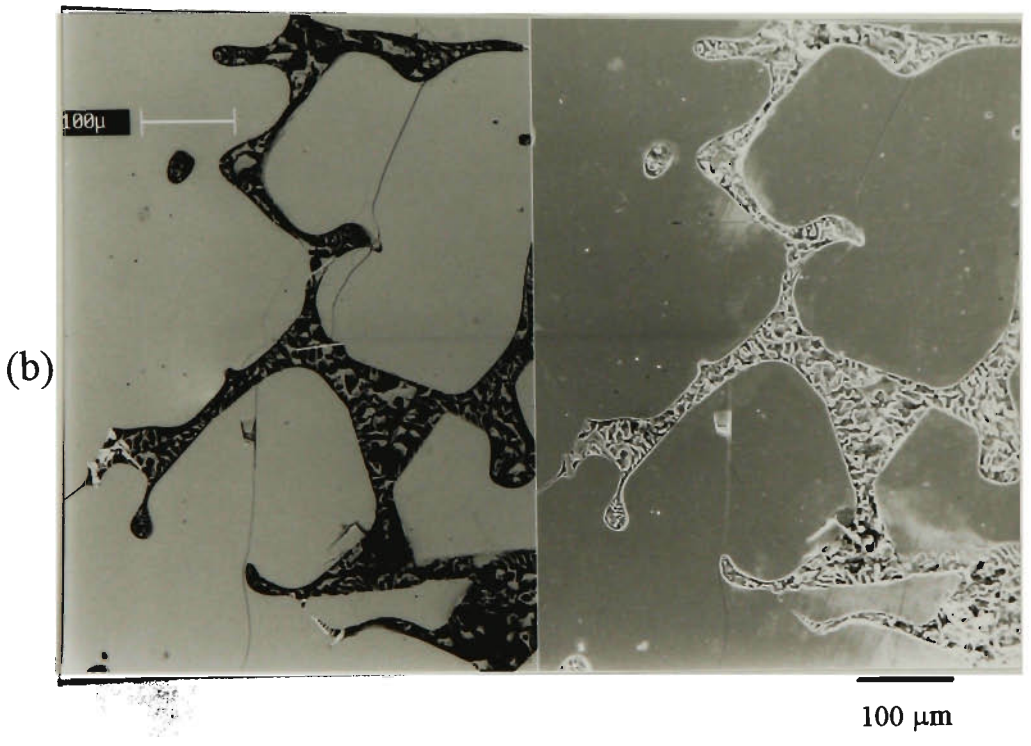

Figure 4.11 Secondary electron images (right side) and back scatter electron images (left side) of $Mg_{1.95}M_{0.05}Ni$ (M = Al, Ca, La, Ti, V) alloys. (a) M = Al; (b) M = Ca; (c) M = La; (d) M = Ti; (e) M = V.

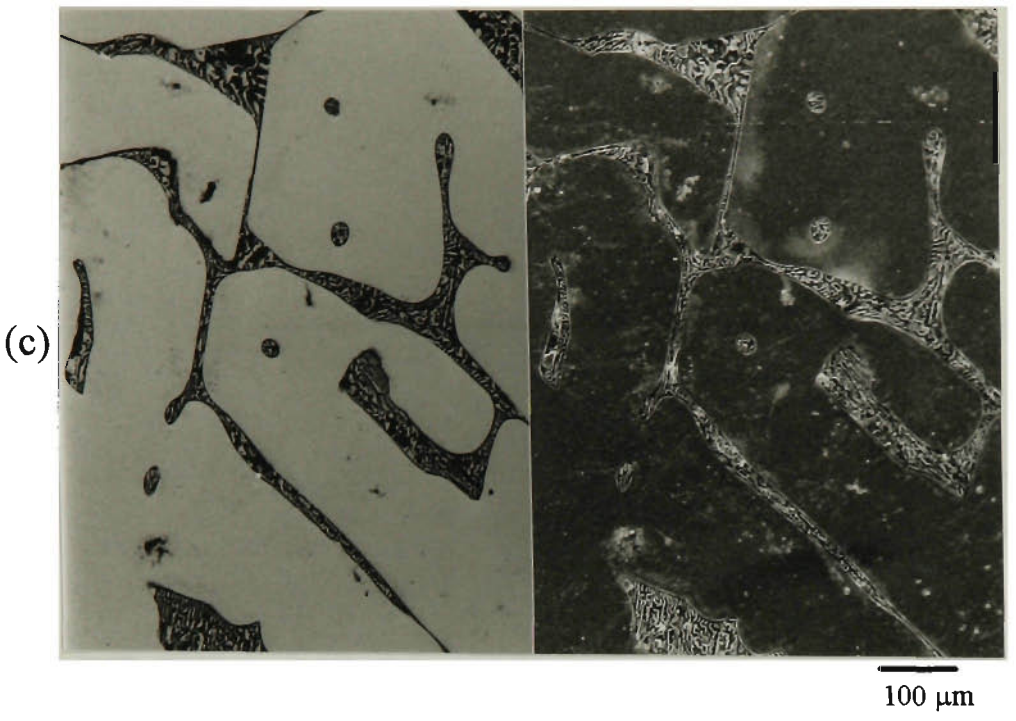

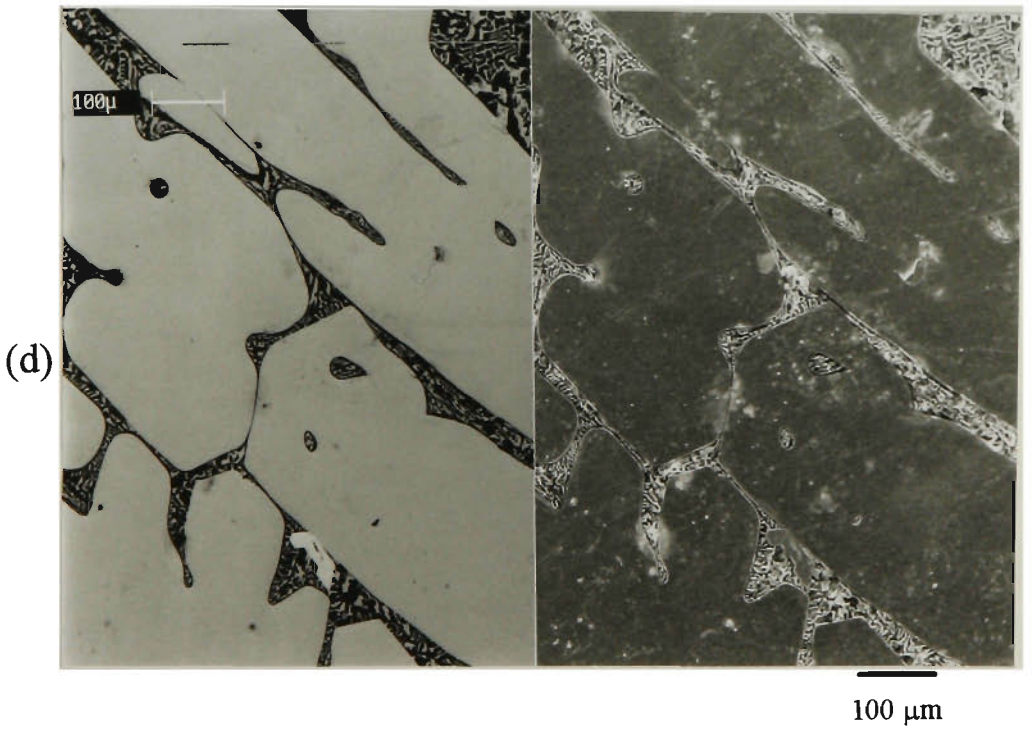

Figure 4.11 (continued)

(e)

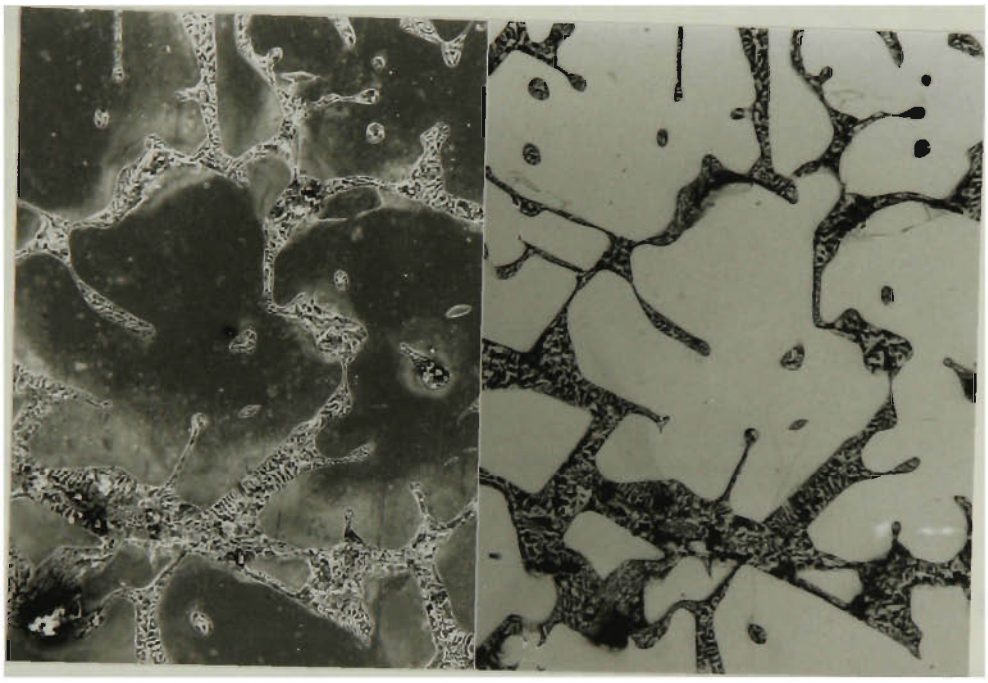

Figure 4.11 (continued)

atomic radius of the host elements (r_h) and that of the substituent elements (r_s) [246]. When r_h is larger than r_s, the cell volume decreases. Conversely, when r_h is smaller than r_s, the cell volume increases. The unit cell volumes as a function of the ingredient radius [250] of substituting elements (M = Al, Ca, La, Ti, V) are shown in Figure 4.12. The data in Figure 4.12 indicate that the unit cell volumes of $Mg_{1.95}M_{0.05}Ni$ alloys increase linearly with the increasing radius of substituent elements. This is similar to the results reported by Iwakura *et. al* for the rare earth-nickel based AB_5 alloys [239] and Zr-based AB_2 alloys [241].

4.3.2 Discharge Performance

The typical discharge curves of $Mg_{1.95}M_{0.05}Ni$ alloys are shown in Figure 4.13. It has been noted that the discharge performance of the electrode changes with the various substituents for Mg in Mg_2Ni. The discharge capacity improves with the ternary substituents studied in the order Ca < La < Ti < V < Al. The addition of small amounts of aluminum or vanadium significantly improves the electrode capacity, which makes the specific capacity more than double (from 8 mAh/g of Mg_2Ni to 18 mAh/g of $Mg_{1.95}Al_{0.5}Ni$ and 17.4 mAh/g of $Mg_{1.95}Al_{0.5}Ni$, respectively). Titanium substitution seems also to increase effectively the discharge capacity, while Ca and La have almost no positive effects on the electrode capacity. This result indicates that it is possible to improve the poor discharge characteristics of Mg_2Ni anodes by a small amount of substitution for the Mg in Mg_2Ni.

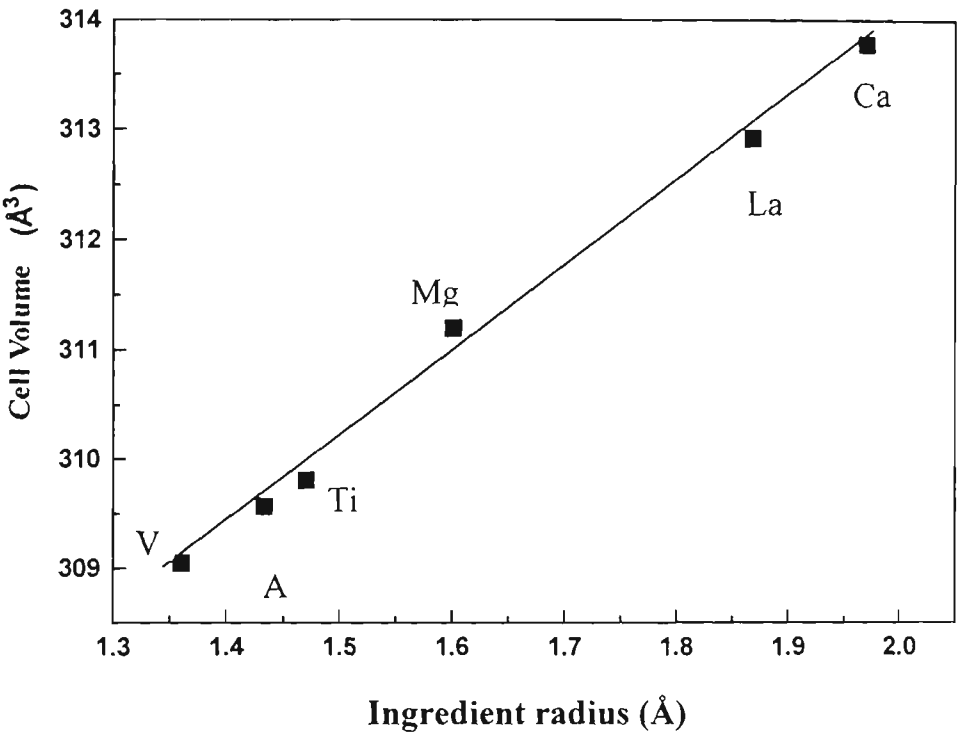

Figure 4.12 Unit cell volume of $Mg_{1.95}M_{0.05}Ni$ as a function of the ingredient radius of substituted elements.

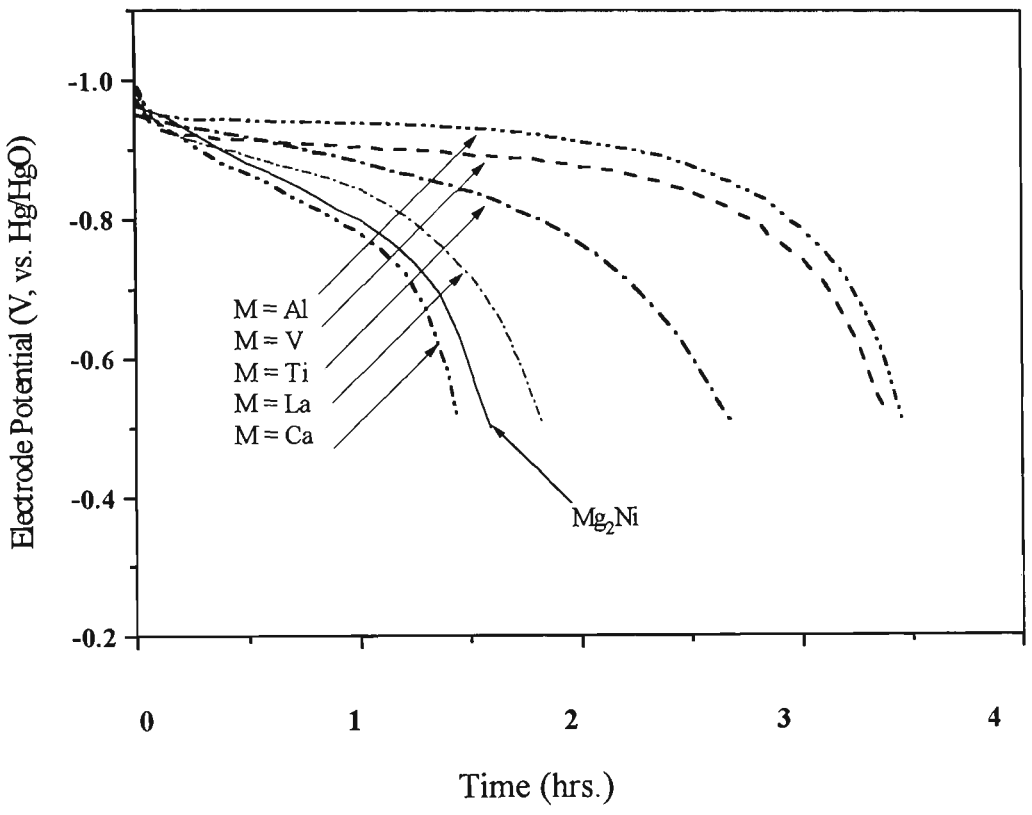

Figure 4.13 Galvanostatic discharge curves of $Mg_{1.95}M_{0.5}Ni$ (M = Ca, La, Mg, Ti, V, Al) alloy electrodes in 6M KOH aqueous solution at room temperature. (discharge current density: 5mA/g)

It was reported that the logarithm of the equilibrium plateau pressure ($\ln P_{eq}$) for the the rare earth-nickel based AB_5 alloys and Zr-based AB_2 alloys linearly increased with decreasing unit cell volume [246-248], which means that the hydride stability was reduced. The reason for this was ascribed to the "size effect" [68, 249], *i.e.* the decreasing unit cell volume could cause a reduction in the size of hydrogen occupation site and thereby, result in a reduction in hydride stability. The unit cell volume of Mg_2Ni base alloy, as shown in Figure 4.12, was decreased by the substitution of smaller atomic radius atoms of aluminum and vanadium. Consequently, it is believed that the "size effect" may be one of the main factors which lead to a notable increment of discharge capacity of Mg_2Ni based alloy. However, it should be noted that the discharge capacity of $Mg_{1.95}Al_{0.05}Ni$ is somewhat larger than that of $Mg_{1.95}V_{0.05}Ni$ although the reduction of the unit cell volume by substituting V was more than that by substituting Al. This fact is not consistent with the "size effect" because a smaller cell volume is expected to reduce the hydride stability leading to a higher discharge capacity. Therefore, there must be some other factors, *e.g.* the intrinsic chemical nature of the substituted metallic element such as electrocatalytic activity and/or stability in an alkaline solution, which are also responsible for modifying the discharge capacity.

The mean discharge potentials (the potential averaged over the whole discharge capacity at a low discharge rate of 5 mA/g) of $Mg_{1.95}M_{0.05}Ni$ alloy electrodes are listed in Table 4.2. It is apparent that $Mg_{1.95}V_{0.05}Ni$ and $Mg_{1.95}Al_{0.05}Ni$ electrodes have a

lower mean discharge potential, which suggests that substitution of magnesium with aluminum and vanadium may be effective in lowering the anodic overpotentials during discharging. This would be expected to improve the discharge behaviour of the Mg_2Ni-type alloy electrodes, resulting in an increase of the discharge capacity.

Table 4.2 The mean discharge potential (MDP) of the $Mg_{1.95}M_{0.05}Ni$ alloy electrode at a discharge current density of 5mA/g.

M =	Mg	Ca	La	Ti	Al	V
MDP (V,*vs.* Hg/HgO)	-0.789	-0.775	-0.801	-0.859	-0.871	-0.880

From the above the results it is obvious that the initial discharge capacity of Mg_2Ni alloy can be markedly improved by the substitution of small amounts of elements such as Al, V and Ti, for Mg in Mg_2Ni. This improvement is probably due to a reduction of the hydride stability and/or a change in the kinetics of electrochemical dehydriding in the electrolyte. In order to clarify the effects of the substituent elements on the kinetics of hydriding and dehydriding, electrochemical measurements were performed.

4.3.3 Electrochemical Characteristics

According to electrochemical theory, for a one-electron electrochemical reaction, *i.e.* the reduction of a water molecule on a metal hydride surface in alkaline solution

$$H_2O + e^- \xleftrightarrow{M} H_{ad} + OH^- \tag{4.3-1}$$

the current density-overpotential relationship can be expressed as:

$$i = i_0\left\{\left(\frac{c_H}{c_H^0}\right)^n\left(\frac{a_{OH^-}}{a_{OH^-}^0}\right)^n \exp\left(\frac{\beta F\eta}{RT}\right) - \left(\frac{a_{H_2O}}{a_{H_2O}^0}\right)^p \exp\left(\frac{(1-\beta)F\eta}{RT}\right)\right\} \tag{4.3-2}$$

where c_H (c_H^0) is the concentration of H at the electrode surface (in the electrode bulk), and a_{OH^-} ($a_{OH^-}^0$) and a_{H_2O} ($a_{H_2O}^0$) are respectively the activities of OH^- and H_2O at the electrode/electrolyte interface (in the electrolyte bulk), n, m, p are the reaction orders of H, OH^- and H_2O respectively. β is the symmetry factor, R is the gas constant, T is the absolute temperature, F is the Faraday constant, η is the overpotential, i is the current density and i_o is the exchange current density.

If the mass-transport limitations can be neglected and the charge transfer is the rate-determining step (RDS), $c_H \cong c_H^0$, $a_{OH^-} \cong a_{OH^-}^0$ and $a_{H_2O} \cong a_{H_2O}^0$; then

$$i = i_0\left\{\exp\left(\frac{\beta F\eta}{RT}\right) - \exp\left(\frac{(1-\beta)F\eta}{RT}\right)\right\} \tag{4.3-3}$$

When ($\beta F\eta/RT$)<<1, *i.e.* for micropolarization, the exponential terms can be written as Taylor expressions, and for small values of the arguments $\beta F\eta/RT$ and $(1-\beta)F\eta/RT$, the first two terms can be combined to give

$$i = i_0\frac{F\eta}{RT} \tag{4.3-4}$$

At low $|\eta|$ (micropolarization) the current density varies linearly with the overpotential. The charge transfer resistance R_t near equilibrium can be defined as [251]

$$R_t = \left(\frac{\partial \eta}{\partial i}\right)_{i \to 0} = \frac{RT}{i_0 F} \qquad (4.3\text{-}5)$$

After rearrangement equation (4.3-5), one obtains

$$i_0 = \frac{RT}{F} \frac{1}{\left(\frac{\partial \eta}{\partial i}\right)_{i \to 0}} \qquad (4.3\text{-}6)$$

In the linear polarization region, the charge transfer resistance, R_t is readily obtained from the slope of the experimental η *vs.* i plots and i_0 can be calculated by using equation (4.3-6).

The electrocatalytic activity for the reaction (4.3-1) would be strongly affected by the alloy composition. To evaluate the electrocatalytic nature of the modified alloy electrodes, the micropolarization was performed on the alloys $Mg_{1.95}M_{0.05}Ni$ (M = Al, Ca, La, Ti, V) under potentiodynamic conditions at a scan rate of 0.01 mV/s. The scan rate was chosen to provide near-steady-state conditions with minimal changes in the state of charge of the electrode or its surface condition [244]. Figure 4.14 shows the micropolarization curves of the various $Mg_{1.95}M_{0.05}Ni$ alloys. These curves follow a good linear relationship between the overpotential η and the current density i over the range measured. The apparent exchange current density might be taken as a measure [239, 252] of the electrochemical catalytic activity for reaction (4.3-1) on the porous hydride electrodes. Assuming that the charge transfer is the RDS, the

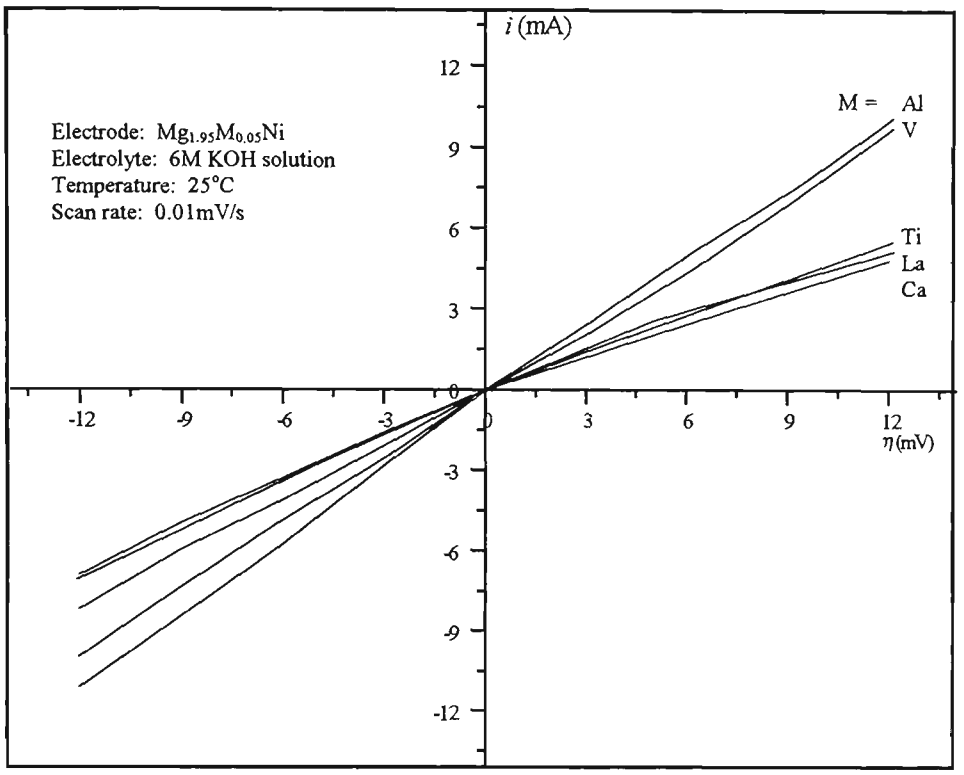

Figure 4.14 Linear polarization curves of $Mg_{1.95}M_{0.05}Ni$ (M = Al, Ca, La, Ti, V) alloys.

values of charge transfer resistance R_t and apparent exchange current density i_0 for the $Mg_{1.95}M_{0.05}Ni$ alloy electrodes then can be estimated from the linear polarization curves (Figure 4.14), equation (4.3-6). The results are listed in Table 4.3. The exchange current densities of Al- and V-substituted alloys are 21.40 and 20.71 mA/g respectively, which are much higher than those of Ti-, La- and Ca-substituted alloys. The value of i_0 was increased by the substituted metals in the order of Al > V > Ti > La > Ca. This is in good agreement with the results for discharge capacity with different substituents for the $Mg_{1.95}M_{0.05}Ni$ alloys as mentioned in section 4.3.2. This indicates that the electrocatalytic activity for the reaction (4.3.1) was significantly improved by substituting small amounts of Al and V for Mg in Mg_2Ni. Also this was beneficial to the hydriding/dehydriding kinetics of the electrode reaction, with charge transfer being the RDS, leading to a significant increase in the discharge capacity.

4.4 $Mg_{2-x}Al_xNi_{1-y}Y_y$ Quaternary Alloys

4.4.1 Phase Structure

The alloys of the overall formula $Mg_{1.9}Al_{0.1}Ni_{1-x}Y_x$ (x = 0, 0.05, 0.1, 0.15, 0.2, 0.25, 0.3) were analysed by powder X-ray diffraction technique. It was concluded that the alloy was of a multiphase structure. The main phase has a hexagonal symmetry identical to the Mg_2Ni phase. The coexisting phase contains a small amount of Al-Ni intermetallic compounds (*i.e.* $AlNi_3$ and AlNi) and a Y-Ni intermetallic compound (*i.e.* YNi_3). However, a change in the relative intensities and broadening in the

Table 4.3 Charge transfer resistance and apparent exchange current densities for various $Mg_{1.95}M_{0.05}Ni$ alloys

Substituent	R_t (Ω g)	i_o (mA/g)
Al	1.20	21.40
V	1.24	20.71
Ti	2.20	11.67
La	2.36	10.88
Ca	2.52	10.19

diffraction lines indicate a small distortion of the Mg_2Ni lattice. The lattice constants a, c and the crystal cell volume increased slightly when yttrium was added (Table 4.4). This may be explained if yttrium, having a larger atomic radius (1.81Å) than nickel (1.25Å) [250], when partially substituted for nickel in the Mg_2Ni lattice, causes an increase of the lattice constants (a, c) and the crystal cell volume.

4.4.2 Discharge Capacity

Figure 4.15 shows typical discharge curves for $Mg_{1.9}Al_{0.1}Ni_{1-x}Y_x$ alloy electrodes with various yttrium contents. The effect of yttrium content on the discharge

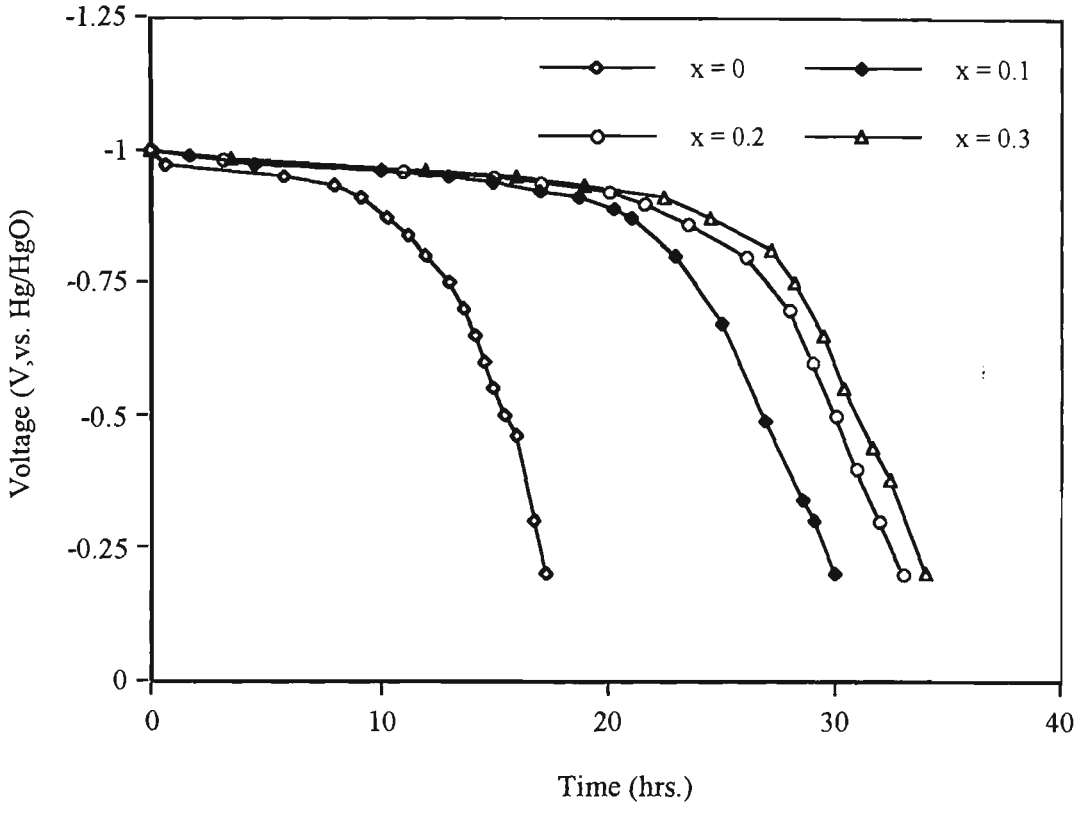

Figure 4.15 Discharge curves of $Mg_{1.9}Al_{0.1}Ni_{1-x}Y_x$ alloy electrodes with various Y content (discharge at 5 mA/g).

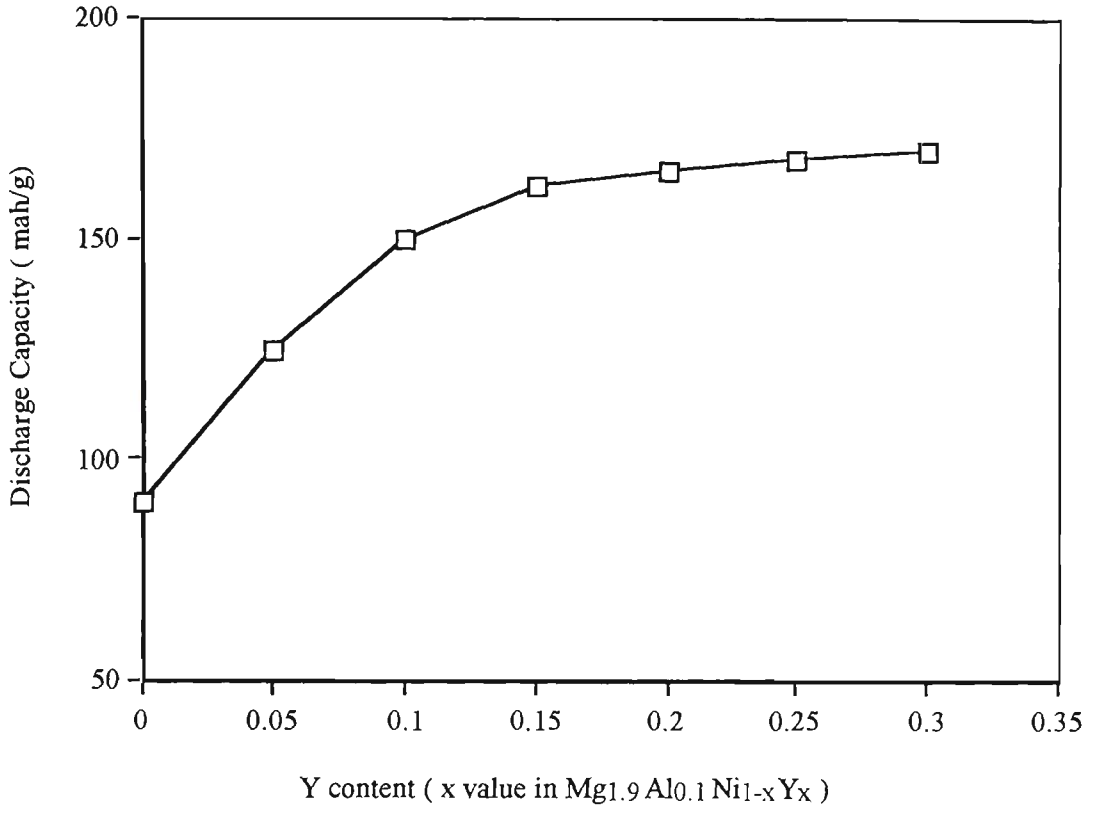

Figure 4.16 Discharge capacity of $Mg_{1.9}Al_{0.1}Ni_{1-x}Y_x$ alloy electrodes *vs.* Y content (discharge at 5 mA/g).

capacity of Mg_2Ni-type alloy electrodes is shown in Figure 4.16 as a function of x value in $Mg_{1.9}Al_{0.1}Ni_{1-x}Y_x$. It can be seen that the addition of yttrium significantly improves the discharge capacity of the electrodes. An asymptotic relation between discharge capacity and yttrium addition was observed. The discharge capacity increases rapidly with increasing yttrium content up to 5.2 *at.*% (*i.e.* $x = 0.15$ in $Mg_{1.9}Al_{0.1}Ni_{1-x}Y_x$). Beyond this value, the discharge capacity increases at a much slower rate with increasing yttrium content. For $Mg_{1.9}Al_{0.1}Ni_{0.7}Y_{0.3}$ alloy electrode, the discharge capacity reached up to 170 mAh/g at low discharge rate (5 mA/g), which was almost comparable to the capacity of the Ti_2Ni electrode [254]. It should be noted that, in spite of the increase in the unit cell volume of $Mg_{1.9}Al_{0.1}Ni_{1-x}Y_x$ with increasing Y content, which might be expected to result in the increase in an stability of the alloy hydrides, the electrochemical capacity of the alloys, however, increases. Consequently, the change in hydriding kinetics should be taken into account to interpret the dependence of the discharge capacity on Y substitution.

As described in the previous section, the discharge capacity of the unmodified Mg_2Ni alloy electrode is very low (only 8 mAh/g) [41], although Mg_2Ni alloy has a high hydrogen storage capacity (3.8 *wt.* %) in gas-solid phase reaction. This is due to its hydriding/dehydriding difficulties at ambient temperature and oxide film formation on the surface of alloy powder exposed to alkaline solution, which results in a high discharge overpotential and low electrochemical capacity. Figure 4.16 clearly shows that the discharge capacity of Mg_2Ni-type alloy electrode is enhanced by the addition of yttrium. This behaviour may be attributed to the following factors: (i) an addition

Table 4.4 The lattice parameters and unit cell volume of $Mg_{1.9}Al_{0.1}Ni_{1-x}Y_x$ alloys before cycling

x	a (Å)	c(Å)	V(Å^3)
0	5.198	13.302	933.77
0.1	5.203	13.314	936.41
0.2	5.206	13.321	937.99
0.3	5.207	13.326	938.70

of yttrium would improve the electrocatalytic activity for the hydrogen evolution reaction and added yttrium (or YNi_3 phase) may act as active sites for hydriding/dehydriding [42]. (ii) as discussed above, the crystal cell volume of the alloys increases with increasing yttrium content. This is beneficial for hydrogen diffusion in the alloys although it might cause an increment of hydride stability simultaneously.

4.4.3 Dependence of Discharge Capacity on Discharge Rate

Figure 4.17 shows the relationship between discharge current density and discharge capacity for the $Mg_{1.9}Al_{0.1}Ni_{1-x}Y_x$ alloy electrodes. To consider the dependence of discharge capacity on discharge rate (discharge rate characteristics), the relationship between the capacity ratio Cn/C_5 (C_n refers to the discharge capacity at a discharge

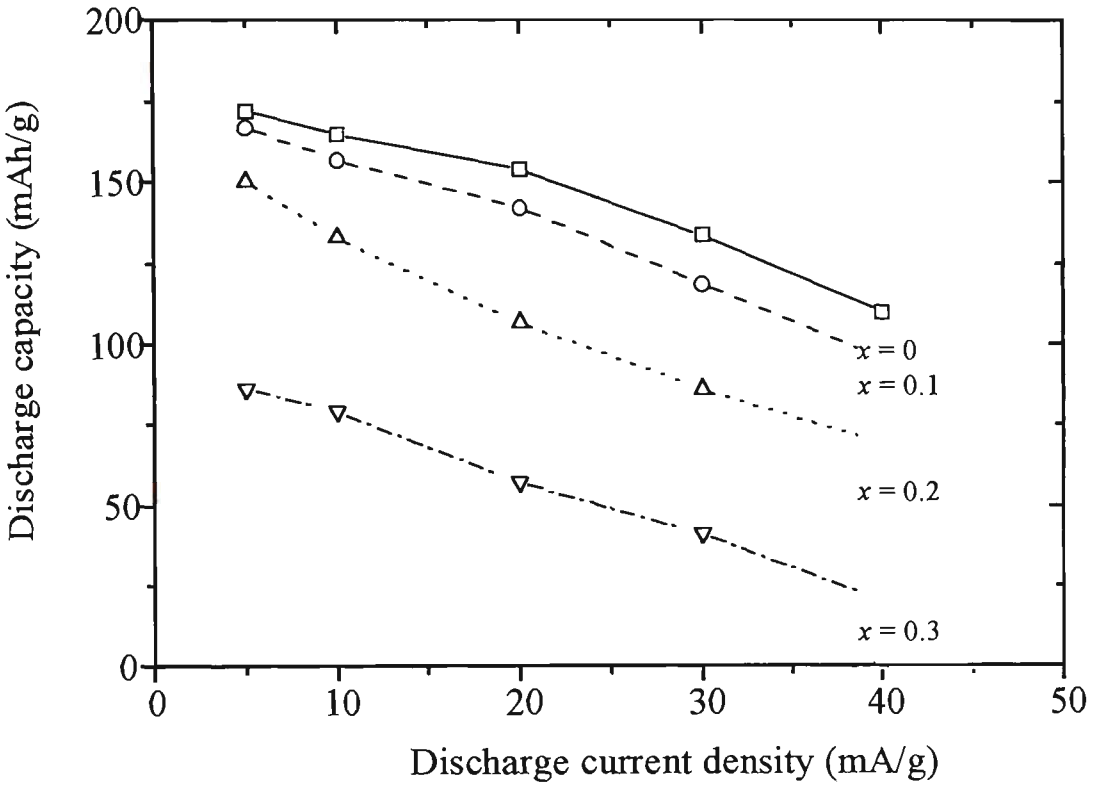

Figure 4.17 Discharge current density dependence of discharge capacity for the $Mg_{1.9}Al_{0.1}Ni_{1-x}Y_x$ alloy electrodes.

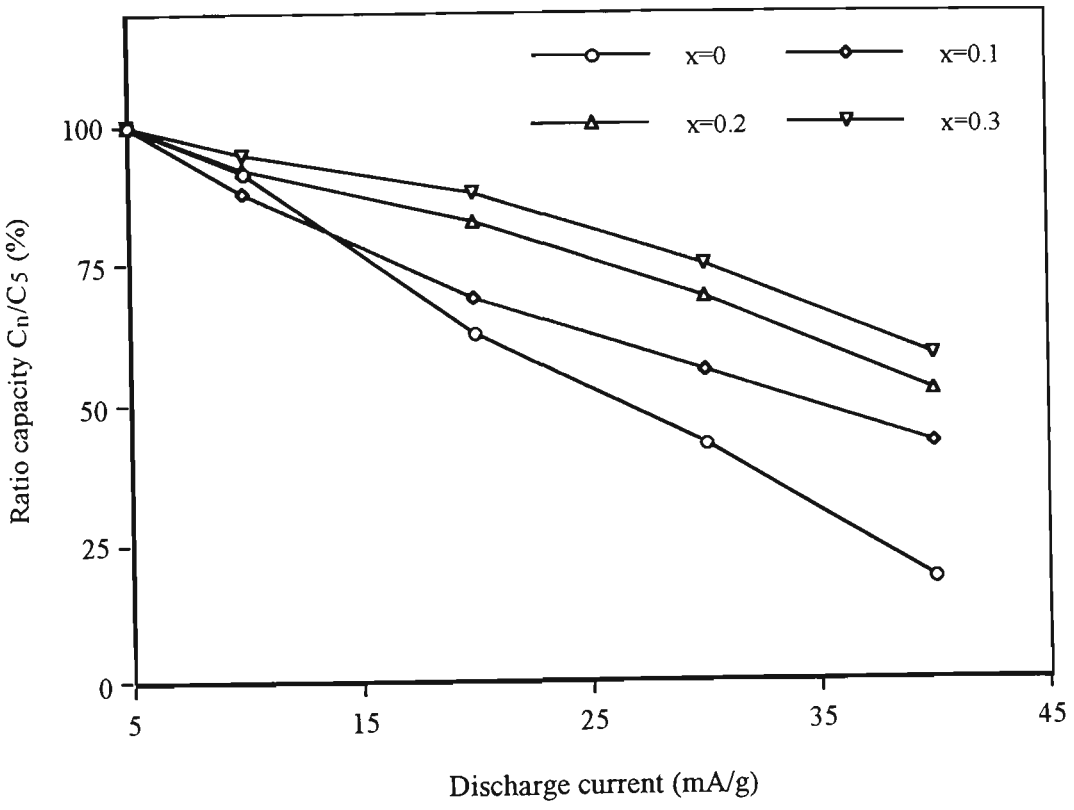

Figure 4.18 The relationship between the capacity ratio C_n/C_5 and discharge current density. (C_n refers to the discharge capacity at a discharge current density of n mA/g).

current density of n mA/g) and discharge current density is given in Figure 4.18. As seen in Figure 4.18, yttrium additions appreciably improve the discharge rate characteristics of the Mg_2Ni-type electrodes. The discharge capacity obtained at 20 mA/g was approximately 88% of that obtained at 5 mA/g for $Mg_{1.9}Al_{0.1}Ni_{0.7}Y_{0.3}$ alloy electrode, while for the yttrium-free Mg_2Ni-type alloy electrode (*i.e.* $Mg_{1.9}Al_{0.1}Ni$ alloy electrode) the discharge capacity obtained at 20 mA/g was only 62% of that obtained at 5 mA/g. It seems likely that this change in the discharge rate characteristics was because the electrocatalytic activity was improved with the addition of yttrium in the alloys.

4.4.4 Exchange Current Density and High-Rate Dischargeability

In order to compare the discharge current dependence of the discharge capacity of the Mg_2Ni-type alloy electrodes, a high-rate dischargeability (HRD) was defined as the ratio of discharge capacity at 40 mA/g (C_{40}) and at 5 mA/g (C_5) in this experiment. The effect of yttrium addition on the apparent exchange current density (i_0) and the high-rate dischargeability (C_{40}/C_5) was then considered as shown in Figure 4.19. The exchange current density (i_0), which is a measure of electrochemical activity for the hydrogen evolution reaction [239,240], increases significantly with increasing yttrium content in the alloys. The same trend was observed for the high-rate dischargeability. It was found that changes in the high-rate dischargeability appear to be well

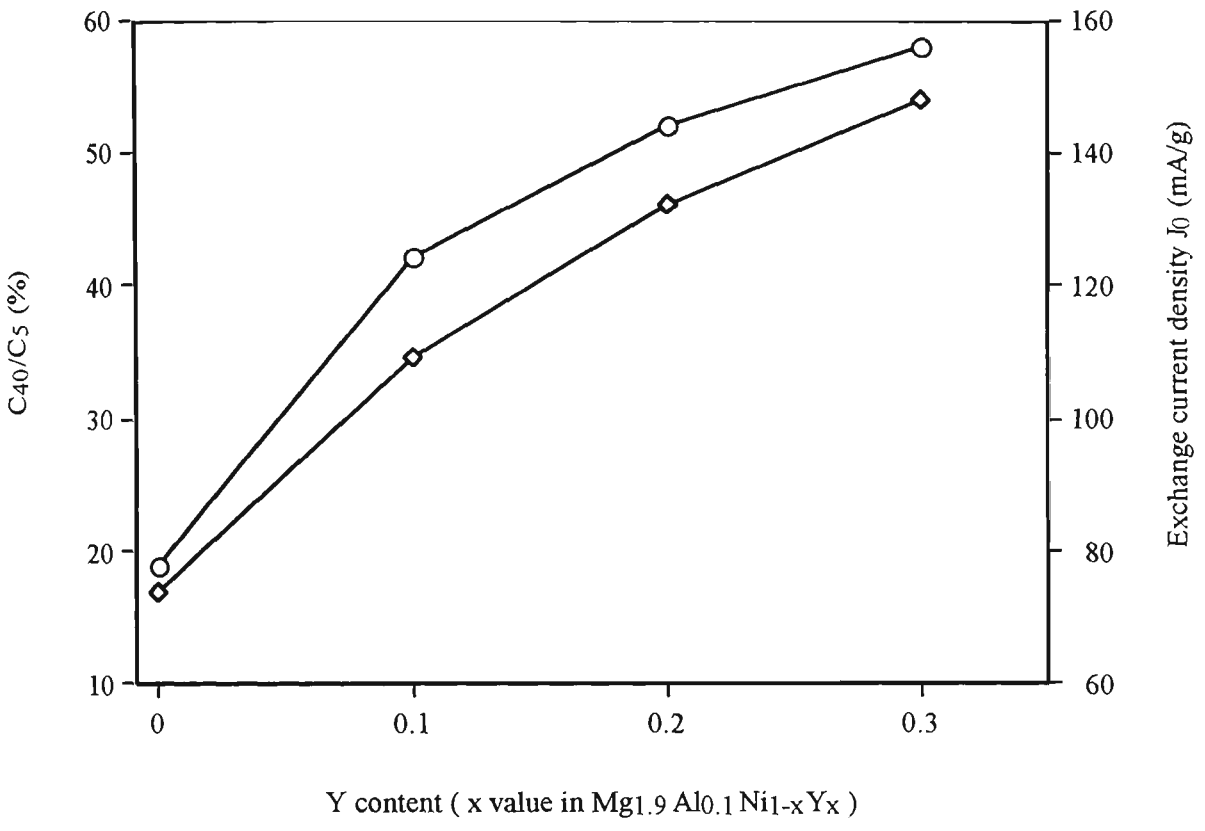

Figure 4.19 Exchange current density and rate capability as a function of Y content for $Mg_{1.9}Al_{0.1}Ni_{1-x}Y_x$ alloy electrodes. (C_{40}, C_5 refer to the discharge capacity at discharge current density of 40 mA/g, 5 mA/g respectively).

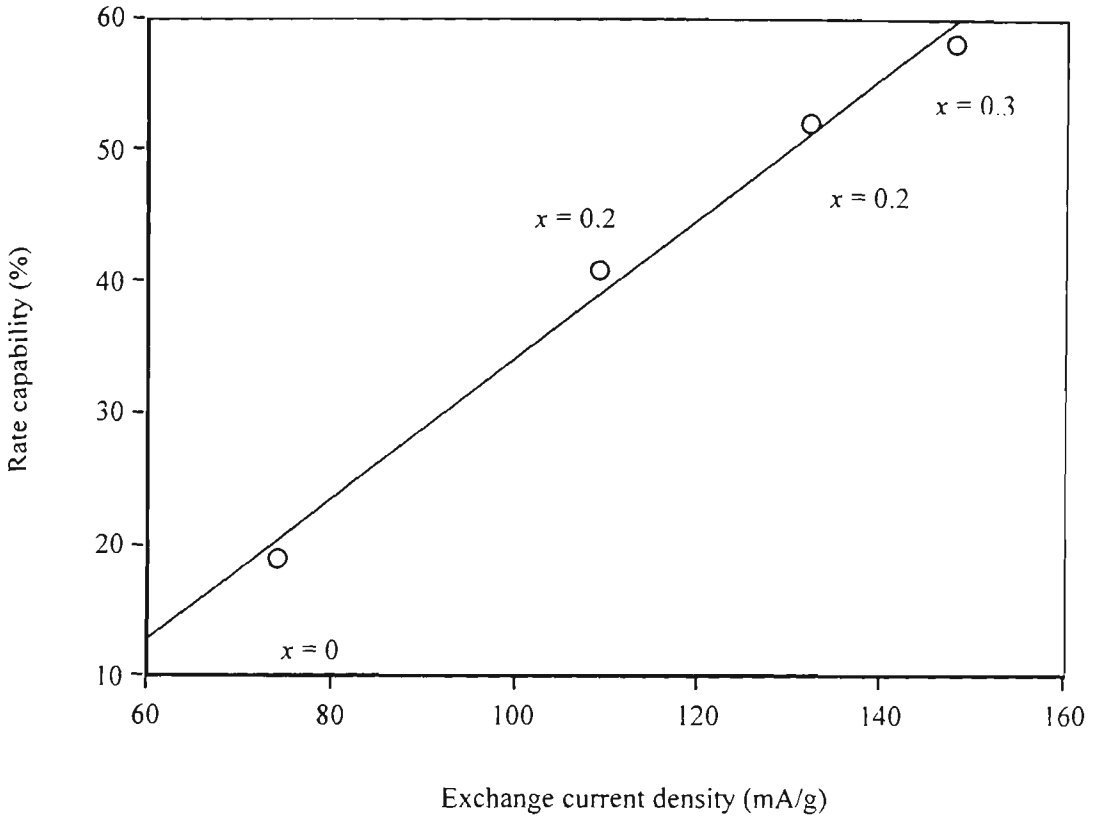

Figure 4.20 The relationship between exchange current density and high-rate dischargeability of $Mg_{1.9}Al_{0.1}Ni_{1-x}Y_x$ alloy electrodes.

correlated with the changes in the apparent exchange current density (i_0). The linear relationship between i_0 and HRD is shown in Figure 4.20. This indicates that the improvement of the high rate discharge capability may be attributed to the increase of electrochemical activity for the hydrogen evolution reaction with increasing x values in $Mg_{1.9}Al_{0.1}Ni_{1-x}Y_x$ alloys. This result is similar to that obtained for rare-earth system alloys by M. Matsuoka *et. al.* [240].

4.4.5 Cycle Life

The discharge capacity *vs.* cycle number curves for the various magnesium-based alloy electrodes are shown in Figure 4.21. The cycle life (CL), which is defined as the cycle number at which the discharge capacity decreases to half of the initial capacity [253], decreases with increasing yttrium content, i.e. CL = 30 for $x = 0$, CL =1 0 for $x = 0.1$, CL = 6 for $x = 0.2$ and CL = 5 for $x = 0.3$. This may be attributed to the presence of that the new phase, YNi_3, formed in the Y-containing alloys.

As is well known, multiphase alloys are characterised of having a lower corrosion resistance in comparison to monophase alloys. XRD results show that the addition of yttrium changes the structure of the Mg_2Ni-type alloys. The amount of YNi_3 phase formed in the alloys increases with increasing yttrium addition, resulting in an increase of the corrosion rate and a consequent decrease in durability of electrodes. Hence, in order to further improve the cycle life of the Mg_2Ni-type alloy electrodes,

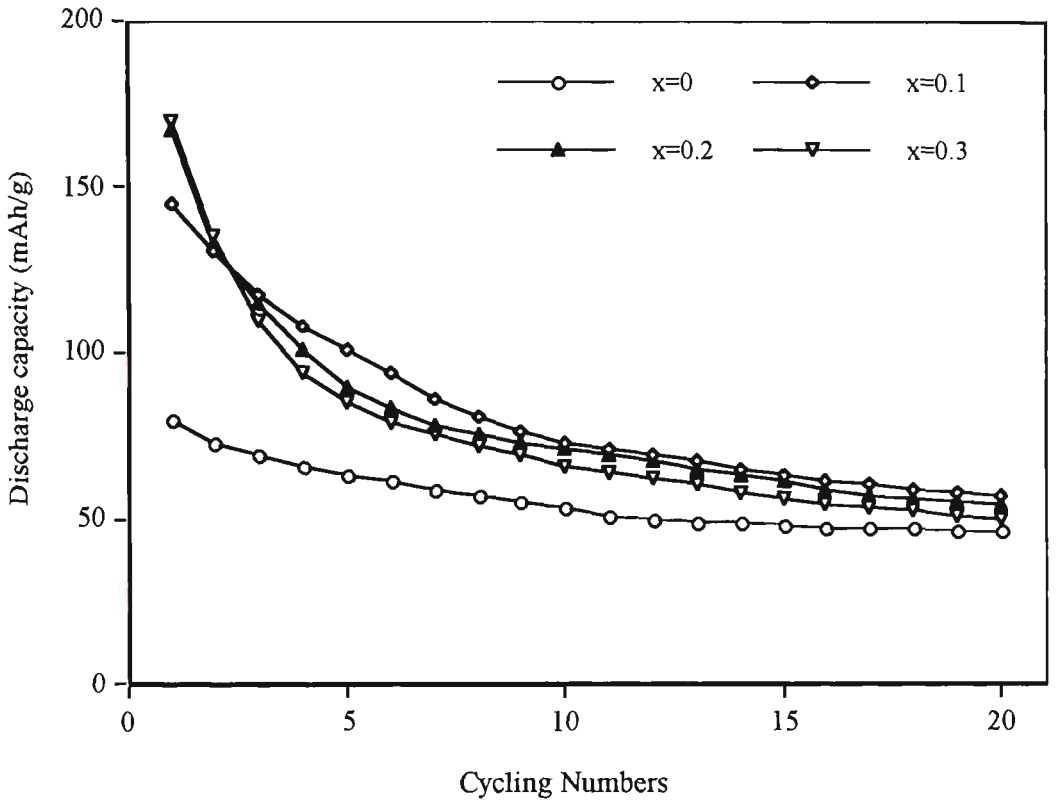

Figure 4.21 Discharge capacity *vs.* cycle number for $Mg_{1.9}Al_{0.1}Ni_{1-x}Y_x$ alloy electrodes (discharge at 5 mA/g).

other elements (*e.g.* Al, Co, Si *etc.*) should be considered for substitution as well as microencapsulation of the alloy powders.

4.5 Conclusions

The effects of alloy composition on the charge and discharge performance of Mg_2Ni-type alloys in 6M KOH aqueous solution were investigated at room temperature, using the alloy $Mg_{1.95}M_{0.05}Ni$ (M = Al, Ca, La, Mg, Ti, V) and $Mg_{1.9}Al_{0.1}Ni_{1-x}Y_x$ (x = 0 ~ 0.3). The following conclusions can be derived from this chapter:

1. Compared to its theoretical capacity, Mg_2Ni alloy exhibited an extremely low electrochemical capacity in the electrolyte at room temperature even at the very low discharge current of 5 mA/g. The reasons for this may be attributed to its easy oxidation and incomplete hydriding reaction, which result in a very poor electrochemical hydriding and dehydriding behaviour in the electrolyte. Thus, it is suggested that unmodified Mg_2Ni is not suitable for the rechargeable anode material in an alkaline solution.

2. Surface micro-encapsulation of Mg_2Ni alloy powder with Ni-P electroless plating was proved to be an effective approach to improve the electrode performance of Mg_2Ni. Both discharge capacity and rate dischargeability were remarkably enhanced by the surface modification of the alloy powder. The improvement of the modified Mg_2Ni electrode was ascribed to protection of the alloy from oxidation and improvement in the electrocatalytic activity for hydrogen evolution reaction. However, the electrode properties of micro-encapsulted Mg_2Ni are still far from satisfactory, and the incomplete hydriding of Mg_2Ni is barely improved.

3. The effects of the substitution of some of the Mg with small amounts of Al, Ca, La, Ti and V in Mg_2Ni on the electrochemical behaviour were investigated. Discharge capacity was found to increase in the order of Al > V > Ti > La > Ca-substitution. Among the substituent elements tested, the Al and V were effective for increasing the initial electrode capacity, as well as Ti. The exchange current values, i_0 of Al- and V-substituted alloys were found to be much higher than other alloys and the change of i_0 shown good correlation with the discharge capacity. This suggests that charge transfer is the RDS for the dehydriding reaction of $Mg_{1.95}M_{0.05}Ni$ (M = Al, Ca, La, Mg, Ti, V) alloy electrodes.

4. The yttrium and aluminium substituted Mg_2Ni-type alloy electrodes were found to have a much higher electrochemical capacity and better discharge rate performance than Mg_2Ni. The discharge capacity and discharge rate characteristics of the electrodes were considerably improved with increasing x value in $Mg_{1.9}Al_{0.1}Ni_{1-x}Y_x$. A specific discharge capacity of 170 mAh/g was achieved at a low discharge current (5 mA/g) for the $Mg_{1.9}Al_{0.1}Ni_{0.7}Y_{0.3}$ electrode at room temperature. Although this improvement is insufficient for practical applications, it indicates that further improvement may be possible by partial substitution of Ni and/or Mg in the Mg_2Ni-type alloy. This could enable the development of Mg_2Ni-type alloys for the anode materials of Ni-HM batteries. However, it should be noted, on the other hand, that an increase in the yttrium content leads to a decrease of cycle life of the electrodes.

CHAPTER 5

DISCHARGE BEHAVIOR OF Mg_2Ni-TYPE HYDROGEN STORAGE ALLOY ELECTRODES BY ELECTROCHEMICAL IMPEDANCE SPECTROSCOPY

5.1 Introduction

Mg_2Ni-type hydrogen storage alloys have been extensively studied as hydrogen storage materials because of their extremely large hydrogen absorbing capacity, (up to 3.6 *wt.*%), and the relatively low cost and abundance of the constituent elements in the earth's crust. Although Mg_2Ni alloy has a higher gas-phase hydrogen storage capacity than $LaNi_5$-type and $Zr(NiV)_2$ Laves phase hydrogen storage alloys, it seems not to be used as a hydride electrode material in alkaline solution without any modification. More recently, it has been found that it is feasible for modified Mg_2Ni-type alloys to be used for hydriding/dehydriding in alkaline solution at ambient temperature.[41,42,97]. One of the most significant improvements in electrochemical hydriding/dehydriding performance in alkaline solution, as discussed in the Chapter 4, was realized by partial substitution of the Mg and/or Ni in Mg_2Ni by other elements.

However, the practical electrochemical capacity of this alloy now is still much less than its theoretical capacity (999 mAh/g) [41], and even less than the practical electrochemical capacities of $LaNi_5$ and Ti_2Ni alloys although the practical gaseous capacity of Mg_2Ni is much more than that of $LaNi_5$ and Ti_2Ni [263-268]. Furthermore, the high-rate dischargeability and cycle lifetime of the magnesium-based alloys in the alkaline electrolyte was unsatisfactory. Thus, fundamental studies of the kinetics of the charge/discharge processes are required if further improvement is to be obtained in the electrochemical hydriding/dehydriding performance of this alloy in alkaline solution.

Electrochemical impedance spectroscopy (EIS) is a powerful method for understanding interfacial processes and electrode behaviour [269-271]. It has been also extensively used for the study of primary and secondary batteries [272-275]. Recently, Kuriyawa *et al.* [276] applied EIS to characterise $MmNi_5$-type alloy hydride electrodes and to study the deterioration behaviour of these electrodes. They proposed [277] that the deterioration of a metal-hydride electrode using copper-coated alloy powder was caused by passivation of the alloy surface only, while the performance of an electrode using uncoated alloy was dominated by an increase in the contact resistance. Ratnakumar and co-workers [278] studied the kinetics of charge-discharge and diffusion during hydrogen absorption and desorption of $LaNi_5$-Sn_x type metal hydride electrodes using AC impedance spectroscopy. They observed the absence of a diffusion impedance in the charged state on Nyquist plots of the data.

This is the similar to our previous results for $LaNi_5$ alloy electrodes [279], although, they did not investigate the change of impedance versus the DOD.

In this Chapter, the electrochemical behaviour of the Mg_2Ni-type alloy electrodes in the electrolyte was studied using electrochemical impedance spectroscopy, and compared with those of $LaNi_5$ electrode. The kinetics of the discharge process for the Mg_2Ni-type alloy at various DOD are discussed.

5.2 Comparison of Discharge Characteristics

The comparison of electrode charge/discharge characteristics for Mg_2Ni-type alloys, and $LaNi_5$ alloy is given in Table 5.1. The discharge capacity of the unmodified Mg_2Ni alloy electrode is only 8 mAh g^{-1}, which is almost negligible compared to its theoretically electrochemical capacity [41]. The aluminium and yttrium additive Mg_2Ni-type alloy, $Mg_{1.9}Al_{0.1}Ni_{0.9}Y_{0.1}$, however, has a much higher discharge capacity, viz.,150 mAh g^{-1}. This indicates that the electrode behaviour of Mg_2Ni alloy electrode is improved significantly by the substitution of alloy elements. The reasons for this have been investigated using a linear polarization technique (see Chapter 4). Although the rate-dischargeability of magnesium-based alloys is effectively improved by the additions of aluminium and yttrium, it is still much lower than that of $LaNi_5$ and Ti_2Ni alloys. In order to understand the dehydriding kinetics of magnesium-based alloys in an alkaline solution and the effects of aluminium and yttrium additives on the

electrochemical behaviour, the EIS of magnesium-based alloy electrodes have been measured. The EIS results of these electrodes are compared with those of the $LaNi_5$ electrode.

Table 5.1 Comparison of the electrode characteristics of different alloys

Alloy	Discharge capacity		Rate-dischargeablity
	C_5^* (mAh/g)	C_{20}^* (mAh/g)	C_{20}/C_5 (%)
Mg_2Ni	8	–	–
$Mg_{1.9}Al_{0.1}Ni_{0.9}Y_{0.1}$	150	104	69
Ti_2Ni	171	163	95
$LaNi_5$	336	327	97

*C_n refers to the discharge capacity at a discharge current density of n mA g^{-1}.

5.3 Electrochemical Impedance Spectra

5.3.1 Electrochemical Hydriding and Dehydriding Reactions

In alkaline solutions, the overall reactions of hydrogen storage alloy electrodes during charge and discharge processes are as follows:

(i) solid-liquid interface reaction:

$$H_2O + M + e^- \underset{\leftarrow \text{discharge}}{\overset{\text{charge} \rightarrow}{\Leftrightarrow}} MH_{ad} + OH^- \qquad (5.1)$$

(ii) solid-state reaction:

$$MH_{ad} \underset{\leftarrow \text{discharge}}{\overset{\text{charge} \rightarrow}{\Leftrightarrow}} MH_{lattice} \qquad (5.2)$$

When charging, hydrogen is generated by electrolysing water according to reaction (5.1), and adsorbs at the electrode surface in a highly active atomic state. Then, it diffuses into the lattice positions of the metal phases to form a metal hydride as expressed by reaction (5.2). During discharging, the atomic hydrogen diffuses from the lattice position in the alloy to the metal/electrolyte interface. The hydrogen atom is oxidised at this interface. It should be noted that atomic hydrogen is supplied directly by electrolysis on the electrode surface, rather than dissociation into hydrogen atoms from hydrogen molecules, which is the analogous process in the gaseous phase.

5.3.2 Mg_2Ni Alloy Electrode

Typical Nyquist, Bode-modulus and Bode-phase plots for Mg_2Ni electrodes at various DODs at room-temperature are shown in Figures 5.1 – 5.3, respectively. As seen in the Nyquist plot (Figure 5.1), the loci are composed of a distorted capacitive

semicircular arc at high frequencies and a mildly curved line at low frequencies. The former is considered to be due to a charge transfer process at the electrode/electrolyte interface as shown in equation (5.1), while the latter resulting from mass transfer effects is called the Warburg impedance. For the hydriding/dehydriding reaction in an alkaline

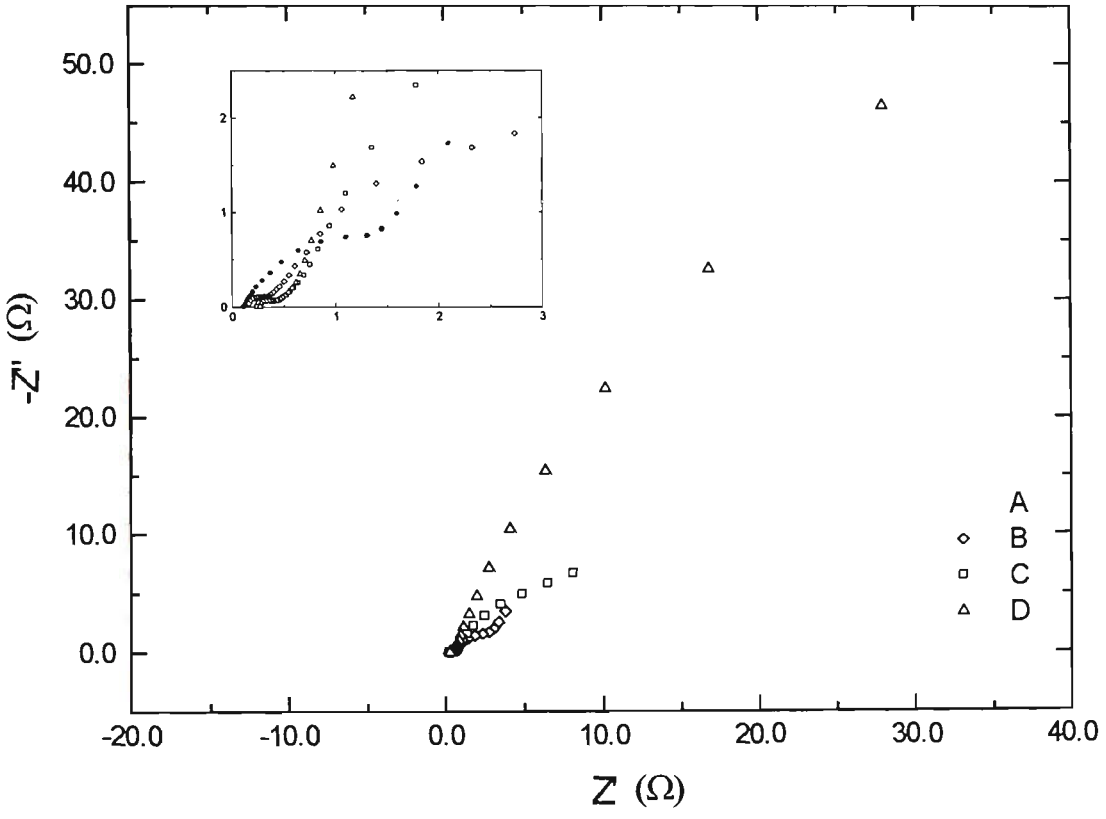

Figure 5.1 Nyquist plots for Mg_2NiH_x / 6M KOH at various DOD. The figure inset on the left-above is a magnified plot for the high-frequency data. A, 5 % DOD; B, 20 % DOD; C, 70 % DOD; D, 90 % DOD.

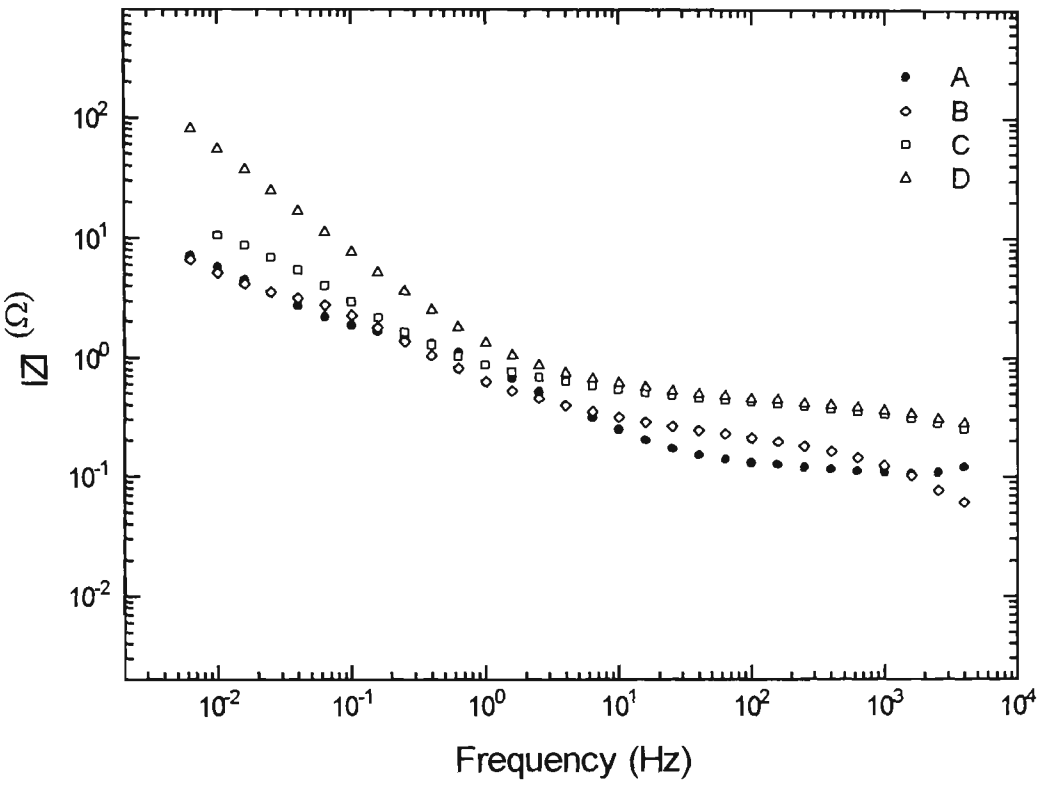

Figure 5.2 Bode-modulus plots for Mg_2NiH_x / 6M KOH at various DOD. A, 5 % DOD; B, 20 % DOD; C, 70 % DOD; D, 90 % DOD.

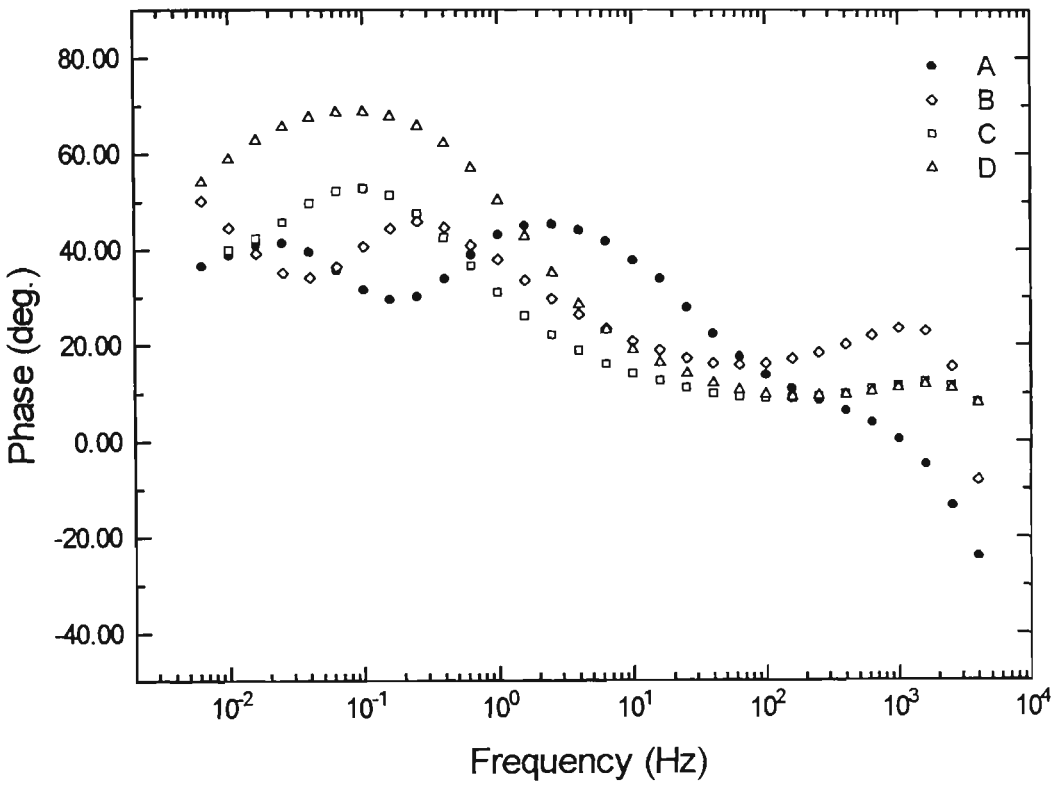

Figure 5.3 Bode-phase plots for Mg_2NiH_x / 6M KOH at various DOD. A, 5 % DOD; B, 20 % DOD; C, 70 % DOD; D, 90 % DOD.

solution, the mass-transfer process generally includes the diffusion of H, OH^- and H_2O. Because the diffusivity of OH^- and H_2O in the alkaline solution are much larger than that of the hydrogen atom in the solid phases (hydrides, alloys or oxides), the diffusion of hydrogen atom in solid phases is considered to be mainly responsible for the mass transfer effects of the metal hydride electrodes.

The impedance analysis was carried out by using the Randles-Ershler equivalent circuit model (Figure 5.4), in which an ohmic resistance, R_s, is in series with a parallel combination of the double-layer capacitance, C_d, and the charge transfer resistance, R_t, which is a series combination of the Warburg impedance Z_w. As shown in Figure 5.1, an increase of ohmic resistance R_s with increasing DOD was observed for the Mg_2Ni hydride electrode, which is believed to be associated with the formation and growth of an oxide layer on the alloy surface.

Analysis of the EIS data (Figures 5.1 - 5.3) reveals that the electrode kinetics change with DOD. At the initial stage of discharge (DOD = 5 %), as seen on the locus A in Figure 5.1, both a partially resolved semicircle locus at high frequencies and a linear impedance locus at low frequencies are observed, and neither of them is negligible. This indicates that the discharging process of the Mg_2Ni hydride electrode is dictated by both the charge transfer process at the electrode/electrolyte interface and the diffusion of hydrogen atom in the alloy. The Warburg impedance region originating from atomic hydrogen diffusion in electrode greatly increases with increasing DOD. This is due to the fact that the concentration of hydrogen in the metal hydride

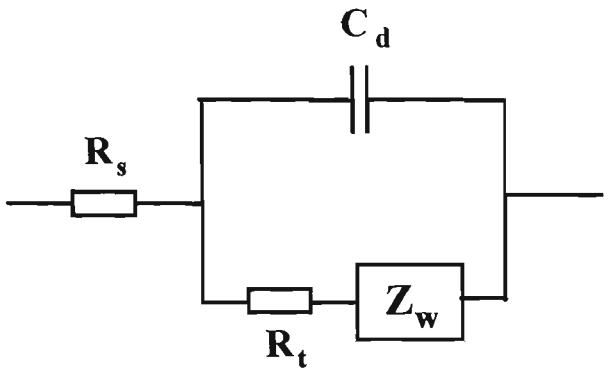

Figure 5.4 Randles-Ershler equivalent circuit model to represent the interfacial impedance for dehydriding reaction of the hydrogen storage alloy electrode in 6M KOH solution.

electrodes decreases with increasing DOD. Lower concentrations could increase the mass transfer impedance [280]. When the DOD increases to or beyond 70 %, the absence of a semicircle in the complex-plane indicates a fast charge transfer process and slow diffusion for hydrogen in the alloy at this stage. Thus, the controlling-step of the discharge process for the Mg_2Ni electrode changes with DOD, from the mixed rate-determining at the initial discharging stage to the hydrogen diffusion-controlled reaction at final discharging stage.

The dependence of the modulus and the phase, respectively, versus frequency for Mg_2Ni are shown in Figures 5.2 and 5.3, respectively. The modulus are found to increases with increasing DOD, and a large increase is observed when DOD reaching to 90%. Phase angles in Fig. 5.3 generally show two maxima within the frequency range studied. The high frequency maximum value of the phase angles decreases and shifts remarkably to higher frequencies with increasing DOD corresponding to reduction of adsorbed hydrogen atom at the electrode surface. The low frequency maximum value increases sharply with increasing DOD at the final stage of discharging (90% DOD), which may be indicating the surface film transformation from Mg_2Ni alloy to an oxide, so that the diffusion resistance of hydrogen is raised sharply. Both the modulus and the phase angles exhibit similar features at the final stage of discharging.

5.3.3 $LaNi_5$ Alloy Electrode

As well known, $LaNi_5$ alloy has a very good electrochemical hydriding/dehydriding performance when used as a metal hydride electrode in alkaline solution. For the purposes of comparison, the EIS of a $LaNi_5$ electrode was measured at the various DODs. The results are displayed in Figures 5.5 – 5.7. At the initial stage of discharging (5 % DOD), the locus A in Fig.5.5 is composed of only a semicircle arc, which differs from the locus A in Fig.1 for Mg_2Ni. The linear region at low frequencies expressed as the Warburg impedance was not observed for $LaNi_5$ at 5%

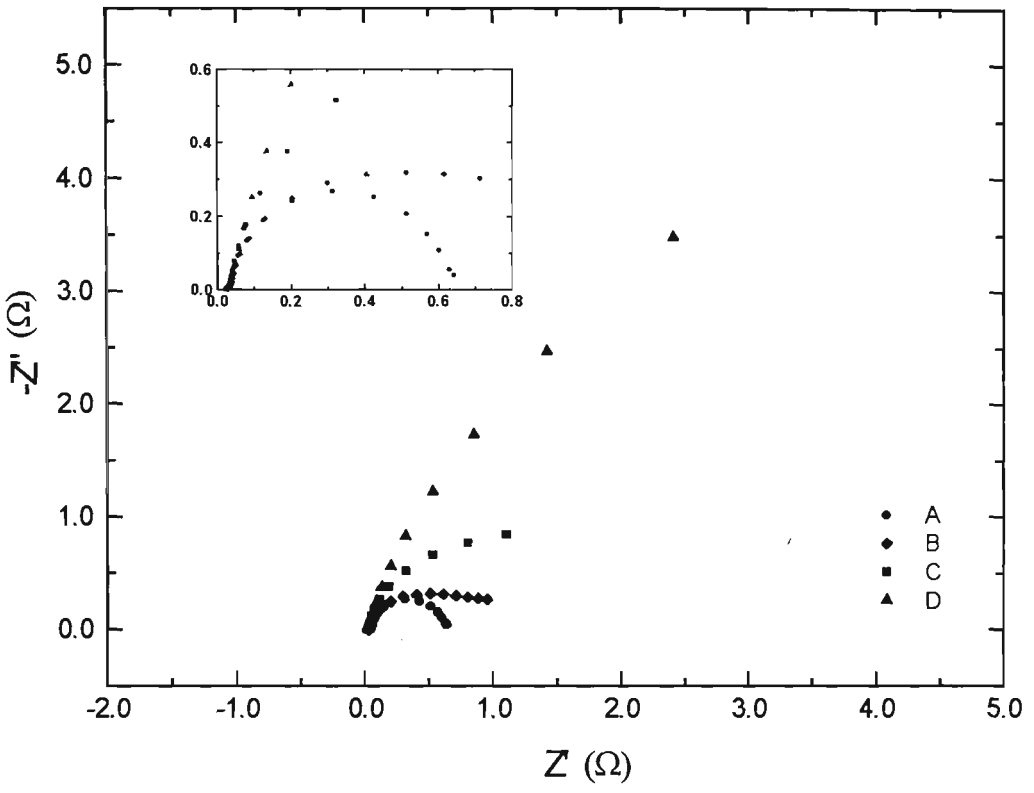

Figure 5.5 Nyquist plots for $LaNi_5H_x$ / 6M KOH at different DOD. The figure inset on the left-above is a magnified plot for the high-frequency data. A, 5 % DOD; B, 20 % DOD; C, 70 % DOD; D, 90 % DOD.

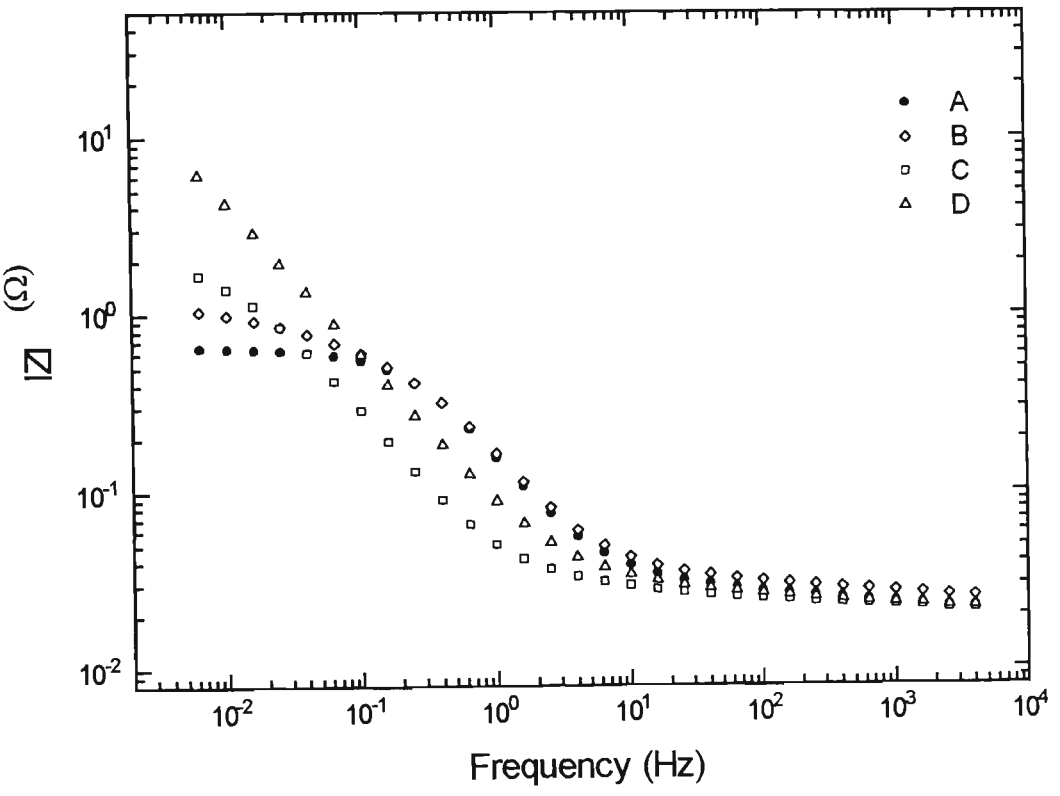

Figure 5.6 Bode-modulus plots for $LaNi_5H_x$ / 6M KOH at various DOD. A, 5 % DOD; B, 20 % DOD; C, 70 % DOD; D, 90 % DOD.

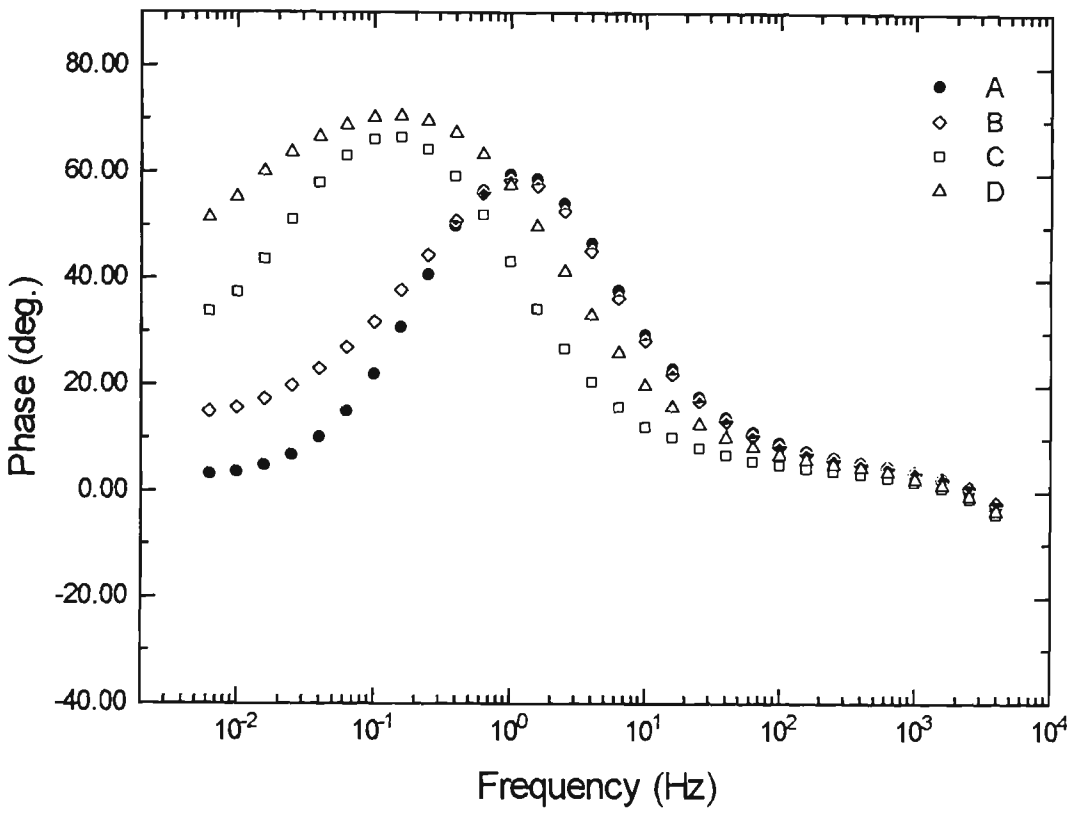

Figure 5.7 Bode-phase plots for $LaNi_5H_x$ / 6M KOH at various DOD. A, 5 % DOD; B, 20 % DOD; C, 70 % DOD; D, 90 % DOD.

DOD. Therefore, discharging process of the $LaNi_5$ hydride electrode is believed to be controlled by the charge transfer at the electrode/electrolyte interface at this stage. With increasing DOD, the semicircle develops a Warburg region. This indicates that the Warburg impedance gradually dominates the discharging current. By a comparison of Figure 5.2 with Figure 5.6, it is noticed that at both the high-frequency end and the low-frequency end, the modulus of unmodified Mg_2Ni is one order of magnitude higher than for that for $LaNi_5$ at all DODs. The values of modulus at high frequency for Mg_2Ni is high and dependent on DOD, whilst for $LaNi_5$ it is not. This confirms the previous results that the oxide layer forms and grows on Mg_2Ni surface with increasing DOD, thereby, increasing the electronic resistance. At low frequencies, however, it can be seen that the modulus of Mg_2Ni, even at 5 % DOD, is still larger than that of $LaNi_5$ at 90 % DOD. These results explain why the Mg_2Ni electrode has a very low discharge capacity and sluggish kinetics.

5.3.4 $Mg_{1.9}Al_{0.1}Ni_{0.9}Y_{0.1}$ Alloy Electrode

The impedance spectra of the Mg_2Ni alloy modified by aluminium and yttrium additions are shown in Figures 5.8 - 5.10. The results in Figure 5.8 indicate that the ohmic resistance, R_s, for $Mg_{1.9}Al_{0.1}Ni_{0.9}Y_{0.1}$ is much smaller compared with that of Mg_2Ni, and R_s hardly changes with DOD. This suggests that the addition of aluminium in the alloy improves the passivating behaviour of Mg_2Ni alloy, which is probably similar to that in Ti_2Ni systems as previously reported [17]. It can be seen also in Figure 5.8 that, at the initial stage of discharging (5 % DOD), the locus A is a

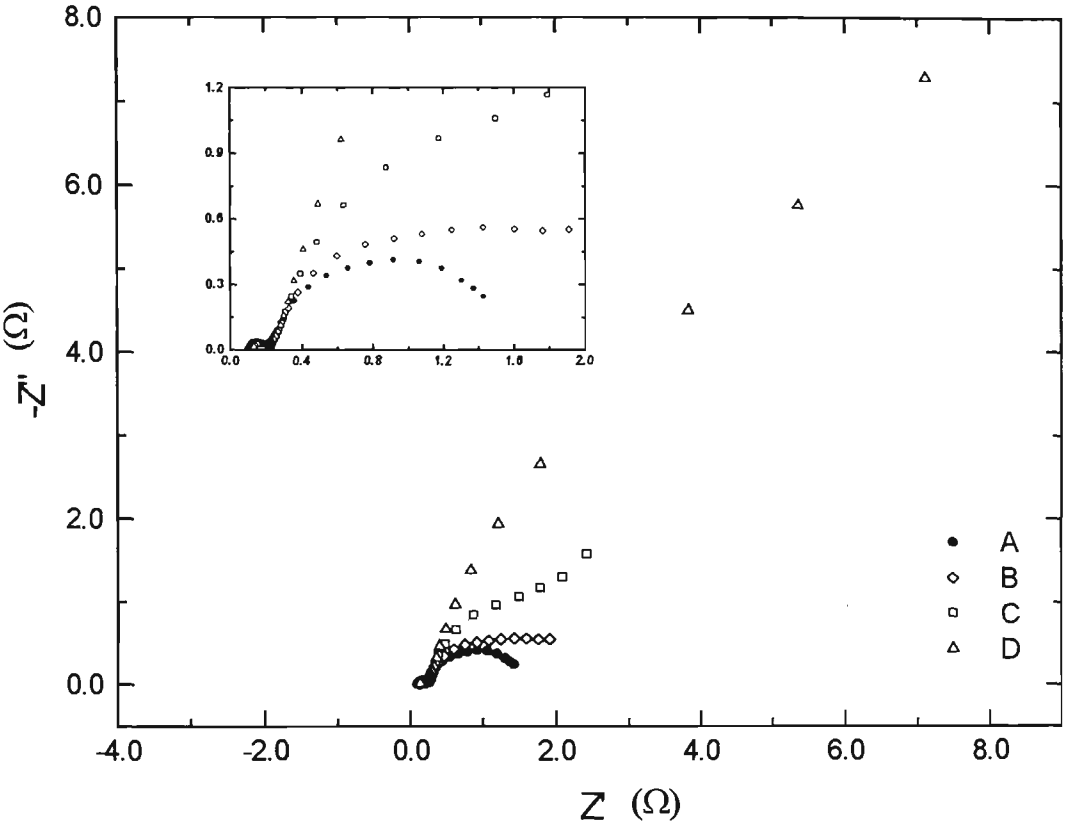

Figure 5.8 Nyquist plots for $Mg_{1.9}Al_{0.1}Ni_{0.9}Y_{0.1}H_x$ / 6M KOH at various DOD. The figure inset on the left-above is a magnified plot for the high-frequency data. A, 5 % DOD; B, 20 % DOD; C, 70 % DOD; D, 90 % DOD.

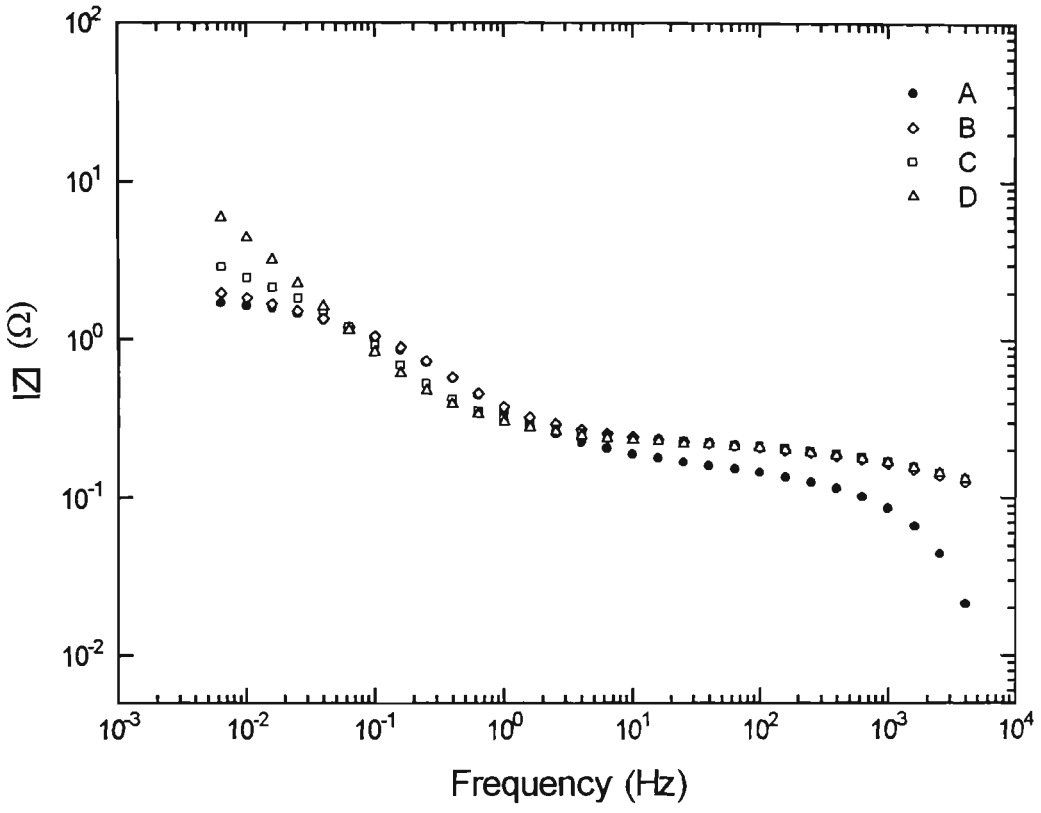

Figure 5.9 Bode-modulus plots for $Mg_{1.9}Al_{0.1}Ni_{0.9}Y_{0.1}H_x$ / 6M KOH at various DOD. A, 5 % DOD; B, 20 % DOD; C, 70 % DOD; D, 90 % DOD.

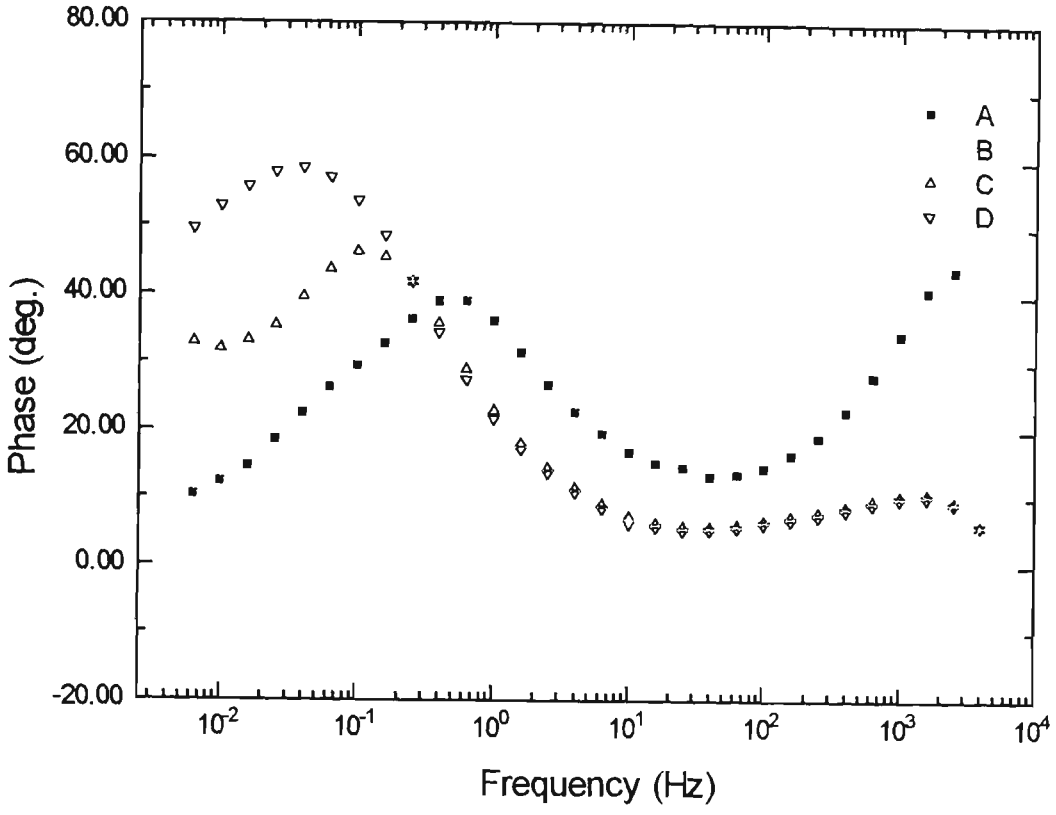

Figure 5.10 Bode-phase plots for $Mg_{1.9}Al_{0.1}Ni_{0.9}Y_{0.1}H_x$ / 6M KOH at various DOD. A, 5 % DOD; B, 20 % DOD; C, 70 % DOD; D, 90 % DOD.

semicircle arc at all measured frequencies, and a Warburg impedance region does not appear at low frequencies. This seems to be similar to that obtained with the $LaNi_5$ hydride electrode (Figure 5.5). Consequently, for the $Mg_{1.9}Al_{0.1}Ni_{0.9}Y_{0.1}$ hydride electrode, the rate-determining step at 5 % DOD is the charge transfer at the electrode/electrolyte interface, rather than the mixed rate-determining process witnessed with unmodified Mg_2Ni. At the various DOD, the modified Mg_2Ni displays a lower charge-transfer resistance and mass-transfer resistance than unmodified Mg_2Ni. These results demonstrate that the modified Mg_2Ni has better electrochemical activity for hydrogen oxidisation at the surface and faster hydrogen diffusion in the solid phases. Therefore, the additions of aluminium and yttrium in Mg_2Ni result in a considerable increase in discharge capacity and rate-dischargeability.

5.4 Hydrogen Diffusion Resistance

The effect of mass transfer is manifested through the Warburg coefficient, σ. The Randles plots for various alloy hydride electrodes are shown in Figures 5.11-5.13. These plots provide further evidence for a low-frequency Warburg response. The plots also show that the experimentally measured the Warburg coefficient, $\sigma = dZ'/d\omega^{-1/2}$, is strongly dependent on the electrode materials and the DOD. The DOD dependence of Warburg coefficient, σ, for various electrode is given in Figure 5.14. The values of σ at 90 % DOD for unmodified Mg_2Ni (11.8 Ω $s^{-1/2}$) and $LaNi_5$ (0.98 Ω

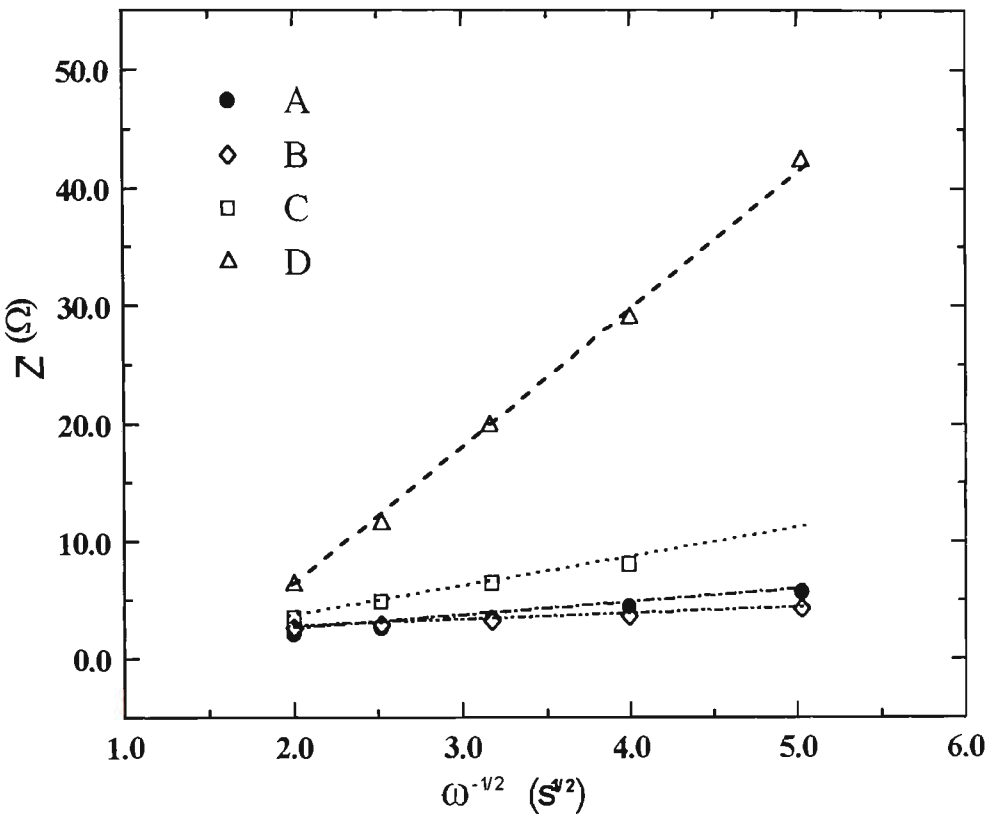

Figure 5.11 Randles plots for Mg_2NiH_x/6M KOH atvarious DOD

A, 5% DOD; B ,20% DOD; C, 70% DOD; D, 90% DOD

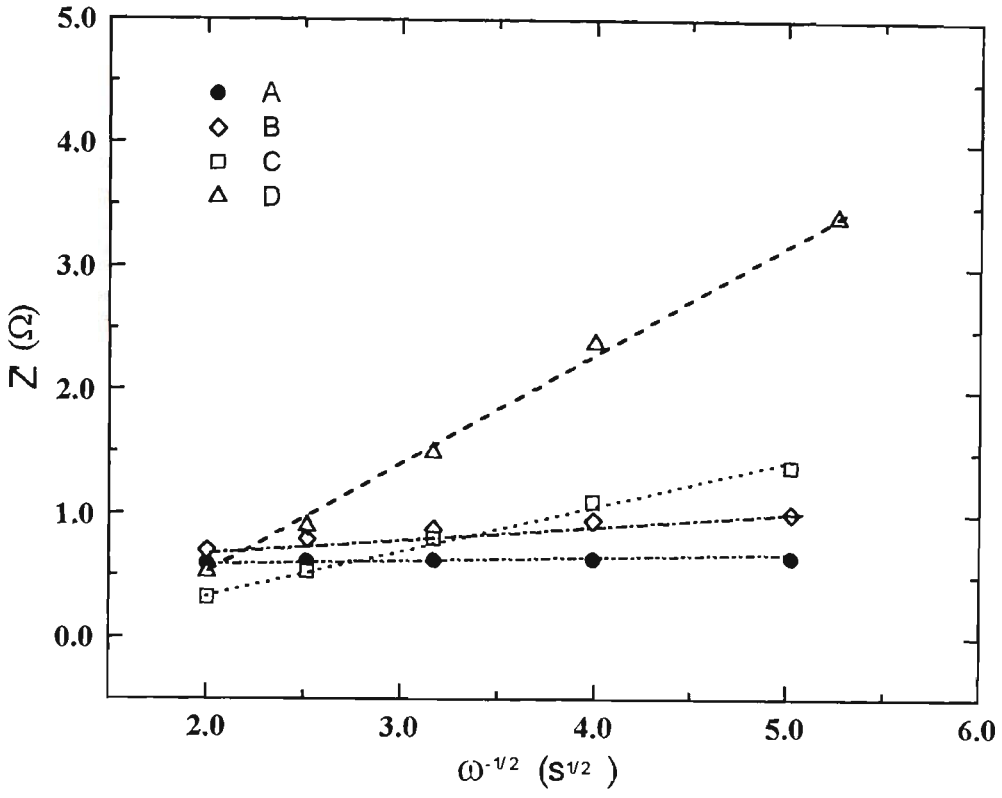

Figure 5.12 Randles plots for $LaNi_5H_x$ / 6M KOH at various DOD.

A, 5 % DOD; B, 20 % DOD; C, 70 % DOD; D, 90 % DOD.

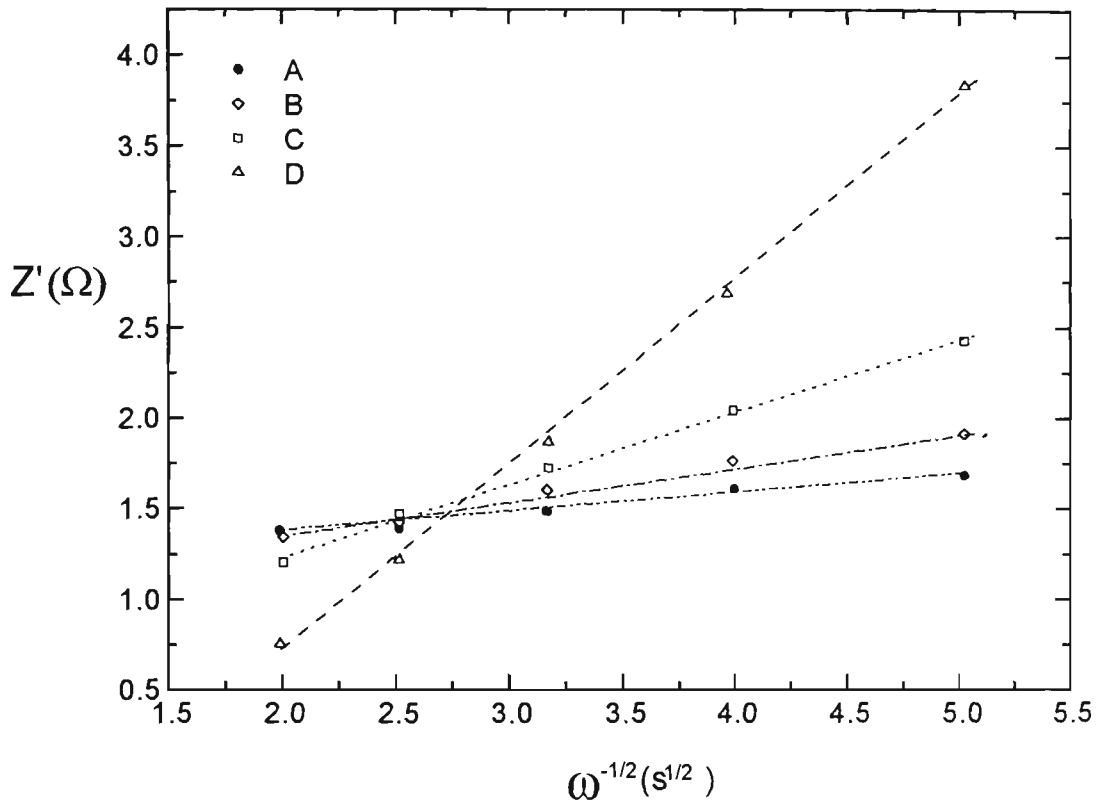

Figure 5.13 Randles plots for $Mg_{1.9}Al_{0.1}Ni_{0.9}Y_{0.1}H_x$ / 6M KOH at various DOD. A, 5 % DOD; B, 20 % DOD; C, 70 % DOD; D, 90 % DOD.

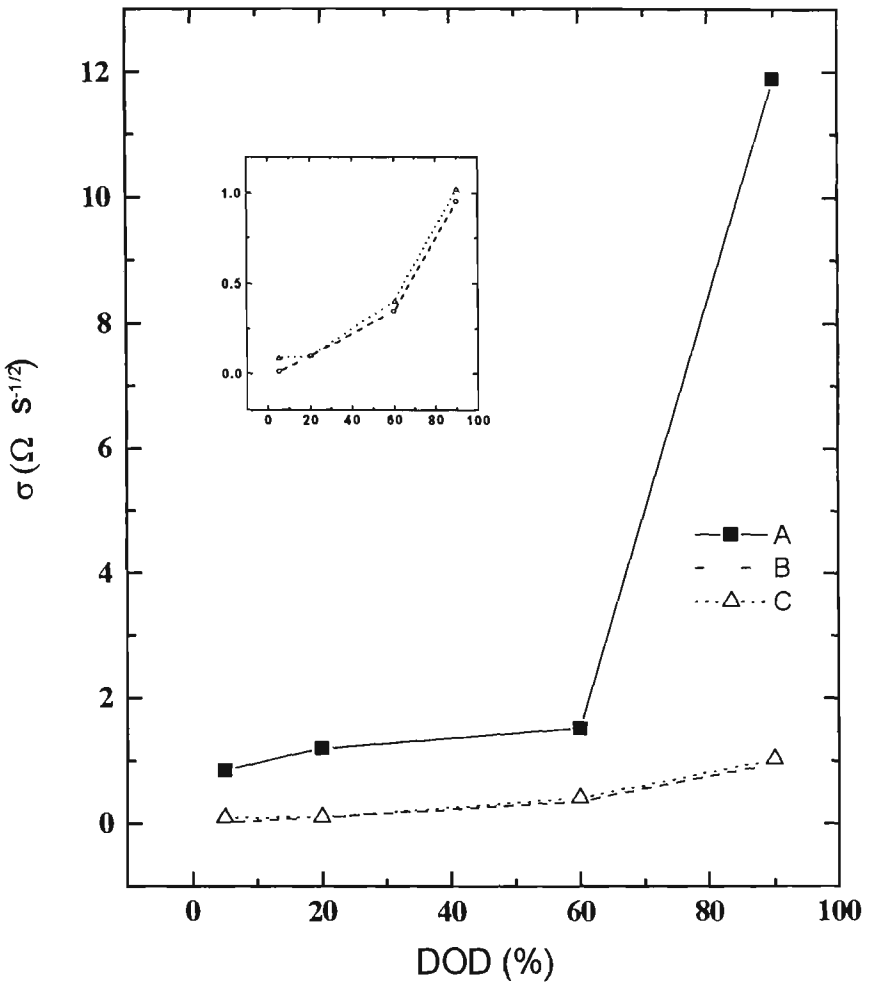

Figure 5.14 DOD dependence of Warburg coefficient, σ, for various alloys.

A, Mg_2Ni; B, $LaNi_5$; C, $Mg_{1.9}Al_{0.1}Ni_{0.9}Y_{0.1}$

$s^{-1/2}$) differ by a factor of 12. This can be explained by the fact that the activation energy of hydrogen diffusion is 460 meV for Mg_2Ni and 275 meV for $LaNi_5$ [281, 2982]. The diffusion coefficient can be expressed as: $D = D_0 \exp(-E_a/RT)$, where E_a is the activation energy of diffusion reaction, R is a gas constant, and T is the absolute temperature. Hence, hydrogen diffusion in Mg_2Ni is expected to be slower than that in $LaNi_5$. Moreover, as mentioned above, the magnesium oxide and/or hydroxide layer forms and grows on the surface of the electrode with increase in DOD, which may also block hydrogen transfer from bulk to surface for discharging. Thus, the unmodified Mg_2Ni has a larger mass transfer resistance than $LaNi_5$.

The results in Figure 5.14 clearly show that an addition of aluminium and yttrium in Mg_2Ni decreases the value of σ. This is probably due to the fact that the substitution of yttrium for nickel in Mg_2Ni alloy causes an increase in the lattice constant (*a, c*) and the crystal cell volume [42], which is beneficial for hydrogen diffusion in the alloys. Furthermore, the addition of aluminium in the alloy is assumed to improve the passivating behaviour of Mg_2Ni alloy. Thus, the formation and growth of oxide film is limited, and the hydrogen migration resistance through this passivating layer is reduced. This is supported by the R_s data and the modulus data of $Mg_{1.9}Al_{0.1}Ni_{0.9}Y_{0.1}$ (see Figures 5.8 and 5.9).

5.5 Conclusions

The discharge behaviour of Mg_2Ni-type hydrogen storage alloys in an alkaline solution at ambient temperature have been investigated and compared with $LaNi_5$. EIS results indicate that the very low discharge capacity and sluggish kinetics of the unmodified Mg_2Ni electrode in alkaline solution are caused by the presence of both a larger charge-transfer resistance and a mass-transfer resistance. The formation and growth of magnesium oxide and/or a hydroxide layer on unmodified Mg_2Ni increase the electronic resistance at the electrode/electrolyte interface and result in a large discharging overpotential. The additions of yttrium and aluminium in Mg_2Ni considerably reduce the hydrogen-diffusion resistance in the alloy and the charge-transfer resistance on the electrode/electrolyte interface. As a result, the discharge capacity and rate-dischargeability of the electrodes are remarkably improved.

CHAPTER 6

EFFECT OF SURFACE TREATMENT OF ALLOY POWDER ON THE ELECTROCHEMICAL BEHAVIOUR

6.1 Introduction

The capacity loss of hydrogen storage alloys have been attributed to causes: (i) oxidation of the alloys by oxygen and/or the electrolyte solution and (ii) disintegration of the alloy related to hydrogen absorption-desorption process which causes large changes of the lattice cell volume. Surface treatment has shown great benefits for improving the hydriding/dehydriding performance of AB_5-type alloys both in the gas-solid system and in the liquid-solid system [34,195-204]. Sakai *et al.* [255] found that $LaNi_{4.3}Al_{0.3}$ alloy exhibited characteristics suitable for electrode materials when the surface of fine particles of the alloy was microencapsulted with a porous thin film of copper or nickel. They have attributed this to the following: (i) increases in the electrical and thermal conductivity of alloy powder. (ii) improvement in the oxidation resistance of the alloy surface. (iii) reduction of the alloy lost as fine powder produced by charge-discharge cycling. (iv) easier electrode preparation from alloy powder because of improved adhesion between the coated alloy particles.

In this chapter, the effect of the surface modifications to the $Mg_{1.9}Y_{0.1}Ni_{0.9}Al_{0.1}$ alloy on its electrochemical properties are described. An ultrasound treatment was used in alkaline solution containing small amount of sodium hypophosphite (NaH_2PO_2). In addition, an electroless Ni-P alloy coating was used and its effect on electrocatalytic activity for the hydrogen electrode reaction (HER) was investigated. The electrode characteristics were examined including the electrochemical capacity, high-rate dischargeability and cycle life, in comparison with those of an electrode prepared from untreated alloy powder. The electrochemical performance of modified Mg_2Ni - type alloy was characterised using *dc* polarisation and *ac* impedance techniques, and its phase composition and microstructure were analysed by X-ray diffraction (XRD) and scanning electron microscopy (SEM). It was found that surface oxidation is mainly responsible for the electrode capacity decay of the magnesium-based alloy, while the disintegration of the alloy seems to have a relatively small influence on the capacity loss of the electrode.

6.2 Surface Treatment of Alloy Powder

6.2.1 Ultrasound Surface Treatment

The sieved alloy powder was soaked in a solution containing 1M KOH + 0.01M NaH_2PO_2 and then treated in an ultrasonic cleaner (Sanophon, Ultrasonic Industries Pty. Ltd. Sydney) for 2 hours. After that it was rinsed and dried in vacuum.

Table 6.1 Bath composition and operating conditions for the microencapsulation of $Mg_{1.9}Y_{0.1}Ni_{0.9}Al_{0.1}$ alloy

Coating	Bath	Composition	Operating conditions	
Ni-P alloy	$Ni_2SO_4 \cdot 6H_2O$	100 g l^{-1}	pH	7-10
	$NiCl_2 \cdot 6H_2O$	50 g l^{-1}	Temp.	25 °C
	$NaH_2PO_2 \cdot H_2O$	50 g l^{-1}	Time	1 hr.
	$C_2H_5CO_2H$	10 ml l^{-1}	Stirring	yes
	$Na_3C_6H_5O_7 \cdot 6H_2O$	75 g l^{-1}		
	$CH_3COONa \cdot 3H_2O$	80 g l^{-1}		
	H_2NCSNH_2	10 mg l^{-1}		
	NaOH	12 g l^{-1}		

6.2.2 Low-temperature Surface Microencapsulation

A low-temperature surface microencapsulation of alloy powder was developed for the modification of magnesium alloys. The electroless plating bath composition and operation conditions is given in Table 6.1. The series of steps in the electroless plating operation are the follows: The surface of the alloy powder was pickled in phosphoric acid (85% H_3PO_4) for 30 seconds at room temperature then activated in a solution containing 20 ml l^{-1} H_3PO_4 and 10 g l^{-1} NH_4HF_2 for 20 minutes. The activated powder was immersed and stirred in the electroless plating solution as shown in Table 6.1. After the coating on the surface of the alloy powder reached the thickness required (about 1 μm), the powder was water rinsed and then dried in a vacuum. The surface morphology of coated alloy powder before and after cycling was examined by SEM.

Both the surface modified and unmodified alloy powders (0.2g) were mixed with 0.8 g fine nickel powder (ϕ < 3 μm) and 10% poly(vinyl alcohol) solution. The mixture was filled into a porous nickel substrate and pressed after drying.

6.3 Discharge Characteristics

The discharge capacities of the $Mg_{1.9}Y_{0.1}Ni_{0.9}Al_{0.1}$ electrodes fabricated from the surface modified and unmodified alloy powders are shown in Figure 6.1 as a function of the cycle number. As can be seen in this figure, the initial discharge capacity of the electrode was significantly increased from 150 mAh g^{-1} for the unmodified $Mg_{1.9}Y_{0.1}Ni_{0.9}Al_{0.1}$ to 195 and 220 mAh g^{-1} for the ultrasound treated alloy powder and Ni-P coated powder, respectively. The capacity decay of the electrode fabricated from coated powder proceeds more slowly than that of the electrodes produced from unmodified powder and ultrasound treated powder. The results given in Figure 6.2 clearly show that both the ultrasound treatment and the surface microencapsulation of alloy powder effectively improved the high-rate dischargeability of the electrode. The discharge capacity obtained at 50 mAh g^{-1} was approximately 71 % and 83 % of that obtained at 5 mAh g^{-1} for ultrasound treated and coated alloy powders respectively, while for the unmodified $Mg_{1.9}Y_{0.1}Ni_{0.9}Al_{0.1}$ alloy the discharge capacity obtained at 50 mAh g^{-1} was only 37 % of that obtained at 5 mAh g^{-1}. These results indicate that the surface modifications of alloy powder play an important role to improve the electrode properties of the magnesium alloy.

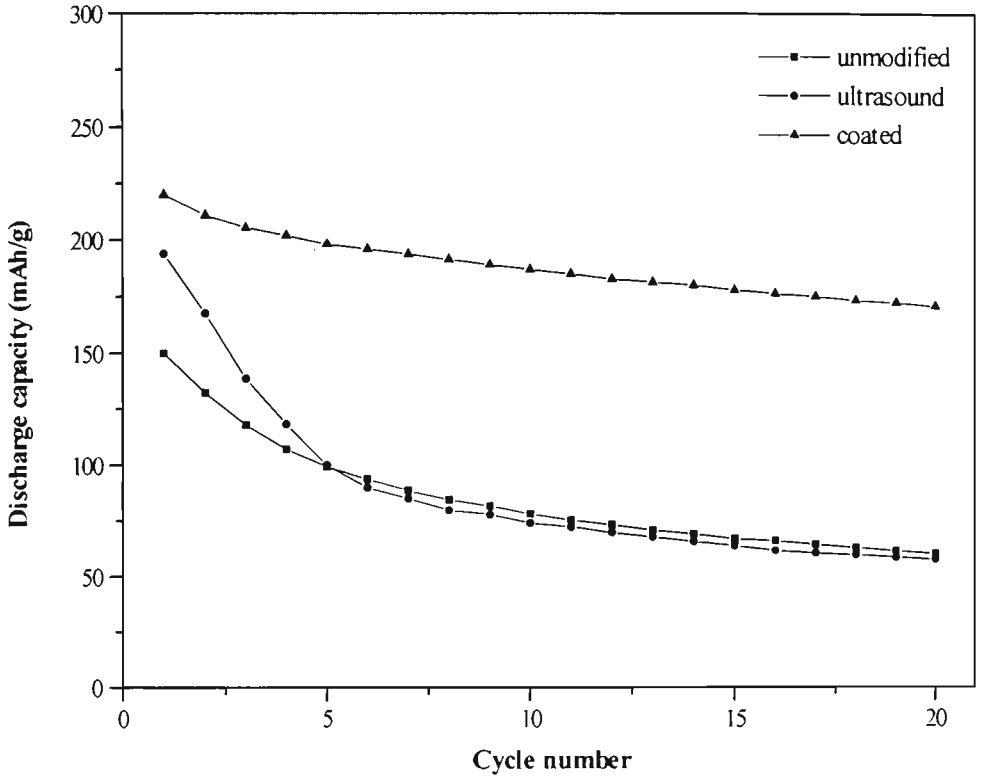

Figure 6.1 Discharge capacity of the unmodified and modified $Mg_{1.9}Y_{0.1}Ni_{0.9}Al_{0.1}$ electrode as a function of cycle number (discharge at 5 mA g^{-1}).

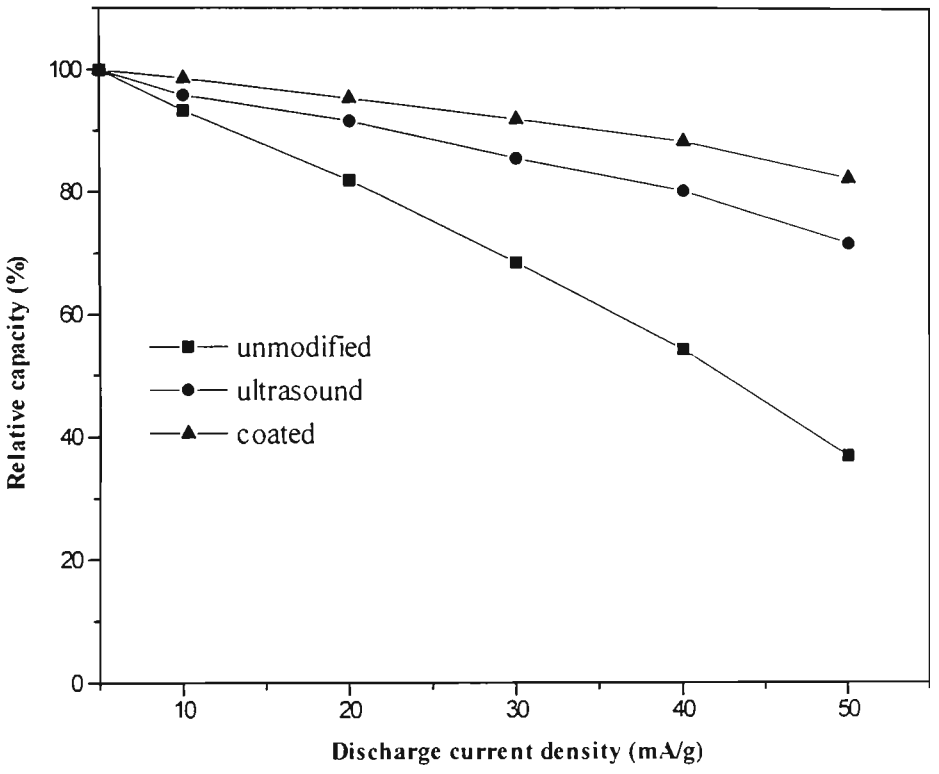

Figure 6.2 Discharge rate dependence of rate discharge capability for the unmodified and modified $Mg_{1.9}Y_{0.1}Ni_{0.9}Al_{0.1}$ electrode.

6.4 Surface Morphology and Composition

6.4.1 Alloy Powder with Ultrasound Treatment

As pointed out by many authors [17, 239, 256, 257], the electrode performance, such as discharge capacity, high-rate dischargeability and cycle life, is critically dependent on the surface morphology and the composition of the alloy powder. The surface composition of $Mg_{1.9}Y_{0.1}Ni_{0.9}Al_{0.1}$ alloy modified by the ultrasound treatment was analysed by EDS. The results are shown in Table 6.2. As can be seen in Table 6.2, a Ni-rich surface layer was produced by an ultrasound treatment, which is similar to that observed by Iwakura *el. al.* [211, 240] for AB_5-type hydrogen storage alloys treated by immersing in an alkaline or a reducing solution. This might be attributed to the preferential dissolution of magnesium as well as aluminium on the alloy surface. It has been reported that the Ni-rich layer has a high electrochemical activity for the HER. Thus, the alloy modified by the ultrasound treatment displayed good electrode properties, such as discharge capacity and high-rate dischargeability.

Figure 6.3 shows the typical XRD pattern of unmodified $Mg_{1.9}Y_{0.1}Ni_{0.9}Al_{0.1}$ alloy powder and the powder after the ultrasound treatment. The result in Figure 6.3 (a) reveals that the surface of unmodified alloy powder obtained is contaminated by a magnesium oxide layer, which probably resulted from the alloy powder process and/or storage. This surface oxide is believed to inhibit both the charge-transfer on the alloy/electrolyte interface and the hydrogen-diffusion towards (or: out of) alloy bulk when charging (or: when discharging). It is noticed from Figure 6.3 (b) that the MgO

Table 6.2 Surface atomic ratio of $Mg_{1.9}Y_{0.1}Ni_{0.9}Al_{0.1}$ alloy powder modified by ultrasound*

Sample	No.	Mg	Ni	Y	Al
Unmodified	1	67.23	25.47	3.11	4.19
	2	65.87	26.94	3.21	3.98
	3	68.64	24.04	3.09	4.23
	av.	67.25	25.48	3.13	4.13
ultrasound	1	62.13	31.24	3.25	3.38
treated	2	57.82	35.72	3.14	3.32
	3	59.08	34.20	3.65	3.07
	av.	59.92	33.48	3.34	3.26

* Composition analyses were carried out at three different spots on each of the alloy powders

peak disappeared after the ultrasound treatment, *i.e.* the surface oxide layer was eliminated by an ultrasound treatment in a (1M KOH + 0.01M NaH_2PO_2) solution. Thus, an ultrasound treatment of the alloy powder may improve greatly the hydriding and dehydriding kinetics of the magnesium-based alloy, leading to an increment in its discharge capacity and rate dischargeability. However, this surface modification seems to have no improvement on the cycle life of the electrode because it is unable to prevent the magnesium alloy from oxidisation in the electrolyte.

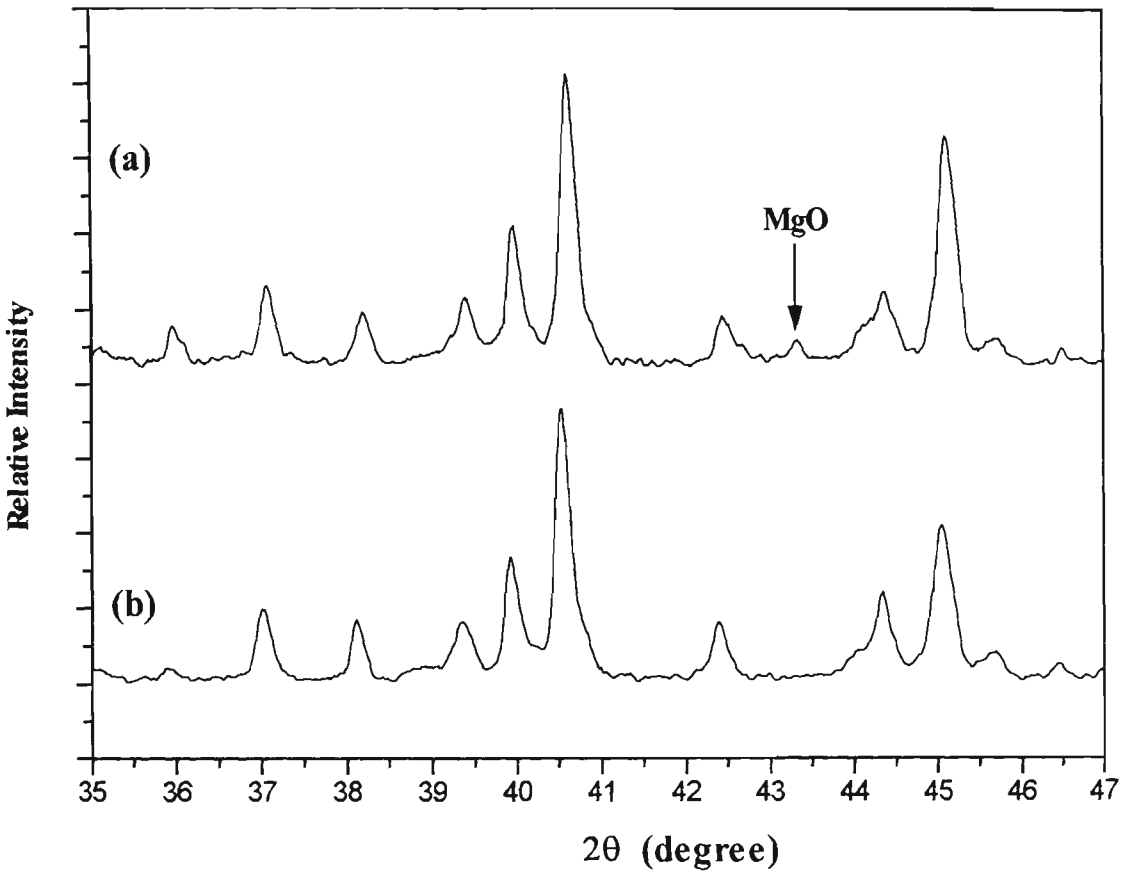

Figure 6.3 XRD patterns of $Mg_{1.9}Y_{0.1}Ni_{0.9}Al_{0.1}$ alloy powder before (a) and after (b) ultrasound treatment.

6.4.2 Surface Microencapsulation with Ni-P Alloy Coating

The microencapsulation of the alloy powder with a porous thin film of electroless metallic coating has been found to be an effective method to improve the electrode performance of rare-earth system (AB_5-type) hydrogen storage alloy [34,255]. Considering the reactive and easily oxidised nature of magnesium alloys in an aqueous solution, a low temperature Ni-P electroless plating was developed in this study and used for microencapsulating $Mg_{1.9}Y_{0.1}Ni_{0.9}Al_{0.1}$ alloy powder. The surface morphology of the coated alloy powder was shown in Figure 6.4. It is clearly seen that the surface of the alloy powder was covered with different size Ni-P alloy spheres which were confirmed by EDS analysis. Due to the fact that Ni-P coating has good corrosion resistance in an alkaline solution, the coating can protect the alloy from oxidation in an alkaline solution and also increase the electrical conductivity of the electrode. Simultaneously, the Ni-P alloy on the surface of $Mg_{1.9}Y_{0.1}Ni_{0.9}Al_{0.1}$ alloy powder may provide for a fast HER because of its high electrocatalytic activity. Since the Ni-P coating was composed of different size Ni-P alloy spheres, the apparent surface area of the powder was increased considerably and, thereby the active sites for redox of hydrogen was enhanced. In addition, the coating also plays the role of microcurrent collector when charging and discharging. All of these factors are believed to be beneficial to the hydriding and dehydriding of the electrode, resulting in a remarkable improvement of the electrode performance.

(a)

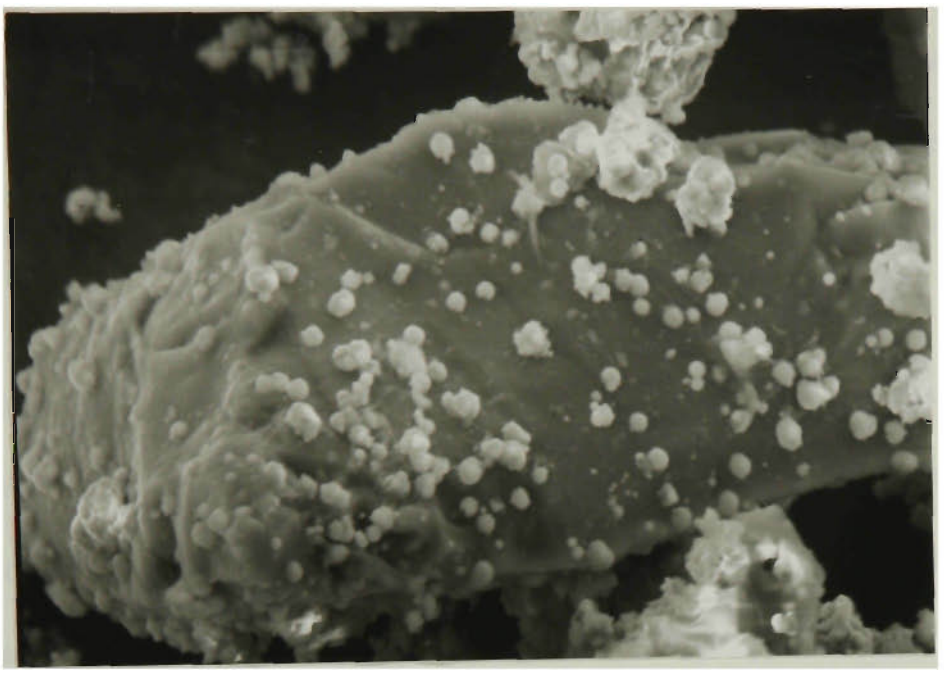

(b)

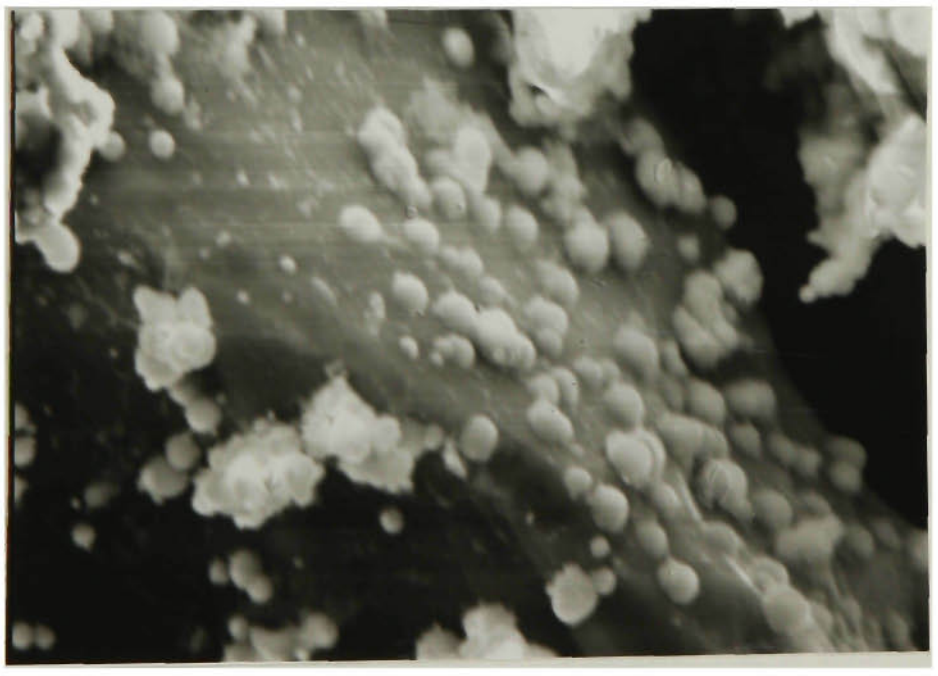

Figure 6.4 SEM image of microencapsulated $Mg_{1.9}Y_{0.1}Ni_{0.9}Al_{0.1}$ alloy showing the alloy powder covered with different size Ni-P alloy spheres.

The capacity decay of the hydrogen storage alloy electrode when subjected to charge-discharge cycles has been attributed to the oxidation and disintegration of alloy powder [254,255,258]. Figure 6.5 shows the surface morphology of the modified alloy powder after 20 charge-discharge cycles. Both the ultrasound treated powder and the coated powder were found to suffer serious disintegration. This indicates that surface microencapsulation with Ni-P coating has little effect on the disintegration of magnesium alloy powder. However, it can protect effectively the alloy powder from the oxidation in the alkaline solution. SEM and EDS results revealed that the surface of ultrasound treated powder was covered with an oxide layer which may block the hydriding-dehydriding reaction, resulting in a capacity decay. Consequently, it is reasonable to say that the surface oxidation is a major contributor to the capacity decay of the magnesium alloy electrode.

The disintegration and surface oxidation of the coated Mg_2Ni-based powder with charge/discharge cycling can be described simply by the schematic illustration in Figure 6.6. Due to the expansion and contraction of the lattice cell with cycling, the alloy powder cracked and new interfaces of alloy/electrolyte were produced. These fresh interfaces oxidise promptly when they are exposed in an alkaline solution. The surface oxide layer, as discussed above, is believed to inhibit both the hydrogen electrode reaction (HER) at the electrode/electrolyte interface and the hydrogen atom diffusion in the electrode, resulting in a poor hydriding/dehydriding performance. Therefore, it was suggested that the new surface resulting from powder cracking made little contribution to the electrode performance. However,

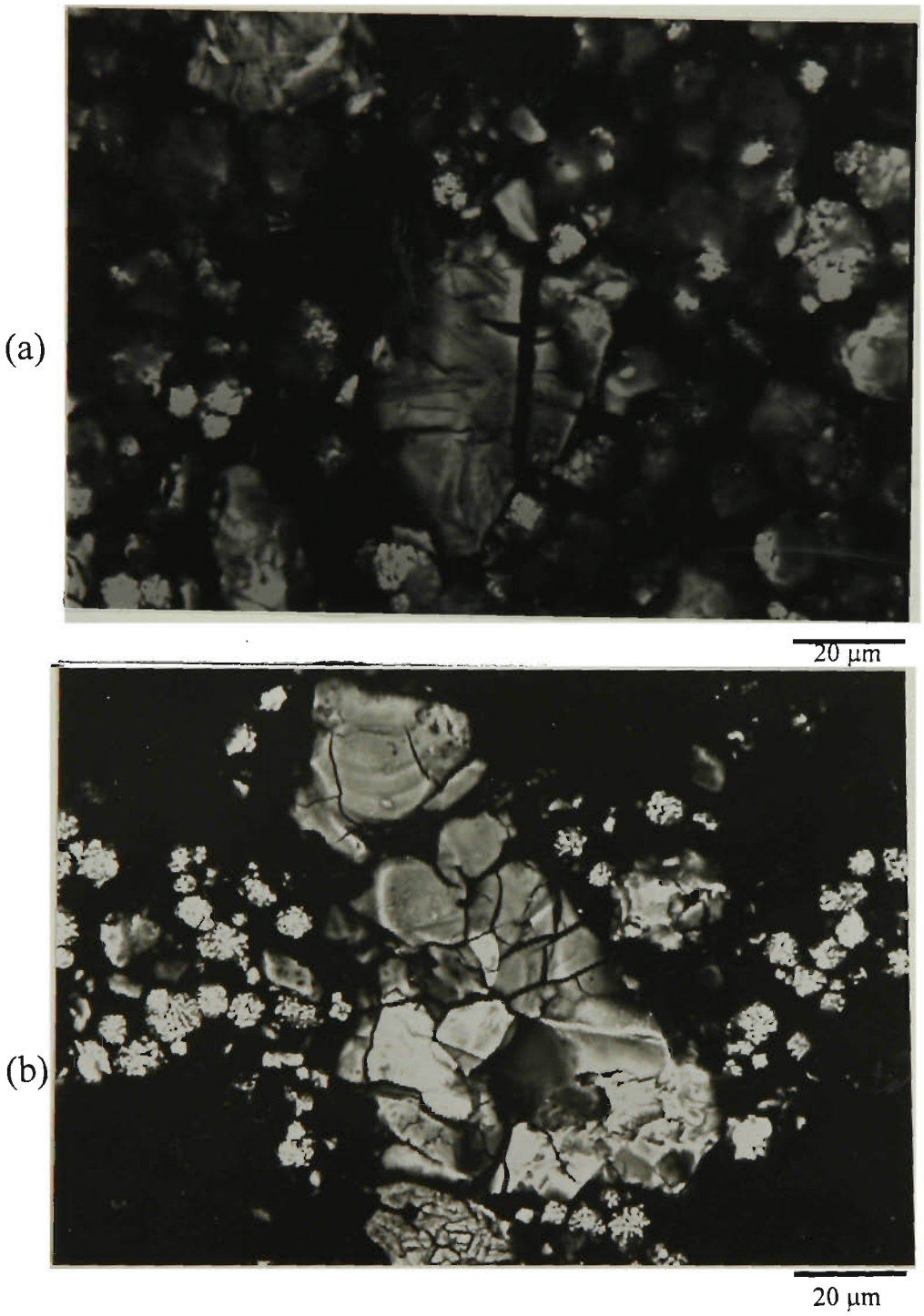

Figure 6.5 Surface morphology of $Mg_{1.9}Y_{0.1}Ni_{0.9}Al_{0.1}$ alloy powder after 20 cycles showing both the bare alloy powder and the microencapsulated powders suffering serious disintegration. (a) bare alloy powder; (b) Ni-P coated alloy powder.

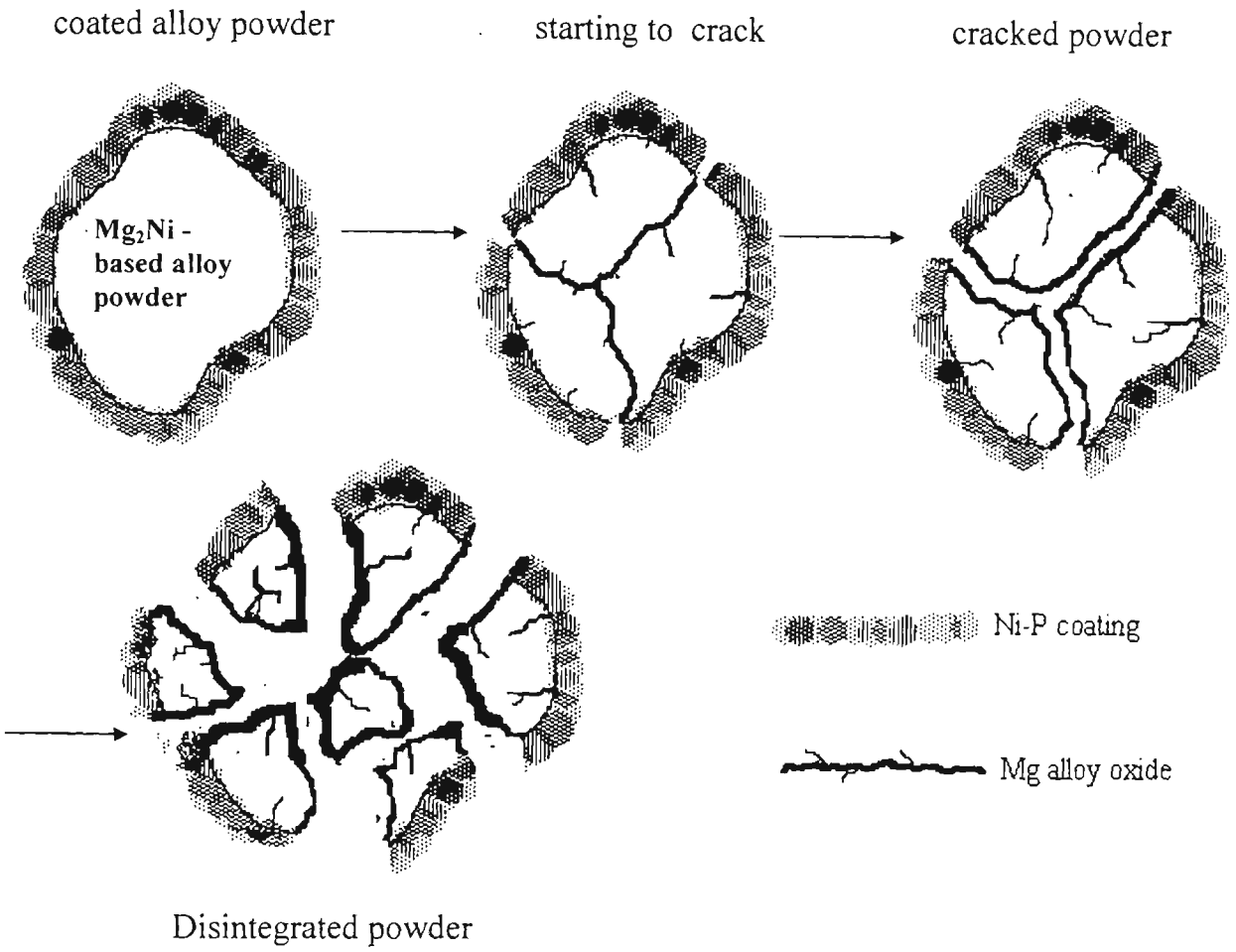

Figure 6.6 A simple model of disintegration and surface oxidation for Ni-alloy coated $Mg_{1.9}Y_{0.1}Ni_{0.9}Al_{0.1}$ alloy powder when subjected to charge/discharge cycles.

even for the disintegrated Mg_2Ni-based alloy powder, the Ni- coating on the surface still can provide both the active sites for the redox reaction of hydrogen and the pathway for the diffusion of hydrogen (as shown in Figure 6.7), leading to a slower capacity decay and longer cycle life.

6.5 Electrochemical Characteristics

Figure 6.8 shows cyclic voltammograms for the surface modified and unmodified $Mg_{1.9}Y_{0.1}Ni_{0.9}Al_{0.1}$ alloy electrodes in the 6M KOH solution at room-temperature. The anodic peak current at around -700mV *vs.* Hg/HgO was ascribed to the oxidation of hydrogen absorbed in the alloy according to the equation [19]:

$$MH_n + nOH^- \rightarrow M + nH_2O + ne^- \qquad (6.1)$$

It can be seen from Figure 6.8 that the surface modifications of alloy powder give a remarkable rise of anodic peak current of hydrogen oxidation. The electrode fabricated from the coated alloy powder has the highest catalytic activity for the hydrogen oxidation, whilst the unmodified alloy appears to have the lowest catalytic activity. The catalytic reactivity for the hydrogen oxidation on the alloy electrode surface was also improved effectively by the ultrasound treatment. This may be attributed to the cavitation effect of the ultrasound field. It has been estimated from ultrasound theory that the instantaneous pressure at the centre of a collapsing cavitation bubble is about 75,000 psi. and the temperature can reach a value as high as 13,000°F [259]. Cavitation formed at a liquid/surface oxide film interface of

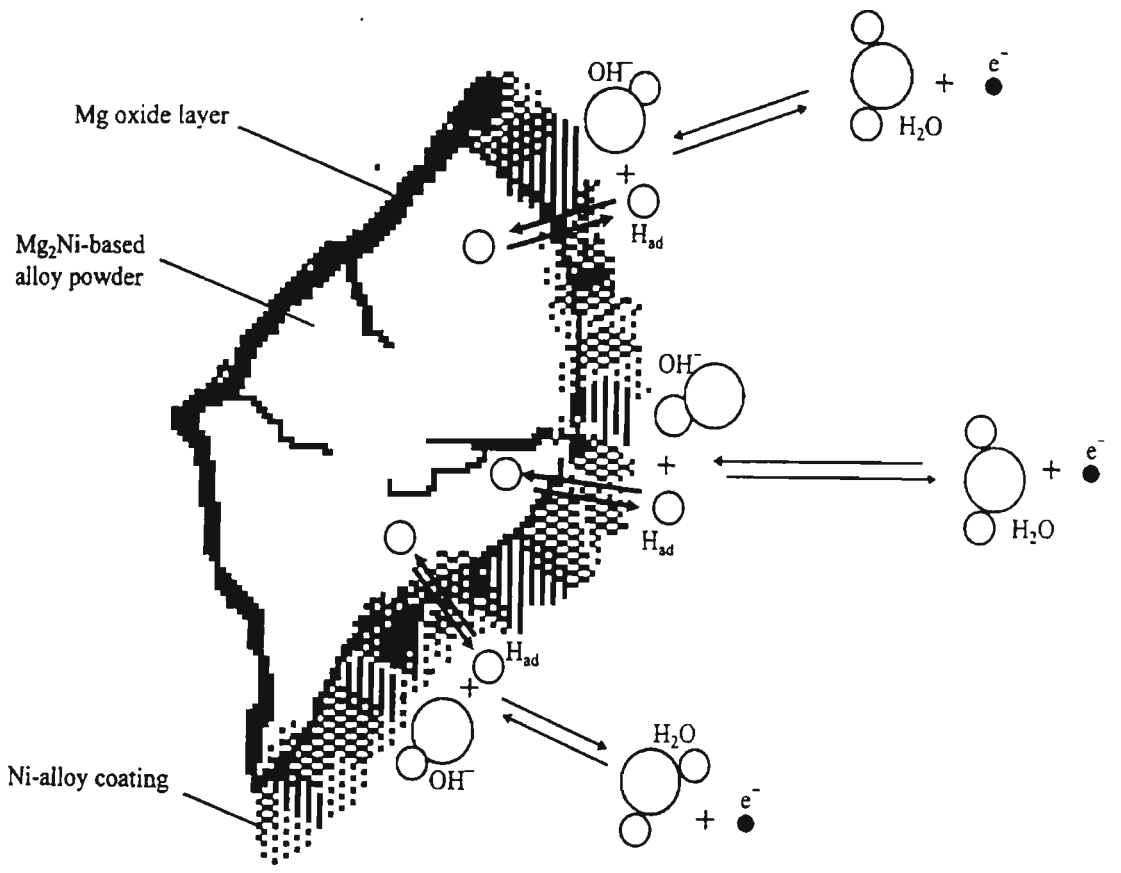

Figure 6.7 The charging/discharging model of Ni- alloy coated Mg_2Ni-based alloy powder after disintegrating.

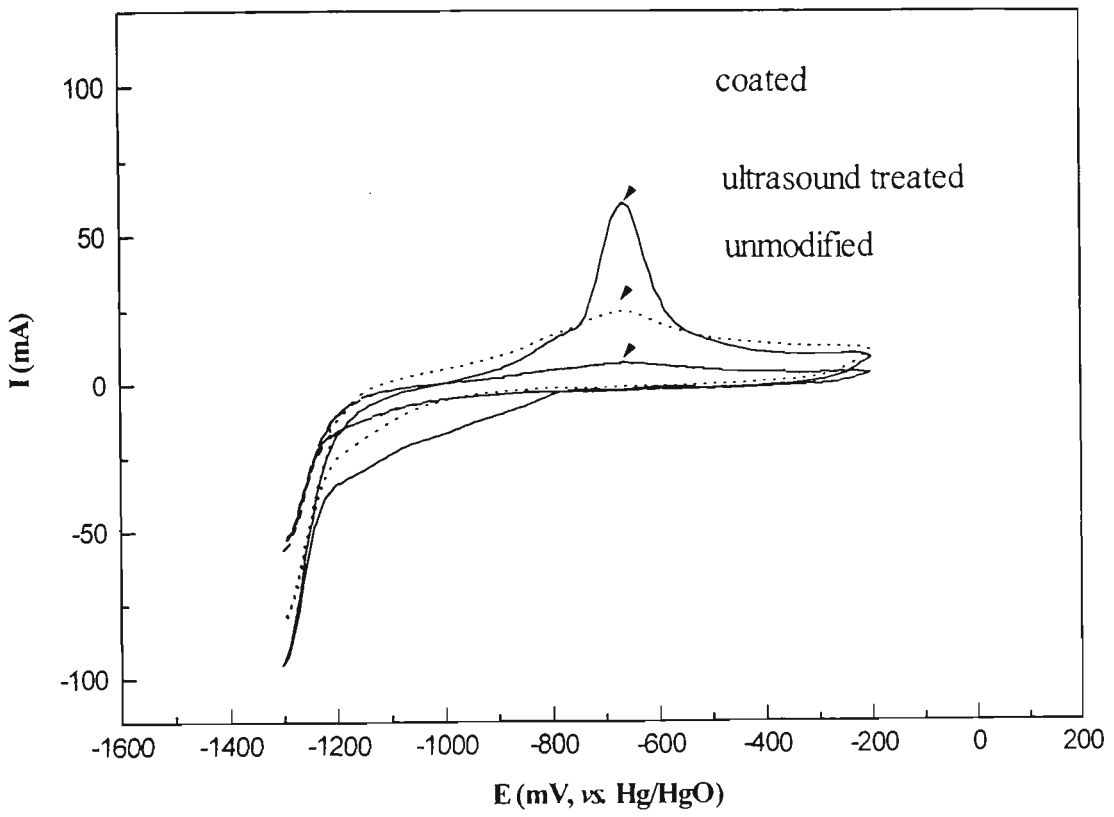

Figure 6.8 Cyclic voltammograms of the surface modified and unmodified $Mg_{1.9}Y_{0.1}Ni_{0.9}Al_{0.1}$ alloy electrode after fully charging.

the sample can impose such severe stresses on the surface oxide film that the surface film may be severely eroded [260] and a fresh alloy surface will be exposed, which is beneficial to the hydriding-dehydriding reaction on the alloy electrode. This is supported by the XRD results in Figure 6.3.

Figure 6.9 presents the variation in anodic peak current of hydrogen oxidation with the number of charge-discharge cycles for the surface-modified electrodes. The results given in Figure 6.9 (a) show clearly that the decay of anodic peak current with charge-discharge cycle proceeds much slower for the coated electrode compared to the ultrasound treated electrode. This indicates that the catalytic reactivity for hydrogen oxidation on the coated electrode declines slowly. The reason for this is probably due to the Ni-P coating on the surface of alloy powder being very stable in an alkaline solution and, protecting effectively the active sites on alloy powder from oxidation. This will result in an increment of cycle life for the Ni-P coated electrode.

In order to further confirm the effect of surface modification on the electrode behaviour of magnesium alloy, the impedance spectra of the electrodes fabricated from modified alloy powder and unmodified alloy powder were investigated. The Nyquist diagrams for modified and unmodified electrodes after 20 cycles are presented in Figure 6.10. As is shown in this figure, the loci are composed of a distorted capacitive semicircular arc at high frequencies and a linear region at low frequencies. The high frequency capacitive semicircular arc in the Nyquist diagram has been regarded as relating to the charge-transfer process while the diffusion of hydrogen in the electrode is related to the linear part at lower frequency [261-263]. The semicircular depression in the Nyquist diagram has been attributed to the following causes [262, 263]: (i) the heterogeneity of the surface, (ii) the surface

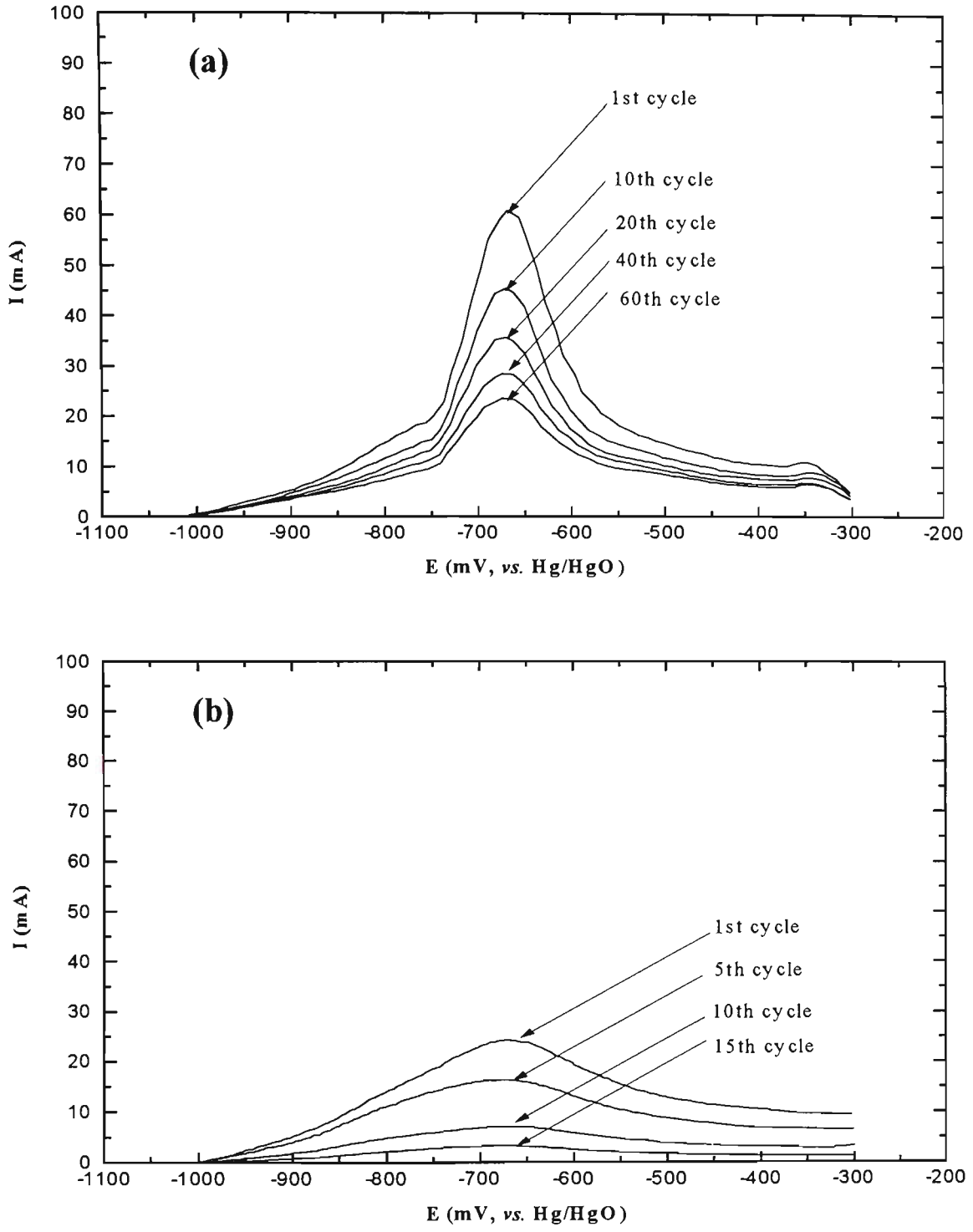

Figure 6.9 Anodic peak current changes with charging/discharging cycle for (a) Ni-P coated and (b) uncoated $Mg_{1.9}Y_{0.1}Ni_{0.9}Al_{0.1}$ alloy powder.

roughness and (iii) the existence of two different processes with the same relaxation time. The equivalent circuit used to describe the impedance spectra obtained in this experiment is also presented in Figure 6.10, where R_s is the electrolyte resistance, C_d is the double- layer capacitance, R_t is the charge-transfer resistance of interfacial reaction and Z_w is Warburg impedance used to describe the diffusion process. It can be seen by the comparison of the loci of the modified and unmodified electrodes in Figure 6.8 that the coated electrode exhibits a remarkable decrease of impedance over the frequency range measured, *i.e.*, the Ni-P coating on the powder surface reduces both charge-transfer resistance and hydrogen-diffusion resistance on the electrode, thereby reducing the overpotential during the process of charge/discharge and resulting in an increase of discharge capacity of the electrode. This result confirmed that,for the Ni-P coated powder, the very small Ni-P alloy spheres on the surface of $Mg_{1.9}Y_{0.1}Ni_{0.9}Al_{0.1}$ powder provide both the active sites for the redox reaction of hydrogen and the pathway for the diffusion of hydrogen.

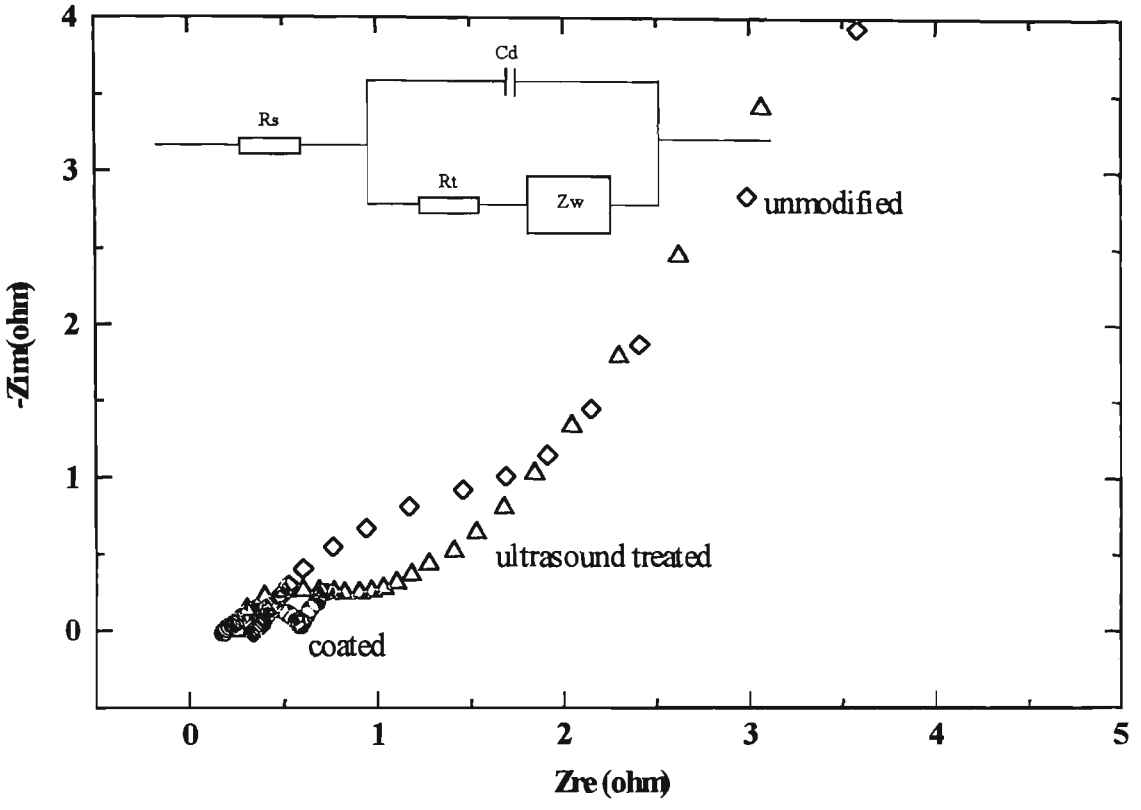

Figure 6.10 Nyquist plots for Ni-P coated and uncoated $Mg_{1.9}Y_{0.1}Ni_{0.9}Al_{0.1}$/ 6M KOH after 20 cycles.

6.6 Conclusions

The effects of surface modification on the discharge capacity, rate capability and durability of $Mg_{1.9}Y_{0.1}Ni_{0.9}Al_{0.1}$ alloy electrodes have been investigated. It was found that the modification with ultrasound pre-treatment significantly improved the electrocatalytic activity of the negative electrode and also reduced the overpotential of charging/discharging. This resulted in a marked increase of electrode capacity and high-rate discharge capability but was ineffective in improvement of the cycle life. The Ni-P coated alloy electrode was found to have a higher electrochemical capacity, better discharge rate performance and slower capacity decay than the ultrasound-treated alloy. A specific discharge capacity of 220 mAh/g was achieved which is comparable with the capacities of commercial alloys. This capacity was achieved at a low discharge current (5 mA/g) for Ni-P coated $Mg_{1.9}Y_{0.1}Ni_{0.9}Al_{0.1}$ at room temperature. Although this improvement is insufficient for practical applications because of the limited cycle life, it indicates that further improvement may be possible by various modifications similar to those described in this work.

CHAPTER 7

SYNTHESIS AND ELECTRODE CHARACTERISTICS OF $Mg_2Ni - Ti_2Ni$ COMPOSITE ALLOYS

7.1 Introduction

Although hydrogen content in Mg_2NiH_4 (3.6 *wt.*%) is much higher than that in $LaNi_5H_6$ (1.5 *wt.*%), Ti_2NiH_2 (1.4 *wt.*%) and $ZrMn_2H_{3.6}$ (1.7 *wt.*%) [102-107], it has been demonstrated in chapter 4 that this alloy is not suitable for rechargeable anode materials in an alkaline solution without any modification. The reasons for this may be attributed to [41]: (1) Mg_2NiH_4 being too stable to dehydride at ambient temperature, resulting in an extremely high discharge overpotential, and (2) a stable and dense passive oxide film layer formed on the surface of alloy particles when it comes into contact with the highly corrosive electrolyte (6M KOH) and/or during the process of anodic polarisation (discharging), which blocks both charge-transfer on the alloy/electrolyte interface and hydrogen-diffusion towards the alloy bulk. The electrode characteristics of this alloy, however, can be remarkably improved by alloy modification [41,42] as discussed in chapter 4.

Another approach to increasing the surface activity is to prepare magnesium-based composites such as Mg–$LaNi_5$ [184], La_2Mg_{17}–$LaNi_5$ and Mg–FeTi [185]. It was reported [191, 192, 283] that the hydriding rate of magnesium and magnesium-based alloys may be considerably improved by using Mg-bearing composite materials. Tanguy *et al.*'s studies [284] indicated that the reactivity of magnesium with hydrogen in the gas-phase would be strongly increased by addition of $LaNi_5$. However, the mechanism by which $LaNi_5$ addition accelerates the hydriding rate has not yet been completely elucidated [184]. In addition, element La is too expensive to practical use, and metallic magnesium is easily oxidised in an alkaline solution. This makes these composites rather poor candidates for application in Ni-MH batteries.

It is known that titanium-based alloy is a promising anode material for Ni-MH batteries because of its relatively fast hydriding-dehydriding kinetics, reasonable specific capacity and stability in an electrolyte [285]. The electrochemical behaviour of Ti_2Ni alloy in an alkaline solution has been extensively investigated [254, 264, 289, 290]. This alloy has favourable charging/discharging kinetics in alkaline solution even at room-temperature. Thus, the composite of Mg_2Ni with Ti_2Ni was expected to improve the characteristics of the electrodes.

In this chapter, another approach – the use of composite alloys – was applied to improve Mg_2Ni electrode performance. A new composite alloy Mg_2Ni–x*wt.*%Ti_2Ni has been successfully synthesised using a novel "particle inlaying" method, which inlays very small Ti_2Ni particles on to a relatively large Mg_2Ni particle to form a

composite particle. The effects of Ti_2Ni addition on the charging and discharging characteristics, and the microstructure of Mg_2Ni were investigated. A model, in which the fine Ti_2Ni particles inlaid on the surface of Mg_2Ni both electrocatalyzed charging/discharging of Mg_2Ni and provided a bypass for hydrogen atoms, was suggested to explain the electrode behaviour of Mg_2Ni – *x wt.*%Ti_2Ni composite alloys. This is supported by an analysis of discharge behaviour and electrochemical impedance spectra (EIS) studies.

The electrode characteristics of Mg_2Ni–*x wt.*%Ti_2Ni alloys for various values of *x* have been evaluated and compared with those of Mg_2Ni and Ti_2Ni. The discharge capacity of the composite alloy electrode was effectively improved from 8 mAh/g for Mg_2Ni to 165 mAh/g for Mg_2Ni–40*wt.*%Ti_2Ni at ambient temperature, which is comparable with that for the Ti_2Ni electrode (170 mAh/g). However, it should be noted that the electrode cycle life of the composite alloy Mg_2Ni–40*wt.*%Ti_2Ni is much longer than that of Ti_2Ni alloy.

7.2 Synthesis of Mg_2Ni –*x wt.*%Ti_2Ni Composite Alloys

The primary alloy Mg_2Ni was made by the conventional powder-metallurgical technique in a high vacuum furnace and Ti_2Ni alloy was prepared by vacuum arc melting under argon protection as described detail in the section 3.2. The primary alloy obtained, Mg_2Ni, was then crushed and preground into a coarse powder (size

between 75 μm and 150 μm). The Ti_2Ni was ground into a very fine powder (size below 3 μm).

Composite alloys Mg_2Ni–*x*wt.%Ti_2Ni were synthesised by using a "particle inlaying" method. The scheme for the synthesising procedure is shown in Figure 7.1. The preground alloy powders Mg_2Ni (75 μm < d < 150 μm) and Ti_2Ni (d < 3 μm) were used as starting materials for the alloy composite. The mechanical treatment began with processing in a planetary mill (Fritsch Pulverisette 5) under argon protection. After that, the powders were transferred into an alumina crucible and sintered in a high purity argon atmosphere at 750 ~ 765 °C for various time from 0.5 ~ 2 hrs. depending on the amount of sintering required.

7.3 Surface Morphology and Phase Composition

7.3.1 SEM and EDS Investigations

In order to gain further insight into the structural/microstructural characterization, scanning electron microscopic investigations have been carried out for the primary alloys and as-synthesised composite alloy Mg_2Ni–*x*wt.%Ti_2Ni for $x = 10$. Figures 7.2 (a) and (b) show the typical morphology of primary alloy Mg_2Ni and Ti_2Ni powders respectively. In order to inlay Ti_2Ni particles on to the surface of Mg_2Ni particle as evenly as possible, Ti_2Ni particles with much smaller size than the Mg_2Ni particles were used for synthesis of secondary alloy. It can be seen from the figure, the sizes

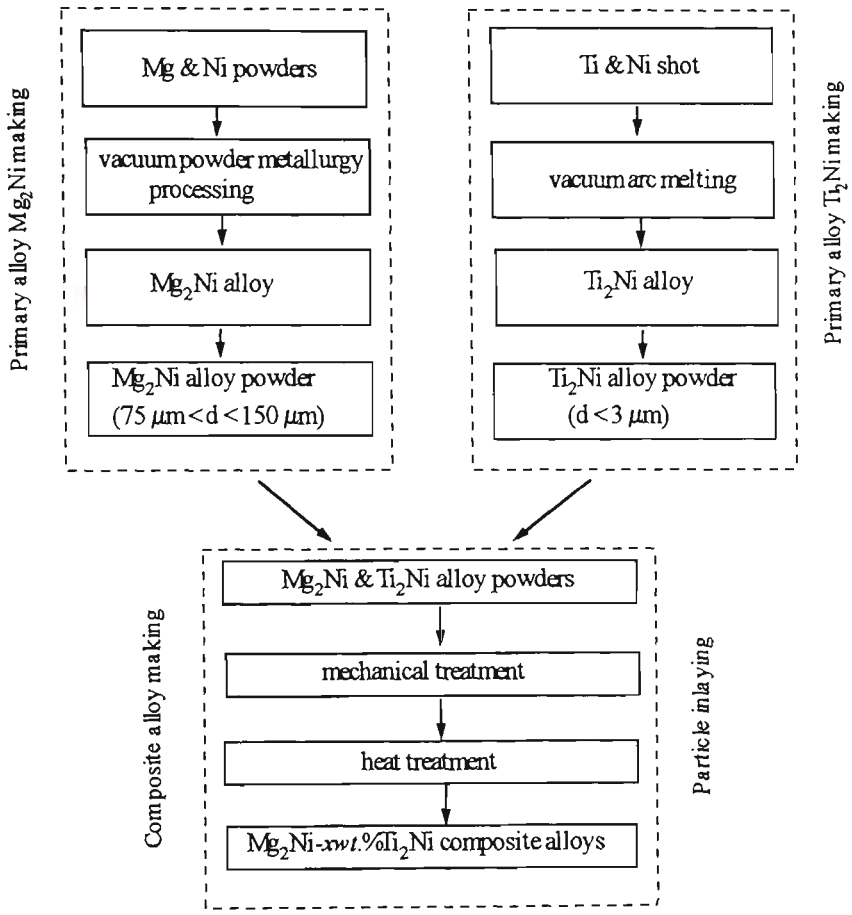

Figure 7.1 Schematic diagram of synthesising procedure for composite alloys Mg_2Ni - *x wt.*%Ti_2Ni.

(a)

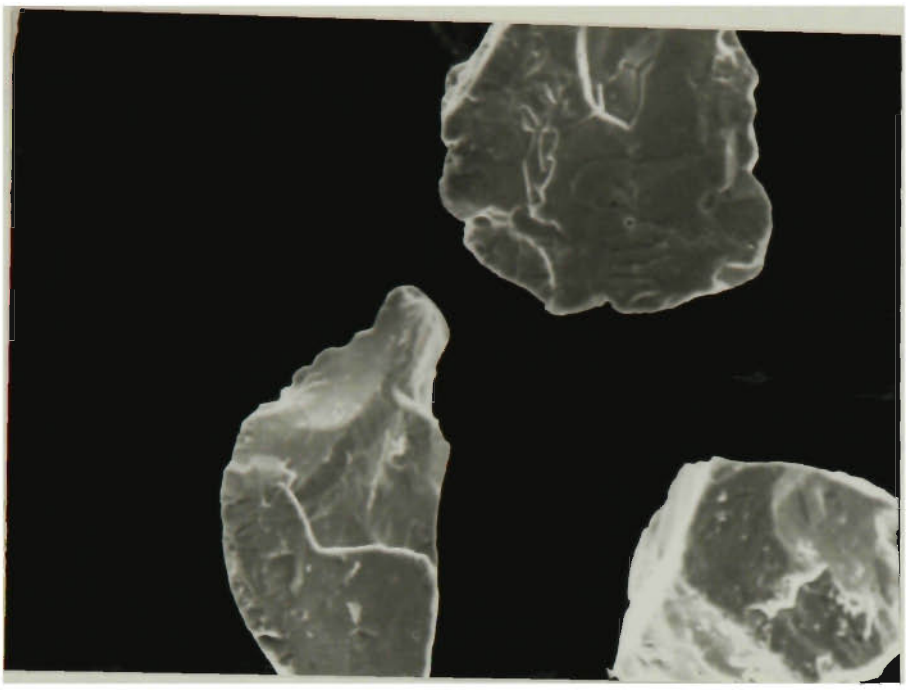

(b)

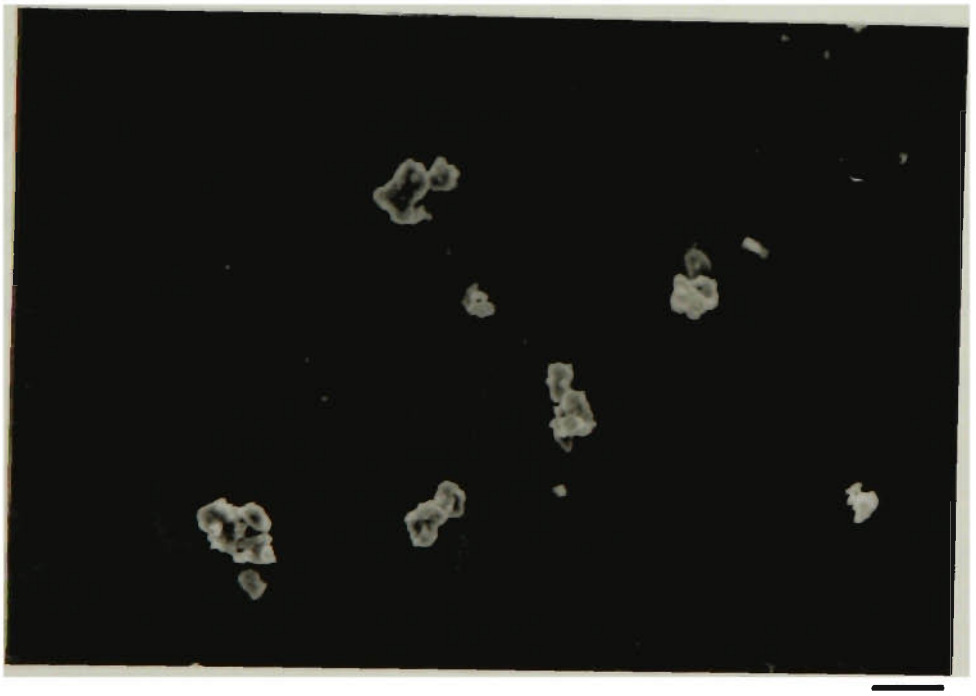

Figure 7.2 SEM micrographs of starting materials for the synthesising of the composite alloys: (a) Mg_2Ni alloy powder, (b) Ti_2Ni alloy powder

of the selected Mg_2Ni particles are between 75 μm and 150 μm, while the sizes of the Ti_2Ni particles are less than 3 μm. The surface topography of the composite after mechanical treatment only, is shown in Figure 7.3. It may be seen clearly that there are several small particles attached to the surface of larger particles and that they were distributed fairly homogeneously at this stage. The numbers of the small particles on the each large particle surface are considerably dependant on the mechanical treatment parameters (ball size, rotating speed, milling time and liquid additives). EDS qualitative analysis results confirmed that the large particles shown in the figure were Mg_2Ni , and most of the small particles were Ti_2Ni. It is known [145], that the melting point of Mg_2Ni (760 °C) is much lower than that of Ti_2Ni (984 °C). By the process of heat treatment, it is noticeable that the very small Ti_2Ni particles attached to the surface of large Mg_2Ni particles were firmly inlaid since there is some surface melting of the Mg_2Ni particles apparent in Figure 7-4 (b). This implies that the joint formed between Mg_2Ni and Ti_2Ni particles has been transformed from a purely mechanical attachment to a strong metallurgical bond. It should be noticed that the appropriate milling and sintering techniques are very important to synthesize good composite particles so that electrode may be readily hydrided/dehydride in the electrolyte. Idealy, the sintering temperature must be chosen so that the surface of the Mg_2Ni particles in the composite is slightly melted while the Ti_2Ni is not.

(a)

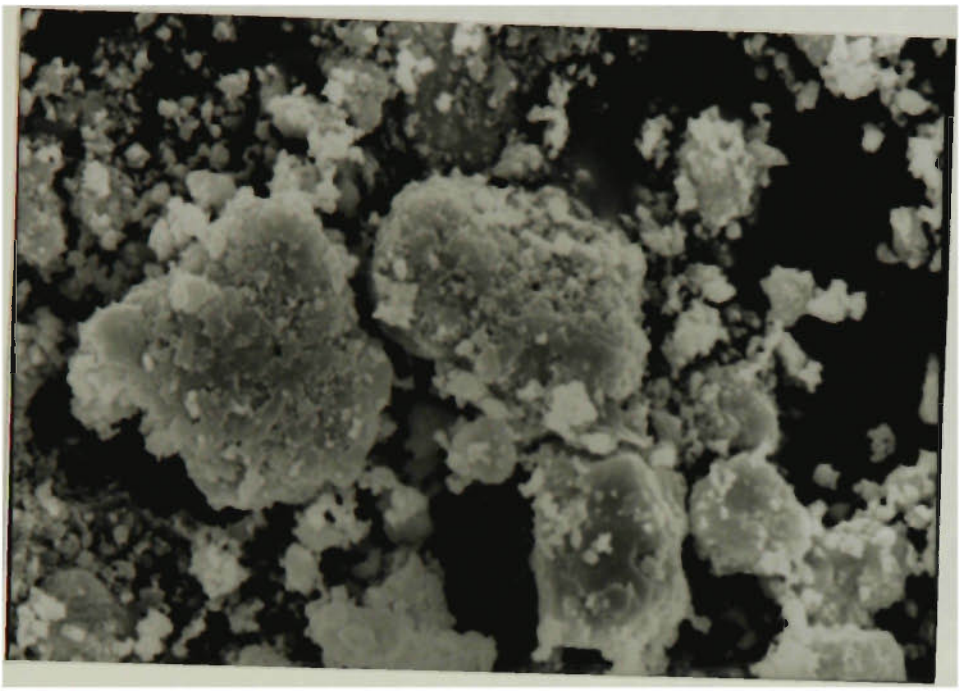

(b)

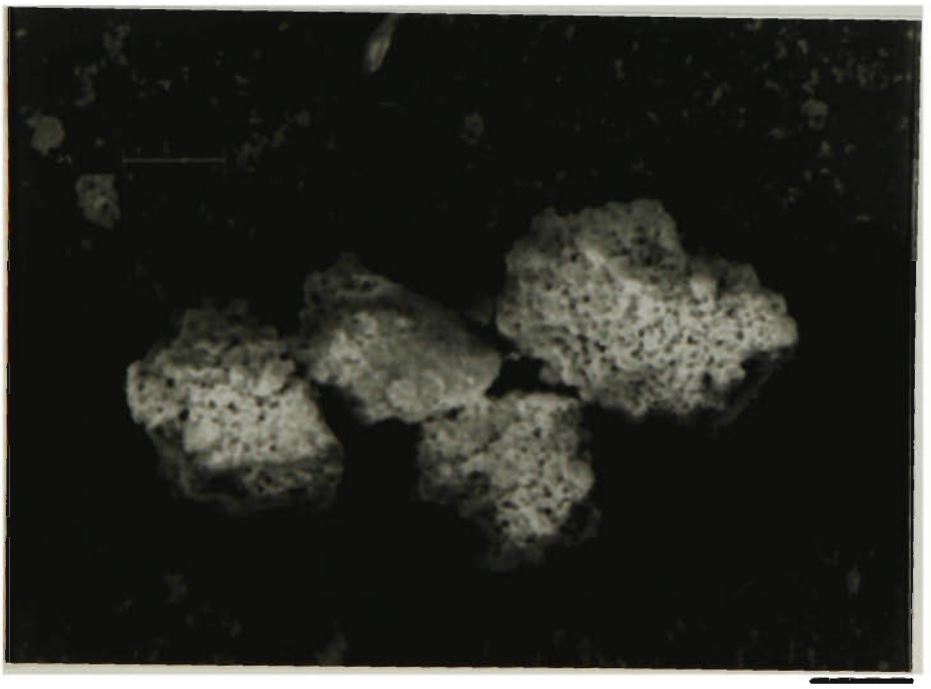

Figure 7.3 SEM micrographs of a (Mg_2Ni + 10 *wt.*%Ti_2Ni) composite after ball milling for various times. (a) 0.5 hour and (b) 2.5 hours.

(a)

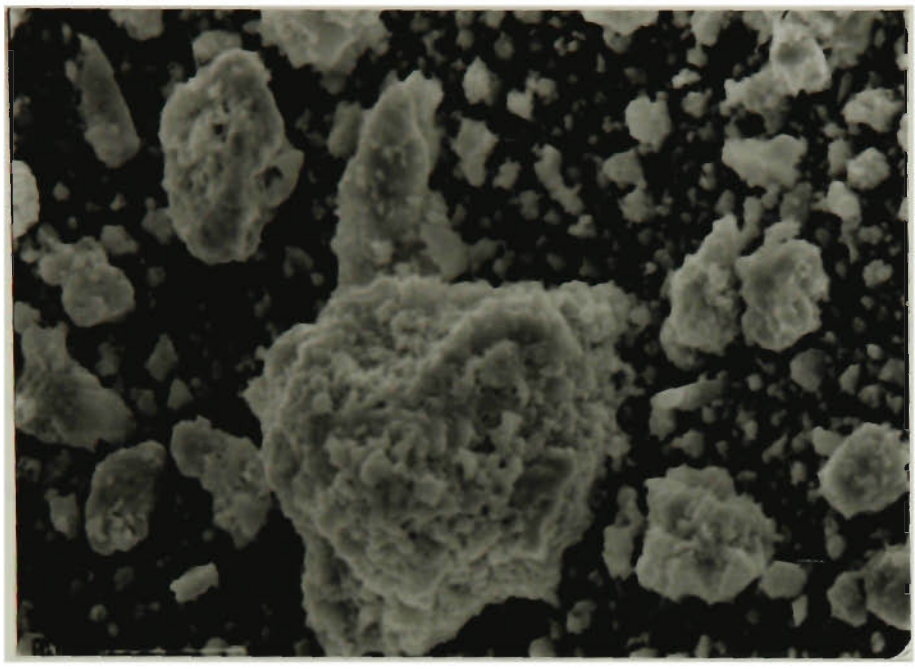

(b)

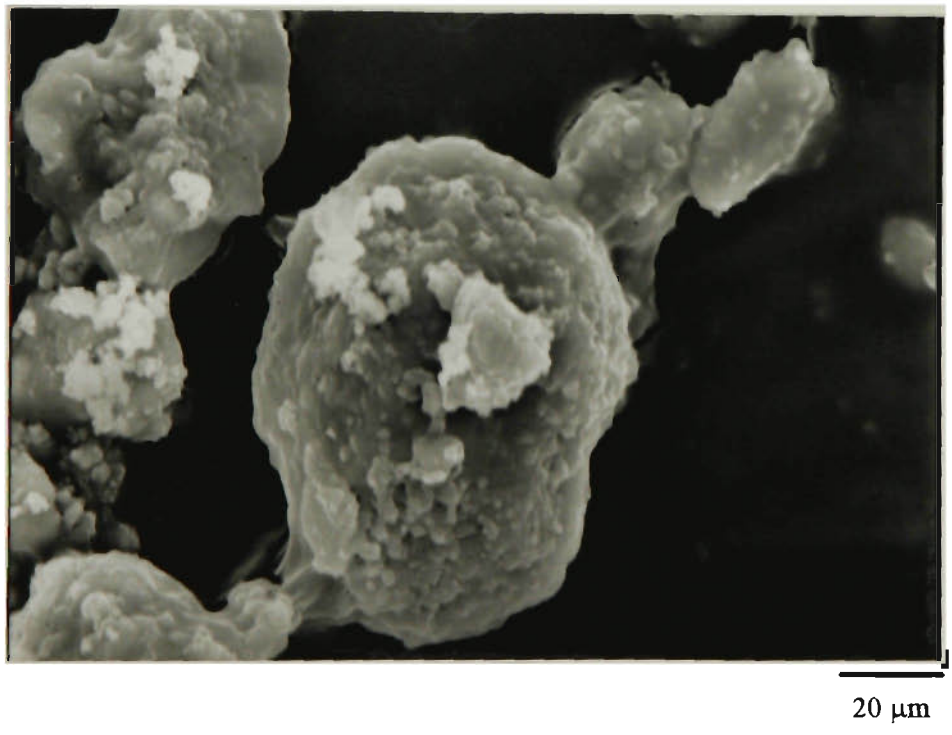

Figure 7.4 SEM micrographs of the ball-milled composite Mg_2Ni -10 *wt.*%Ti_2Ni after different sintering process: (a) 755 °C for 0.5 hour and (b) 760 °C for 2 hours.

7.3.2 XRD Analysis

The phase compositions of these alloys were analysed by an X-ray powder diffraction technique and the results are shown in Figure 7.5. The XRD pattern of the alloys revealed that the primary alloys Mg_2Ni and Ti_2Ni were monophase and of hexagonal and of cubic structure respectively (Figure 7.5 (a), (b)). The composite alloy after the process of mechanical treatment consisted of only primary alloys Mg_2Ni and Ti_2Ni (Figure 7.5 (c)). There were no newly formed phases to be observed at this processing stage. Figure 7.5 (d), however, shows that the composite alloy after both mechanical treatment and heat treatment contained Mg_2Ni, Ti_2Ni, and newly formed TiNi, Ti-Mg [291] phases. Therefore, it is believed that Ti-Mg and TiNi phases were formed at the interface of Mg_2Ni-Ti_2Ni during heat treatment. This suggests that a strong metallurgical bond between Mg_2Ni and Ti_2Ni particles was indeed formed as discussed above.

7.4 Electrode Behaviour in an Alkaline Solution

7.4.1 Discharge Capacity

Figure 7.6 shows the typical discharge curves of the electrodes fabricated from primary alloys Mg_2Ni, Ti_2Ni and composite alloys Mg_2Ni–x*wt.*%Ti_2Ni (x = 10, 20,

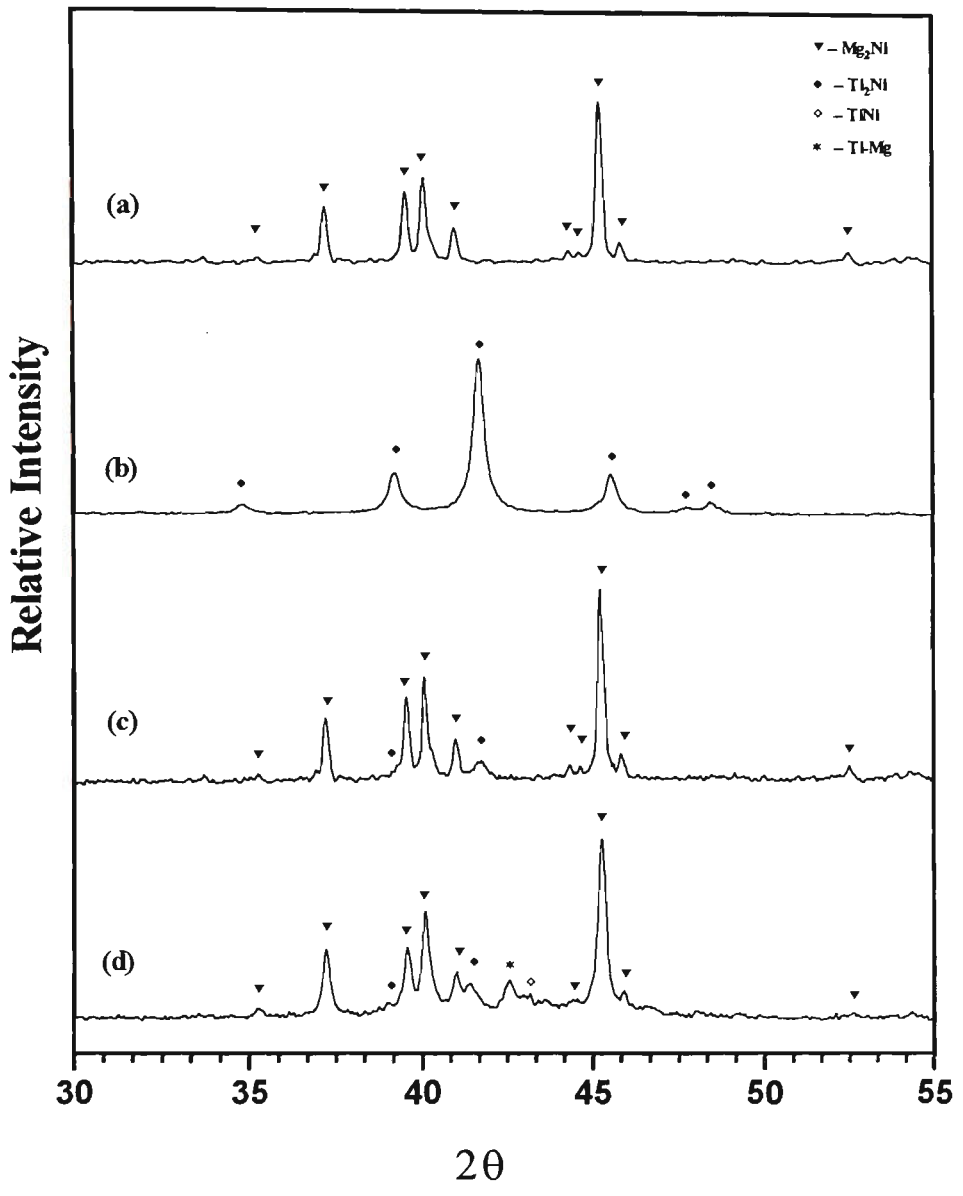

Figure 7.5 XRD pattern of the alloy powders

(a) primary alloy Mg_2Ni; (b) primary alloy Ti_2Ni;

(c) Mg_2Ni - 10 *wt.*%Ti_2Ni only after mechanical treatment;

(d) Mg_2Ni - 10 *wt.*%Ti_2Ni after mechanical treatment and sintering.

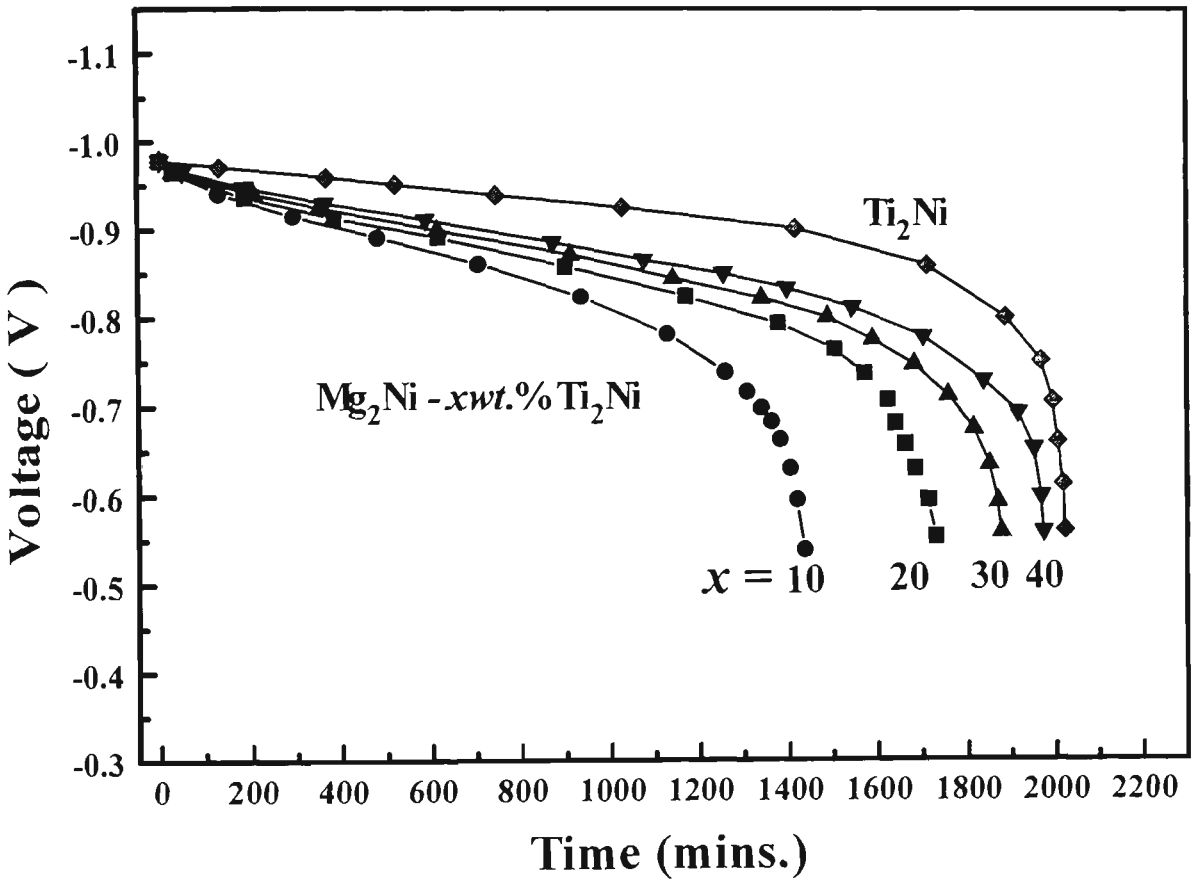

Figure 7.6 Galvanostatic discharge curves of Ti_2Ni alloy electrode and Mg_2Ni-*x wt.* % Ti_2Ni (x = 10, 20, 30, 40) composite alloy electrodes at a current density of 5 mA/g in 6 M KOH aqueous solution.

30, 40). The effect of the addition of Ti_2Ni on the discharge capacity of the composite alloy electrodes is represented in Figure 7.7. It can be seen from Figure 7.6 and Figure 7.7 that a composite of Mg_2Ni alloy with Ti_2Ni alloy significantly improves the specific capacity of the electrode. The discharge capacity of the electrode increases from 8 mAh/g of Mg_2Ni alloy without any modification to 165 mAh/g for Mg_2Ni-40*wt.*%Ti_2Ni alloy, which is very close to 170 mAh/g observed for Ti_2Ni alloy [254,264].

The increasing discharge capacity of the composite alloy electrode with increasing Ti_2Ni addition might be attributed to at least two factors:

Firstly, it is known that Ti_2Ni alloy acts as a hydrogen storage material itself and that it has 170 mAh/g of discharge capacity as an electrode material during charging-discharging in alkaline solution alone. Thus, assuming that the discharge capacity of Ti_2Ni in the composite alloy Mg_2Ni - x *wt.*% Ti_2Ni is the same as for that of Ti_2Ni alone, it is reasonable that the direct contribution of Ti_2Ni alloy to the discharge capacity of composite alloy is *x* times 170 mAh/g.

Secondly, the redox reaction of hydrogen proceeds much more easily at the surface of Ti_2Ni than on Mg_2Ni since Ti_2Ni has a relative low activation energy of reaction with hydrogen and it is relatively stable in alkaline solution in comparison with Mg_2Ni. The Ti_2Ni particles inlaid on the surface of Mg_2Ni, therefore, may concurrently provide active sites for the redox reaction of hydrogen. This means the

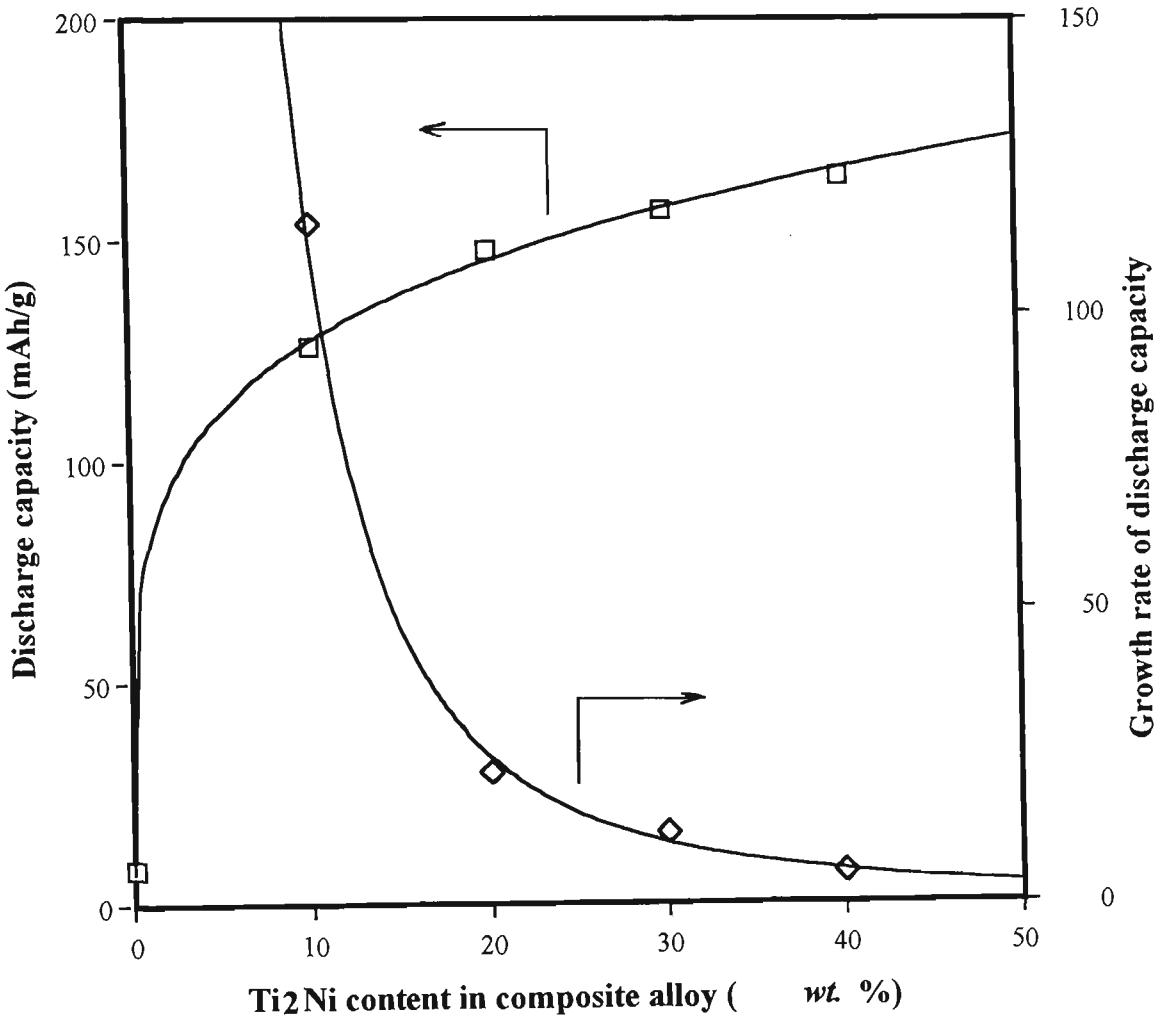

Figure 7.7 Discharge capacity of the electrodes fabricated from Mg_2Ni -*x wt.*%Ti_2Ni composite alloys *vs.* Ti_2Ni content in the composite alloys.

redox reaction of hydrogen is expected to take place at the surface of inlaid Ti_2Ni particles. Some hydrogen atoms reduced at the surface diffuse into Ti_2Ni to form Ti_2NiH_x and some of them diffuse into the underlying Mg_2Ni matrix via Ti_2NiH_x to form Mg_2NiH_x during charging. The hydrogen atoms from Mg_2NiH_x diffuse to the interface of Ti_2Ni–electrolyte via Ti_2Ni to be oxidised there when discharging. A schematic representation of the charging/discharging process for a composite alloy particle in contact with an alkaline solution is shown in Figure 7.8. Since the Mg_2Ni particles were partially covered by finer Ti_2Ni particles, the Ti_2Ni overlay protected the Mg_2Ni from oxidising during the anodic polarisation process (discharging process) and provided a passage-way for hydrogen atoms to diffuse. Furthermore, the hydriding-dehydriding of Mg_2Ni was effectively improved by this "bypass effect", which is similar to that in the Mg–Mg_2Cu composite suggested by J. Genossar and P.S. Rudman [125].

Figure 7.7 also reveals that the growth rate of discharge capacity decreased significantly with Ti_2Ni content although the discharge capacity always increased within the experimental range studied. This may be explained, as discussed above, if the Ti_2Ni in the composite acted as both a hydrogen storage material and an accelerator for hydriding/dehydriding of Mg_2Ni. When most of the surface of each Mg_2Ni particle had been surrounded by Ti_2Ni, the number of Ti_2Ni particles inlaid on the surface of the Mg_2Ni increased only slightly with further additions of Ti_2Ni. The newly increased Ti_2Ni thus only acted as a hydrogen storage material rather than an

(a)

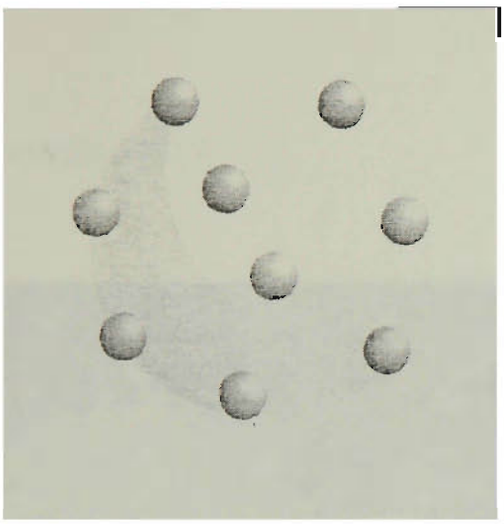

Large Sphere – Mg_2Ni

Small Sphere – Ti_2Ni

(b)

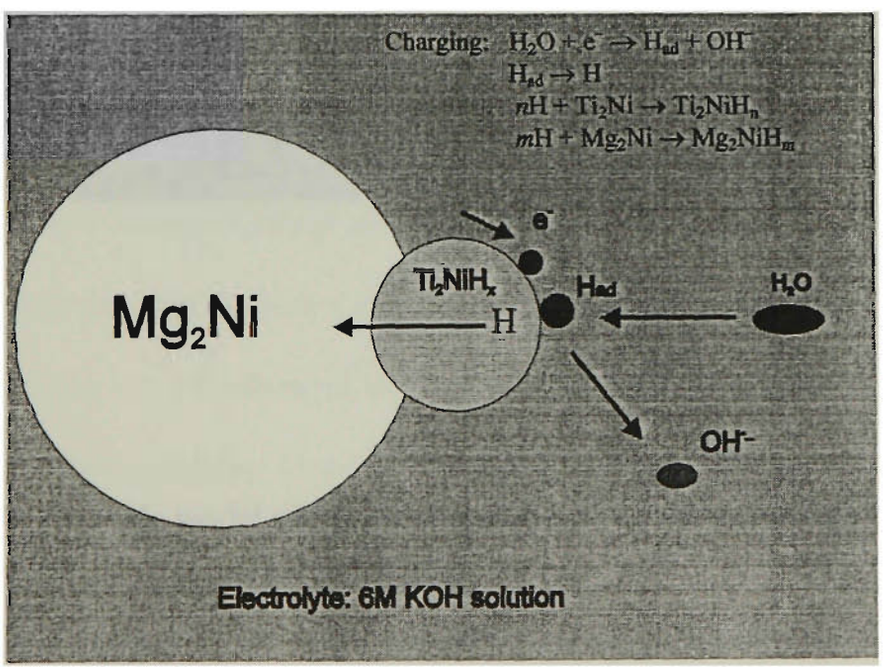

Figure 7.8 (continues)

(c)

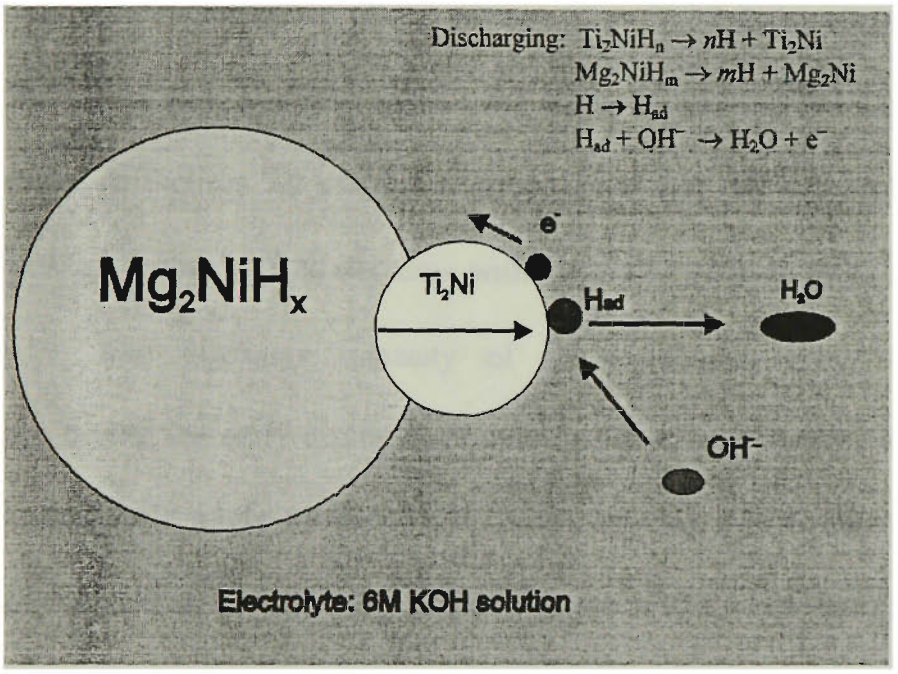

Figure 7.8 A simple model of Mg_2Ni - *x wt.*%Ti_2Ni composite alloy particle charging/discharging in 6M KOH solution.

(a) Schematic diagram of the composite alloy particle; (b) Charging procedure; (c) Discharging procedure.

accelerator simultaneously.

7.4.2 Capacity Decay

The capacity decay curves of the primary alloy Ti_2Ni and composite alloys Mg_2Ni–*x*wt.%Ti_2Ni (x = 10, 20, 30, 40) are given in Figures 7.9 and 7.10. The data presented in Figures 7.9 and 7.10 clearly show that the cycle life of the composite alloys Mg_2Ni–*x*wt.%Ti_2Ni decrease with increasing content of Ti_2Ni in the composite alloys. The discharge capacity of the composite alloy electrodes severely decays during the early cycles, then much more slowly during the later cycles. The reasons for this might be that Ti_2Ni has an extremely short cycle life (normally less than three cycles) [254]. As mentioned above, Ti_2Ni in the composite alloys acts as both a hydrogen storage material and an accelerator for the hydriding/dehydriding of Mg_2Ni. Thus, the total capacity of the composite alloy electrodes should come from two sources, *i.e.* the contributions of Ti_2Ni and Mg_2Ni in the composites. After the first two discharging cycles, Ti_2Ni in the composite is no longer responsible for the discharge capacity due to the formation and accumulation of $Ti_2NiH_{0.5}$, a hydride phase that cannot be reversibly charged/discharged [264]. Therefore, it is believed that only the Mg_2Ni in the composite alloys is responsible for the electrode capacity

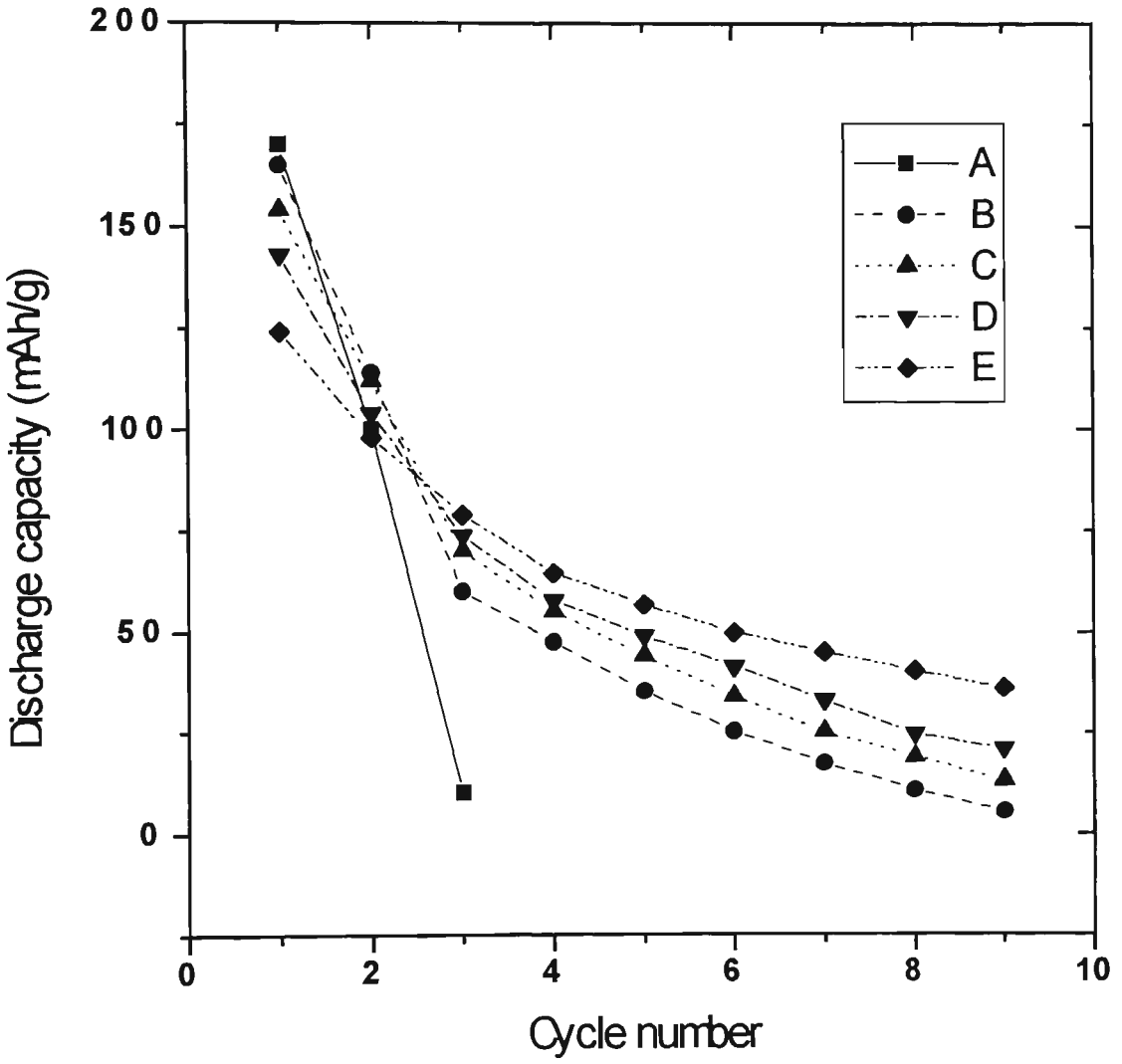

Figure 7.9 The discharge capacity *vs.* cycle number for the primary alloy Ti_2Ni and composite alloys Mg_2Ni – x*wt.*%Ti_2Ni (x = 10, 20, 30, 40).

A – Ti_2Ni; B – x = 40, C – x = 30, D – x = 20, E – x = 10.

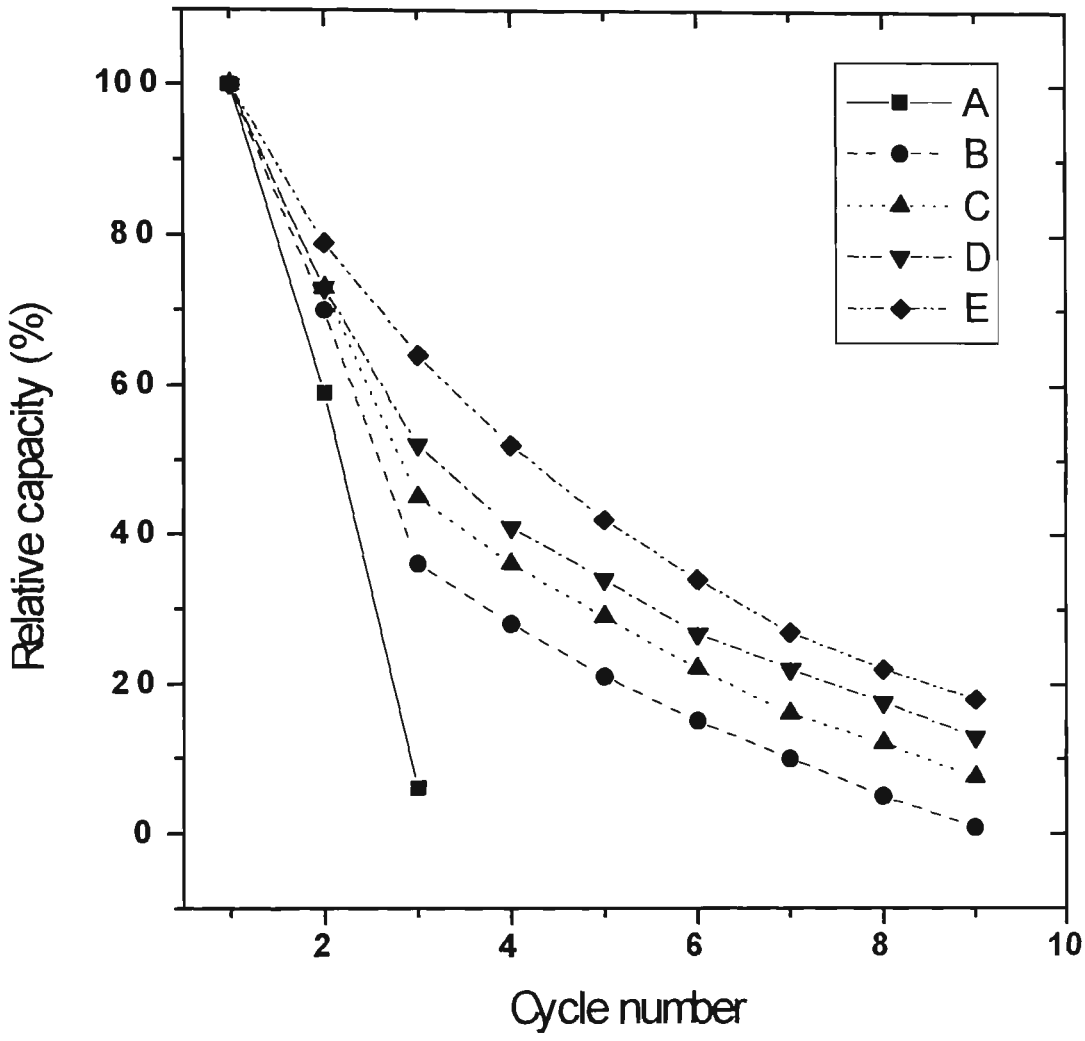

Figure 7.10 Capacity decay curves of the primary alloy Ti_2Ni and composite alloys $Mg_2Ni - x wt.\% Ti_2Ni$ (x = 10, 20, 30, 40).

A – Ti_2Ni; B – x = 40, C – x = 30, D – x = 20, E – x = 10.

during later cycling. The rapid decay of the composite alloy electrode capacity during the initial cycles, thus, is thought to be caused mainly by the capacity decay of Ti_2Ni. Because the capacity decay of the composite alloy electrodes becomes much slower during later cycling, it is reasonable to suggest that the $Ti_2NiH_{0.5}$ phase, which was formed during the early cycles, still acts as an accelerator for Mg_2Ni hydriding/dehydriding in the electrolyte.

7.4.3 Discharge Rate Characteristics

Figure 7.11 shows the relationship between the discharge current density and specific capacity for an initial charge-discharge cycle of the Ti_2Ni and Mg_2Ni–x*wt.*%Ti_2Ni (x = 10, 20, 30, 40). It can be seen clearly from the Figure 7.12 that the rate discharge capability of the composite alloys depends on the Ti_2Ni content in the composites. The rate discharge capability of Mg_2Ni–x*wt.*%Ti_2Ni alloys significantly increases with increasing x value. This may be probably attributed to the better discharge rate characteristics of Ti_2Ni alloy (see Figures 7.11 and 7.12). It is believed that Mg_2Ni alloy performs a poor discharge rate capability because of its sluggish hydriding/dehydriding kinetics [41,42]. When Ti_2Ni was inlaid on the surface of the Mg_2Ni particle, as discussed in the section 7.4.1, it did accelerate the redox reaction of hydrogen at the interface of alloy particle and electrolyte resulting in the improvement of discharge capacity. Ti_2Ni inlaid on the surface of Mg_2Ni

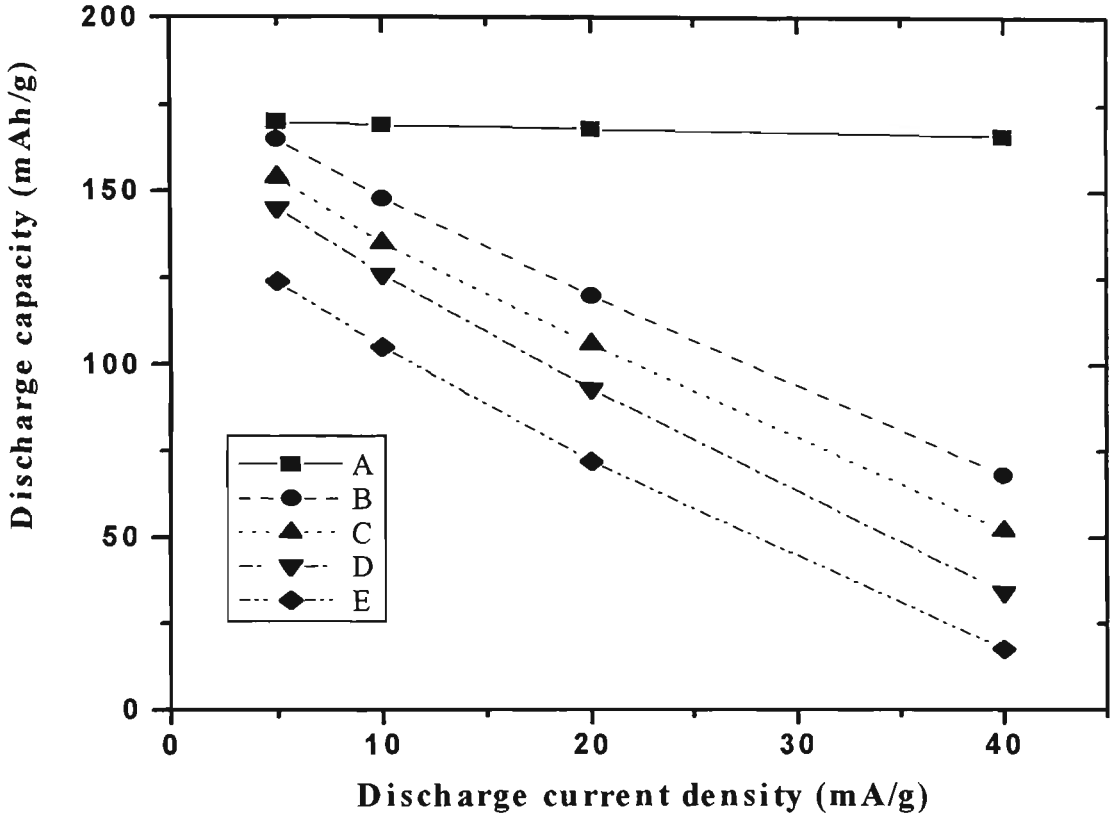

Figure 7.11 Discharge capacity *vs.* discharge current density for the primary alloy Ti_2Ni and composite alloys $Mg_2Ni - x$*wt.*%Ti_2Ni (x = 10, 20, 30, 40).

A – Ti_2Ni, B – x = 40, C – x = 30, D – x = 20, E – x = 10.

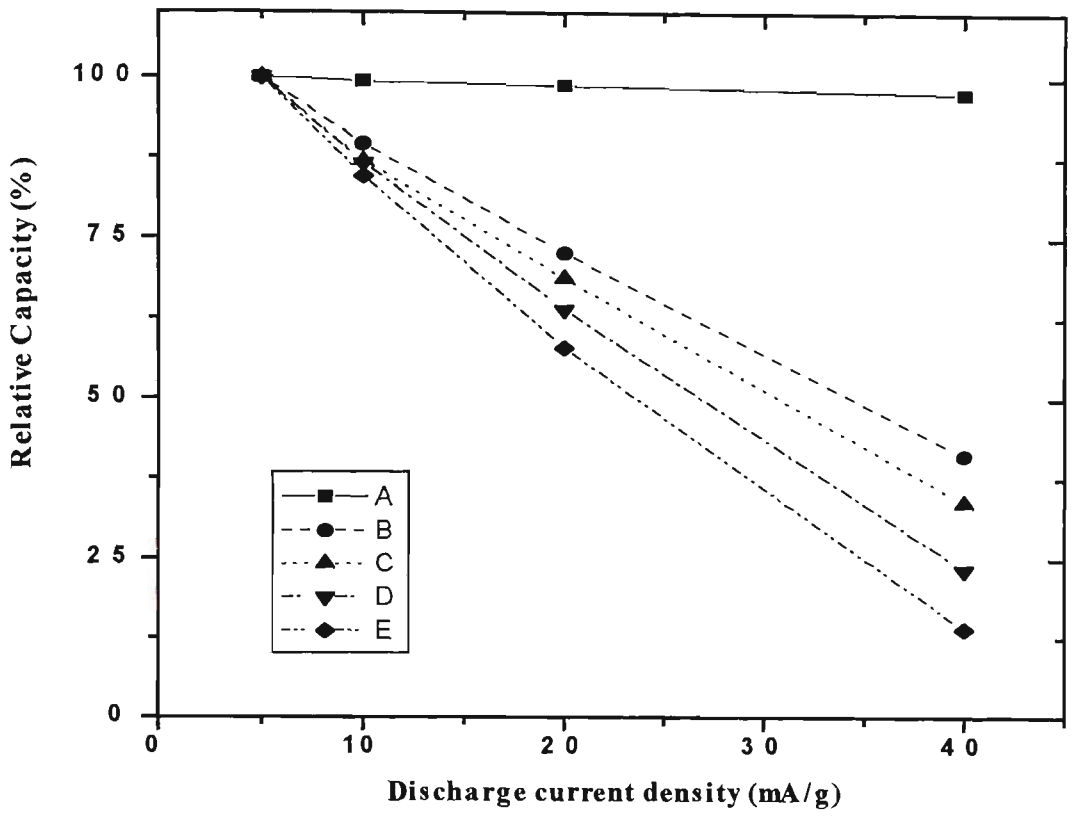

Figure 7.12 Discharge rate dependence of rate discharge capability for the alloy Ti_2Ni and composite alloys $Mg_2Ni - x wt.\% Ti_2Ni$ (x = 10, 20, 30, 40).

A – Ti_2Ni, B – x = 40, C – x = 30, D – x = 20, E – x= 10.

particle, however, has relatively little effect on the internal characteristics of Mg_2Ni particle (*e.g.* the diffusion of hydrogen in Mg_2Ni).

7.5 Electrochemical Impedance Spectroscopy

In order to further confirm the effect of "particle inlaying" on the electrode behaviour of the composite alloys, the electrochemical impedance spectra of the electrodes fabricated from composite alloys and primary alloy were investigated. Mg_2Ni–10 *wt.*%Ti_2Ni was used as an example of the composite alloys to compare with electrode fabricated from primary alloys Mg_2Ni and Ti_2Ni. The Nyquist diagrams for Mg_2Ni, Ti_2Ni and Mg_2Ni–10 *wt.*%Ti_2Ni are presented in Figure 7.13. As is shown in this figure, the loci are composed of a distorted capacitive semicircular arc at high frequencies and a linear region at low frequencies. The high frequency capacitive semicircular arc in the Nyquist diagram has been regarded as relating to the charge-transfer process and the diffusion of hydrogen in the electrode has been associated with the linear part at lower frequency [292-294]. The semicircle depression in the Nyquist diagram has been attributed to the following causes [286,287]: (i) the heterogeneity of the surface, (ii) the surface roughness and (iii) the existence of two different processes with the same relaxation time. The equivalent circuit used to describe the impedance spectra obtained in this experiment is presented in Figure 7.14, where R_s is the electrolyte resistance, C_d is the

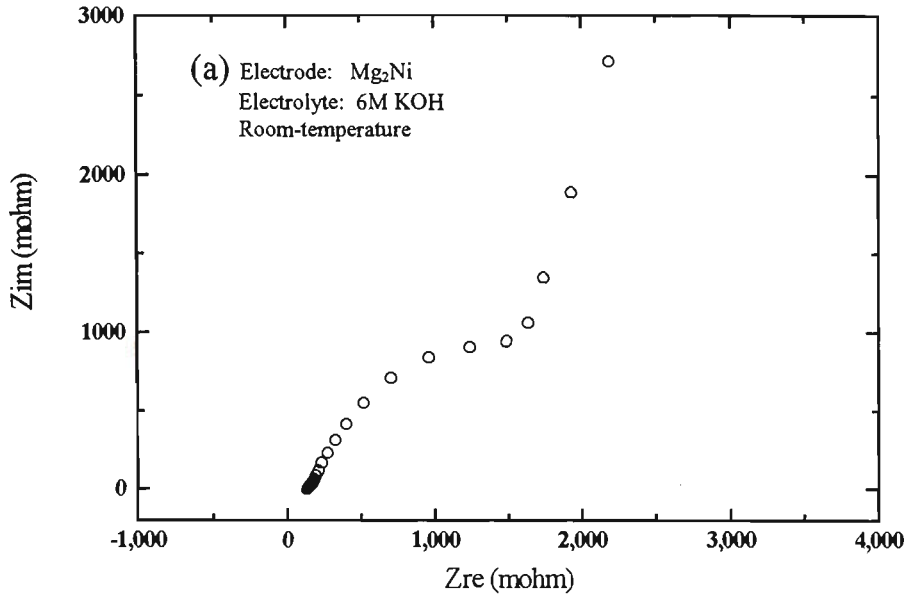

(a)

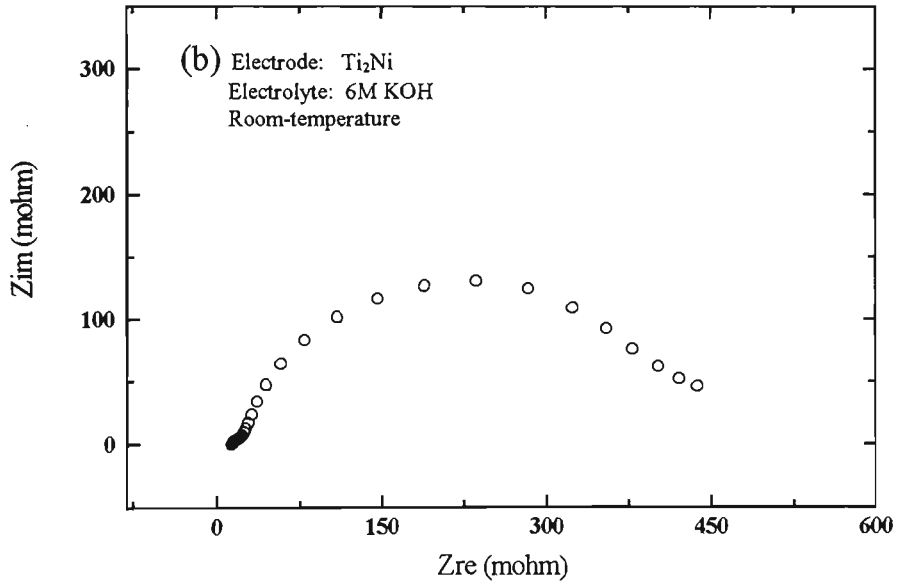

(b)

Figure 7-13 (continues)

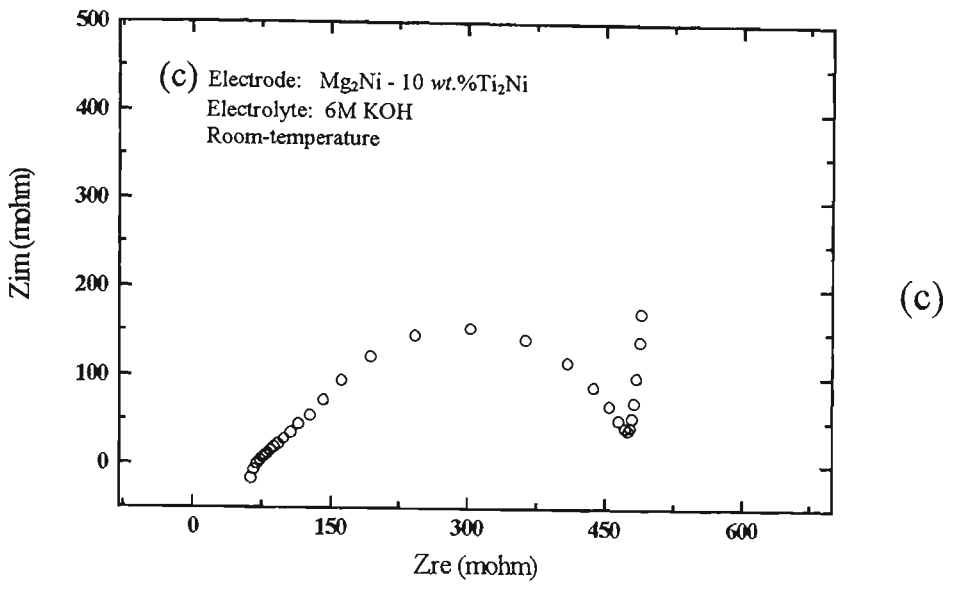

Figure 7.13 Nyquist diagrams for: (a) Mg_2Ni primary alloy; (b) Ti_2Ni primary alloy; and (c) Mg_2Ni - *x wt.*% Ti_2Ni composite alloy electrodes.

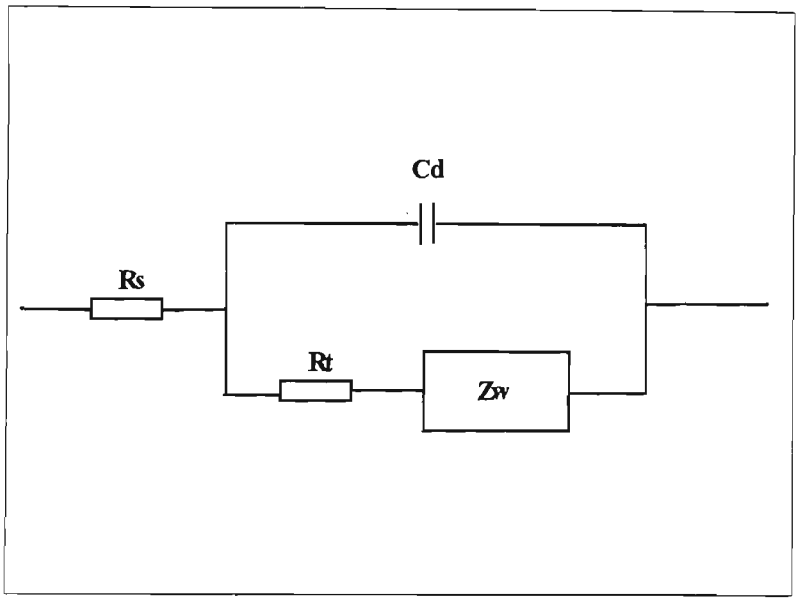

Figure 7.14 An equivalent circuit for Mg_2Ni - 10*wt.*%Ti_2Ni composite alloy electrode in 6M KOH solution at room-temperature.

double-layer capacitance, R_t is the charge-transfer resistance of the interfacial reaction and Z_w is the Warburg impedance used to describe the diffusion process. It can be found by comparison of the loci of Mg_2Ni–10*wt.*%Ti_2Ni and Mg_2Ni in Figures 7.13 (a) and (c) that the composite alloy electrode exhibits a remarkable decrease of impedance within the measured frequency range, *i.e.*, the formation of the composite alloy decreases both charge-transfer resistance and hydrogen-diffusion resistance on the electrode, thereby reducing the overpotential during the process of charge/discharge and resulting in an increase of discharge capacity of electrode. This result confirmed that, for the composite alloys, the fine Ti_2Ni particles inlaid on the surface of Mg_2Ni particles provides both the active sites for the redox reaction of hydrogen and the pathway for the diffusion of hydrogen as presented above.

7.6 Conclusions

A novel method - "particle inlaying" - has been successfully developed for synthesising magnesium-based hydrogen storage alloy anode materials for a Ni-MH battery. The discharge capacity and rate discharge capability of the composite alloys Mg_2Ni–*x wt.*%Ti_2Ni increases with increasing Ti_2Ni addition in the composite. A discharge capacity of 165 mAh/g has been obtained at ambient temperature for the electrode fabricated from Mg_2Ni–40*wt.*%Ti_2Ni composite alloy. However, the

capacity decay curves indicates the cycle life of the composite alloy electrodes decreases with increasing x value.

The following model was suggested to explain the electrode behaviour of Mg_2Ni–x*wt.*%Ti_2Ni composite alloys: *i.e.* Ti_2Ni inlaid on the surface of Mg_2Ni particles provided both an electrocatalysis effect for the hydriding/dehydriding of Mg_2Ni and a bypass for hydrogen atoms. Electrochemical studies indicated that Ti_2Ni particles inlaid on the surface of Mg_2Ni particles improved both the hydrogen redox reaction at the surface of alloy and the diffusion of hydrogen in the electrode. This is beneficial to the charge-discharge efficiency of the electrode, resulting in a significant increase of the specific capacity of the electrode. Additionally, Ti_2Ni itself concurrently acts as a hydrogen storage material also, and provides additional specific capacity (equivalent to x times of 170 mAh for the composite alloy, Mg_2Ni–x*wt.* %Ti_2Ni). However, it has little direct contribution to the electrode capacity after the first three cycles since $Ti_2NiH_{0.5}$ phase was formed and it cannot be reversibly charged/discharged. The formed $Ti_2NiH_{0.5}$ phase still seems to have some indirect effect on the discharge capacity, namely, accelerating the hydriding/dehydriding of Mg_2Ni.

CHAPTER 8 SUMMARY

8.1 The General Conclusions

The feasibility of utilizing magnesium-based hydrogen storage alloys as a low cost and high performance anode material for the Ni-MH secondary battery was exploited for the first time in this study. The electrode performance was markedly improved by three approaches, *i.e.* alloy element substitutions, surface modification of the alloy powder and preparing composites of magnesium-based alloy with Ti_2Ni alloy. A modified Mg_2Ni-type alloy with a specific discharge capacity of 220 mAh/g at the room-temperature has been obtained by this study, which is almost matches that of rare-earth system anodes used now in commercial batteries. The electrochemical behaviour of magnesium-based hydrogen storage alloy electrodes was characterised. The following general conclusions can be summarised from this study:

1. Compared to its theoretical capacity, Mg_2Ni alloy exhibited an extremely low electrochemical capacity in the electrolyte at room temperature even at the very low discharge current of 5 mA/g. The reasons for this may be attributed to its easy oxidation and incomplete hydriding reaction, which results in a very poor electrochemical hydriding and dehydriding behaviour in the electrolyte. Thus, it is

suggested that Mg_2Ni is not suitable as a rechargeable anode material in an alkaline solution without any modification.

2. Surface micro-encapsulation of Mg_2Ni alloy powder with Ni-P electroless plating was proved to be an effective approach to improve the electrode performance of Mg_2Ni. Both discharge capacity and rate dischargeability were remarkably enhanced by the surface modification of the alloy powder. The improvement of the modified Mg_2Ni electrode was attributed to protection of the alloy from oxidation and improvement in the electrocatalytic activity for hydrogen evolution reaction. However, the electrode properties of micro-encapsulated Mg_2Ni is still far from satisfactory, and the incomplete hydriding of Mg_2Ni is barely improved.

3. The effects of the substitution of Mg with small amounts of Al, Ca, La, Ti and V in Mg_2Ni on the electrochemical behaviour were investigated. Discharge capacity was found to increase in the order of Al > V > Ti > La > Ca-substitution. Among the tested substituent elements, the Al and V were effective for increasing the initial electrode capacity, as well as Ti. The exchange current values, i_0 of Al- and V-substituted alloys were found to be much higher than other alloys and the change of i_0 shown good consistency with the discharge capacity, which suggests that charge transfer is the RDS for the dehydriding reaction of $Mg_{1.95}M_{0.05}Ni$ (M = Al, Ca, La, Mg, Ti, V) alloy electrodes.

4. The yttrium and aluminium substituted Mg_2Ni-type alloy electrodes were found to have a higher electrochemical capacity and better discharge rate performance than Mg_2Ni. The discharge capacity and discharge rate characteristics of the electrodes were considerably improved with increasing x value in $Mg_{1.9}Al_{0.1}Ni_{1-x}Y_x$. A specific discharge capacity of 170 mAh/g was achieved at a low discharge current (5 mA/g) for the $Mg_{1.9}Al_{0.1}Ni_{0.7}Y_{0.3}$ electrode at room temperature. Although this improvement is insufficient for practical applications, it indicates that further improvement may be possible by partial substitution of Ni and/or Mg in the Mg_2Ni-type alloy. This could enable the development of Mg_2Ni-type alloys for the anode materials of Ni-HM batteries. However, it should be noted, on the other hand, that an increase in the yttrium content leads to a decrease of cycle life of the electrodes.

5. The discharge behaviour of Mg_2Ni-type hydrogen storage alloys in an alkaline solution at ambient temperature was investigated and compared with $LaNi_5$. EIS results indicate that the very low discharge capacity and sluggish kinetics of the unmodified Mg_2Ni electrode in alkaline solution are caused by the presence of both a larger charge-transfer resistance and a mass-transfer resistance. The formation and growth of magnesium oxide and/or hydroxide layer on unmodified Mg_2Ni increase the electronic resistance at the electrode/electrolyte interface and result in a large discharging overpotential. The additions of yttrium and aluminium in Mg_2Ni considerably reduce the hydrogen-diffusion resistance in the alloy and the charge-

transfer resistance on the electrode/electrolyte interface. As a result, the discharge capacity and rate-dischargeability of the electrodes are remarkably improved.

6. The effects of surface modification on the discharge capacity, rate capability and durability of $Mg_{1.9}Y_{0.1}Ni_{0.9}Al_{0.1}$ alloy electrodes have been investigated. It was found that the modification with ultrasound pre-treatment significantly improved the electrocatalytic activity of the negative electrode and also reduced the overpotential of charging/discharging. This resulted in a marked increase of electrode capacity and high-rate discharge capability but was ineffective in improvement of the cycle life. The Ni-P coated alloy electrode was found to have a higher electrochemical capacity, better discharge rate performance and slower capacity decay than the ultrasound-treated alloy. A specific discharge capacity of 220 mAh/g was achieved at a low discharge current (5 mA/g) for Ni-P coated $Mg_{1.9}Y_{0.1}Ni_{0.9}Al_{0.1}$ at room temperature.

7. A novel method - "particle inlaying" - has been successfully developed for synthesising magnesium-based hydrogen storage alloy anode materials for a Ni-MH battery. The discharge capacity and rate discharge capability of the composite alloys Mg_2Ni–*x*wt.%Ti_2Ni increases with increasing Ti_2Ni addition in the composite. A discharge capacity of 165 mAh/g has been obtained at ambient temperature for the electrode fabricated from Mg_2Ni–40*wt.*%Ti_2Ni composite alloy. However, the capacity decay curves indicates the cycle life of the composite alloy electrodes decreases with increasing *x* value.

8. The following model was suggested to explain the electrode behaviour of Mg_2Ni–*xwt.*%Ti_2Ni composite alloys: *i.e.* Ti_2Ni inlaid on the surface of Mg_2Ni particles provided both an electrocatalytic effect for the hydriding/dehydriding of Mg_2Ni and bypass for hydrogen atoms. Electrochemical studies indicated that Ti_2Ni particles inlaid on the surface of Mg_2Ni particles improved both the hydrogen redox reaction at the surface of the alloy and the diffusion of hydrogen in the electrode. This is beneficial to the charge-discharge efficiency of the electrode, resulting in a significant increase of the specific capacity of the electrode. Additionally, Ti_2Ni itself concurrently acts as a hydrogen storage material also, and provides additional specific capacity (equivalent to x times of 170 mAh for the composite alloy, Mg_2Ni–*xwt.* %Ti_2Ni). However, it has little direct contribution to the electrode capacity after the first three cycles since $Ti_2NiH_{0.5}$ phase was formed and it cannot be reversibly charged/discharged. The formed $Ti_2NiH_{0.5}$ phase still seems to have some indirect effect on the discharge capacity, namely, accelerating the hydriding/dehydriding of Mg_2Ni.

8.2 Recommendations for Future Work

This study has shown that Mg_2Ni-type hydrogen storage alloy has a great potential for the application of Ni-MH batteries. The various modifications in this work have been proved to be effective for improving the electrode performance of magnesium-based hydrogen storage alloys. The discharge capacity of modified Mg_2Ni-type alloy electrode has reached 220 mAh/g by this preliminary investigation. However, the practical electrochemical capacity of this alloy now is still much less than its theoretical capacity and the high-rate dischargeability and cycle life are still not very satisfactory. Thus, in order to further improve the electrochemical hydriding and dehydriding behaviour in an alkaline solution, the following work is suggested:

8.2.1 Optimization of Alloy Composition

The partial substitution of Mg and/or Ni in Mg_2Ni by Al, Ti, V and Y in this study has shown a remarkable improvement for the electrode performance. Other alloying additions, *e.g.* Co, Cu, Mn, Sc, and Sn should be considered for investigation in future work. The alloy composition needs to be optimised according to the consideration of discharge capacity, high-rate dischargeability, as well as cycle life. The multicomponent and/or multiphase magnesium-based alloy, in which the main phase has a high hydrogen storage capacity and the second-phase has a high electrocatalytic activity for the redox reaction of hydrogen, might be an ideal negative electrode material for Ni-MH battery.

8.2.2 Synthesis of Alloy Composites

The "particle inlaying" method invented in this study has been proved to be an effective approach for synthesising alloy composites with better hydriding/dehydriding behaviour for a Ni-MH battery. The electrode properties of composite alloys Mg_2Ni–*xwt.*%Ti_2Ni have been investigated. The composite Mg_2Ni-type alloy with other high catalytic activity metals and alloys, *e.g.* Pd, Pt, and $LaNi_5$, TiNi Ti-Zr-V Laves phase type hydrogen storage alloys using the "particle inlaying" method, are expected to achieve more promising results.

8.2.3 Surface Analysis and in situ Neutron Diffraction Study

The surface analysis methods, such as AES and XPS, are suggested to be adopted for the better understanding the effects of ultrasound pre-treatment on the electrode performance. An in situ neutron diffraction study during the processes of charging and discharging of the magnesium-based alloy electrodes is also suggested to use for locating the position of the hydrogen atom in the alloy. This would provide more information on the fundamental aspects of electrochemical hydriding/dehydriding processes.

REFERENCES

[1] R. E. Billings, M. Sanchez, P. Cherry and D. B. Eyre, *Int. J. Hydrogen Energy*, 16 (1991) 829.

[2] K.A. Striebel, F. R. McLarnon and E. J. Cairs, *J. Power Sources*, 47 (1994)1.

[3] J. P. Cornu, *J. Power Sources*, 51 (1994) 19.

[4] J. Toepler, O. Bernaure and H. Buchner, *J. Less-Common Met.*, 74 (1980) 385

[5] S. R. Ovshinsky, M. A. Fetcenko, and Ross, *Science*, 260 (1993) 176.

[6] H. F. Bitter and C. C. Badcock, *J. Electrochem. Soc.* 130 (1983) 193.

[7] J. J. G. Willems and K. H. J. Buschow, *Less-Common Met.*, 129 (1987) 13.

[8] T. L. Markin and R. M Dell, *J. Electroanal. Chem.*, 118 (1981) 217.

[9] C. Iwakura, Y. Kajia and H. Yoneyama, *J. Electrochem. Soc.*, 136 (1989) 1351.

[10] T. Sakai, A. Yuasa, H. Ishikawa, H. Miyamura and N. Kuriyama, *J. Less-Common Met.*, 172-174 (1991) 1194.

[11] A. Visintin, S. Srinivasan and A. J. Appleby, *J. Electrochem. Soc.*, 139 (1992) 985.

[12] T. Sakai, A. Takagi, N. Kuriyama, H. Miyamura and H. Ishiawa, *Progess in Batteries & Solar Cells*, 9 (1990) 269.

[13] T. Sakai, K. Oguro, H. Miyamura, N. Kuriyama, A. Kato and H. Ishikawa, *J. Less-Common Met.*, 161 (1990) 203.

[14] C. Iwakura and M. Matsuoka, *Progress in Batteries & Battery Materials*, 10 (1991) 81.

[15] M. Tadokoro, M. Nogami, Y. Chikno, M.Kimoto, T. Ise, K. Nisho and N. Furukawa, *J. Alloys and Compounds*, 192 (1993) 179.

[16] T. Sakai, H. Miyamura, N. Kuriyama, H. Ishikawa and I. Uehera, *J. Alloys Comp.*, 192 (1993) 155.

[17] C. Iwakura, M.. Matsuoka, K. Asi and T. Kohno, *J. Power Source*, 38 (1992) 149.

[18] F. Meli, T. Sakai, A. Zuttel, L. Schlapbach, *J. Alloys Comp.*, 221 (1995) 284.

[19] M. Masao, M. Terashima and C. Iwakura, *Electrochimica Acta*, 38 (1993) 1087.

[20] S. Wakao, H. Sawa and J. Furukawa , *J. Less-Common Met.*, 172-174 (1991) 1219.

[21] S. R. Kim, J. Y. Lee and H. H. Park, *J. Alloys Comp.*, 205 (1994) 225.

[22] A. Ohta, *Progress in Batteries & Solar Cells*, 8 (1989) 185.

[23] T. Sakai, H. Miyamura, N. Kuriyama, H. Ishikawa and I. Uehera, *J. Alloys Comp.*, 192 (1993) 158.

[24] A. Anani, A. Visintin, K. Petrov and S. Srinivasan, *J. Power Sources*, 47 (1994) 261.

[25] *ITE Fax Battery Newsletter*, No.8, April 15, 1995, p3.

[26] *ITE Fax Battery Newsletter*, No.5, March 1, 1995, p4.

[27] M. Fetcenko, S.Venkatesan and S. Dhar, *Progress in Batteries & Solar Cells*, 9 (1990) 252.

[28] W. M. Mueller, J. P. Blackledge, G. G. Libowitz, *Metal Hydrides*, Academic Press, New York, 1968.

[29] M. H. Mintz, Z. Gavra and Z. Hadari, *J. Inorg. Nucl. Chem.* 40 (1978) 765.

[30] B. Darriet, M. Pezat, A. Hbike and P.Hagenmuller, *Int. J. Hydrogen Energy*, 5 (1980) 173.

[31] B. Darriet, M. Pezat, A. Hbike and P.Hagenmuller, *Mat. Res. Bull.*, 14 (1979) 377.

[32] J. C. Bolcich, A. A. Yawuy, H. L. Corso, H. A. Pertti and C. O. Anala, *Int. J. Hydrogen Energy*, 19 (1994) 605.

[33] K. Dutta, P. Mondal, K. Ramakrishna and O.N. Srivastava, *Int. J. Hydrogen Energy*, 19 (1994) 253.

[34] H. Imamura, *J. Less-Common Met.*, 172-174 (1991) 1064.

[35] S. Orimo, H. Fujii and M. Tabata, *J. Alloys Comp.*, 210 (1994) 37.

[36] B. Bogdanovic, T. H. Hartwig and B. Spliethof, *Int. J. Hydrogen Energy*, 18 (1993) 575.

[37] M. Y. Song, E. Ivanov, B. Darriet, M. Pezat and P. Hagenmuller, *J. Less-Common Met.*, 131 (1987) 71.

[38] H. Imamura, Y. Murata and S. Tsuchiya, *J. Less-Common Met.*, 135 (1987) 277.

[39] M. Pezat, B. Darriet and P. Hagenmuller, *J. Less-Common Met.*, 74 (1980) 427.

[40] D. Lupu, A. Biris, E. Indera, N. Alda and R.V.Bucur, *Int. J. Hydrogen Energy*, 8 (1983) 701 & 797.

[41] N. Cui, B. Luan, H. J. Zhao, H. K. Liu and S. X. Dou, *J. Power Source*, 55 (1995) 263.

[42] N. Cui, B. Luan, H. J. Zhao, H. K. Liu and S. X. Dou, *J. Alloys Comp.*, 233 (1996) 236.

[43] T. R. P. Gibb, *J. Electrochem. Soc.*, 93 (1948) 198.

[44] *Metal Hydrides*, (W. M. Mueller, J. P. Blackledge and G. G. Libowitz eds.), Academic Press, NY, (1968).

[45] A. J. Maeland, *Hydrides for Energy Storage*, (A. F. Andresen and A. J. Maeland ads.), Pergamon Press, Oxford, (1978), p19.

[46] D. G. Ivey and D. O.Northwood, *J. Mat. Sci.*, 18 (1983) 321.

[47] T. R. P. Gibb, Jr., *Progress in Inorganic Chemistry,* Interscience, New York. 3 (1962) 315

[48] G. G. Libowitz, *The Solid-State Chemistry of Binary Metal Hydrides,* W.A. Benjamin, Inc., New York, 1965.

[49] W. M. Mueller, J. P. Blackledge and G.G. Libowitz, *Metal Hydrides,* Academic Press, New York, 1968.

[50] K. M. Mackay, *Hydrogen Compounds of the Metallic Elements,* E. & F. N. Spon Ltd., London, 1966.

[51] G. G. Libowitz, *Solid State Chemistry,* (L.E.J. Roberts ed.), Butterwirths Ltd., London, 1972, p79.

[52] N. F. Mott and H. Jones, *The Theory of the Properties of Metals and Alloys,* Dover Publications, Inc., New York, 1936.

[53] G. G. Libowzti and T. R. P. Gibb, Jr., *J. Phys. Chem.*, 60 (1956) 510.

[54] C. D. Gellett, *Hydrides for Energy Storage* (A.F. Andresen and A.J. Maeland ads.), Pergamon Press, Oxford, (1978), p169.

[55] A. C. Switendick, *Solid State Commun.*, 8 (1970) 1463.

[56] A. C. Switendick, *Int. J. Quant. Chem.*, 5 (1971) 459.

[57] A. C. Switendick, *J. Less-Common Met.*, 49 (1976) 283.

[58] A. C. Switendick, *Topics in Applied Physics: V 28, Hydrogen in Metals I,* (G. Alefeld and J. Voklkl eds.), Springer Verlag, NY, 1978, p101.

[59] W. E. Wallace and S. K. Malik, *Hydrides for Energy Storage,* (A.F. Andresen and A.J. Maeland eds.), Pergamon Press, Oxford, 1978, p33.

[60] D. G. Westlake, C. B. Satterthwaite and J. H. Weaver, *Physics Today,* Nov. 1978, p32.

[61] J. H. Van Vucht, F. A. Kuijpers and H. C. Brunning, *Phillips Res. Repts* 25 (1970) 133.

[62] M. Gambini, *Int. J. Hydrogen Energy,* 19 (1994) 81.

[63] D. M. Gruen, *Metal-Hydrogen Systems* (T.N. Veziroglu ed.), Pergamon Press, Florida, USA (1982), p3.

[64] M. Groll, A. Isselhorst and M. Wierse, *Int. J. Hydrogen Energy,* 19 (1994) 507

[65] H. Buchner, *Hydrides for Energy Storage* (A.F. Andresen and A.J. Maeland ads.), Pergamon Press, Oxford, (1978), p569.

[66] A. J. Maeland, *ibid,* p19.

[67] J. J. Reilly, *ibid,* p301.

[68] D. G. Ivey and D. O. Northwood, *Z. Phys. Chem. N.F.*, 147 (1987) 191.

[69] G. D. Sandrock and P. D. Goodell, *J. Less-Common Met.*, 73 (1980) 161.

[71] R. L. Cohen, K. W. West and J.H. Wernick, *ibid,* 70 (1980) 229.

[72] S. Suda, Y. Komazaki, H. Narasaki and M. Uchida, *J. Less-Common Met.*, 172 (1991) 1092.

[73] K. S. Dhathathreyan, B. L. Brinda, S. Devanathan and S. Parthasarathy, *Int. J. Hydrogen Energy,* 18 (1993) 391.

[74] A. J. Maeland, *Hydrides for Energy Storage*, (A.F. Andresen and A.J. Mealand eds.), Pergamon Press, Oxford, (1978), p19.

[75] J. J. Reilly, *USNTIS,* DE92005000.

[76] I. P. Jain and Y. K. Vijay, *Progress in Hydrogen Energy*, (R.P. Dahiya ed.), D. Reidel Publishing Company, New Delhi, (1985), p111.

[77] D. G. Westlake, *J. Less-Common Met.*, 91 (1983) 1

[78] C. E. Lundin, F. E. Lynch and C. B. Magee, *J. Less-Common Met.*, 56 (1977) 19

[79] M. H. Mendelsohn, D. M. Gruen and A. E. Dwight, *J. Less-Common Met.*, 63 (1979) 193

[80] J. C. Achard, A. Percheron-Guegan, H. Diaz and F. Briaucourt, *Proc. 2nd Int. Cong. on Hydrogen in Metals*, (F.Demany ed.), Paris, June 1977, Vol.3, Pergamon, Oxford, 1978, Paper 1E12.

[81] T. Takeshita, K. A. Gschneidner, D. K. Thome and O. D. McMasters, *Phys. Rev.* B, 21 (1980) 5653.

[82] D. O.Welch and M. A. Pick, *Phys. Lett.* A, 99 (1983) 183.

[83] J. Clinton, H. Bittner and H. Oesterreicher, *J.Less-Common Met.*, 35 (1974) 65.

[84] K. H. J. Buschow, P. C .P. Bouten and A. R. Miedema, *Rep. Prog. Phys.*, 45 (1982) 937.

[85] H. H. Van Mal, K. H. J. Buschow and A. R. Miedema, *J. Less-Common Met.*, 35 (1974) 65.

[86] A. Pasturel, F. Liautaud, C. Colinet, A. Percheron-Guegan and J.C. Achard, *J. Less-Common Met.*, 96 (1984) 93.

[87] R. Griessen and A. Driessen, *J. Less-Common Met.*, 103 (1984) 235.

[88] W. E. Wallace and F. Pourarian, *J. Phys. Chem.*, 86 (1982) 4958.

[89] R. V. Bucur and D. Lupu, *J. Less-Common Met.*, 90 (1983) 203.

[90] S. D. Goren and C. Korn, *J. Less-Common Met.*, 73 (1980) 261.

[91] A. C. Switendick, *Z. Phys. Chem. N.F.*, 117 (1979) 89.

[92] E. L. Huston and G. D. Sandrock, *J. Less-Common Met.*, 74 (1980) 435.

[93] A. R. Miedema, R. Boom and F. R. deBoer, *J. Less-Common Met.*, 41(1975)283.

[94] A. R. Miedema, *J. Less-Common Metals*, 32(1973)117.

[95] E. Akiba, H. Hayakawa, Y. Ishido and K. Nomura, *J. Less-Common Met.*, 172-174 (1991)1071.

[96] J. J. Reilly, *Hydrides for Energy Storage*, (Gielo, Norway, A. F. Andresen and A. J. Mealand eds.), Pergamon Press, Oxford, (1978), p301.

[97] N. Cui, B. Luan, H. J. Zhao, H. K. Liu and S. X. Dou, *J. Alloys Comp.*, in press (1996).

[98] S. Wakao and Y. Yonemura, *J. Less-Common Met.*, 89 (1983) 481.

[99] C. Iwakura, T. Asaoka, H. Yoneyama, T. Sakai, K. Oguro, and H. Ishikawa, *Nippon Kagaku Kaishi*, (1988) 1482.

[100] T. Sakai, H. Miyamura, N. Kuriyama, A. Kato, K. Oguro, and H. Ishikawa, *J. Electrochem. Soc.*, 137 (1990) 795.

[101] T. Sakai, H. Miyamura, N. Kuriyama, A. Kato, K. Oguro, and H. Ishikawa, *J. Less-Common Met.*, 159 (1990) 127.

[102] H. H. Vanmal, K. H. J. Buschow and A. R. Miedema, *J. Less-Common Met.*, 35 (1974) 65.

[103] J. F. Lakner, F. S. Uribe and S. A. Steward, *J. Less-Common Met.*, 72 (1980) 87.

[104] H. Oesterreicher, *Mater. Res. Bull.*, 13 (1978) 83.

[105] V. K. Sinha, F. Pourarian and W. E. Wallace, *J. Phys. Chem.*, 86 (1982) 4952.

[106] F. Pourarian, V. K. Sinha and W. E. Wallace, *J. Phys. Chem.*, 86 (1982) 4956.

[107] P. Selvam, B. Viswanathan, C. S. Swamy and V. Srinivasan, *Int. J. Hydrogen Energy*, 11 (1986) 169.

[108] F. H. Ellinger, C. E. Holley, B. B. McInteer, D. Pavone and R. M. Potter, *J. Amer. Chem. Soc.*, 77 (1955) 2647.

[109] W. H. Zachariasen, C. E. Holley, Jr., and J.F. Stampfer, Jr., *Acta Crystallogr.*, 16 (1963) 352.

[110] W. Freundlich and B. Claudel, *Bull. Soc. Chim., Frence*, 23 (1956) 967.

[111] R. Yu and P. K. Lam, *Phys. Rev.* B, 37 (1980) 8730

[112] A. Karty, J. Grunzweig-Genossar and P.S. Rudman, *J. Appl. Phys.*, 50 (1979) 7200.

[113] M. H. Mintz, Z. Gavra, G. Kimmel and Z. Hadari, *J. Less-Common Met.*, 74 (1980) 263.

[114] Z. Luz, J. Senossar and P. S. Rudman, *J. Less-Common Met.*, 73 (1980) 113.

[115] A. Sailer, L. Schlaphach, T. Waldkrich, D. Schltiel and F. Stucki, *J. Less-Common Met.*, 73 (1980) 193.

[116] J. A. Kenneley, J. W. Warwing and H. W. Myers, *J.Phys.Chem.*, 64 (1960) 703.

[117] H. Nagai, H, Tomizawa and T. Ogaswara, *J. Less-Common Met.*, 157 (1990) 15.

[118] Y. Kume and A. Weiss, *J. Less-Common Met.*, 136 (1987) 51.

[119] B. Vigeholm, J. Kjoller, B. Larsen and A.S. Pederson, *J. Less-Common Met.*, 89 (1983) 135.

[120] K. Videm, *Hydrides for Energy Storage*, (A.F. Andresen and A.J. Maeland eds.), Pergamon Press, Oxford, 1978, p463.

[121] A. Karty, J. Grunzweig-Genossar and P.S. Rudman, *J. Appl. Phys.*, 50 (1979) 7200.

[122] A. Seiler, *J. Less-Common Metals*, 73 (1980) 193.

[123] G. G. Libowitz, *J. Phys. Chem.*, 76 (1958) 62.

[124] J. J. Reilly and R. H. Wiswall, *Inorg. Chem.*, 6 (1967) 2220.

[125] J. Genossar and P. S. Rudman, *Z. Phys. Chem. N.F.*, 116 (1979) 215.

[126] A. Karty, J. Genossar and P. S. Rudman, *J. Appl. Phys.*, 50 (1979) 7200.

[127] M. E. Hammioui, L. Belkbir and N. Gerard, *J. Alloys Comp.*, 202 (1993) 199.

[128] L. Schlapbach, A. Seiler, H. C. Siegmann, T. V. Waldkirch and P. Zurcher, *Int. J. Hydrogen Energy*, 4 (1979) 21.

[129] S. H. Lim and J. Y. Lee, *Int. J. Hydrogen Energy*, 8 (1983) 369.

[130] C. N. Park and J.Y. Lee, *J. Less-Common Met.*, 83 (1980) 39.

[131] J. M. Boulet and N. Gerard, *J. Less-Common Met.*, 89 (1983) 151

[132] M. Pezat, B. Darriet and P. Hagenmuller, *J. Less-Common Metals*, 74 (1980) 427.

[133] J. J. Reilly and R. H. Wiswall, *Inorg. Chem.*, 7 (1968) 2254.

[134] V. I. Mikheeva, Z.K. Sterlyadkina, A. I. Konstantinova and O. N. Kryukova, *Russ. J. Inorg. Chem.*, 8 (1963) 682.

[135] M. Pezat, B. Darriet and P. Hagenmuller, *J. Less-Common Met.*, 74 (1980) 427.

[136] K. Ogawa, H. Aoki and T. Kobayashi, *J. Less-Common Met.*, 88 (1982) 283.

[137] J. M. Welter and P. S. Rudman, *Scripta Metall.*, 16 (1982)285.

[138] J. J. Didisheim, P. Zolliker, K. Yvon, P. Fischer, J. Schefer, M. Gubelman and A. F. Williams, *Inorg. Chem.*, 23 (1984) 1953.

[139] J. J. Didisheim, P. Zolliker, K. Yvon, P. Fischer, J. Schefer, M. Gubelman and A. F. Williams, *Z. Kristallogr.*, 162 (1983) 61.

[140] D. L. Douglass, *Hydrides for Energy Storage*, (A.F. Andresen and A.J. Maeland eds.), Pergamon Press, Oxford, 1978, p151.

[141] D. L. Douglass, *Metall. Trans.*, 6A (1975) 2179

[142] J. F. Nachman and D. A. Rohy, *Metal-Hydrogen System*, (T.N. Veziroglu ed.), Pergamon Press, New York, 1982, p577.

[143] M. H. Mintz, S. Malkiely, Z. Gavra and Z. Hadari, *J. Inorg. Nucl. Chem.* 40 (1978) 1949.

[144] F. G. Eisenberg, D. A. Zagnoli and J. J. Sheridan, *J. Less-Common Met.*, 74 (1980) 323.

[145] A. A. Nayeb-Hashemi and J. B. Clark, *Phase Diagrams of Binary Nickel Alloys* (P. Nash ed.), Materials Park, Ohio, 1991, p193.

[146] K. Schubert and K. Anderko, *Z. Metallkd.*, 42 (1951) 321.

[147] J. Schefer, P. Fischer, W. Halg, F. Stucki, L. Schlapbach, J. J. Didisheim, K. Yvon and A. T. Andresen, *J. Less-Common Met.*, 88 (1980) 63.

[148] B. Darriet, J. L. Soubeyroux and M. Pezat, *J. Less-Common Met.*, 104 (1983) 153.

[149] Z. Gavra, M.H. Mintz, G. Kimmel and Z. Hadri, *Inorg. chem.*, 18 (1979) 3595.

[150] J. Schefer, P. Fisher, W. Halg, F. Stucki, L. Schlapbach, J.J. Didisheim, K. Yvon and A.F. Andresen, *J. Less-Common Met.*, 74 (1980) 65.

[151] K. Yvon, J. Schefer and F. Stucki, *Inorg. Chem.*, 20 (1981) 2776.

[152] D. Noreus and L. G. Olsson, *J. Chem. Phys.*, 78 (1983) 2419.

[153] D. Noreus and P. E. Werner, *J. Less-Common Met.*, 97 (1984) 215.

[154] D. Noreus and P. E. Werner, *Mater. Res. Bull.*, 16 (1981) 199.

[155] S. Ono, H. Hayakawa, A. Suzuki, K. Nomura, N. Nishimiya and T. Tabata, *J. Less-Common Met.*, 88 (1982) 63.

[156] H. Hayakawa, Y. Ishido, K. Nomura, H. Uruno and S. Ono, *J. Less-Common Met.*, 103 (1984) 277.

[157] J. L. Soubeyroux, D. Fruchart, A. Mikou, M. Pezat and B. Darriet, *Mater. Res. Bull.*, 19 (1984) 1119.

[158] J. P. Darnaudery, M. Pezat and B. Darriet and P. Hagenmuller, *Mater. Res. Bull.*, 16 (1981) 1237.

[159] T. Hirata, T. Matsumoto, M. Amano and Y. Sasaki, *J. Phys. F.*, 11(1981) 521.

[160] Z. Gavra, G. Kimmel, Y. Gefen and M. H. Mintz, *J. Appl. Phys.*, 57 (1985) 4548.

[161] P. Zolliker, K. Yvon, J. D. Jorgensen and F. J. Rotella, *Inorg. Chem.*,25 (1986) 3590.

[162] S. Hayashi and K. Hayamizu, *Less-Common Metals*, 155 (1989) 31.

[163] S. Hayashi, K. Hayamizu and O.Yamamoto, *J. Chem. Phys.*, 79 (1983) 2308.

[164] S. Hayashi, K. Hayamizu and O.Yamamoto, *J. Chem. Phys.*, 79 (1983) 5572.

[165] P. Zolliker and K. Yvon, *Less-Common Met.*, 115 (1986) 65.

[166] P. Zolliker and K. Yvon, *Mater. Res. Bull.*, 21 (1986) 415.

[167] J. L. Soubeyroux, D. Fruchart, A. Mikou, M. Pezat and B. Darriet, *Mater. Res. Bull.*, 19 (1984) 969.

[168] J. Genossar and P. S. Rudman, *J. Phys. Chem. Solids*, 42 (1981) 611.

[169] S. Orimo and H. Fujii, *J. Alloys Comp.*, 232 (1996) L16.

[170] K. Nomura, E. Akiba and S. Ono, *Int. J. Hydrogen Energy*, 6 (1981) 295.

[171] D. Lupu, A. Biris, G. Mihailescu, R. Sarbu and D. Vonica, *Int. J. Hydrogen Energy*, 13 (1988) 685.

[172] M. Y. Song, B. Darriet, M. Pezat, J. Y. Lee and P. Hagenmuller, *J. Less-Common Met.*, 118 (1986) 235.

[173] M. Y. Song, *J. Less-Common Met.*, 157 (1990) 155.

[174] H. Oesterricher, K. Ensslen, A. Kerlin and E. Bucher, Mater. *Res. Bull.*, 15 (1980) 275.

[175] P. Selvam, B. Viswanathan, C. S. Swamy and V.Srinivasan, *Int. J. Hydrogen Energy*, 13 (1988) 87.

[176] S. Ono, K. Nomura, K. Suzuki, S. Higano and K. Kamino, *Trans. Japan Inst. Met. Suppl.*, 21 (1980) 361.

[177] D. Lupu, A. Biris, E. Indera, N. Alda and R. V. Bucur, *Int. J. Hydrogen Energy*, 7 (1982) 783.

[178] T. Hirata, T. Matsumoto, M. Amano and Y. Sasaki, *J. Less-Common Met.*, 89 (1983) 85.

[179] J. P. Darnaudery, M. Pezat and B. Darriet, *J. Less-Common Met.*, 92 (1983) 199.

[180] J. P. Darnaudery, B. Darriet and M. Pezat, *Int. J. Hydrogen Energy*, 8 (1983) 705.

[181] P. Selvam, B. Viswanathan, C. S. Swamy and V. Srinivasan, *Bull. Mater Sci.*, 9 (1987) 21; Agency of industrial Sciences and technology, Mitsubishi Steel Manufacturing Company Ltd, Appl. 79/111, 422, 31 August 1979, *Chem. Abst.* 95, No. 118464u (1981).

[182] H. Fujii, S. Orimo, K. Yamamoto, K. Yoshimoto and T. Ogasawara, *J. Less-Common Met.*, 175 (1991) 243.

[183] S. Orimo, H. Fujii, K. Yamamoto, K. Yoshimoto and T. Ogasawara, *J. Japan Inst. Metals,* 54 (1990) 1154.

[184] H. Nagai, H. Tomizawa, T. Ogasawara and K. Shoji, *J. Less-Common Met.*, 157 (1992) 15.

[185] P. Mandal, K. Dutta, K. Ramakrishna, K. Sapru and O.N. Srivastava, *J. Alloys Comp.*, 184 (1992) 1.

[186] P. Mandal and O. N. Srivastava, *J. Alloys Comp.*, 205 (1994) 111.

[187] S. Orimo, H. Fujii and M. Tabata, *J. Alloys Comp.*, 210 (1994) 37.

[188] S. Orimo, M. Tabata and H. Fujii, *J. Alloys Comp.*, 203 (1994) 61.

[189] Zhou Ye, L. C. Erickson, B. Hjorvarsson, *J. Alloys Comp.*, 209 (1994) 117.

[190] K. Dutta and O. N. Srivastava, *Int. J. Hydrogen Energy*, 18 (1993) 397.

[191] M. Khrussanova, M. Terzieva, P. Peshev and E. Ivanov, *Mater. Res. Bull.*, 22 (1987) 405.

[192] M. Khrussanova, M. Terzieva, P. Peshev, I. Konstanchuk and E. Ivanov, *Z. Phys. Chem. N.F.*, 164 (1989) 1261.

[193] M. Khrussanova, M. Terzieva and P. Peshev, *Int. J. Hydrogen Energy*, 15 (1990) 799.

[194] M. Khrussanova, M. Terzieva and P. Peshev, *Int. J. Hydrogen Energy*, 16 (1991) 265.

[195] B. Bogdanovic, T. H. Hartwig and B. Spliethoff, *Int. J. Hydrogen Energy*, 18 (1993) 575.

[196] H. Imamura, M. Takashima and S. Tsuchiya, *J. Less-Common Met.*, 95 (1983) 157.

[197] P. Selvam, B. Viswanathan, C. S. Swamy and V. Srinivasan, *Int. J. Hydrogen Energy*, 11 (1986) 169.

[198] B. Bogdanovic, *Int. J. Hydrogen Energy*, 9 (1984) 937.

[199] H. Y. Zhu, C. P. Chen, Y. Q. Lei, J. Wu and Q. D. Wang, *J. Less-Common Met.*, 172-172 (1991) 873.

[200] H. Imamura, T. Takahashi, R. Galleguilos and S. Tsuchiya, *J. Less-Common Met.*, 89 (1983) 251.

[201] H. Imamura, T. Nobunaga and S. Tsuchiya, *J. Less-Common Met.*, 106 (1985) 229.

[202] H. Imamura, *J. Less-Common Met.*, 153 (1989) 161.

[203] H. Imamura and M.Takashima, *Int. J. Hydrogen Energy*, 15 (1990) 911.

[204] F. G. Eisenberg, D. A. Zagnoli and J. J. Sheridan III, *J. Less-Common Met.*, 74 (1980) 323.

[205] F. J. Liu, G. Sandrock and S. Suda, *Z. Phys. Chem.*, 183 (1994) 163.

[206] F. J. Liu and S. Suda, *J. Alloys Comp.*, 232 (1996) 212.

[207] F. J. Liu and S. Suda, *J. Alloys Comp.*, in press.

[208] X. L. Wang and S. Suda, *Z. Phys. Chem.*, 183 (1994) 385.

[209] N. Haraikawa, H, Hagiwara, K. Iwatake, Y. Sugiyama, S. Okamoto, X.L. Wang, S. Suda, *Res. Reps. Kogakuin's University*, 77 (1994) 57.

[210] S. R. Ovshinsky, M. A. Fetcenko and J. Ross, *Science*, 260 (1993) 176.

[211] C. Iwakura and M. Matsuoka, *Prog. Batt. & Solar Cells*, 10 (1991) 81.

[212] E. W. Justi, H. H. Ewe, A. W. Kalberlah, N. M. Saridaki and M. H. Schaefer, *Energy Conversion*, 10 (1970) 183.

[213] M. A. Fetcenko and S. Venkatesan, *Prog. Batt. & Solar Cells*, 9 (1990) 259.

[214] K. S. Nahm, W. Y. Kim, S. P. Hong and W. Y. Lee, *Int. J. Hydrogen Energy*, 17 (1992) 333.

[215] O. Boser, *J. Less-Common Met.*, 46 (1976) 91.

[216] M. Miyamoto, K. Yamaji and Y. Nakata, *J. Less-Common Met.*, 89 (1983) 11.

[217] S. Tanaka, J. D. Clewley and T. B. Flnagan, *J. Phys. Chem.*, 81 (1977) 1648.

[218] B. R. Livesay and J. W. Larsen, *Proc. JIMIS-2, Hydrogen in Metals*, 1979, p.345.

[219] W. E. Wallace, R. F. Karlicek, Jr and H. Imamura, *J. Phys. Chem.*, 83 (1979) 1708.

[220] K. Soga, H. Imamura and S. Ikeda, *J. Phys. Chem.*, 81 (1977) 601.

[221] Lu Man-qi, O. Zhen-Zhong and W. Ping-sen, *Proc. JIMIS-2, Hydrogen in Metals*, 1979, p431.

[222] C. N. Park and J. Y. Lee, *J. Less-Common Met.*, 83 (1982) 39.

[223] P. Huang, A. J. Goudy and J. T. Koh, *J. Less-Common Met.*, 155 (1989) 111.

[224] K. S. Nahm, W. Y. Kim, S. P. Hong and W. Y. Lee, *Int. J. Hydrogen Energy*, 17 (1992) 333.

[225] K. S. Nahm, W. B. Jung and W. Y. Lee, *Int. J. Hydrogen Energy*, 15 (1990) 635.

[226] W. B. Jung, K. S. Nahm and W. Y. Lee, *Int. J. Hydrogen Energy*, 15 (1990) 641.

[227] E. Akiba, K. Nomura, S. Ono and S. Suda, *Int. J. Hydrogen Energy*, 7 (1982) 787.

[228] K. Nomura, E. Akiba and S. Ono, *Int. J. Hydrogen Energy*, 6 (1981) 295.

[229] H. M. Lutz and O. de Pous, *2nd Int. Congress Hydrogen in Metals*, 1980, p295.

[230] F. Stucki, *Int. J. Hydrogen Energy*, 8 (1983) 49.

[231] M. Y. Song, M. Pezat, B. Darriet, J. Y. Lee and P. Hagenmuller, *J. Mater. Sci.*, 21 (1986) 346.

[232] J. S. Han and J. Y. Lee, *J. Less-Common Met.*, 131 (1987) 109.

[233] S. Mattsoff and D. Noreus, *Int. J. Hydrogen Energy*, 12 (1987) 333.

[234] M. Y. Song, M. Pezat, B. Darriet, J. Y. Lee and P. Hagenmuller, *J. Less-Common Met.*, 103 (1984) 145.

[235] G. Sandrock, *Hydrogen Energy System*, (Yuda Yürüm ed.), Kluwer Academic Publishers, Dordrecht, 1994, p275.

[236] JCPDS, *Powder Diffraction File*, 38-948, 40-1206, 40-1204, 1989.

[237] Y. Zhou, L.C. Erickson, B. Hjorvarsson, *J. Alloys Comp.*, 209 (1994) 117.

[238] J.J. Podesta, R.C.V. Pitti, A.J. Arvia, P.Ekdung, K. Juttner and G. Kreysa, *Int. J. Hydrogen Energy*, 17 (1992) 9.

[239] M. Matsuoka, M. Terashima and C. Iwakura, *Electrochim. Acta*, 38 (1993) 1087.

[240] M. Matsuoka, K. Asai, Y. Fukumoto and C. Iwakura, *Electrochim. Acta*, 38 (1993) 659.

[241] H. Inoue, K. Yamataka, Y. Fukumoto and C. Iwakura, *J. Electrochem. Soc.*, 143 (1996) 2527.

[242] G.G. Libowtiz and A.J. Maeland, *Mater. Sci. Forum*, 177 (1989) 31.

[243] A.Y. Esayed and D.O. Northwood, *Int. J. Hydrogen Energy*, 17 (1992) 41.

[244] B.V. Ratnakumar, C. Witham, R.C. Bowman, Jr., A. Hightower and B. Fultz, *J. Electrochem. Soc.*, 143 (1996) 2578.

[245] F. Pourarian, V.K. Sinha, W.E. Wallace and H.K. Smith, *J. Less-Common Met.*, 88 (1982) 451.

[246] M. Yoshida and E. Akiba, *J. Alloys Comp.*, 224 (1995) 121.

[247] M.H. Mendelsohn, D.M. Gruen and A.E. Dwight, *Nature*, 269 (1977) 45.

[248] S. Fujitani, I. Yonezu, T. Satio, N. Furukawa, E. Akiba, H. Hayakawa and S. Ono, *J. Less-Common Met.*, 172-174 (1991) 220.

[249] J.M. Park and J.Y. Lee, *J. Less-Common Met.*, 160 (1990) 259.

[250] Goodfellow Catalogue 1996/1997, *Metal Data Table*, p17-25.

[251] I. Rubinstein, *Physical Electrochemical*, Marcel Dekker, Inc., New York, 1995, p16.

[252] C. Iwakura, Y. Fukumoto, M.. Matsuoka, T. Kohno and K. Shinmou, *J. Alloys Comp.*, 192 (1993) 152.

[253] T. Sakai, H. Miyamura, N. Kuriyama, A. Kato, K. Ogura and H. Ishikawa *J. Electrochem. Soc.*, 137 (1990) 795

[254] B. Luan, N. Cui, H. J. Zhao, H. K. Liu and S. X. Dou, *J. Power Sources*, 52 (1994) 295.

[255] T. Sakai, *J. Electrochem. Soc.*, 134 (1987) 558.

[256] J. J. Willems, *Philips J. Res.* 39 (1984) 54.

[257] P.H.L. Notten and P. Hokkeling, *J. Electrochem. Soc.*, 138 (1991) 1877.

[258] A. I. Shilow, M.E. Kost and N.T. Kuznesov, *J. Less-Common Met.*, 144 (1988) 23.

[259] Julian R. Frederick, *Ultrasonic Engineering*, John Wiley & Sons, New York, 1965.

[260] D. Ensminger, *Ultrasonics*, 2nd ed., Marcel Dekker, New York, 1988.

[261] N. Kuriyama, T. Sakai, H. Miyamura, I. Uehara, H. Ishikawa, *J. Alloys Comp.*, 202 (1993) 183.

[262] P. L. Cabot, J. A. Garrido, E. Perez, A. H. Moreira, P. T. A. Sumodjo and W. Proud, *Electrochimica Acta*, 40 (1995) 447.

[263] J. Pang, A. Briceno and S. Chander, *J. Electrochem. Soc.*, 137 (1990) 3347.

[264] B. Luan, N. Cui, H. J. Zhao, H. K. Liu and S. X. Dou, *J. Power Source*, 55 (1995) 101.

[265] B. Luan, N. Cui, H. J. Zhao, H. K. Liu and S. X. Dou, *Int. J. Hydrogen Energy*, 21 (1996) 373.

[266] B. Luan, N. Cui, H. J. Zhao, H. K. Liu and S. X. Dou, *J. Alloys Comp.*, 233 (1996) 225.

[267] B. Luan, N. Cui, H. J. Zhao, H. K. Liu and S. X. Dou, *J. Power Source*, 55 (1995) 263

[268] F. Meli, A. Zuttel, and L. Schlapbach, *J. Alloys Comp.*, 202 (1993) 81.

[269] R. Varma, J.R. Selman, *Techniques for Characterization of Electrodes and Electrochemical Processes*, John Wiley & Sons, Inc., New York, 1991.

[270] J. Ross Macdonald, *Impedance Spectroscopy*, John Willey & Sons, Inc., New York, 1987.

[271] Israel Rubinstein, *Physical Electrochemistry*, Marcel Dekker, Inc., New York, 1995.

[272] R.G. Kelly and P.J. Mora, *J. Electrochem. Soc.*, 134 (1987) 25.

[273] W. Jenseit, O. Bohme, F.U. Leidich and H. Wendt, *Electrochim. Acta* 38 (1993) 2115.

[274] S. Brinic, M. Metikos-Hukovic and R. Babic, *J. Power Sources*, 55 (1995) 19.

[275] M. Bojinov, Y. Geronov, G. Pistoia and M. Pasquali, *J. Electrochem. Soc.*, 140 (1993) 294.

[276] N. Kuriyama, T. sakai, H. Miyamura, I. Uehara, H. Ishihawa and T. Iwaski, *J. Alloys Comp.*, 202 (1993) 183.

[277] N. Kuriyama, T. sakai, H. Miyamura, I. Uehara, H. Ishihawa and T. Iwaski, *J. Electroch. Soc.*, 139 (1992) L72.

[278] B.V. Ratmakumar, C. Witham, R.C. Bowman, Jr., A. Hightower, and B. Fultz, *J. Electrochem. Soc.*, 143 (1996) 2578.

[279] N. Cui, B. Luan, H. K. Liu and S. X. Dou, *J. Alloys Comp.*, 248 (1997) 159.

[280] A.J. Bard and L.R. Faulkner, *Electrochemical Methods Fundamenyals and Applications*, John Wiley & Sons, New York, 1980, p329.

[281] J.J.G. Willems and K.H.J. Buschow, *J. Less-Common Met.*, 129 (1987) 13.

[282] S.D. Goren and C. Korn, *J. Less-Common Met.*, 73 (1980) 261.

[283] K. Dutta, P. Manda, K. Ramakrishna and O. N. Srivastava, *Int. J. Hydrogen Energy*, 19 (1994) 253.

[284] B. Tanguy, J. L. Soubeyroux, M. K. Pezat, J. Portier and P. Hagenmuller, *Mater. Res. Bull.*, 11 (1976) 14441.

[285] K. Videm, *Hydrides for Energy Storage*, (A. F. Andresen and A. J. Maeland ads.), Pergamon Press, Oxford, (1978), p463.

[286] P. L. Cabot, J. A. Garrido, E. Perez, A. H. Moreira, P. T. A. Sumodjo and W. Proud, *Electrochimica Acta*, 40 (1995) 447.

[287] J. Pang, A. Briceno and S. Chander, *J. Electrochem. Soc.*, 137 (1990) 3347

[288] B. Luan, N. Cui, H. J. Zhao, H. K. Liu and S. X. Dou, *Int. J. Hydrogen Energy*, 21 (1996) 373.

[289] B. Luan, N. Cui, H. J. Zhao, H. K. Liu and S. X. Dou, *J. Alloys Comp.*, 233 (1996) 225.

[290] B. Luan, N. Cui, H. J. Zhao, H. K. Liu and S. X. Dou, *J. Power Source*, 55 (1995) 263.

[291] P. Mandal, K. Dutta, K. Ramakrishna, K. Sapru and O. N. Srivastava, *J. Alloys Comp.*, 184 (1992) 1.

[292] N. Kuriyama, T. Sakai, H. Miyamura, I. Uehara and H. Ishikawa, *J. Electrochem.* Soc., 139 (1992) L72.

[293] N. Kuriyama, T. Sakai, H. Miyamura, I. Uehara and H. Ishikawa, *J. Alloys Comp.*, 192 (1993) 161.

[294] N. Kuriyama, T. Sakai, H. Miyamura, I. Uehara, H. Ishikawa, *J. Alloys Comp.*, 202 (1993) 183.

[295] P. Sewam, B. Viswanathan, C.C. Swanny and V. Srinivasan, *Int. J. Hydrogen Energy*, Vol.13, No.2 (1988) 82.

[296] J.J. Podesta, R.C.V. Pitti, A.J. Arvia, P. Ekdung, K. Juttner and G. Kreysa, *Int. J. Hydrogen Energy*, Vol. 17, No. 1 (1992) 9.

[297] P. Sewam, B. Viswanathan, C.C. Swanny and V. Srinvasan, *Int. J. Hydrogen Energy*, Vol.10, No.3 (1986) 169.

PUBLICATIONS

I. Refereed papers:

1 **N. Cui**, B. Luan, H. Zhao, H.K. Liu, and S.X. Dou, "Comparative study of electrochemical behaviour of single-crystalline and polycrystalline $LaNi_5$ alloy electrodes", *J. Alloys Comps.*, 248 (1997)159.

2 **N. Cui**, B. Luan, H. Zhao, H.K. Liu, and S.X. Dou, "Discharge behaviours of Mg_2Ni-Type Hydrogen storage alloy electrode in 6M KOH solution by electrochemical impedance spectroscopy", *J. Power Sources*, 63 (1997) 209.

3 **N. Cui**, B. Luan, H. Zhao, H.K. Liu, and S.X. Dou, "Synthesis and electrode characteristics of the new composite alloys Mg_2Ni-x *wt.*%Ti_2Ni", *J. Alloys Comps.*, 240 (1996) 229.

4 **N. Cui**, B. Luan, H. Zhao, H.K. Liu, and S.X. Dou, "Effects of yttrium additions on the electrode performance of magnesium-based hydrogen storage alloys", *J. Alloys Comps.*, 223 (1996) 236.

5 B. Luan, **N. Cui**, H. Zhao, H.K. Liu, and S.X. Dou, "Effects of potassium-boron addition on the performance of titanium based hydrogen storage alloy electrodes"; *Int. J. Hydrogen Energy*, 21 (1996) 373.

6 B. Luan, **N. Cui**, H. Zhao, H.K. Liu, and S.X. Dou, "Studies on the performance of $Ti_2Ni_{1-x}A_x$ hydrogen storage alloy electrodes", *J. Alloys Comps.*, 223 (1996) 225

7 **N. Cui**, B. Luan, H. Zhao, H.K. Liu, and S.X. Dou; "Characteristics of magnesium-based hydrogen storage alloy electrodes", *J. Power Sources*, 55 (1995) 263.

8 B. Luan, **N. Cui**, H. Zhao, H.K. Liu, and S.X. Dou, "Effect of cobalt addition on the performance of titanium-based hydrogen storage electrodes", *J. Power Sources*, 55 (1995)197.

9 B. Luan, **N. Cui**, H. Zhao, H.K. Liu, and S.X. Dou, "Mechanism of early capacity loss of Ti_2Ni hydrogen storage alloy electrode", *J. Power Sources*, 55 (1995) 101.

10 B. Luan, **N. Cui**, H. Zhao, H.K. Liu, and S.X. Dou, "Low-temperature surface micro-encapsulation of Ti_2Ni hydrogen storage alloy powders", *J. of Power Sources*, 52 (1994) 295.

II. Conference Papers

11 **N. Cui**, B. Luan, D. H. Bradhurst, H.K. Liu, and S.X. Dou, "Modified Mg_2Ni-type negative electrode materials for Ni-MH battery", *Proc. the 12th Annual Battery Conf. on Applications and Advances*, (Harvey A. Frank and Eddie T. Seo ed.), Long Beach CA, Jan. 1997, IEEE, p317.

12 **N. Cui**, B. Luan, H.K. Liu, and S.X. Dou, "Electrochemical study on the Mg_2Ni-type hydrogen storage alloy electrode materials", *Proc. the 2nd Int. Sym. of New Materials for Fuel Cell and Modern Battery Systems*, Montreal, July 1997, (in press).

13 J. Chen, **N. Cui**, D. Bradhurst, B. Luan, H.K. Liu, and S.X. Dou, "Metal hydride electrodes for rechargeable batteries" *Proc. of the Symposium on*

Electrochem. Surf. Sc. of Hydrogen Adsorption and Absorption, (G. Jerkiewicz and P. Marcus ed.), Montreal, May 1997, The Electrochemical Society, p259.

14 **N. Cui**, B. Luan, H. Zhao, H.K. Liu, and S.X. Dou, "Electrochemical behaviour of magnesium-based hydrogen storage alloys", *Extended Abstracts of the 190th American Electrochemical Society conference*, San Antonio, Texas, America, Oct. 6-11, 1996.

15 **N. Cui**, B. Luan, H. Zhao, H.K. Liu, and S.X. Dou, "Synthesis and electrochemical behaviour of Mg_2Ni - *x wt.*% Ti_2Ni composite alloys", *The 125th TMS Annual Meeting*, Anaheim, California, America, Feb. 5-7, 1996.

16 B. Luan, N. **Cui**, H. Zhao, H.K. Liu, and S.X. Dou, "On the performance of Ti based hydrogen storage alloy electrode with Al additions", *The 125th TMS Annual Meeting*, Anaheim, California, America, Feb. 5-7, 1996.

17 **N. Cui**, B. Luan, H. Zhao, H.K. Liu, and S.X. Dou, "Effects on the ultrasound pre-treatment on the activation behaviour of $ZrCr_{0.8}Ni_{1.2}$ alloy electrode", *Extended Abstracts of the 188th American Electrochemical Society conference*, Volume 95-2, p158, Chicago, Illinois, America, Oct. 8-13, 1995.

18 **N. Cui**, B. Luan, H. Zhao, H.K. Liu, and S.X. Dou, "Electrode performance of $Mg_{1.8}Al_{0.2}Ni_{1-x}Y_x$ hydrogen storage alloy", *Extended Abstracts of the 188th American Electrochemical Society conference*, Volume 95-2, p168, Chicago, Illinois, America, Oct. 8-13, 1995.

19 B. Luan, **N. Cui**, H. Zhao, H.K. Liu, and S.X. Dou, "Studies on the electrochemical cycle life of $Ti_2Ni_{1-x}(KB)_x$ hydrogen storage alloy electrode", *Extended Abstracts of the 188th American Electrochemical Society conference*, Volume 95-2, p19, Chicago, Illinois, America, Oct. 8-13, 1995.

20 **N. Cui**, B. Luan, H. Zhao, H.K. Liu, and S.X. Dou, "Magnesium-based hydrogen alloy anodes for Ni-MH battery", *The 20th ANNUAL Condensed Matter Physics Meeting*, Paper WP19, Wagga Wagga, NSW, Australia, 30 January-2 February 1996.

21 H.K. Liu, B. Luan, **N. Cui**, H. Zhao and S.X. Dou, "Effects of cobalt, aluminium, and potassium-boron additions on the performance of titanium based alloy electrodes", *The 20th ANNUAL Condensed Matter Physics Meeting*, 30 January-2 February 1996, Paper WP20, Wagga Wagga, NSW, Australia.